Mesures de précision des propriétés du boson de Higgs via la désintégration en deux photons avec l'expérience ATLAS

Luca Franco

To cite this version:

Luca Franco. Mesures de précision des propriétés du boson de Higgs via la désintégration en deux photons avec l'expérience ATLAS. Physique des Hautes Energies - Expérience [hep-ex]. Université Savoie Mont Blanc, 2022. Français. NNT : 2022CHAMA001 . tel-04072010

HAL Id: tel-04072010
https://theses.hal.science/tel-04072010

Submitted on 17 Apr 2023

UNIVERSITÉ
SAVOIE
MONT BLANC

THÈSE

Pour obtenir le grade de

DOCTEUR DE L'UNIVERSITÉ SAVOIE MONT BLANC

Spécialité : **Physique Subatomique et Astroparticules**

Arrêté ministériel : 25 Mai 2016

Présentée par

Luca FRANCO

Thèse dirigée par **Marco DELMASTRO**

préparée au sein du **Laboratoire d'Annecy de Physique des Particules**
dans **l'École Doctorale de Physique**

Mesures de précision des propriétés du boson de Higgs via la désintégration en deux photons avec l'expérience ATLAS

Precision measurements of the Higgs Boson properties with the decay into two photons at the ATLAS experiment

Thèse soutenue publiquement le **13 janvier 2022**,
devant le jury composé de :

Monsieur Florian BEAUDETTE
LLR-CNRS (Palaiseau), Rapporteur
Monsieur Stéphane JEZEQUEL
LAPP-CNRS (Annecy), Président
Monsieur Karsten KÖNEKE
Albert-Ludwigs-Universität (Freiburg), Examinateur
Monsieur André David TINOCO MENDES
CERN (Genève), Examinateur
Monsieur Guillaume UNAL
CERN (Genève), Examinateur
Madame Isabelle WINGERTER-SEEZ
CPPM-CNRS (Marseille), Rapporteuse

Résumé

La découverte du boson de Higgs en 2012 a représenté un véritable jalon dans l'histoire de la physique des particules : la dernière pièce manquante du Modèle Standard (MS) a finalement été observée au Large Hadron Collider (LHC) par les collaborations ATLAS et CMS. Depuis lors, des physiciens du monde entier se demandent si cette particule est en fait le boson de Higgs ou simplement une particule très similaire à celui-ci. La seule façon de répondre à cette question est d'étudier ses propriétés avec la plus grande précision et de les comparer avec les prédictions théoriques fournies par le MS. Si un écart significatif était présent dans les mesures, ce serait un indice important de la physique au-delà du MS. Malgré un rapport de branchement très faible (environ 0,2%), la désintégration du Higgs en deux photons représente l'un des canaux les plus intéressants pour étudier les propriétés du Higgs : il bénéficie d'un rapport signal sur bruit de fond important, grâce à la signature expérimentale propre de seulement deux photons ; il est possible de profiter de la très haute résolution expérimentale en énergie des photons atteinte par le détecteur ATLAS. Les études présentées dans ce manuscrit exploitent des collisions proton-proton à une énergie de centre de masse de 13 TeV enregistrées par ATLAS au LHC, ce qui correspond à l'ensemble de données complet du Run 2 de 139 fb^{-1}. Celles-ci incluent les mesures des sections efficaces de production de Higgs et des Simplified Template Cross Sections (STXS), ainsi qu'une analyse qui vise à contraindre la largeur de la désintégration du Higgs. Tous sont entièrement réalisés avec des événements de désintégration diphotonique. Afin d'atteindre un haut niveau de précision, un étalonnage correct de l'énergie des photons est nécessaire. Dans ce contexte, une étude détaillée des non-linéarités dans l'électronique du calorimètre électromagnétique ATLAS est également présentée, ce qui contribue de manière significative à améliorer la précision de la prochaine mesure de la masse du boson de Higgs dans le canal de désintégration diphotonique.

Abstract

The discovery of the Higgs boson in 2012 represented a milestone in the history of particle physics: the last missing piece of the Standard Model (SM) was finally observed at the Large Hadron Collider (LHC) by the ATLAS and CMS collaborations. Since then, physicists around the world have questioned whether this particle is in fact the Higgs boson or another particle very similar to it. The only way to answer this question is studying its properties with the highest accuracy and comparing with the theoretical predictions provided by the SM. If any significant deviation was present in the measurements, it would be an important hint of physics Beyond the SM (BSM). Despite a very low branching ratio (about 0.2%), the Higgs decay into two photons represents one of the most interesting channel to study Higgs properties: it profits from a favorable signal over background ratio, thanks to the clean experimental signature of only two energetic photons; it is possible to take advantage of the very high experimental photon energy resolution achieved by the ATLAS detector. The studies presented in this manuscript exploit proton-proton collisions at a center-of-mass energy of 13 TeV recorded by ATLAS at the LHC, corresponding to the full Run 2 dataset of 139 fb^{-1}. These studies include the measurements of the Higgs production cross sections and Simplified Template Cross Sections (STXS), as well as an analysis which aims to constrain the Higgs decay width. All of them are carried out entirely using diphoton decay events. In order to achieve a high level of accuracy, a correct calibration of the photon energy is necessary. In this context, a detailed study of the non-linearities in the electronics of the ATLAS electromagnetic calorimeter is also presented, which significantly contributes to enhance the precision of the upcoming Higgs mass measurement in the diphoton decay channel.

Contents

Introduction

The origin of mass of the elementary particles is one of the most fundamental questions in particle physics. It is answered by the electroweak symmetry breaking (EWSB), for which the W and Z bosons become massive and from which a new particle, the Higgs boson, arises and it gives mass to the fermions through its Yukawa interaction with them.

The Higgs boson has been discovered by the ATLAS and CMS collaborations in 2012 [1] at the Large Hadron Collider (LHC) at CERN, using proton-proton collision data at the center-of-mass energy of $\sqrt{s} = 7$ and 8 TeV. All measurements done at LHC after the discovery confirm that the properties of the new particle are compatible with those predicted for the Higgs boson by the Standard Model (SM) within the size of statistical and systematic uncertainties. The investigation of the new particle properties is central to retrieve information on its couplings with gauge bosons and fermions. Studying Higgs boson properties in detail will allow us to understand if the discovered particle at LHC is really the one predicted by the SM or if it is an indirect evidence of new physics beyond the Standard Model (BSM). New physics models could explain some cosmological puzzles related to particle physics that are not explained by the SM (e.g. dark energy, dark matter, matter/anti-matter asymmetry).

Among all possible decays of the Higgs boson predicted by the SM, the decay into two photons ($H \to \gamma\gamma$) played a major role in the discovery of the particle back in 2012 and it is a key channel to study its properties. In this thesis, measurements of the Higgs boson properties in the diphoton decay channel are presented. These measurements use proton-proton collisions at a center-of-mass energy of 13 TeV recorded by ATLAS at the LHC during Run 2, corresponding to 139 fb^{-1} of integrated luminosity.

The manuscript is structured as follows: Chapter 1 consists in a brief overview of the theoretical framework which the main content of the thesis relies on; in Chapter 2 a synthetic description of the ATLAS experiment at the LHC is given; Chapter 3 introduces the reader to the problem of the energy calibration of photons in ATLAS; Chapter 4 presents a work which lead to improve the energy calibration of photons for the benefit of the analyses using diphoton events; Chapter 5 presents the measurements of the Higgs boson production cross sections and Simplified Template Cross Sections (STXS) in the diphoton decay channel; Chapter 6 presents an analysis aiming to constrain the Higgs boson decay width exploiting the interference between signal and background in $H \to \gamma\gamma$.

Chapter 1

Theoretical overview

This chapter represents a short overview of particle physics at hadron colliders and a reminder of the main concepts of the Higgs phenomenology required for the reading of the next chapters. It also gives a description of the context in which the analyses presented later in the thesis are carried out.

1.1 The Standard Model

The Standard Model of Particle Physics (SM) [2–4] currently provides the best description of the nature of fundamental particles, it explains how each particle interacts with others through three fundamental forces of our universe: **strong force**, **weak force** and **electromagnetic force**. The fourth fundamental force, the **gravitational force**, is not included in the SM. The SM describes two basic types of particle: semi-integer spin [1] particles called **fermions** and integer spin particles called **bosons**. The fundamental fermions are quarks (u, d, c, s, t, b) and leptons (e, μ, τ and their respective neutrinos ν_e, ν_μ, ν_τ), which are arranged in three generations. The quarks u and d and the lepton e (i.e. the electron) compose the ordinary matter. Every fermion has an antimatter partner with the same mass and opposite charge. The bosons are: the force-carrying particles (the gluons g, the photon γ, the weak bosons $W^{\pm}$ and Z), which are exchanged by fermions during interactions and the Higgs boson H, whose *field* is responsible for the mass of all elementary particles (Figure 1.1).

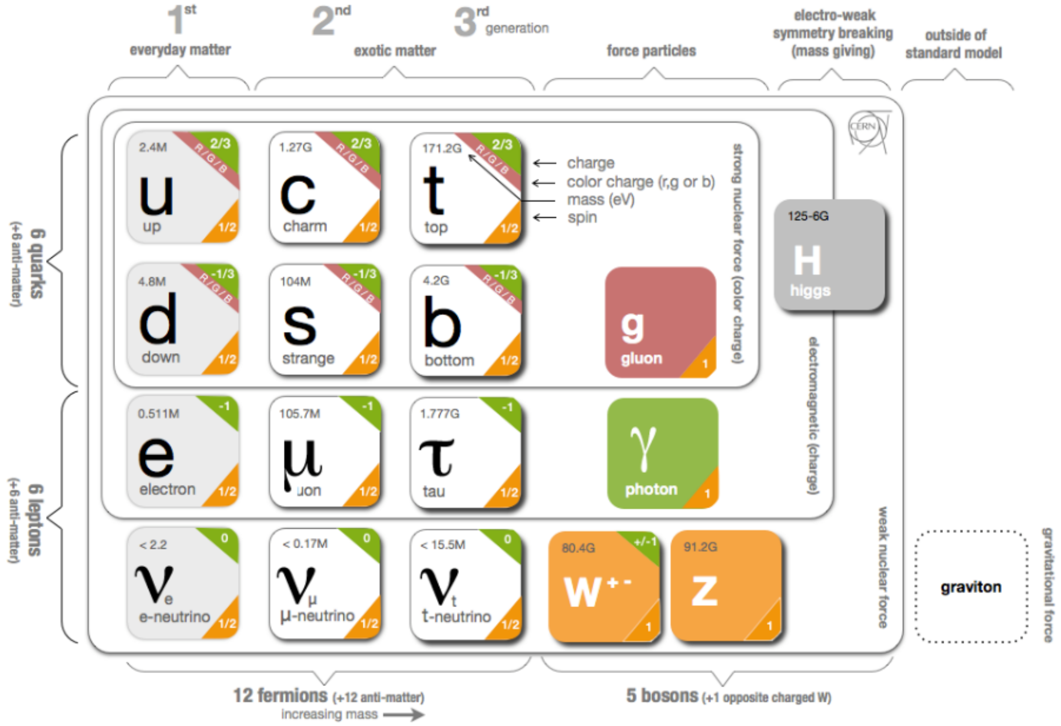

Figure 1.1: Fundamental constituents of matter (fermions), force-carriers (gauge bosons) and the Higgs boson with their properties (electric charge, color charge, mass and spin) [5].

1.1.1 Gauge invariance of the theory

The SM is a quantum field theory (QFT) that relies on the gauge symmetry group $SU(3) \times SU(2)_L \times U(1)_Y$. What we call *particles* are in fact excited states of the corresponding relativistic quantum fields. The interaction among the fields is obtained

---

[1] In quantum mechanics and particle physics, spin is an intrinsic form of angular momentum carried by the particles.

by requiring local gauge invariance under the transformations of the symmetry group. In other words, the fermions do not interact directly between themselves but through gauge bosons, that arise mathematically by requiring the local gauge invariance.
As a simple example of this concept, one can consider the Dirac Lagrangian of a freely propagating fermion of spin $\frac{1}{2}$ and mass m (e.g. an electron):

$$\mathcal{L}_e = i\bar{\psi}\gamma^{\mu}\partial_{\mu}\psi - m\bar{\psi}\psi \tag{1.1}$$

A local $U(1)$ gauge transformation acting on the field ψ is defined as

$$\psi \rightarrow e^{i\theta(x)}\psi \tag{1.2}$$

In order to make 1.1 gauge invariant under 1.2, the vector field A_{μ} must be introduced, which transforms like

$$A_{\mu} \rightarrow A_{\mu} + \frac{1}{q}\partial_{\mu}\theta(x) \tag{1.3}$$

It represents a spin 1 massless boson (e.g. a photon), whose free evolution is described by the Lagrangian

$$\mathcal{L}_p = -\frac{1}{4}F^{\mu\nu}F_{\mu\nu} \tag{1.4}$$

where $F^{\mu\nu} = (\partial^{\mu}A^{\nu} - \partial^{\nu}A^{\mu})$. The Lagrangian of the total system is thus obtained:

$$\mathcal{L} = -\frac{1}{4}F^{\mu\nu}F_{\mu\nu} + \left[i\bar{\psi}\gamma^{\mu}\partial_{\mu}\psi - m\bar{\psi}\psi\right] + \left(q\bar{\psi}\gamma^{\mu}\psi\right)A_{\mu} \tag{1.5}$$

This is the Lagrangian of the Quantum Electrodynamics (QED) and the term $\left(q\bar{\psi}\gamma^{\mu}\psi\right)A_{\mu}$ describes the electromagnetic interaction between the fermion field ψ and the boson field A_{μ}. It is now sufficient to define the covariant derivative $\not{D} = \gamma^{\mu}(\partial_{\mu} - iqA_{\mu})$ and one can show that under this form, the Lagrangian is invariant against a U(1) gauge transformation:

$$\mathcal{L} = -\frac{1}{4}F^{\mu\nu}F_{\mu\nu} + \bar{\psi}(i\not{D} - m)\psi \tag{1.6}$$

It is important to notice that the invariance of the Lagrangian could not have been achieved without the assumption of a massless boson.

An essential concept of quantum field theory is **renormalizability** [6, 7]. Some quantities predicted by the SM theory contain terms which are divergent in integration over the momentum space. The renormalization process allows to redefine the physical fields, masses and charges as the 'bare' quantities times artificial constants, which absorb the divergences and become dependent on the energy. This method introduces a renormalization scale in the calculations, often referred as μ_R. When computing the value of a physical quantity, like the cross section of a process, μ_R is chosen to be equal to the typical energy scale of that specific process.

1.2 Phenomenology of the strong interactions

Quantum Chromodynamics (QCD) is a non-Abelian gauge theory whose symmetry group is SU(3). It describes strong interactions between quarks, antiquarks and gluons, the only SM particles that carry color charge. In QCD, a quark's color can take one of three values (or charges): red, green, and blue. An antiquark can take one of three anticolors: called antired, antigreen, and antiblue. Gluons are mixtures of two colors, such as red and antigreen, which constitutes their color charge. QCD considers eight gluons of the possible nine color–anticolor combinations to be unique. Gluons are the massless bosons responsible for the interaction and, unlike photons in QED, they can interact with other gluons too. The strong coupling constant is given, at leading order, by the following expression

$$\alpha_s(Q^2) = \frac{\alpha_s(\mu_R^2)}{1 + \frac{(33-2n_f)}{12\pi}\ln(Q^2/\mu_R^2)} \tag{1.7}$$

where μ_R is the artificial scale introduced by the renormalization procedure, n_f is the number of quark flavours considered and Q^2 is the momentum transferred in the interaction. The dependence of α_s on the energy of the interaction, also known as *running of the coupling* (Figure 1.2), leads to two fundamental properties of QCD: **confinement** and **asymptotic freedom** [8, 9].

In the asymptotic freedom regime, at high energy and small distance, α_s is very small and quarks behave as free particles. In the confinement regime, at low energy and large distance, α_s diverges and a quark antiquark pair configuration becomes more energetically favorable than single quarks. The confinement explains why **partons** (quarks and gluons) are never observed as free particles, instead they always bind together to form composite particles called **hadrons**. Two families of hadrons exist: baryons, made of three valence quarks, and mesons, made of one valence quark and one valence antiquark. The proton is a particular type of baryon, made of two u valence quarks and one d valence quark. Inside protons, gluons can fluctuate into quark antiquark pairs forming the so-called sea quarks, in addition to the valence quarks. Due to the running behavior of the coupling, perturbative calculations are only allowed at high energies while non-perturbative methods must be developed in order to describe strong interactions at low energies.

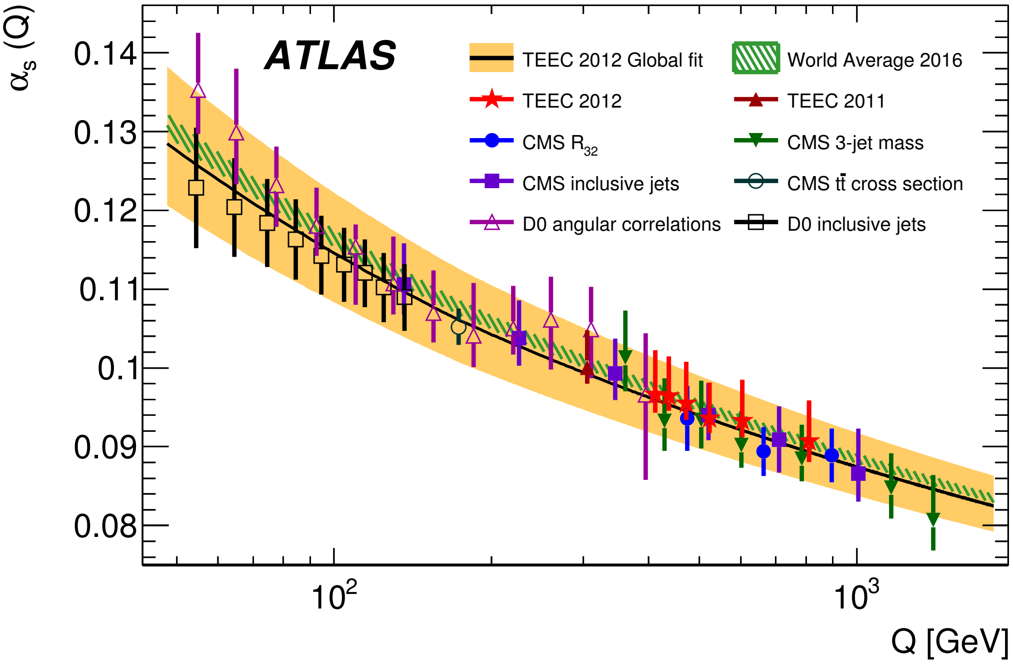

Figure 1.2: Summary of the most important measurements of α_s [10].

1.2.1 The factorization theorem

In hadron collisions, perturbative QCD calculations can only be used for the **hard scattering** part of the process, that is the interaction between partons belonging to different hadrons, while the physics of partons inside hadrons is dominated by non-perturbative QCD effects. The factorization theorem [11] states that the cross section of the collision process between two hadrons, A and B, can be written as the convolution of their Parton Density Functions (PDFs), f^A and f^B, with the partonic cross section $\hat{\sigma}_{i,j}^{(i+j\to X)}$:

$$\sigma(A+B \to X) = \sum_{i,j} \int dx_i f_i^A(x_i, \mu_F^2) \int dx_j f_j^B(x_j, \mu_F^2) \cdot \hat{\sigma}_{i,j}^{(i+j\to X)}(x_i, x_j, \alpha_s(\mu_R^2), \mu_F, \mu_R) \tag{1.8}$$

where μ_F is the factorization scale, introduced to cure divergences in the same spirit of the renormalization scale. The function $f_i^A(x_i, \mu_F^2)$ denotes the probability to find a parton i carrying momentum fraction x_i inside an hadron A when probed at the energy scale μ_F^2. Even though PDFs are extremely non-perturbative and therefore incalculable, they are approximately universal and, once determined in a given process from data obtained in one experiment, can be applied to other hadronic processes. Figure 1.3 shows examples of proton PDFs at two different energy scales. In general, gluons and sea quarks carry a relatively low momentum fraction, while the valence quarks can carry large momentum fractions. At LHC energies, the main contribution to the PDFs comes from the gluons.

The evolution of the PDFs at any scale μ_F^2 is theoretically predicted by the Dokshitzer–Gribov–Lipatov–Altarelli–Parisi (DGLAP) equations [12–14]:

$$\frac{df_i(x, \mu_F^2)}{d\ln(\mu_F^2)} = \sum_j \int_0^1 \frac{dz}{z} P_{ij}(\alpha_s(\mu_F^2), z) f_j\left(\frac{x}{z}, \mu_F^2\right) \tag{1.9}$$

where the splitting function $P_{ij}(\alpha_s(\mu_F^2), z)$ denotes the probability that a parton j converts into a parton i carrying a fraction z of the momentum of j. These functions are independent of the hard process and are usually computed perturbatively.

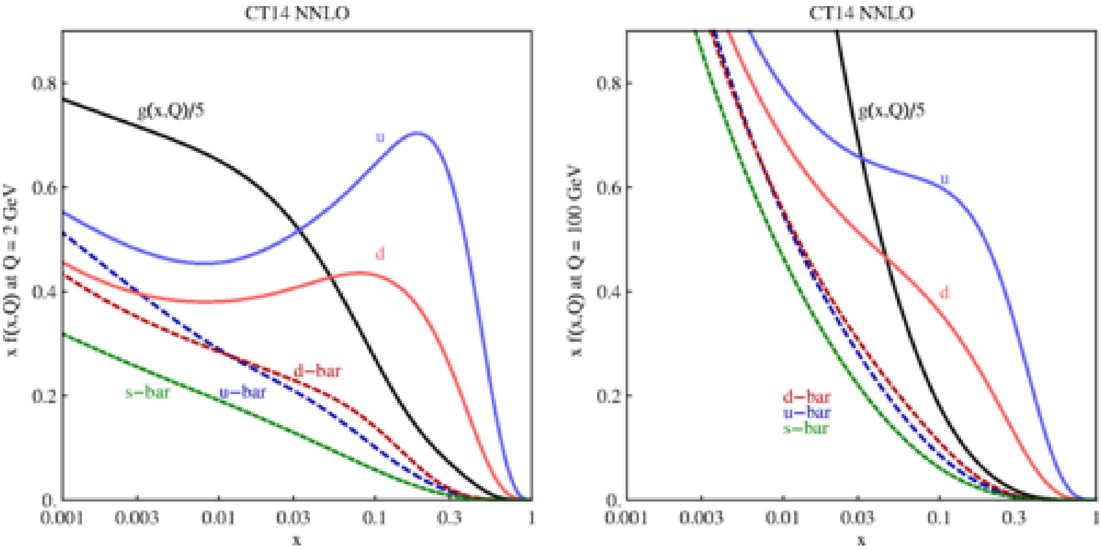

Figure 1.3: Proton PDFs for a momentum exchange $Q = 2$ GeV (left) and $Q = 100$ GeV (right) [15]. These PDFs are computed at next-to-next-to-leading order.

1.2.2 Non-perturbative QCD

Partons constituting the colliding hadrons interact at a high momentum scale to produce outgoing partons. Perturbative QCD calculations may have colored partons in the final state, but only the colorless hadrons they ultimately produce are observed experimentally: this is due to QCD confinement which only allows for colorless states. Monte Carlo (MC) generators are extensively used to compare predictions of the SM with data collected by experiments at hadron colliders. MC generators are first based on the matrix element of the hard process at a fixed perturbative order. Then, cascades of radiation produced by QCD processes and interactions are simulated. MC generators use phenomenological models to simulate non-perturbative effects [16, 17]. All outgoing colored partons must first undergo **parton showering** and then combination of the produced partons into hadrons through a process called **hadronization**. Parton showering produces partons of successively lower energy, and must therefore exit the region of validity for perturbative QCD, then the combination of all colored partons into bound states of colorless hadrons occurs. The tight cone of hadrons and other particles created by the hadronization of a single parton is called a **jet** [18]. In particle detectors, jets are observed rather than original partons, whose properties must be inferred. The reconstruction of these objects is possible through the use of jet algorithms [19].

1.3 The electroweak symmetry breaking

In the SM the photon, the W^+ boson, the W^- boson, and the Z^0 boson physical states arise from enforcing $SU(2)_L \times U(1)_Y$ local gauge invariance. Initially there are three fields associated with the left-hand $SU(2)_L$ group:

$$\{W^1_\mu, W^2_\mu, W^3_\mu\} \in SU(2)_L \tag{1.10}$$

and a so-called hyper-charge field, associated with the $U(1)_Y$ group:

$$B_\mu \in U(1)_Y \tag{1.11}$$

The W^1_μ and W^2_μ combine to form the W^+ and the W^- bosons associated with the charged nuclear weak interactions:

$$W^\pm_\mu \equiv \frac{1}{\sqrt{2}}(W^1_\mu \mp W^2_\mu) \tag{1.12}$$

while the two neutral states (W^3 and B) mix, in GSW[2] theory [2–4], producing two linear combinations which are orthogonal to each other, the photon and the Z^0:

$$A_\mu = B_\mu \cos\theta_w + W^3_\mu \sin\theta_w \tag{1.13}$$

and

$$Z_\mu = -B_\mu \sin\theta_w + W^3_\mu \cos\theta_w \tag{1.14}$$

where θ_w is called 'weak mixing angle' (or 'Weinberg angle'). Unfortunately, all the four obtained bosons are still massless and it is known from experiments that the three weak gauge bosons are heavily massive instead.

According to the SM, the Higgs mechanism is responsible for the masses of such

---

[2] Sheldon Glashow, Abdus Salam and Steven Weinberg gave birth to the SM in the 1960s.

bosons. In order to be massive, gauge bosons need to acquire the longitudinal polarization modes so at least three additional degrees of freedom are required. This mechanism [20–22] introduces a complex doublet containing four real scalar fields:

$$\phi = \begin{pmatrix} \phi^+ \\ \phi^0 \end{pmatrix} = \frac{1}{\sqrt{2}} \begin{pmatrix} \phi_1 + i\phi_2 \\ \phi_3 + i\phi_4 \end{pmatrix} \tag{1.15}$$

with an associated potential of the form (Figure 1.4):

$$V(\phi) = -\mu^2|\phi|^2 + \lambda|\phi|^4 \tag{1.16}$$

where the first term is related to the mass of the field and the second term corresponds to its self-interaction. Selecting $\mu^2 < 0$ and $\lambda > 0$, the minimum of the potential, namely its *vacuum expectation value*, is not at $|\phi_0| = 0$, but at

$$|\phi_0|^2 = \frac{\mu^2}{2\lambda} \equiv \frac{\nu^2}{2} \tag{1.17}$$

Possible solutions for the potential, satisfying (Eq. 1.17), are infinite. A possible choice is

$$\phi_1 = \phi_2 = \phi_4 = 0\ ,\ \phi_3 = \nu \tag{1.18}$$

thus

$$\phi_0 = \frac{1}{\sqrt{2}} \begin{pmatrix} 0 \\ \nu \end{pmatrix} \tag{1.19}$$

and $V(\phi)$ is no longer invariant under $SU(2)_L \times U(1)_Y$ and, consequently, the group symmetry is spontaneously broken. The complex scalar field ϕ is now expanded around the minimum:

$$\phi(x) = \frac{1}{\sqrt{2}} \begin{pmatrix} 0 \\ \nu + h(x) \end{pmatrix} \tag{1.20}$$

where $h(x)$ are ground state fluctuations around the vacuum state.

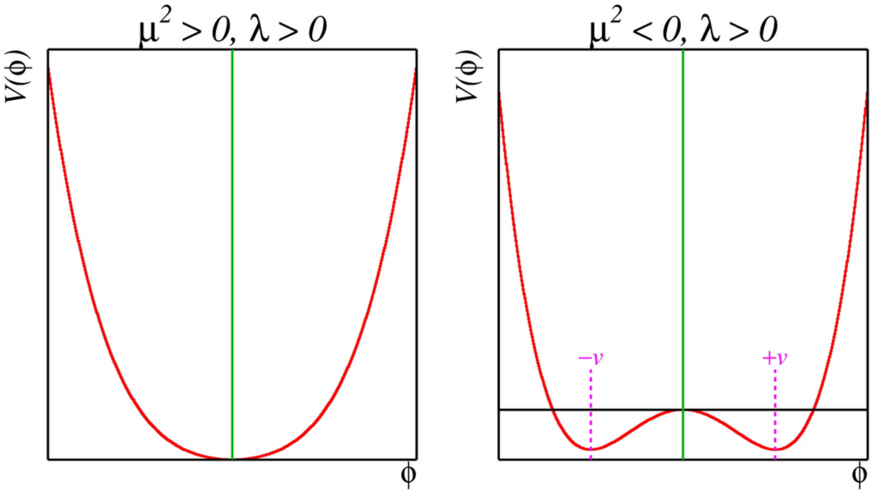

Figure 1.4: Graph of $V(\phi)$ (Eq.1.16) in the two cases where $\mu^2 > 0$ (left) and $\mu^2 < 0$ (right).

According to the Goldstone theorem [23], with four scalar fields and three broken symmetries one obtains three Goldstone bosons and one Higgs boson with mass:

$$m_H = \sqrt{2\lambda\nu^2} \tag{1.21}$$

Finally, this gives rise to mass terms for the W and Z bosons:

$$m_W = \frac{1}{2}\nu g \qquad m_Z = \frac{1}{2}\nu\sqrt{g^2 + g'^2} \tag{1.22}$$

where g and g' are the $SU(2)_L$ and $U(1)_Y$ coupling strengths respectively. It can be shown that the two masses are related by the mixing angle:

$$\frac{m_W}{m_Z} = \cos\theta_w \tag{1.23}$$

In addition, the procedure allows the photon to remain massless. The choice of the vacuum expectation value (i.e. the Higgs mass value) also quantifies the strength of the Higgs boson couplings to the heavy gauge bosons and its self-interaction. Trilinear couplings of the Higgs boson with the other gauge bosons, show that the strength of the coupling is proportional to the square of the mass of the gauge bosons. The Higgs mechanism can provide an explanation for the fermion masses and associated coupling strengths to the Higgs boson. Although it does not predict the masses of each fermion, it predicts that the strength of each fermion coupling to the Higgs boson is proportional to the fermion mass:

$$m_f = \frac{\nu g_f}{\sqrt{2}} \tag{1.24}$$

where g_f is the Yukawa coupling for fermions. The Higgs boson has no direct coupling to massless bosons, i.e. gluons and photons. However, an effective coupling arises from virtual loops involving quarks and massive vector bosons.

1.4 Phenomenology of the Higgs boson

1.4.1 Production modes

The main channels through which the SM Higgs boson can be produced at the CERN LHC[3] with proton-proton (pp) collisions at the center-of-mass energy $\sqrt{s} = 13$ TeV are:

- **Gluon fusion (ggH)** $pp \to H$ (Figure 1.5a)
  Total cross section fraction[4] $\sim 87\%$
  The Higgs boson cannot couple directly to massless particles, such as gluons. Nevertheless, this coupling is allowed via a virtual fermion loop with a heavy quark dominance. For a final state of the partonic interaction corresponding to a Higgs boson mass of $m_H \approx 125$ GeV[5] the proton PDFs involving gluons in the hard scattering process largely dominate over the proton PDFs involving quarks [24]. Because of this, the ggH production mode has the largest cross section at the LHC. The cross-section calculation for this process is currently available at next-to-next-to-next-to-leading order (N^{3}LO) in QCD and at next-to-leading order (NLO) in EW theory [25–27].
- **Vector boson fusion (VBF)** $pp \to qqH$ (Figure 1.5b)
  Total cross section fraction $\sim 7\%$
  This production mode features two quarks in the initial state emitting a pair

---

[3] Protons collided at the LHC at $\sqrt{s} = 13$ TeV, during its latest operational run. More details on the LHC will be provided in Chapter 2.

[4] Ratio between production cross section of each process with respect to the total $pp \to H$ cross section at $m_H = 125.09$ GeV and $\sqrt{s} = 13$ TeV.

[5] The Higgs boson discovered at the LHC in 2012 has a mass $m_H = 125.09$ GeV.

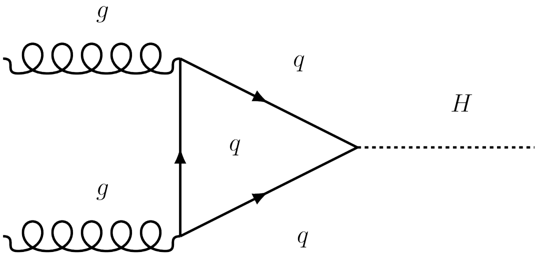

(a) Gluon fusion (ggH)

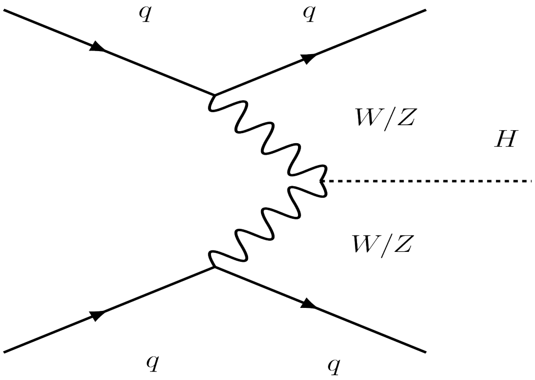

(b) Vector boson fusion (VBF)

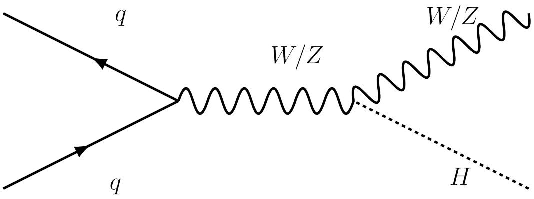

(c) Associated production with a vector boson (VH)

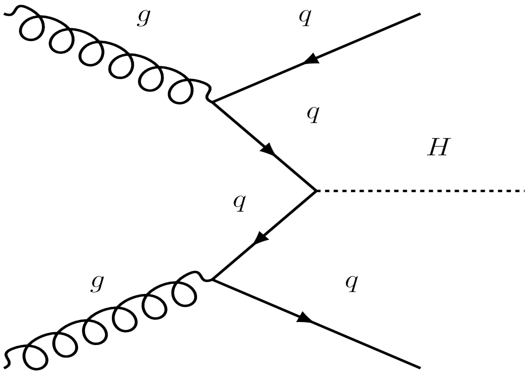

(d) Associated production with a pair of top quarks (ttH)

Figure 1.5: Feynman diagrams at leading order (LO) in perturbation theory for the Higgs boson main production mechanisms.

of heavy gauge bosons (W or Z), which annihilate to produce a Higgs boson. The final state is characterized by a distinct topology, with the presence of two energetic, forward-directed jets from the hadronization of the two initial quarks and the absence of hadronic activity in the central region. Due to the smaller quark-quark contribution in protons' PDFs, and the fact that it is an EW process at LO, its cross section is about ten times smaller than the ggH one. The cross-section calculation for this process is currently available at NNLO in QCD and at NLO in EW theory [28, 29].

- **Associated production with a vector boson (VH)** $pp \to WH/ZH$ (Figure 1.5c)
  Total cross section fraction $\sim 5\%$
  The third most common production channel at the LHC is the "Higgsstrahlung" mechanism, where the Higgs boson is radiated off a virtual gauge boson. These events can be characterized by one or two isolated and high transverse momentum charged leptons yielded by the decay of the weak vector boson in the final state or two quark jets with invariant mass compatible with the W or Z mass. The cross-section calculation for this process is currently available at NNLO in QCD and at NLO in EW theory [29–33].

- **Associated production with a pair of top quarks (ttH)** $pp \to ttH$ (Figure 1.5d)
  Total cross section fraction $< 1\%$
  The ttH production mechanism has the smallest cross section with respect to the channels previously discussed due to the large mass of its final state components. The cross-section calculation for this process is currently available at NLO in QCD and at NLO in EW theory [34–41].

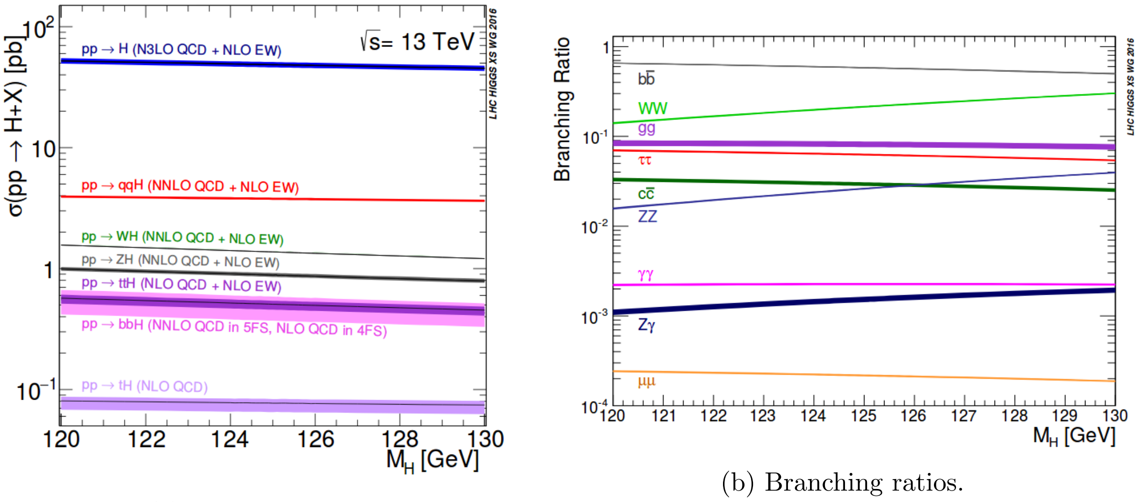

(a) Cross sections.

(b) Branching ratios.

Figure 1.6: Cross sections as a function of m_H for different production modes and corresponding order in perturbation theory at which they have been calculated (left). Branching ratios of the Higgs boson decaying into different final states as a function of m_H (right) [42].

Figure 1.6a shows the SM Higgs boson production cross sections in the mass window 120 GeV $< m_H <$ 130 GeV.

1.4.2 Discovery of the particle

The direct observation of the Higgs boson has represented one of the leading goals of physics research during the past 40 years. In the high energy collider experiments era (starting from the late 80's), experiments at the LEP collider conducted direct searches for the Higgs through the $e^+e^- \to ZH$ process in the mass range up to $\sim$ 120 GeV, setting a lower bound of $m_H >$ 114.4 GeV at the 95% confidence level [43]. Other direct searches, conducted by the CDF and D0 experiments at the $p\bar{p}$ Tevatron collider at the Fermilab (USA), lead to exclusion of the $100 < m_H < 103$ GeV and $147 < m_H < 180$ GeV ranges[44]. Indirect limits from precision measurements of the EW parameters such as the top quark mass and the W boson mass - which depend logarithmically on the Higgs boson mass through radiative corrections - were also extracted, predicting a mass of the Higgs of $m_H = 94^{+29}_{-24}$ GeV [45].

The summer of 2012 was a milestone in the history of particle physics, when both the ATLAS and CMS collaborations at the LHC announced the observation of a particle consistent with the SM Higgs boson with more than 5σ statistical significance [6] at a

---

[6] Statistical significance is used to determine whether a given hypothesis should be rejected or retained. In particle physics, a significance of 5σ is taken as a discovery, a significance of 3σ is taken as an evidence.

mass of approximately 125 GeV [1, 46]. The observation was driven by the analyses of three final states of the Higgs decay to bosons: $H \to ZZ^* \to 4l$, $H \to \gamma\gamma$ and $H \to WW^* \to l\nu l\nu$. In the following years, with more data collected by the two experiments, measurements of the Higgs boson properties have been made, including its mass [47], spin and parity [48], production rates and couplings [49]. All measurements lead to the observation of a Higgs boson whose properties are compatible with those predicted by the SM within the limits of the statistical, systematic and theoretical uncertainties.

1.4.3 Decay modes

For a Higgs boson with a mass around 125 GeV, a large number of final states are accessible for study, whose branching ratios are shown in Figure 1.6b. The dominant decay mode at $m_H = 125.09$ GeV is the decay into $b\bar{b}$ pairs, since b-quarks are the heaviest particles that can be pair-produced on-shell from a Higgs boson decay. Unfortunately, due to the overwhelming background from SM events composed uniquely of jets produced through the strong interaction, referred to as QCD multijet events, this decay is less accessible at the LHC and its observation has recently been possible only through associated production [50]. The same argument holds against the Higgs decay to pairs of gluons and pairs of c quarks. The second largest decay mode into fermions is the $\tau^+\tau^-$ mode, which has been observed at LHC during Run 1 [49]. Decays to pairs of W or Z bosons do not dominate in this Higgs mass region because they cannot be both produced on-shell. However, the large Higgs coupling to these massive particles makes such decays still accessible through production of one off-shell boson in the pair. The $H \to WW^*$ branching ratio is larger than $H \to ZZ^*$ owing to the larger accessible phase space from combinations of $W^\pm W^\mp$. Decays to pairs of muons, whose evidence at LHC has been presented for the first time in 2020 by CMS [51], have a much smaller branching ratio, albeit providing very high dilepton mass resolution.

The decay channel relevant for this thesis, $H \to \gamma\gamma$, has a small branching ratio,

$$BR(H \to \gamma\gamma)|_{m_H=125.09\text{GeV}} \approx 0.227\% \tag{1.25}$$

though it is still a very interesting channel for at least two reasons: it profits from a favorable signal over background ratio, thanks to the clean experimental signature of only two energetic photons; it is possible to take advantage of the very high experimental photon energy resolution achieved by the ATLAS detector [7]. Since photons are massless in the SM, the coupling of the Higgs boson to them is allowed only through loop processes. The main Feynman diagrams of this decay are shown in Figure 1.7. Particles involved in the loop are mostly W bosons or top quarks, where the contribution of the latter to the decay width is negative. Thus, $H \to \gamma\gamma$ is the only channel which can potentially constrain the sign of the top Yukawa coupling.

1.5 Higgs mass

The Higgs boson mass is given by $m_H = \sqrt{2\lambda}\nu$ (Eq. 1.21), where λ is the Higgs self-coupling parameter and ν is the vacuum expectation value of the Higgs field (as discussed in Section 1.3). While ν is related to the Fermi coupling constant G_F, λ is a free parameter in the SM, and for this reason, there is no a priori prediction for the

---

[7] More details on the ATLAS detector will be provided in Chapter 2.

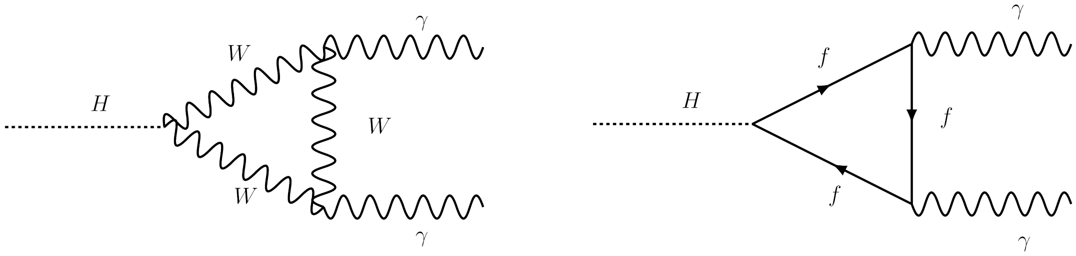

(a) Diphoton decay mediated by a loop of heavy gauge bosons.

(b) Diphoton decay mediated by a heavy fermion loop.

Figure 1.7: Feynman diagrams of the $H \to \gamma\gamma$ decay in the SM. The photons are massless, so the decay is mediated by heavy particle loops.

Higgs mass.
From the experimental point of view, the ideal candidates to study the Higgs mass are the $H \to \gamma\gamma$ and $H \to ZZ^* \to 4l$ decay channels. The invariant mass of the two photons $m_H^{\gamma\gamma}$ as well as the invariant mass of the four leptons m_H^{4l}, can be reconstructed with very high precision by the LHC experiments, as good as 1% in resolution.
A measurement of the Higgs boson mass based on the combined pp collisions data at $\sqrt{s} = 7$ and 8 TeV collected by ATLAS and CMS in the $H \to \gamma\gamma$ and $H \to ZZ^* \to 4l$ decay channels has been published in 2015 [47]:

$$m_H = 125.09 \pm 0.21(\text{stat}) \pm 0.11(\text{syst})\text{GeV} \tag{1.26}$$

which was statistically limited, like many measurements of Run 1. On the other side, the systematic uncertainty is dominated by terms associated to the energy scale of photons, electrons and muons.
In a more recent measurement made by ATLAS using data at $\sqrt{s} = 13$ TeV with $H \to \gamma\gamma$ decays [52], the largest contribution to the systematic uncertainty of $m_H^{\gamma\gamma}$ arises from the "EM calorimeter cell non-linearity" (Table 1.1). This represents the residual miscalibration observed between the gains of the readout electronic stages of the ATLAS electromagnetic calorimeter, which has an impact of 180 MeV. An analysis which leads to a better understanding of the origin of this effect is presented in Chapter 4, in the context of the detector performance studies for the calibration of electrons and photons in ATLAS.

Source	Systematic uncertainty on $m_H^{\gamma\gamma}$ [MeV]
EM calorimeter cell non-linearity	±180
EM calorimeter layer calibration	±170
Non-ID material	±120
ID material	±110
Lateral shower shape	±110
$Z \to ee$ calibration	±80
Conversion reconstruction	±50
Background model	±50
Selection of the diphoton production vertex	±40
Resolution	±20
Signal model	±20

Table 1.1: Main sources of systematic uncertainties on $m_H^{\gamma\gamma}$.

1.6 Higgs width

For a Higgs boson with mass $m_H = 125.09$ GeV, the predicted value for its decay width is $\Gamma_H = 4.07$ MeV in the SM [42]. A precise measurement of it would be of great interest for the physics community, because any deviation from the SM prediction would indicate the presence of unknown particles that couple to the Higgs sector.

Because of the intrinsic resolution in the diphoton invariant mass, being around 1 GeV for ATLAS, a direct constraint on the value of Γ_H through the measurement of the mass lineshape has many limitations. As a result, only an upper limit of 5.0 GeV at 95% CL has been set by ATLAS in the $H \to \gamma\gamma$ channel, together with a 95% CL limit of 2.6 GeV in the other decay channel with a good resolution, namely $H \to ZZ^* \to 4l$ [53].

However, there are other approaches to bounding the Higgs boson width, in a indirect way. For example, measuring the ratio of the off-shell to the on-shell Higgs production in the high-mass $H \to ZZ$ channel, CMS [54, 55] and ATLAS [56] have put a limit of the order $\frac{\Gamma}{\Gamma_{SM}} < 3.5$ at the 95% CL. Although this method is able to provide considerably more stringent limits, it is also more dependent on the assumptions of the Higgs couplings.

1.6.1 Interferometry in the $H \to \gamma\gamma$ channel

Both the resonant Higgs production, $gg \to H \to \gamma\gamma$, and the continuum QCD background, $gg \to \gamma\gamma$, have two gluons in the initial state and two photons in the final state. At higher orders, the gluon-fusion production of Higgs bosons may occur through quark-gluon initiated processes, for which the tree level $qg \to q\gamma\gamma$ plays the role of the background. Feynman diagrams corresponding to these processes are shown in Figure 1.9. Having the same initial and final states, they interfere with each other impacting both the Higgs signal yield and shape. This is shown in Figure 1.8, where both the imaginary and the real component of the interference are plotted. The existence of the imaginary component leads to 2% destructive effects on the on-shell SM cross section, which can be enhanced by BSM physics [57]. The real component gives rise to a shift in the invariant mass of the diphoton system, whose size is found to be proportional to the Higgs width (Figure 1.10). Since the effect of the interference with the background is much smaller in the ZZ^* channel, the mass shift can be obtained from the Run 1 mass measurements by ATLAS and CMS:

$$\Delta m_H = m_H^{\gamma\gamma} - m_H^{ZZ^*} = -80 \pm 490\text{MeV} \tag{1.27}$$

which corresponds to an upper limit at 2σ level of $\frac{\Gamma}{\Gamma_{SM}} < 250$. The uncertainty of (1.27) certainly has a large statistical component, because mass measurements in Run 1 were statistically dominated. This is supposed to be addressed by the increased luminosity of Run 2 and in particular by the dataset collected at the High-Luminosity LHC. On the other hand, systematic uncertainties will eventually become dominant, and reducing them will be the real challenge of this measurement.

The authors of Ref.[58] propose a method to indirectly constrain the Higgs width completely within the diphoton channel, exploiting the strong dependence of Δm_H on the diphoton transverse momentum [59] (as shown in Figure 1.11).

Another approach was proposed in Ref.[60], where it is shown that, in the $H(\to \gamma\gamma)+2$ jets channel, the ggH and VBF production modes generate mass shifts of opposite signs which largely cancel (Figure 1.12). After adjusting the cuts on the associated jets, this region of the phase space becomes a good internal mass reference for measuring Δm_H.

Regardless of the chosen analysis method, using only $\gamma\gamma$ events without having to compare against an external mass reference (e.g. $m_H^{ZZ^*}$) can bring some benefits. It might lead to a partial cancellation of the experimental systematic uncertainties, in particular of those associated with the absolute photon energy scale.

The expected mass shift for a SM Higgs boson has been estimated by ATLAS at Run 1 through MC simulations of the interference with an approximate detector description, and was found to be 35 ± 9 MeV [61].

Chapter 6 presents an analysis of ATLAS data which aims to constrain Γ_H using pp collisions data at $\sqrt{s} = 13$ TeV and exploiting the effect of the interference in the diphoton channel.

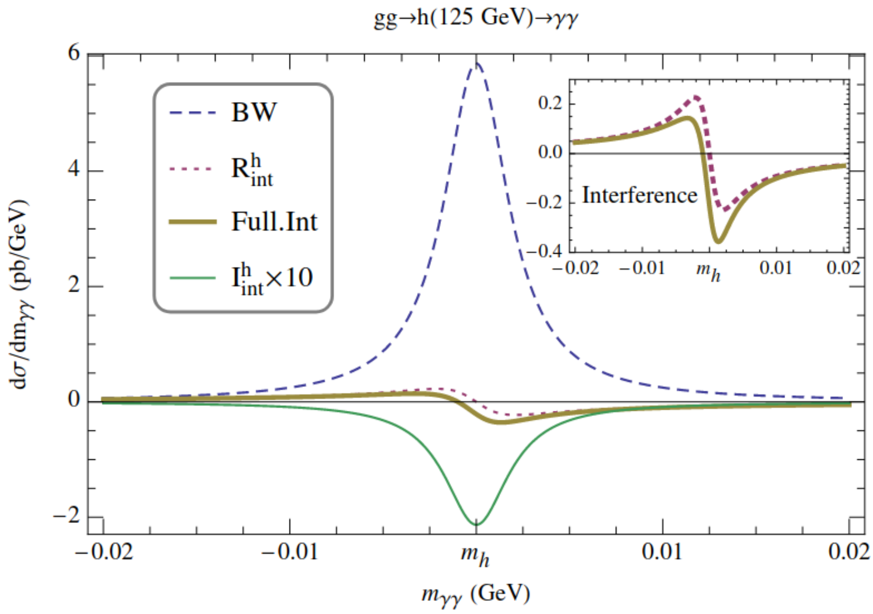

Figure 1.8: The lineshape induced by various contributions to the cross-section for the $gg \to H \to \gamma\gamma$ process in the SM. The Breit-Wigner line-shape, with no interference, is shown in blue (dashed) while the effect of the real and imaginary (the latter is multiplied by a factor of 10) parts are shown in red (dotted) and green (solid), respectively. The overall effect of the interference in the full NLO calculation is given by the brown (solid) line. The insert in the top right is a magnification of the corresponding interference lineshapes (From Ref.[57]).

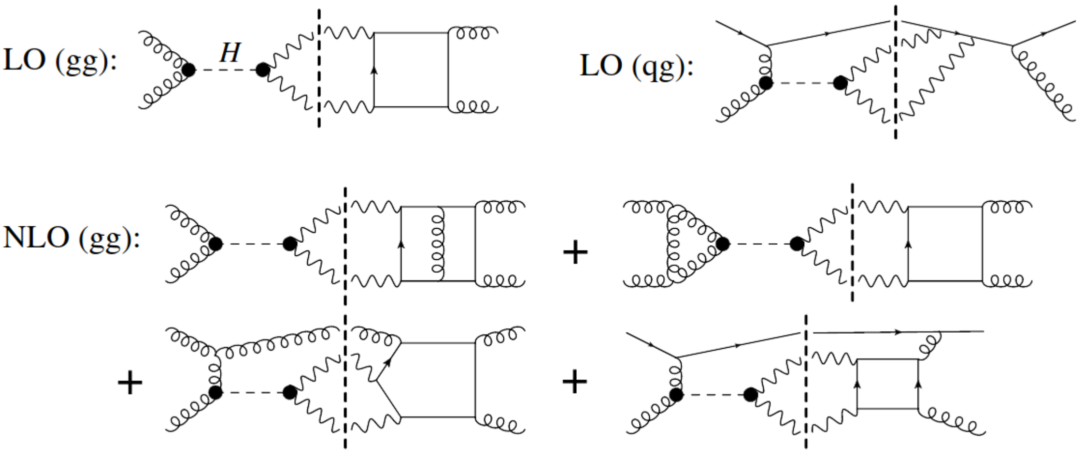

Figure 1.9: Representative diagrams for interference between the Higgs resonance and the continuum in the diphoton channel. The dashed vertical lines separate the resonant amplitudes from the continuum ones.

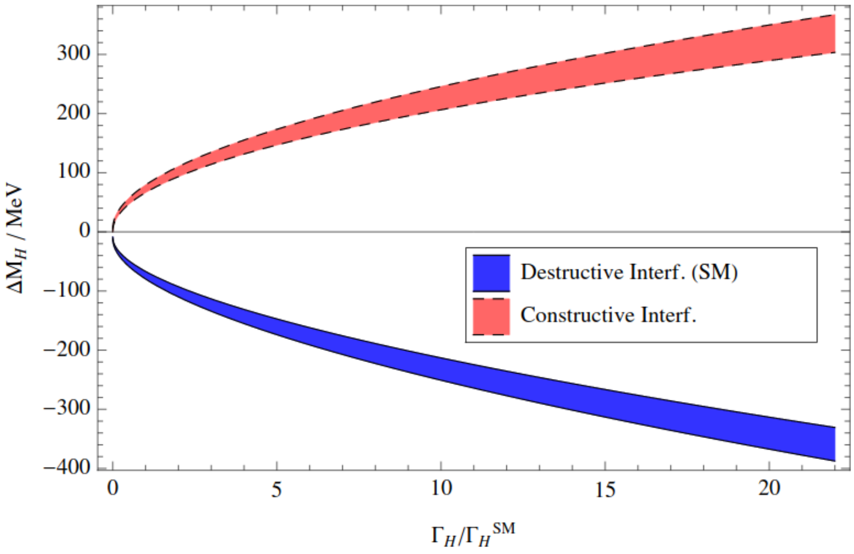

Figure 1.10: Higgs mass shift as a function of the Higgs width (From Ref.[58]).

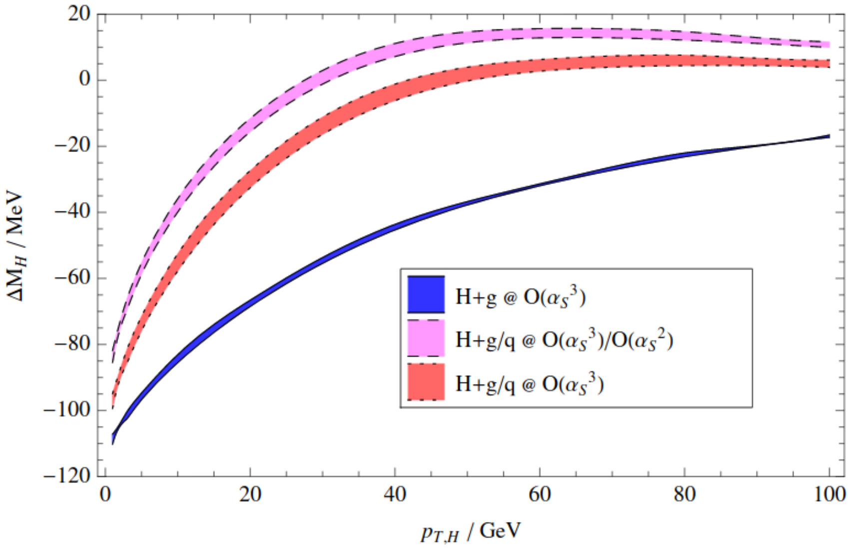

Figure 1.11: Higgs mass shift as a function of the lower cut on the Higgs transverse momentum (From Ref.[58]).

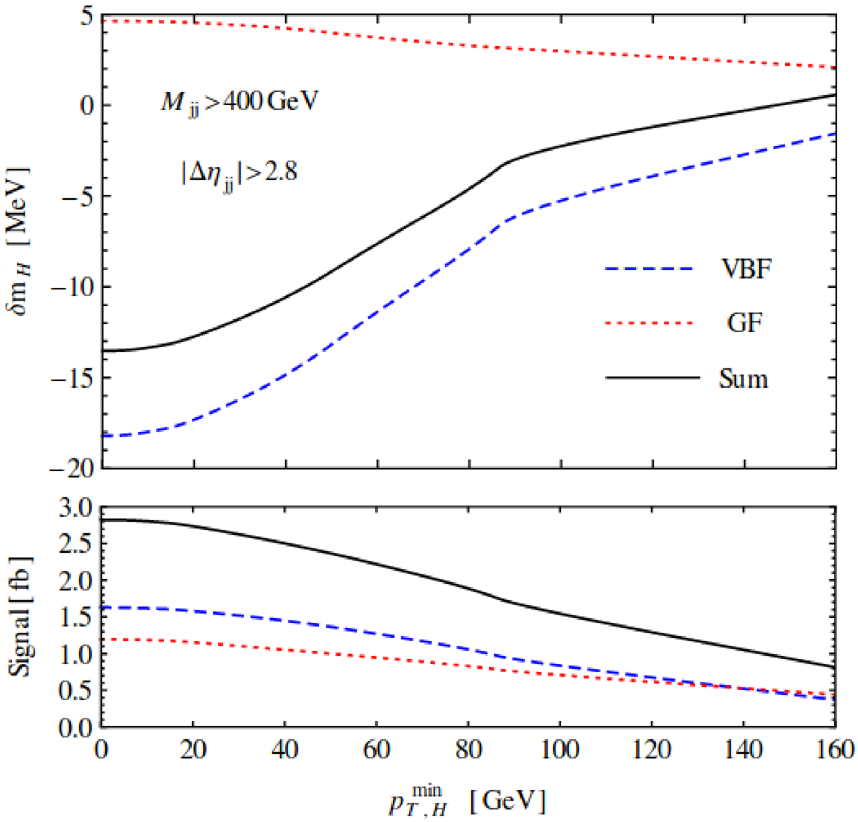

Figure 1.12: Top (Bottom): Higgs mass shift (Total integrated signal) as a function of the lower cut on the Higgs transverse momentum for VBF, GF (i.e. ggH) and total contributions. Kinematical cuts to enhance the VBF sensitivity are applied (From Ref.[60]).

1.7 Simplified Template Cross Sections

At the beginning of Run 2, one of the main goals of the Higgs physics program was to observe all the Higgs boson production modes. The signal strength, defined as the ratio of the observed to the expected signal yield, was measured for each production process, showing results compatible with the SM predictions. The interpretation of these measurements was exclusively performed through the $\kappa-$framework: production cross-sections and decay widths are reparametrized in terms of the couplings modifiers κ_i in order to probe deviations from the SM expectation. However, inclusive measurements are not the most optimal way to search for new physics, because they don't allow to test any change in the shape of the kinematic distributions. With the amount of available data becoming consistently higher during Run 2, simplified template cross sections (STXS) represented a natural way to evolve the measurements of the production mode cross sections. [42, 62–64]. The STXS framework segments the phase space in order to perform more finely-grained measurements, hence providing more information for theoretical interpretations. The measured exclusive regions of phase space, called *bins* for simplicity, are specific to the different production modes and are defined by kinematic selections on the most sensitive observables of the particles in the final state of the event. The definitions of the bins are motivated by:

1. Minimization of the dependence on theoretical uncertainties;
2. Maximization of experimental sensitivity;
3. Isolation of possible BSM effects;
4. Improved combination among different decay channels.

In practice, it is impossible to define a set of bins that satisfies all the above requirements for every analysis at the same time. Some analyses are only able to constrain a subset of all bins or only constrain the sum of a set of bins. In addition, the number of bins that is possible to measure increases with increasing amount of available data. For this reason, the framework evolves in *stages*, with an increasing number of bins in their definition. At stage 0, each main production mode has a single inclusive bin. It corresponds most closely to the measurement of each production mode. Stage 1 defines a binning that is targeted to be used by all analyses on an intermediate time scale and it has actually been used in most recent publications (for instance in Ref.[65]). In particular, the stage 1.2 of the framework, whose binning is schematically shown in Figure 1.13, is used to obtain the results presented in this thesis.

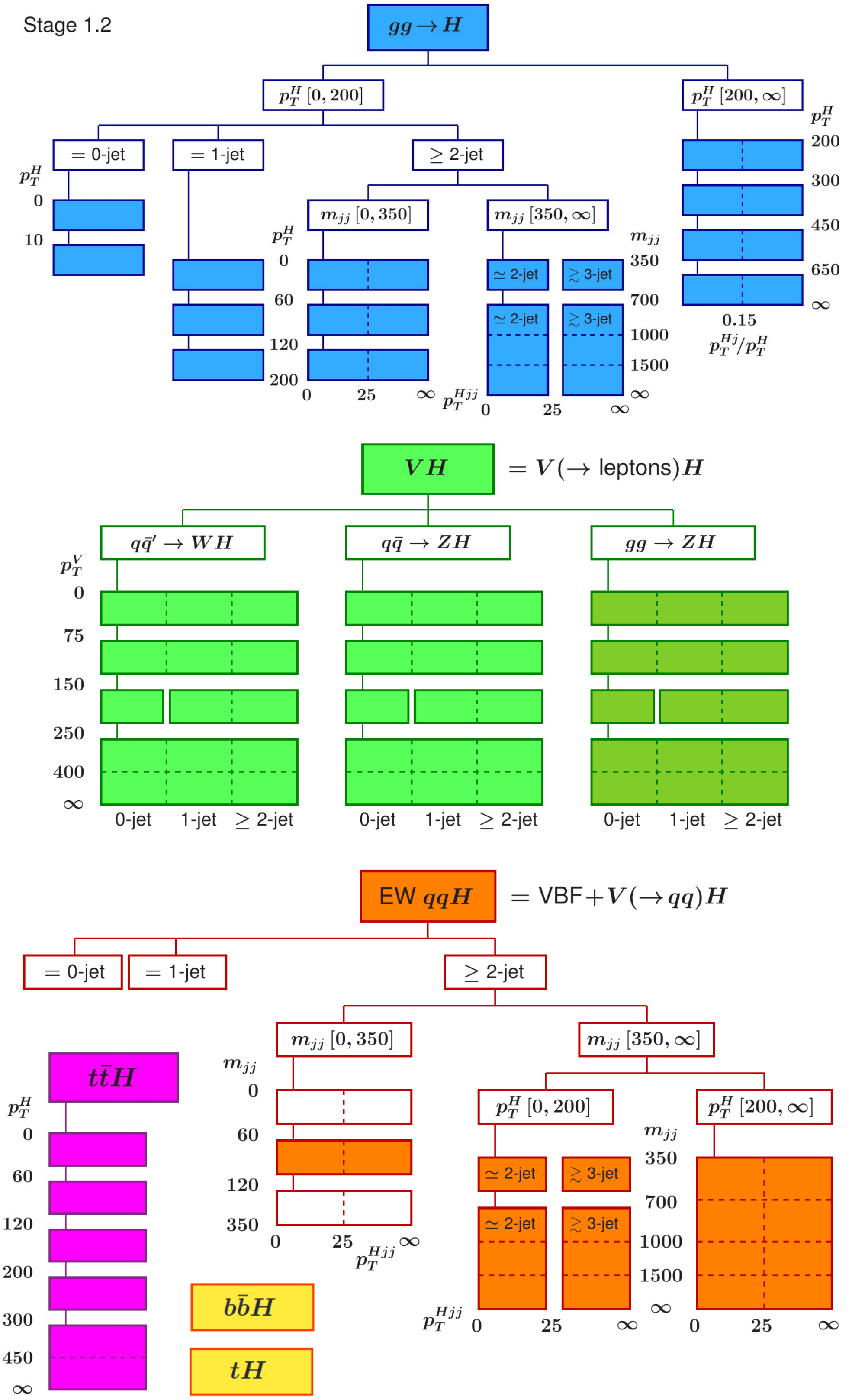

Figure 1.13: Schematic overview of the binning implemented by the stage 1.2 of the STXS framework, for the different production modes.

Chapter 2

The ATLAS experiment

The research work presented in this thesis exploits the excellent operation of the Large Hadron Collider and the ATLAS detector. In this chapter the experimental environment in which the analyses presented later in the thesis are performed is introduced.

2.1 The Large Hadron Collider

The Large Hadron Collider (LHC) (Figure 2.1) is to date the world's largest and most powerful particle accelerator. It first started operations on 10 September 2008 and it is still in operation nowadays. All the controls for the accelerator, its services and technical infrastructure are housed under one roof at the CERN Control Centre. The beams inside the LHC are accelerated and made to collide at four locations around the accelerator ring, corresponding to the positions of four particle detectors – ATLAS [66], CMS [67], ALICE [68] and LHCb [69].

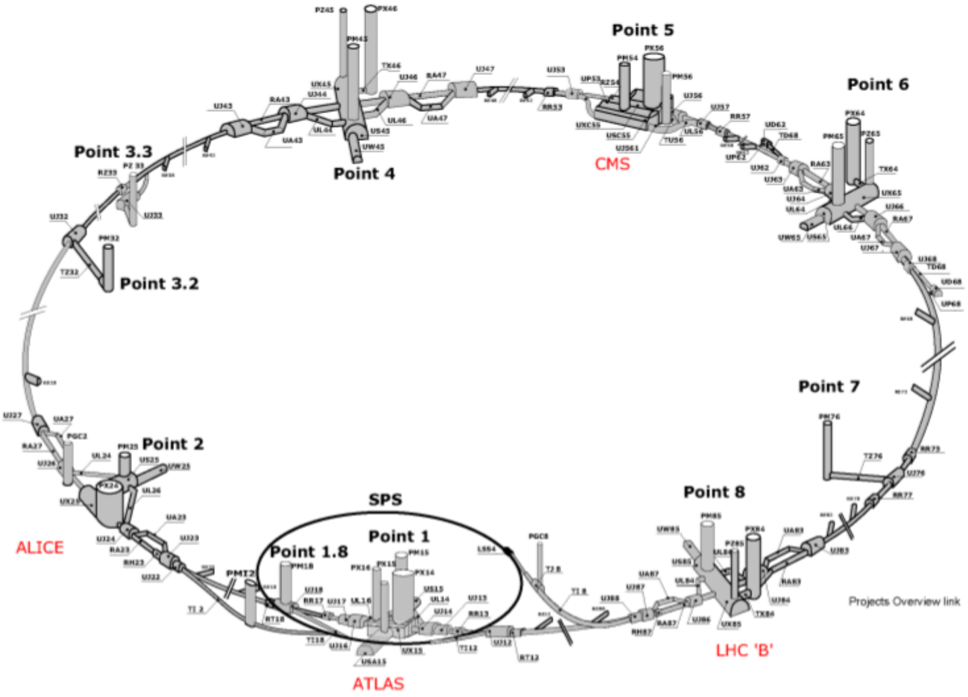

Figure 2.1: A scheme of the LHC accelerator complex.

The LHC consists of a 27 km ring where two high-energy protons beams are first injected with an energy of 450 GeV and then accelerated to 6.5 TeV each before they are made to collide. The beams travel in opposite directions in separate beam pipes – two tubes kept at ultrahigh vacuum. They are guided around the accelerator ring by a 8 T magnetic field maintained by superconducting electromagnets, cooled down to a temperature below 2 K using super-fluid helium. Each beam consists of packets of protons called bunches that are made up of about 130 billion protons. Full details about the underlying technology and performance can be found elsewhere, for example in Ref.[70]. The LHC physics programme is mainly based on proton–proton collisions. However, shorter running periods with heavy-ion collisions are included in the programme, typically one month per year. The first operational run, Run 1, started in 2009 and ended in 2012. During Run 1 protons collided at $\sqrt{s} = 7$ TeV (2010-2011) and 8 TeV (2012). The second operational run, Run 2, started in 2015 and ended in 2018 at $\sqrt{s} = 13$ TeV and its full dataset of pp collisions is used for the physics analyses presented in this manuscript.

A third run is planned to start in the first half of 2022, operating at a center-of-mass energy of 13.6 TeV. A subsequent upgrade of the machine, the so-called High-Luminosity (HL)-LHC, is expected to be completed by the end of 2027 and aims at increasing its instantaneous luminosity (described in Section 2.1.1) by a factor 10.

2.1.1 Luminosity

The instantaneous luminosity L_{inst} is an important parameter for a collider. Indeed, it connects the number of events per unit time (rate, R) to the interaction cross section (σ):

$$R = L_{inst} \times \sigma \tag{2.1}$$

L_{inst} depends on the machine parameters by the relation:

$$L_{inst} = \frac{N_p^2 f_r n_b}{A} \tag{2.2}$$

where N_p is the number of particles per bunch [1], n_b is the number of bunches per beam, f_r is the bunch revolution frequency and A is a factor proportional to the transverse area of the colliding bunches. Table 2.1 shows the values of the most important collision parameters. Luminosity is expressed in units of cm$^{-2}\times$s^{-1} and, when it is integrated over time, it represents a measurement of the collected data sample size in a given period of data taking. Figure 2.2 gives an overview of the amount of data collected by the ATLAS experiment during the Run 2 period. Increasing luminosity is crucial for exploring new sectors of physics that could be characterized by very small cross sections.

Symbol	Parameter	Actual value	Nominal value
$\sqrt{s}$	Centre-of-mass energy [TeV]	13	14
	Bunch spacing [ns]	25	25
f_r	Bunch revolution frequency [kHz]	11.245	11.245
n_b	Max. number of bunches per beam	2208	2808
N_p	Max. number of particles per bunch	1.31×10^{11}	10^{11}
L_{inst}	Peak instantaneous luminosity [cm^{-2} s^{-1}]	2×10^{34}	10^{34}

Table 2.1: Table showing some LHC collision parameters from the latest 2018 run [71], compared with the machine design values.

---

[1] This formula holds for two colliding bunches containing the same number of particles.

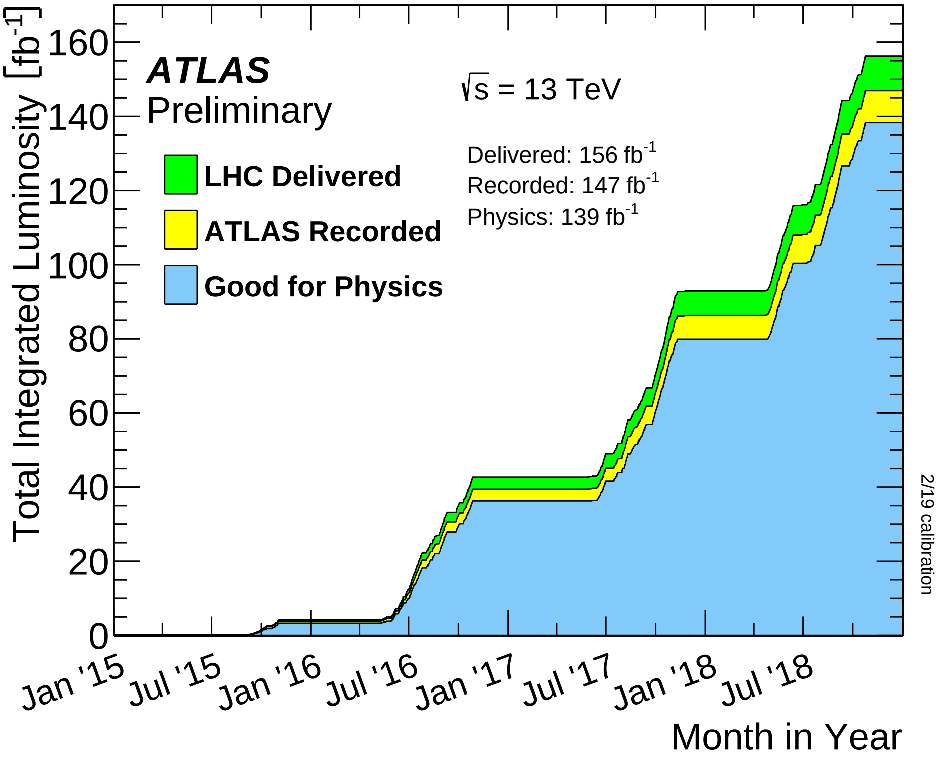

Figure 2.2: Cumulative luminosity versus time delivered to ATLAS (green), recorded by ATLAS (yellow), and certified to be good quality data (blue) during stable beams for pp collisions at 13 TeV centre-of-mass energy in 2015-2018.[72]

2.1.2 Features of *pp* collisions at the LHC

When a hard scattering between two partons happens in *pp* collisions at hadron colliders, other effects manifest in the detector. In the collision between two protons two main effects occur: the interaction between two partons and the interactions between the remaining fragments of the proton, called the **underlying event**. The underlying event can be thought of as all what is seen in a single hadron collision event which is not coming from the primary hard scattering process. It represents the hadronization of the collided proton remnants, as well as all spectator interactions outside the hard scattering event of interest. The overlap of *pp* collision events to the hard scattering of interest is referred to as pile-up (PU). **In-time PU** is the effect of multiple collisions simultaneously happening in a single proton bunch crossing. Conversely, **out-of-time PU** is related to the time window of the detector response, extending over several bunch crossings, and depends on the spacing between proton bunches. For the out-of-time PU activity, the average number of interactions per bunch crossing at the time of the recorded events μ provides a good estimator:

$$\mu = \frac{L\sigma_{inel}}{n_b f_r} \tag{2.3}$$

where L is the average instantaneous luminosity over a rather large window in time, σ_{inel} is the total inelastic *pp* cross section, n_b is the number of colliding bunches and f_r is the bunch revolution frequency [73]. In Figure 2.3, an overview of the pile-up in *pp* collisions recorded by ATLAS during Run 2 is given. PU represents a formidable experimental challenge as it degrades the performance of some physics object reconstruction algorithms by introducing additional activity in the detectors.

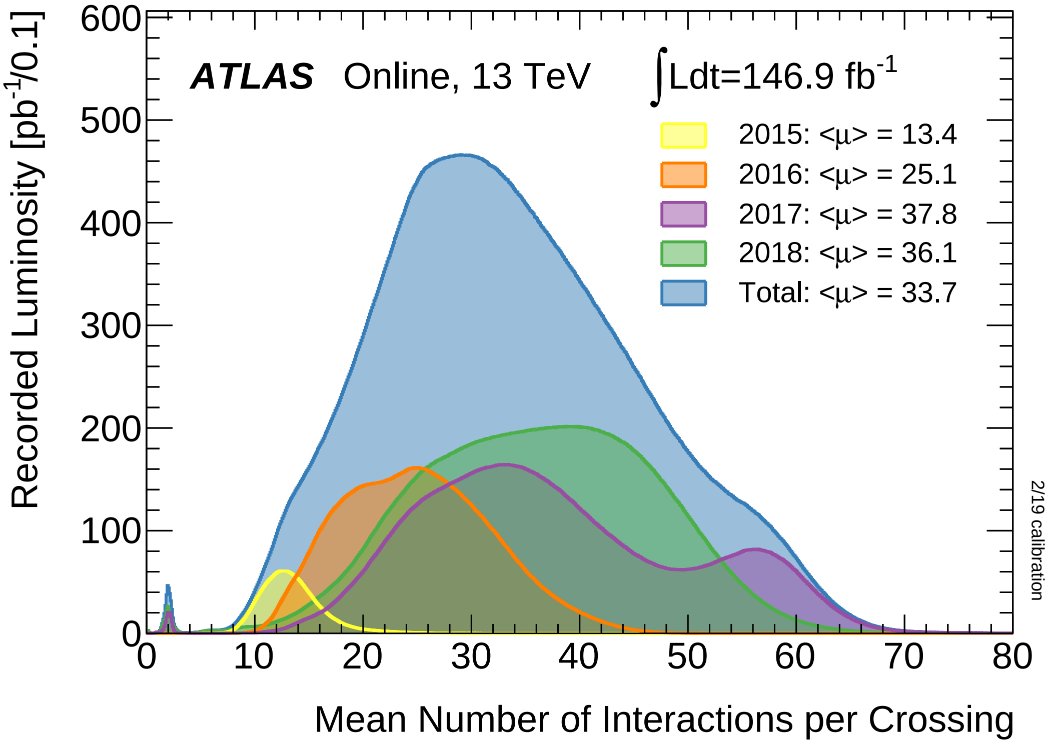

Figure 2.3: Luminosity-weighted distributions of the mean number of interactions per crossing for the pp collision dataset across the full Run 2 period at 13 TeV centre-of-mass energy.[72]

2.2 The ATLAS detector

The ATLAS experiment [66] is a multipurpose detector with a forward-backward symmetric cylindrical geometry and nearly 4π coverage in solid angle. It uses a right-handed coordinate system with its origin at the nominal interaction point (IP) in the center of the detector and the z-axis along the beam pipe. The x-axis points from the IP to the center of the LHC ring, and the y-axis points upward. Cylindrical coordinates (r, ϕ) are used in the transverse plane, ϕ being the azimuthal angle around the beam pipe. The pseudorapidity is defined in terms of the polar angle θ as

$$\eta = -\ln\left[\tan\left(\frac{\theta}{2}\right)\right] \tag{2.4}$$

In this reference frame the transverse momentum p_T is defined as

$$p_T = \sqrt{p_x^2 + p_y^2} \tag{2.5}$$

The distance in the xy plane can be expressed by

$$\Delta R = \sqrt{(\Delta\eta)^2 + (\Delta\phi)^2} \tag{2.6}$$

ATLAS aims to search for new phenomena as well as to test the SM. It is the largest detector at the LHC, since it is about 44 m long, 25 m high and weighs about 7000 tonnes. A scheme of the detector is given in Figure 2.4.

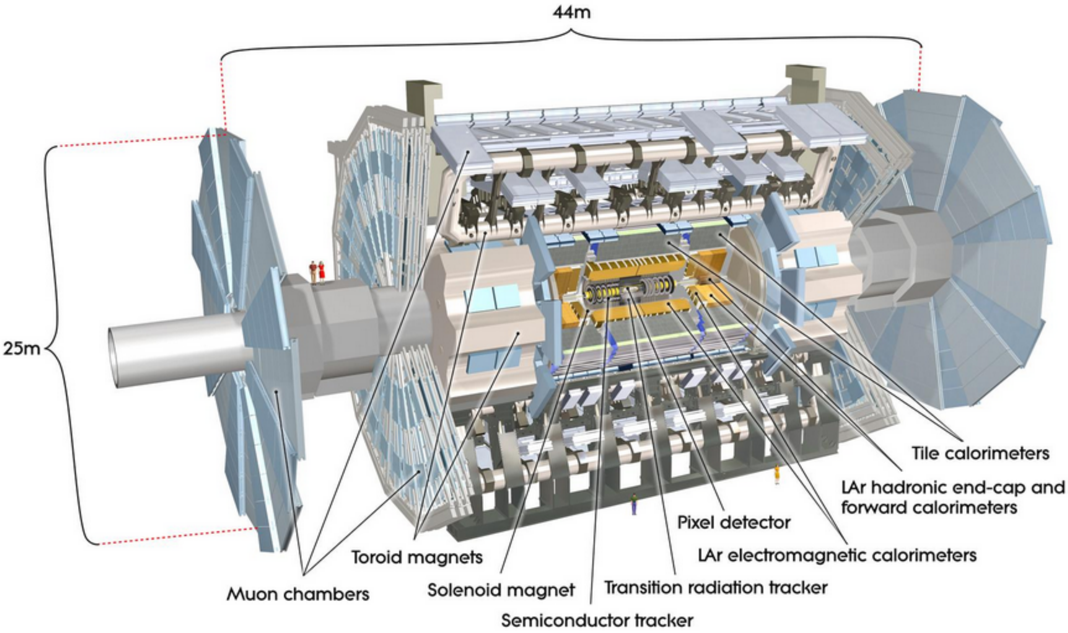

Figure 2.4: A scheme of the ATLAS detector.

2.2.1 Subdetectors

ATLAS is made of several sub-detectors such as an **inner tracking detector**, a system of **electromagnetic** and **hadronic calorimeters** and a **muon spectrometer**. A magnetic field of 2T is provided by a solenoid inserted around the tracker and it's used to measure the momentum of charged particles from the curvature of their tracks.

The inner detector (ID) tracking system (Figure 2.5) provides position measurements for charged particles in the range $|\eta| < 2.5$ by combining information from three sub-detectors. The ID consists of a cylindrical central region (full coverage for $|\eta| < 1.5$) arranged around the beam pipe, and two endcaps. Disks in the endcap region are placed perpendicular to the beam axis, covering $1.5 < |\eta| < 2.5$. Starting from the IP, the high-granularity silicon pixel detector segmented in r–ϕ and z covers the vertex region and typically provides four three-dimensional measurements per track. Since the start of Run 2, the ID includes a new innermost layer, the insertable B-layer (IBL) [74], with a mean radius of 33 mm, while the remaining three layers of the pixel system are located at mean radii of 50.5, 88.5, and 122.5 mm respectively. The coverage in the endcap region is provided by three disks on either side of the IP. A semiconductor tracker (SCT) consisting of modules with two back-to-back silicon microstrip sensors with small-angle stereo readout surrounds the pixel detector, providing typically eight two-dimensional hits translating to four three-dimensional measurements, per track at intermediate radii (275 mm $< r <$ 560 mm). The outermost region of the ID (563 mm $< r <$ 1066 mm) is covered by a transition radiation tracker (TRT) consisting of straw drift tubes filled with a gas mixture consisting of about 70% Xe, 27% CO_2 and 3% O_2,[2] interleaved with polypropylene/polyethylene transition radiators. The ID allows an accurate reconstruction and p_T measurement of tracks from the primary proton–proton collision region. It also identifies tracks from secondary vertices, permitting the efficient reconstruction of photon conversions up to a radial distance of about 80 cm from the beam-line. The intrinsic resolution of the ID in the central barrel without the IBL is around $\sigma\left(\frac{1}{p_T}\right)p_T = 0.036\% p_T[\text{GeV}] \bigoplus 1.3\%$ [75].

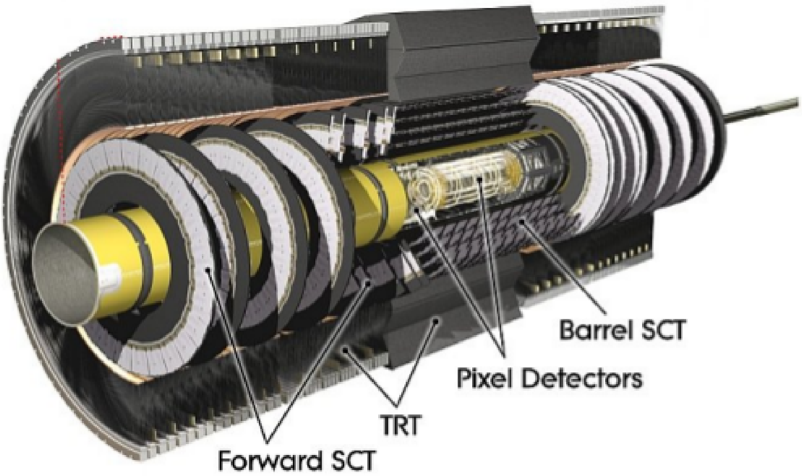

Figure 2.5: A scheme of the ATLAS Inner Detector. The IBL is not shown here.

The electromagnetic (EM) calorimeter (Figure 2.6) is a lead/liquid-argon (LAr) sampling calorimeter with an accordion geometry. It consists of a barrel section, covering the pseudorapidity region $|\eta| < 1.475$, and of two endcap sections, covering $1.375 < |\eta| < 3.2$. The EM calorimeter is divided in three longitudinal layers, for $|\eta| < 2.5$, and in two layers for $2.5 < |\eta| < 3.2$. In the regions $|\eta| < 1.4$ and $1.5 < |\eta| < 2.4$, the first layer has a fine η segmentation to discriminate prompt photons from neutral hadrons decaying to pairs of close-by photons. It also allows, together with the information from the cluster barycenter in the second layer, where most of the energy is collected, a measurement of the shower direction without assumptions on the photon production point. In the range of $|\eta| < 1.8$ a presampler layer allows corrections to be made for energy losses upstream of the calorimeter. The cell granularity in each layer is shown in Figure 2.7.
The target EM calorimeter energy resolution (design for $\eta \approx 0$) is given by $\frac{\sigma_E}{E} = \frac{10\%}{\sqrt{E}} \bigoplus \frac{150\ MeV}{E} \bigoplus 0.7\%$ [66]. More details about the reconstruction and calibration of the energy of a LAr EM cell will be given in Chapter 3.

The hadronic calorimeter (Figure 2.6), which surrounds the EM calorimeter, consists of a steel/scintillator-tile calorimeter in the range $|\eta| < 1.7$ and two copper/LAr calorimeters spanning $1.5 < |\eta| < 3.2$. The acceptance is extended to $|\eta| \leq 4.9$ by two sampling calorimeters longitudinally segmented in shower depth into three sections using LAr as active material and copper (first section) or tungsten (second and third

---

[2] During part of the 2016 data-taking some TRT layers were filled with Argon instead of Xenon.

sections) as absorber. The hadronic calorimeter is designed to measure the energy with a target resolution of $\frac{\sigma_E}{E} = \frac{50\%}{\sqrt{E}} \bigoplus 3\%$ [76].

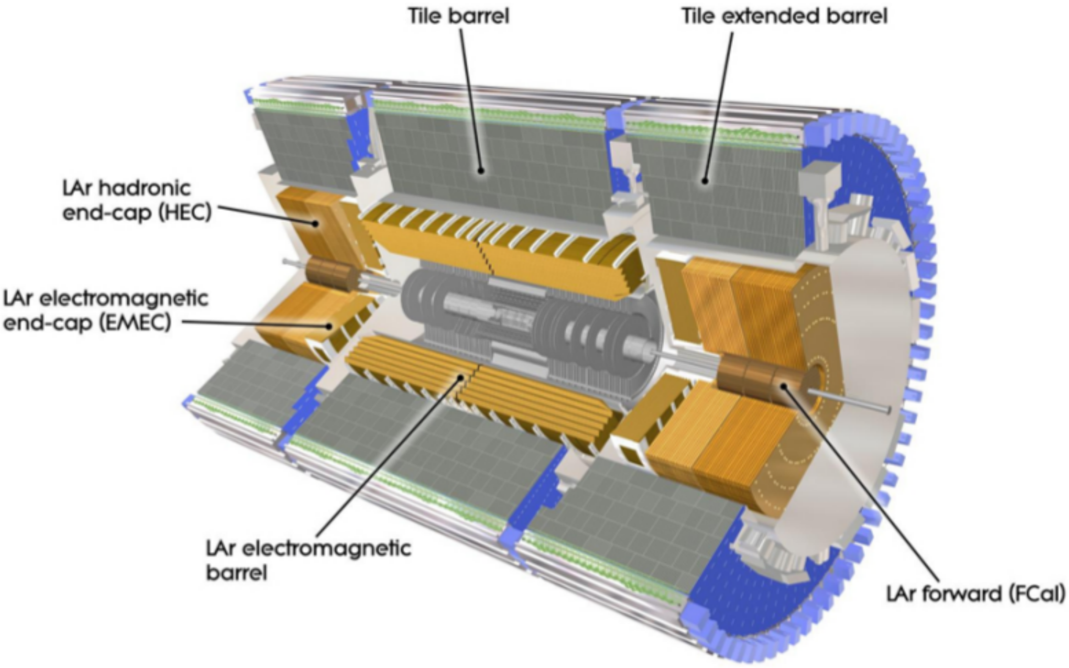

Figure 2.6: A scheme of the ATLAS calorimeters.

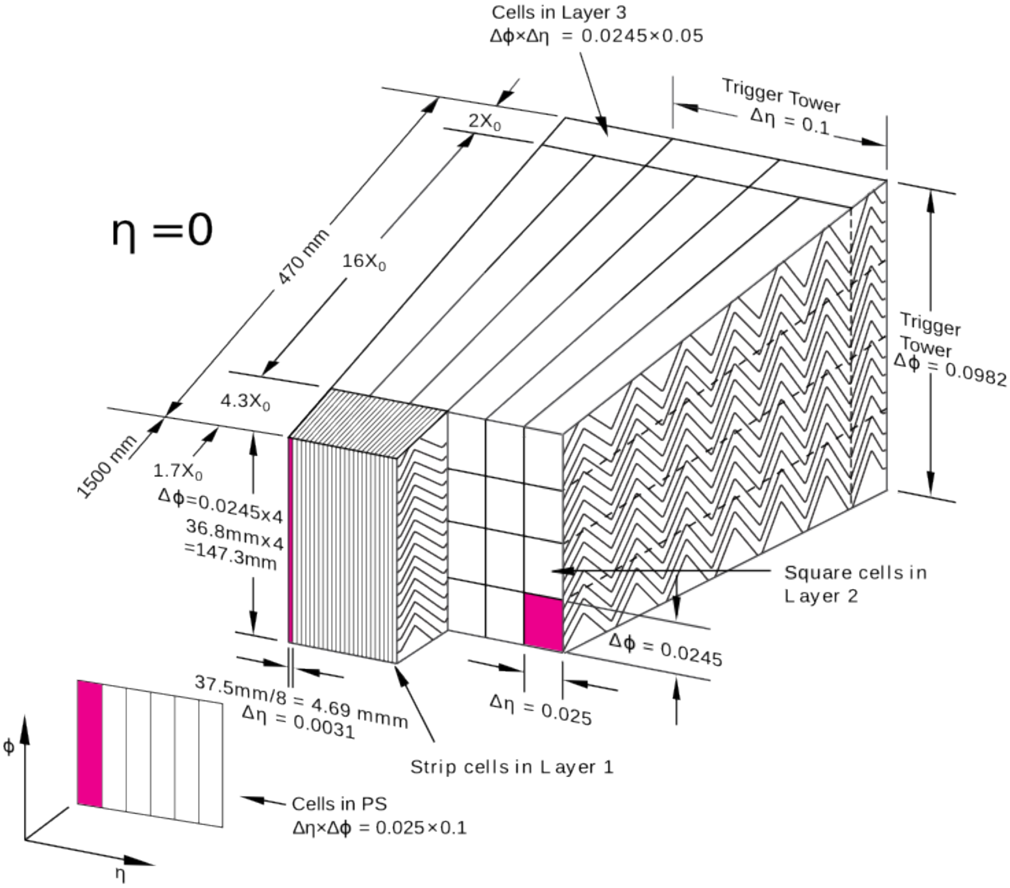

Figure 2.7: Sketch of a section of the LAr calorimeter showing its cells at different layers and their granularity in η and ϕ.

The muon spectrometer (MS), located outside the calorimeters, consists of three large air-core superconducting toroid systems with precision tracking chambers that provide accurate muon tracking for $|\eta| < 2.7$ and fast detectors for triggering for $|\eta| < 2.4$. The overall momentum resolution $\frac{\sigma_{p_T}}{p_T}$ of the muon system is 4% (1%) at 5 GeV (1 TeV)[75].

2.2.2 Trigger

With the very high proton inelastic scattering rate, the ATLAS trigger system is a fundamental component of the detector, being responsible for deciding whether or not to save an event from a bunch crossing for later offline study. A two-level trigger system [77] was used during the $\sqrt{s} = 13$ TeV data-taking period initiated in 2015 and finished in 2018. Dedicated hardware implements the first-level (L1) trigger selection, using only a subset of the detector information and reducing the event rate from about 40 MHz to at most 100 kHz. Events satisfying the L1 requirements are processed by a high-level trigger executing, on a computer farm, algorithms similar to the offline reconstruction software, in order to reduce the event rate to approximately 1 kHz.

2.2.3 Physics objects reconstruction

Events selected by the trigger are stored in order to be later reconstructed by the ATLAS offline software. The reconstruction procedures of the physics objects used within the context of the ATLAS analyses are summarized in this section.

Photons are reconstructed from calorimeter clusters formed using a dynamical, topological cell clustering algorithm [78]. The reconstruction algorithm looks for possible matches between energy clusters and tracks reconstructed in the inner detector and extrapolated to the calorimeter. Well-reconstructed tracks matched to clusters are classified as electron candidates, while clusters without matching tracks are classified as unconverted photon candidates. Clusters matched to pairs of tracks that are consistent with the hypothesis of a $\gamma \to e^+e^-$ conversion process are classified as converted photon candidates. The calibrated energy of photons is obtained from the energy of the corresponding EM cluster, after applying a series of data-driven and MC-based corrections; a more detailed description of the calibration procedure can be found in Chapter 3. The **photon identification** algorithm is based on the lateral and longitudinal energy profiles of the shower measured in the calorimeter [79] and it is optimized to reduce as much as possible contamination from the background, primarily associated with neutral hadrons in jets decaying into photon pairs. Photon candidates are required to deposit only a small fraction of their energy in the hadronic calorimeter, and to have a lateral shower shape consistent with that expected from a single electromagnetic shower. Different working points (WP) are defined and can be used by the analyses according to their needs in terms of quality requirement: typically *loose* criteria are chosen for triggering and preselection purposes, while *tight* criteria ensure the highest purity when defining the final event selection. Typical values of identification efficiency for the tight working point as a function of E_T are shown in Figure 2.8: around 30 GeV the efficiency is about 85%, while after 60 GeV it saturates to 95%. To reject the hadronic jet background, **photon candidates are required to be isolated** from other activity in the calorimeter and the tracking detectors [80]. The calorimeter isolation is computed as the sum of the transverse energies of positive-energy topological clusters in the calorimeter within a cone of $\Delta R = 0.2$ centered around the photon candidate. Candidates with a calorimeter isolation larger than 6.5% of the photon transverse energy are rejected. The track isolation is computed as the scalar sum of the transverse momenta of all tracks with $p_T > 1$ GeV in a cone of $\Delta R = 0.2$ around each photon. Candidates with a track isolation larger than 5% of the photon transverse energy are rejected. Isolation efficiency curves as a function of E_T are shown in Figure 2.9 for the three working points: *loose*, *medium* and *tight*.

Jets are reconstructed using the anti-k_t algorithm [81] with the parameter $R = 0.4$ and using a particle flow algorithm [82]. These algorithms use as input topological clusters in the calorimeters and information about tracks that are matched to them. A jet-vertex-tagger (JVT) multivariate algorithm [83] is applied in order to suppress contributions coming from pileup interactions. Jets with $|\eta| < 2.5$ containing b-hadrons are identified using a b-tagging algorithm [84]. A detailed description of the jet calibration procedure can be found in [85].

Electrons are reconstructed by matching tracks in the ID to topological calorimeter clusters formed using the same algorithm used in the reconstruction of photons [78]. The energy calibration of electrons follows the same procedure of the one for photons, and it is explained in Chapter 3.

Since **muons** leave a very small energy deposit in the calorimeters, they are reconstructed by using tracks from the MS and ID subdetectors. A full description of the reconstruction and calibration procedures is given in [86].

The reconstruction of photons, jets, electrons and muons is performed independently by the ATLAS offline software. Therefore, in order to avoid double-counting objects in the analyses, an **overlap removal** procedure is done. The overlap criterion is based on the value of ΔR (defined in Eq. 2.6) between objects [87].

In a collider, the initial transverse momentum of the colliding particles is zero by construction. The total transverse momentum of all the particles in the final state should be zero as well. For this reason, the **missing transverse energy (MET)** can be defined as the negative vector sum of the transverse momenta of all the reconstructed objects (after overlap removal), plus any transverse momenta not assigned to any of the selected objects but compatible with the primary vertex of the event [88].

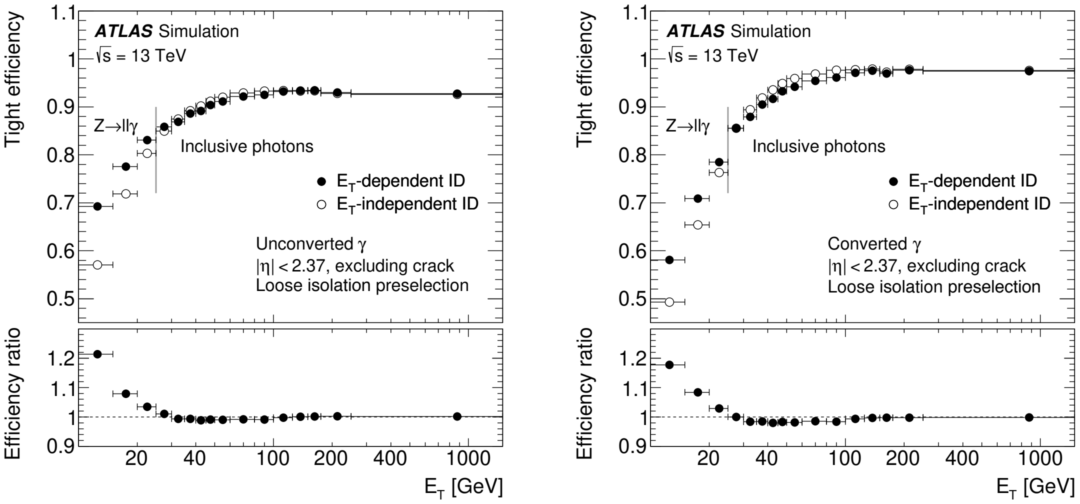

(a) Unconverted photons.

(b) Converted photons.

Figure 2.8: Efficiencies of the Tight photon identification for unconverted (left) and converted (right) photons, plotted as a function of photon E_T [78].

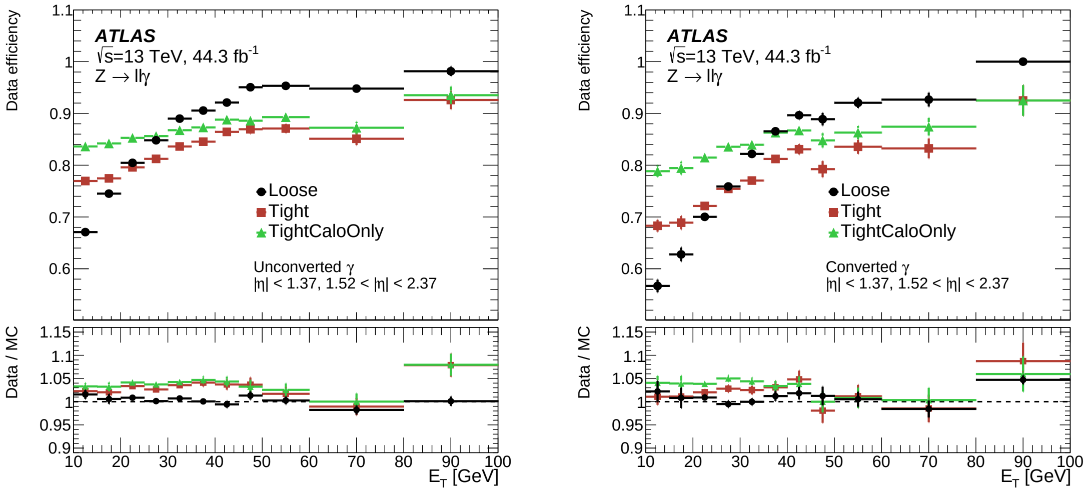

(a) Unconverted photons.

(b) Converted photons.

Figure 2.9: Efficiencies of the photon isolation working points for unconverted (left) and converted (right) photons, plotted as a function of photon E_T [78].

Chapter 3

Electron and photon energy calibration

In order to perform very precise measurements of the Higgs boson properties in the diphoton decay channel, a very accurate calibration of the photon energy is extremely important. The calibration procedure in ATLAS is a complex chain involving many different tasks. This chapter serves as a detailed introduction for the study presented in the next one.

3.1 Energy reconstruction in a LAr calorimeter cell

When an electron or photon reaches the calorimeter, it produces an electromagnetic shower after the interaction with the lead absorbers. The EM showers ionize the LAr in the gaps between the absorbers where a high voltage is applied. The ionization electrons drift, producing an analog signal. The sum of these analog signals associated to the shower is proportional to the energy of the original particle entering the calorimeter (as shown in Figure 3.1). The signal is brought via cables to the Front End Boards (FEBs) where it's pre-amplified, then further amplified and shaped by three linear gains: low (LG), medium (MG) and high (HG). The ratio between the amplification factor of two consecutive gains is about 10. This split into three pipelines is needed to digitize the measurement into a 16 bits dynamic range of energy (from about 10 MeV to about 4 TeV) using 12 bits analog-to-digital converters (ADC). The three amplified signals are sampled at a 40 MHz clock frequency and stored on a switched capacitor array (SCA), then a hardware gain selection is used to choose the most suited gain. The choice is made according to the number of ADC counts[1] recorded for the digitized MG peak:

- $<$ 1300 ADC: HG is selected;
- $\geq$ 1300 ADC and $<$ 3900 ADC: MG is selected;
- $\geq$ 3900 ADC: LG is selected.

The samples of the chosen gain are digitized and routed via optical fibres to the read-out drivers (ROD) (as shown in Figure 3.2) [89]. Figure 3.3 plots the expected signal pulse before and after the shaping and sampling.

Calibration runs use calibration electronics boards to inject precise pulses with programmable amplitudes and delays. These calibration signals are exponential before shaping, approximating the triangular ionization pulse.

The total energy deposited in an EM calorimeter cell is reconstructed as

$$E_{\text{cell}} = F_{\mu\text{A}\to\text{MeV}} \times F_{\text{DAC}\to\mu\text{A}} \times \frac{1}{\frac{M\text{phys}}{M\text{cali}}} \times G \times \sum_{j=1}^{\text{N}_{\text{samples}}} a_j \left(s_j - p\right) \tag{3.1}$$

where:

- E_{cell} is the total energy deposited in an EM calorimeter cell;
- s_j are the samples of the shaped ionization signal digitized in the selected electronic gain, measured in ADC counts in $\text{N}_{\text{samples}} = 4$ time slices spaced by 25ns;
- p is the read-out electronic pedestal, measured for each gain in dedicated calibration runs (also called *pedestal runs*);
- a_j are the optimal filtering coefficients (OFC) derived from the predicted shape of the ionization pulse and the noise autocorrelation, accounting for both the electronic and the pile-up components;
- G is the cell gain and it's computed through the injection of a known calibration signal and the reconstruction of the corresponding cell response (during the *ramp runs*);
- $\frac{M\text{phys}}{M\text{cali}}$ quantifies the ratio of the maxima of the physical and the calibration pulses corresponding to the same input current and it corrects the factor G obtained with the calibration pulses to adapt it to physics-induced signals;
- $F_{\text{DAC}\to\mu\text{A}}$ converts digital-to-analog converter (DAC) counts set on the calibration board to an electric current in μA;

---

[1] It is important to notice that the ADC thresholds are programmable: their value can be changed, for example during *special* runs.

- $F_{\mu \mathrm{A} \rightarrow \mathrm{MeV}}$ converts the ionization current to the total deposited energy at the EM scale and it is determined from test-beam studies.

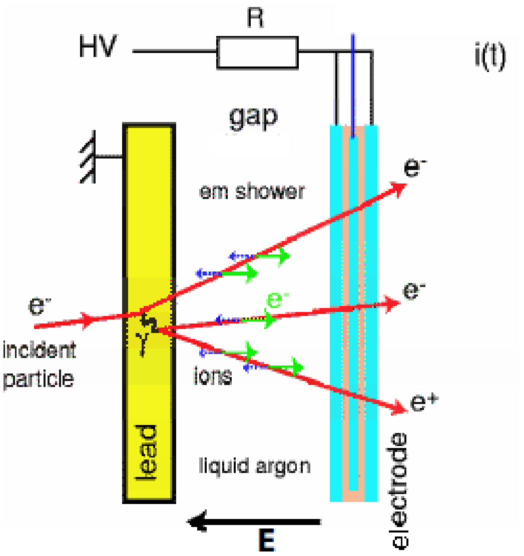

Figure 3.1: Schematic representation of the electric signal produced in a LAr gap.

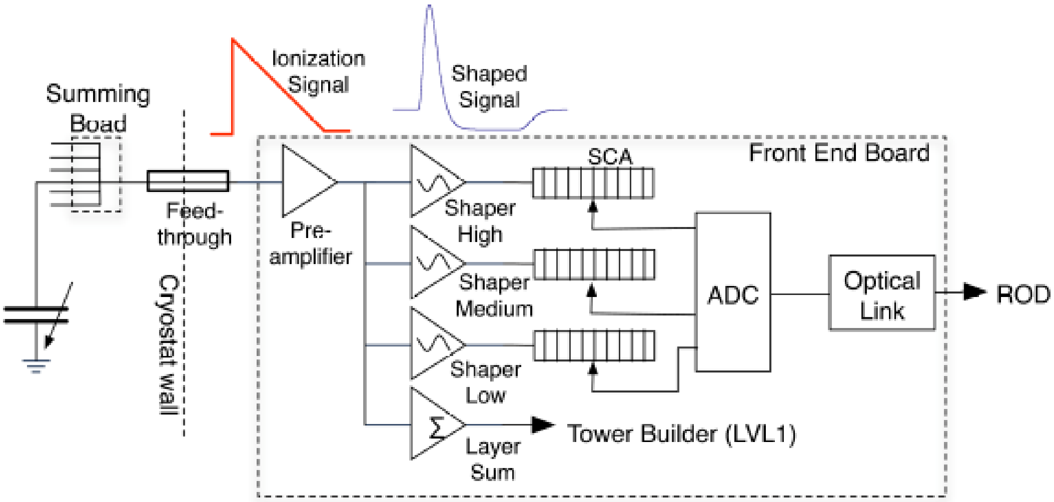

Figure 3.2: Sketch of the LAr front-end readout electronics.

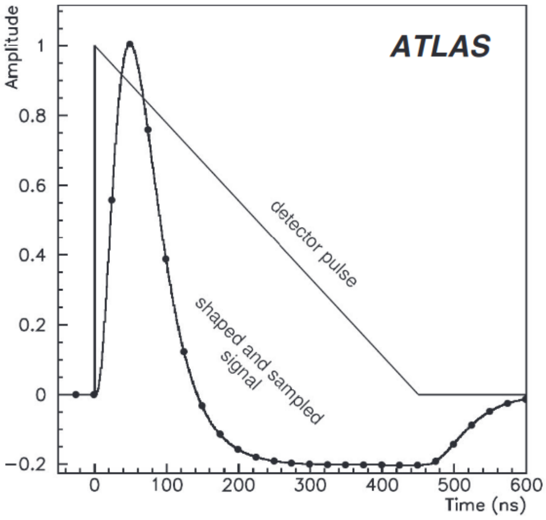

Figure 3.3: Triangular pulse of the current in a LAr EM cell and the FEB output signal after shaping and sampling (25 ns spacing) [66].

3.2 Calibration procedure

Starting from the raw energy of a cluster of cells, one can get the calibrated energy of the incident particle following the pipeline described in Figure 3.4 [89]. This procedure exploits information from both MC simulations and collision data. A very short summary of each step in the pipeline is given:

1. The cluster energy is estimated from the energy deposit in the calorimeter cells in the various layers. Using MC samples of simulated events, a multivariate (MVA) regression is trained, which uses input detector-level variables (such as the energy deposited in the calorimeter, the ratio of the energies deposited in the first and the second layer E_1/E_2, the η impact point of the shower in the calorimeter, etc.). The optimization of the algorithm is performed separately for electrons, converted photons and unconverted photons. This MC-based calibration strongly relies on the validated assumption that the detector geometry and the interactions of particles with matter are accurately described in the simulation;
2. The relative energy scales of the different layers of the EM calorimeter are adjusted and are applied to the data as a correction. The estimation of this layer inter-calibration is based on studies of muon energy deposits and electron showers;
3. The MVA algorithm trained in Step 1 is applied to both MC and data;
4. Several miscalibrations due to detector effects not present in the MC are estimated and corrected in the data. These include high-voltage inhomogeneities, geometric effects or biases associated to the LAr electronics. Chapter 4 will focus on the study of the energy miscalibration due to the non-linearity across the electronic gains;
5. In order to correct residual miscalibrations still present between data and MC at this stage, overall energy scale factors are derived. This is done using a well-known physics process, the Z boson decay into a positron-electron pair ($Z \to ee$).

These in-situ scale factors are computed for an electron energy around 40 GeV, which is the typical value expected from a product of the Z decay. However, they are currently considered to be universal and are applied to both electrons and photons of any energy. They are also presently considered to be independent on p_T.

6. Finally, the whole procedure is also validated using electrons from $J/\psi \to ee$ events in data. Additionally, the universality of the scale factors for photons is tested using photons from $Z \to ll\gamma$ events in data, where l is either an electron or a muon.

The systematic uncertainties associated to the scale factors are computed at energies different than the average energy of an electron produced in a Z boson decay. They are also computed separately for each particle type. Figure 3.5 illustrates the impact of the main systematic uncertainties affecting the energy scale of electrons, unconverted photons and converted photons at $|\eta| = 0.3$ as a function of the transverse energy, as estimated at the beginning of Run 2 [90]. At given values of both E_T and η, the total systematic uncertainty is given by the sum in quadrature of the uncertainties related to each of the independent sources. The uncertainty related to the HG/MG non-linearity (corresponding to the green dashed line in each of the three plots) contributes the most at high energies, especially for electrons and unconverted photons.

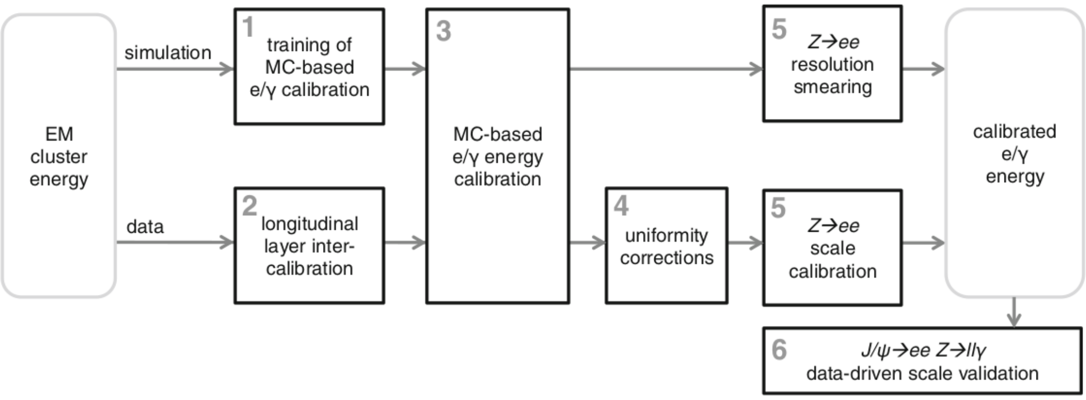

Figure 3.4: Flowchart of the energy calibration of the electrons and photons in ATLAS.[90]

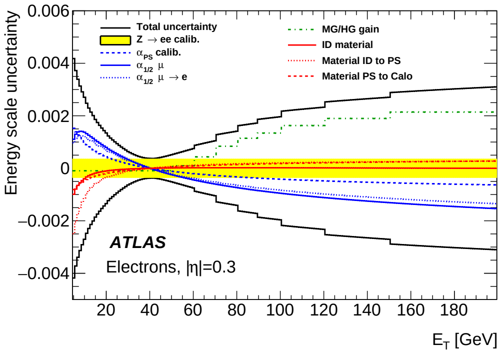

(a) Electrons.

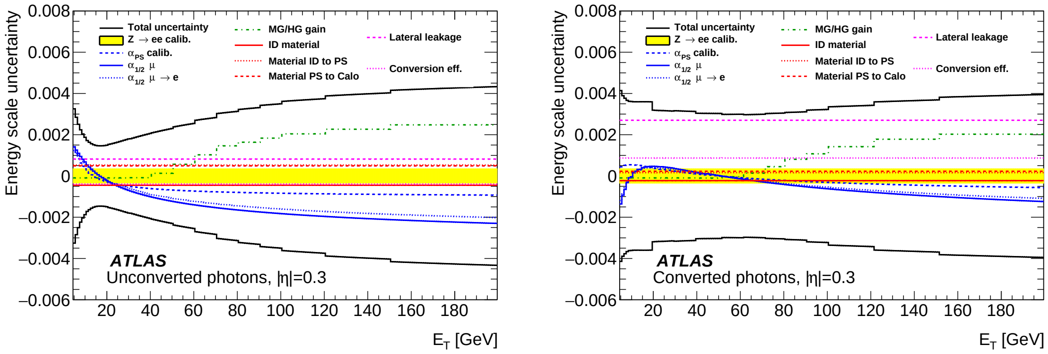

(b) Unconverted photons.

(c) Converted photons.

Figure 3.5: Energy scale uncertainty for different particle types, as a function of E_T and at $|\eta| = 0.3$. The main contributions are shown as well as the total.[90]

Chapter 4

Intercalibration of the high and medium gains of the electromagnetic calorimeter front-end electronics using special $Z \to e^+e^-$ data

The research work contained in this chapter allowed me to achieve the qualification of author within the ATLAS collaboration. Its content is also fully documented in an ATLAS internal note [91].

4.1 Introduction

4.1.1 Motivations

Since the finalization of the electron and photon calibration using Run 1 data [89], a discrepancy between the reconstructed dielectron invariant mass $m_{e^+e^-}$ obtained from $Z \to e^+e^-$ events in data and MC was observed, when events were split according to the electronic high or medium gain of the highest energy cell of the liquid Argon (LAr) EM calorimeter second longitudinal layer (layer 2, middle) [92]. The typical energy depositions in layer 2 is up to about 30 GeV for the high gain and between 30 GeV and 300 GeV for the medium gain. While initially attributed to a miscalibration of the LAr electronic gains in data, subsequent studies have shown that part of the discrepancy was related to the use of the old calibration regression [93], and the residual effect could at least in part be attributed to a sub-optimal calibration regression for very wide or very narrow electromagnetic showers, for which a correction was applied [94].

Further studies were nevertheless performed to estimate in an independent way a possible residual miscalibration of the medium and high LAr gains, using special $Z \to e^+e^-$ runs taken in 2015 and 2017 in the shadow of the toroid-off muon alignment runs. For these runs, the threshold to switch from high gain to medium gain readout in the second layer of the EM calorimeter was significantly lowered, such that almost all electrons from Z decays had at least the highest energy cell in the middle layer recorded using the medium gain readout. The results of the analysis of these runs is documented in Ref. [94]: a residual miscalibration of the medium gain up to about 0.4 % was observed for the pseudorapidity region $|\eta| \in (0.8 - 1.37)$. Since the effect observed in the special run in this η region was at the time not understood, the full size of the effect was adopted as a systematic uncertainty, and no attempt was made to correct it [94, 95].

As previously discussed in Section 1.5, the impact of this systematic uncertainty is, at the time of writing, the largest systematic uncertainty on the Higgs boson mass $m_H^{\gamma\gamma}$ measured with $H \to \gamma\gamma$ decays using collision data collected between 2015 and 2017 [52]. The "EM calorimeter cell non linearity" systematic uncertainties on $m_H^{\gamma\gamma}$, as the impact of the observed discrepancy between the high and medium gain LAr electronic calibration is labeled in Ref. [52], amounts in fact to 180 MeV out of a total systematic uncertainty of 340 MeV.

This chapter presents a revised analysis of new special $Z \to e^+e^-$ runs collected in 2018 with the threshold to switch from high gain to medium gain readout in the second layer of the EM calorimeter again significantly lowered, attempting to confirm and improve the understanding of the results presented in Ref. [94], so that any residual LAr gain miscalibration can be corrected for, significantly reducing the electron and photon energy calibration systematic uncertainty.

4.1.2 Analysis strategy

When the threshold to switch from high gain to medium gain readout in the second layer of the EM calorimeter is significantly lowered, the medium gain is also used in a region where the electronic response can significantly deviate from the expected linear behavior. Since the calibration of the electronic gains performed by analyzing "ramp" runs (see Ref. [96] for details) assume a linear behavior, the standard reconstruction of the these special $Z \to e^+e^-$ runs would introduce a bias to the electron energy reconstruction. Before comparing the special and normal (i.e. with normally-set gain switch threshold) $Z \to e^+e^-$ runs to study the potential discrepancy of the gain response, non-linear corrections to the electronics gains obtained with the ramp runs need to be applied. For this reason, special medium gain ramp runs extending to the region including lower signal amplitude are acquired in proximity of the acquisition the special $Z \to e^+e^-$ runs. The calculation and systematic study of the corrections from these special ramp runs is discussed in Section 4.2, as well as the procedure to apply it to the LAr cells in the cluster associated to the electrons in the special $Z \to e^+e^-$ runs.

Section 4.3 summarizes the study of the bias potentially introduced in the gain calibration by a fixed offset of the output of the LAr calibration boards.

Once the special $Z \to e^+e^-$ runs have been corrected by known non-linearity of the electronics in the region opened by the gain switch threshold lowering, the $m_{e^+e^-}$ response can be compared with that in normal runs acquired immediately before and after the special runs. This comparison, and the measurement of a possible residual energy miscalibration, is discussed in details in Section 4.4, as well as all associated systematic uncertainties.

4.2 Medium Gain ramp recalibration

4.2.1 Special Medium Gain ramp runs

As described in chapter 3, the calibration of the energy deposited by electrons and photons in the EM calorimeter, is based on a panoply of procedures, one being the electronics calibration. An electronics signal, with an exponential shape close to the ionization pulse shape is generated on the calibration board and propagated inside the cryostat onto the mother boards located at the front and back of the calorimeter. The amplitude of the signal is controlled by a digital to analog converter (DAC) providing a dynamic range for each calorimeter layer corresponding to an electron of up to 3 TeV. Each calibration board is equipped with 128 calibration lines; each line serves a group of 8 to 16 channels depending on the layer. The (non-) linearity of the signal delivered by the calibration boards was measured to be at the level of 0.1% during the production of the boards. 120 calibration boards are installed, with typically two per frontend crate.

During periods without beam, typically during inter-fill periods, calibration runs are taken, ramping the DAC value from 0 to a DAC value corresponding to the maximum current that a given cell would receive during LHC data taking. These calibration data allow in particular to measure the linearity of the cell response to the injected signal; this procedure is called ramp run and will be used in the analysis presented below.
Ramp runs are used to extract the response of each cell as a function of the injected current using calibration boards. The ADC to energy conversion in medium gain at reconstruction level is performed using a first order polynomial relation. Since it is not expected to be very accurate at lower ADC values, which are populated in the special runs, an improved calibration is derived using electronics calibration data corresponding to the following runs:

- **Run 362822**: Special medium gain ramp run with also ADC values used normally only in high gain runs;
- **Run 362824**: Standard medium gain ramp run (for reference).

In practice, the aforementioned improved calibration consists in the application of a non-linear correction to the ramp used for reconstruction.

There are 256 × 200 ($\phi - \eta$) cells in the second layer of the LAr calorimeter, each of which has a size of 0.025 × 0.025 in $\Delta\phi \times \Delta\eta$. A certain fraction of these channels suffers from problems in the electronics or the readout.

These so-called bad channels as well as those cells whose center has $1.4 < |\eta| < 1.425$ are not considered in this study and the corresponding value of the correction is taken as zero.

The choice of recorded (ADC, DAC) points to be used when fitting the ramp is dynamically made by the reconstruction software: for each consecutive pair of points the local slope of the ramp is computed and is compared to the average slope of all the previous points. If the difference between the average slope and the local one is less (or equal) than the 10% of the average slope then the latest point is kept and the next one will be checked; otherwise the latest point is discarded and only the previous recorded points are used to fit the ramp. This method prevents reaching the saturation region of the electronic response in MG. Additionally, the first point at DAC=0 is always skipped in the official ramp fit setting the minimum DAC value to 10. As a result, the number of points used to fit the ramp can be different for different cells in the calorimeter.

Since the largest fraction of the energy of an electromagnetic shower induced by an electron in the ATLAS LAr EM calorimeter is deposited in the second longitudinal layer (Middle layer or Layer 2), the following study and the calculation of the associated corrections are exclusively performed for the LAr EM Middle cells.

4.2.2 Improved ramp fit

In order to account for non-linearities in low ADC regions when fitting the ramps, a second order polynomial was proposed in [97], whose functional form is:

$$f^{\text{improved}}(ADC) = ADC\frac{p_0' + p_1' ADC}{p_2' + ADC} \tag{4.1}$$

in contrast to the usual first order polynomial:

$$f^{\text{linear}}(ADC) = p_0 + p_1 ADC \tag{4.2}$$

In theory, Eq.4.1 should be a more suitable function to describe the special run ramps because it smoothly goes to zero for small ADC values, while it behaves like a linear ramp for large ADC values. In practice, this hypothesis must be tested by means of some statistical estimator for all the fitted ramps. The values of two estimators are reported:

- **Worst residual**: it's the largest value of $\left|\frac{DAC-f(ADC)}{DAC}\right|$. It quantifies the disagreement between the fit and the data at low ADC values;
- **RMS of the residuals excluding the worst one**: it's the RMS of the residuals $DAC - f(ADC)$ after removing the worst one. This estimator is correlated to the χ^2 of the fit and it's supposed to not contain much information about the result of the fit at low ADC values.

An example of fit for a given cell is shown in Figure 4.1a, where it is clear, by looking at the value of the worst residual, that the improved fit describes the region with low ADC values better than the linear fit. Another example of fit for a different cell is given in Figure 4.2a: the distribution of the residuals of the improved fit is narrower around zero than the one of the linear fit, which is again a proof of the improvement brought by Eq.4.1.

However, there are some cells for which the previous statements are not true anymore. Figure 4.1b shows the result in one cell where the linear fit has a lower value of the worst residual. Figure 4.2b shows that for some cells the value of the RMS of the residuals excluding the worst one is the same for both the linear fit and the improved fit. This happens because the parameters p_0' and p_1' of Eq.4.1 are always initialized with the values of the parameters p_0 and p_1 obtained by the linear fit. As a result, the improved fit can never be outperformed by the linear fit when describing the region with high ADC values, where the ramp is more likely to follow a linear trend.

Whether or not the improved fit looks like a reasonable choice for a given cell, its global impact must be evaluated over all the cells of the second layer. In the following sections, the goodness-of-fit and its statistical significance are investigated in order to understand if Eq. 4.1 actually brings an improvement to the ramp re-calibration.

Goodness-of-fit

The distributions of the values of the first of the two estimators defined previously are shown in Figure 4.3 for the linear fit and the improved fit. Most of the worst residuals of the linear fits have negative values, implying that the linear fits tend to

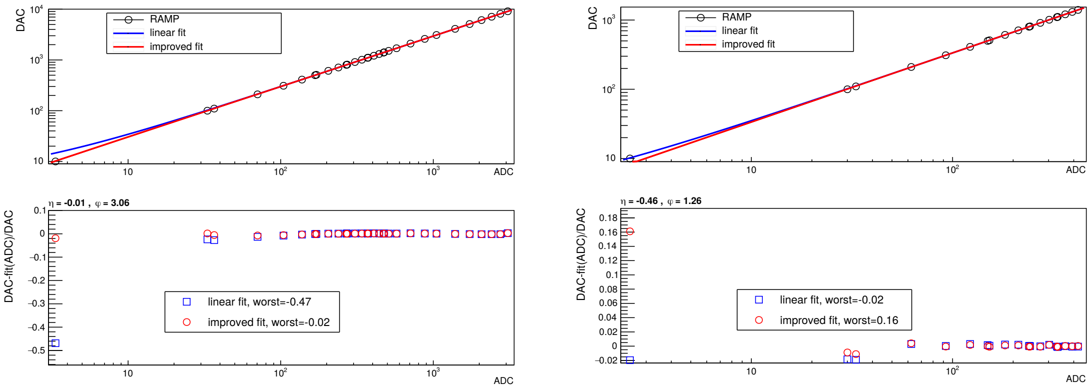

(a) Cell's coordinates $\eta = -0.01$ and $\phi = 3.06$. (b) Cell's coordinates $\eta = -0.46$ and $\phi = 1.26$.

Figure 4.1: (Top) Recorded special run ramp fitted by both Eq.4.1 and Eq.4.2 for different cells. (Bottom) Relative residuals of the two fits as a function of ADC counts.

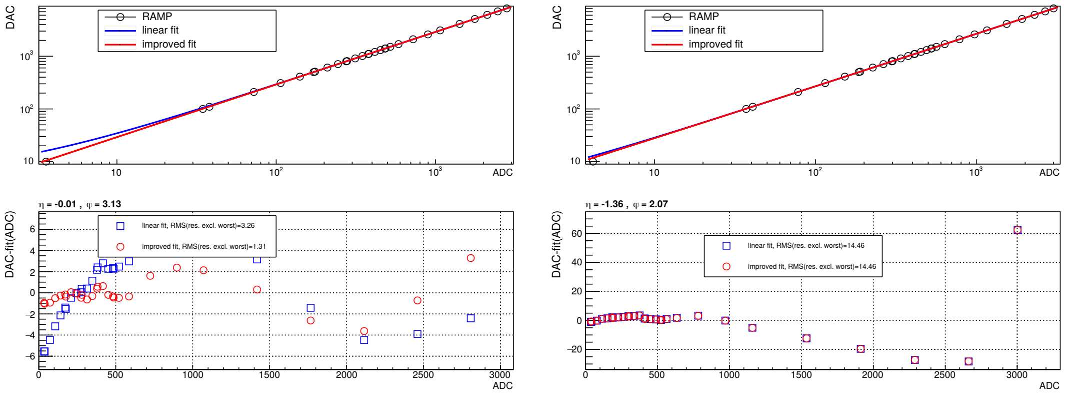

(a) Cell's coordinates $\eta = -0.01$ and $\phi = 3.13$. (b) Cell's coordinates $\eta = -1.36$ and $\phi = 2.07$.

Figure 4.2: (Top) Recorded special run ramp fitted by both Eq.4.1 and Eq.4.2 for different cells. (Bottom) Absolute residuals of the two fits, after the removal of the worst one, as a function of ADC counts.

underestimate the ramps at low ADC; the distribution of the worst residuals of the improved fits is instead quite symmetric around zero, while some structure is nevertheless observed for some cell. In order to quantify how important the differences between the results obtained by the two fits are, two variables are built and their value is reported for each cell:

- The relative difference of the worst residual,

$$\delta\alpha = \frac{\alpha_2 - \alpha_1}{\alpha_1} \tag{4.3}$$

  where α_1 and α_2 are the values of the worst residual obtained by the linear fit and the improved fit, respectively.
- The quadratic difference of the RMS,

$$\delta\beta = \sqrt{(\beta_1)^2 - (\beta_2)^2} \tag{4.4}$$

  where β_1 and β_2 are the values of the RMS of the residuals (excluding the worst one) obtained by the linear fit and the improved fit, respectively.

These two variables provide a good way to compare the two fitting procedures: the more negative (higher) $\delta\alpha$ ($\delta\beta$) is, the better the improved fit describes the ramp at low ADC (elsewhere).

Since the distribution shown in Figure 4.4a has a mean value of -0.84, it's safe to assume that the improved fit function has lower values of the worst residual. In fact, negative values of $\delta\alpha$ are uniformly scattered over the map shown in the same figure.

The distribution in Figure 4.4b has only positive values, since the variable defined in Eq.4.4 is indeed a positive-definite quantity. The position of its highest peak indicates how much better the improved fit describes the ramps with respect to the linear fit overall. The $\eta - \phi$ map of these values shows that neighbour cells show similar results. Some patterns manifest themselves within bands localized near $|\eta| = 0.5$, while some other patterns are spotted around $|\eta| = 1$. Both types of patterns appear with a kind of periodicity along the ϕ direction.

Statistical significance of the fit

A strong evidence of the improved fit describing better most of the Middle cell ramps was given in the previous section. In this section we perform a quantitative analysis to check whether the improvement brought by the additional degree of freedom in the improved fit is statistically significant. In this regard Fisher's F-test is very useful, since it allows the comparison of two *nested* models - i.e. one the representing a simplified version of the other with fewer degrees of freedom, and the the same regression obtained with the simpler model can be achieved by some choice of the parameters of more complex model - that have been fit to the same dataset, in order to establish whether the additional complexity of the improved model is justified given the statistical power of the dataset used in the regressions. The F-test can be summarized as follows:

1. Consider two *nested* models. In our case Model 1 is Eq.4.2 (linear fit) with $d_1 = 2$ degrees of freedom, Model 2 is Eq.4.1 (improved fit) with $d_2 = 3$ degrees of freedom: the linear model is nested within the improved model: $ADC\frac{p_0+p_1ADC}{p_2+ADC} \xrightarrow{p_2=0} p_0 + p_1ADC$.
2. Use the two models to fit the same dataset consisting of N data points and compute the χ^2 for both regressions;

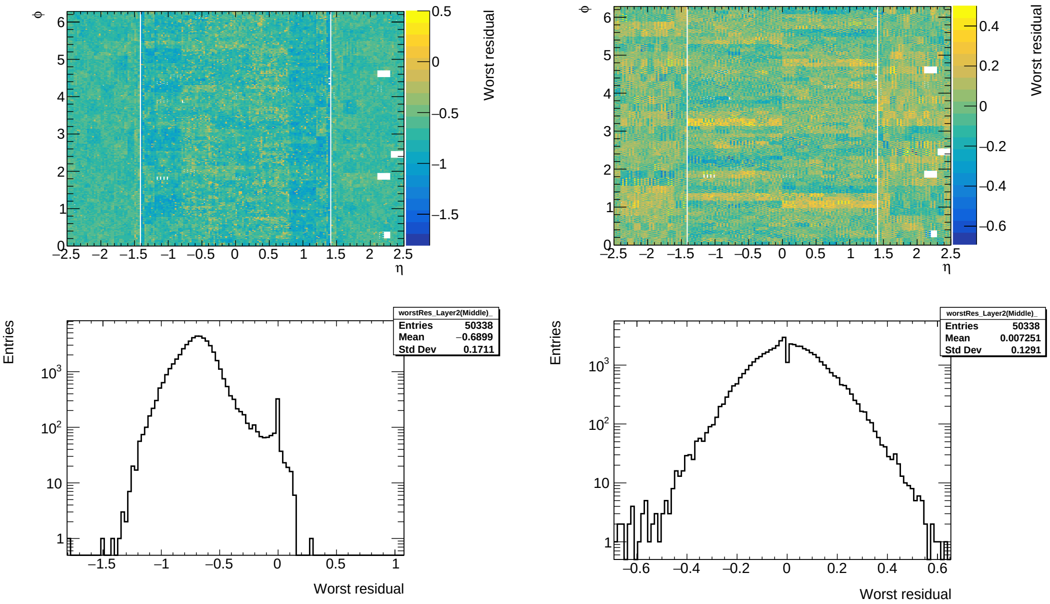

(a) Linear fit.

(b) Improved fit.

Figure 4.3: Top: map of the worst residual in the $\eta - \phi$ space of the second layer of the LAr calorimeter. Bottom: Distribution of the worst residual.

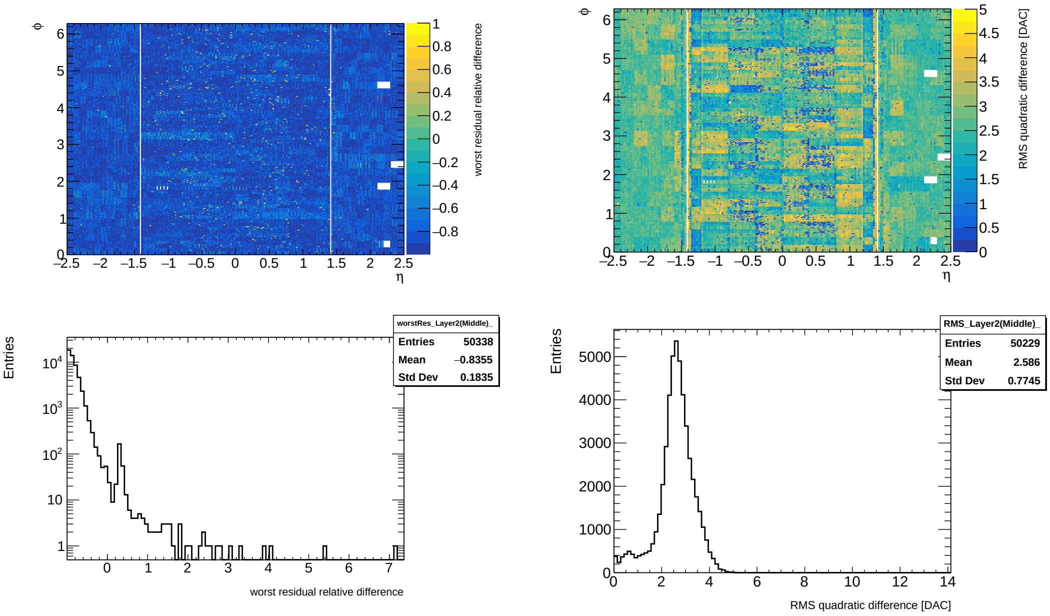

(a) $\delta\alpha$, defined in Eq. 4.3.

(b) $\delta\beta$, defined in Eq. 4.4.

Figure 4.4: Top: map of $\delta\alpha$ ($\delta\beta$) values in the $\eta - \phi$ space of the second layer of the LAr calorimeter. Bottom: Distribution of $\delta\alpha$ ($\delta\beta$).

Number of points in the ramp	Number of ramps	Critical F-value	% of passed tests
30	23126	4.21	91%
31	17703	4.20	98%
32	4024	4.18	52%
29	2866	4.23	99%
35	699	4.1	99%
33	313	4.17	95%
36	306	4.1	35%
34	284	4.1	100%
19	212	4.49	80%
15	173	4.75	77%
11	155	5.32	52%
7	107	7.71	23%
18	88	4.54	73%
14	6	4.84	50%
28	4	4.24	100%
37	4	4.1	75%

Table 4.1: Overview of the results of the F-test in all the 16 categories.

3. Compute the F-statistic:

$$F = \frac{\frac{\chi_1^2 - \chi_2^2}{d_2 - d_1}}{\frac{\chi_2^2}{N - d_2}} \tag{4.5}$$

4. Under the hypothesis that Model 2 does not provide a significantly better fit than Model 1, F will have a Fisher distribution with parameters $(d_2 - d_1, N - d_2)$.
5. This hypothesis is rejected if the F value calculated from the data is greater than the critical value of the F-distribution for some desired false-rejection probability α (in this study, $\alpha = 0.05$).

In our case, The F-test is run for every fitted ramp and the obtained F-value is compared to the critical value each time. The choice of α to be equal to 0.05 implied that a function passing the F-test by chance is only 5% (or less) likely to happen. Since both Eq. 4.5 and the value of the critical F depend on the number of data points N in the fit, and since not all the ramps are recorded with the same number of points (as shown in Figure 4.5), the test is performed separately in different categories depending on the value of N.

The results of the test are exposed in Table 4.1, and the distributions of the computed F-statistic in some example categories are shown in Figure 4.6. The improved fit has passed the F-test most of the times in most of the categories, including those with the highest number of fitted ramps. In one particular category, the one containing only the ramps reconstructed with 32 points, there is a clear distinction in the distribution of the F-statistic between one half of the ramps (those that pass the test) and the other half (those that don't). If we look at the position of the corresponding Middle cells, we see that the two groups of ramps actually belong to two different regions in the $|\eta| - \phi$ space, as shown in Figure 4.7.

In conclusion, for the majority of the L2 cells, the F-test states that Eq.4.1 actually brings a significant improvement to the fit of the ramps.

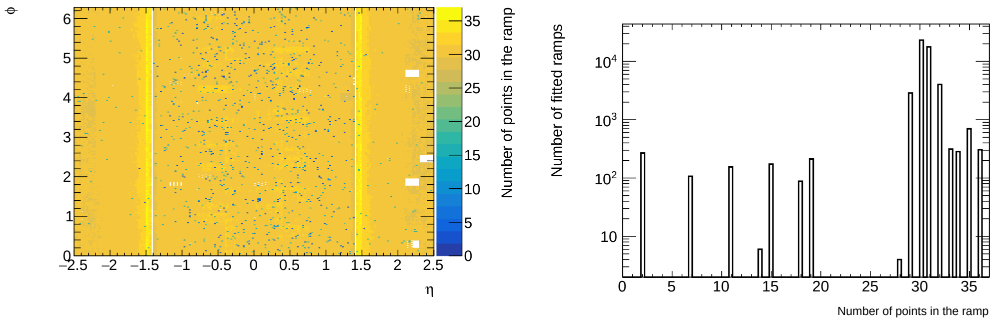

(a) Map in the $\eta - \phi$ space of the second layer of the LAr calorimeter.

(b) Inclusive distribution.

Figure 4.5: Spatial distribution and frequency of the number of points used to fit the ramp in a Middle cell.

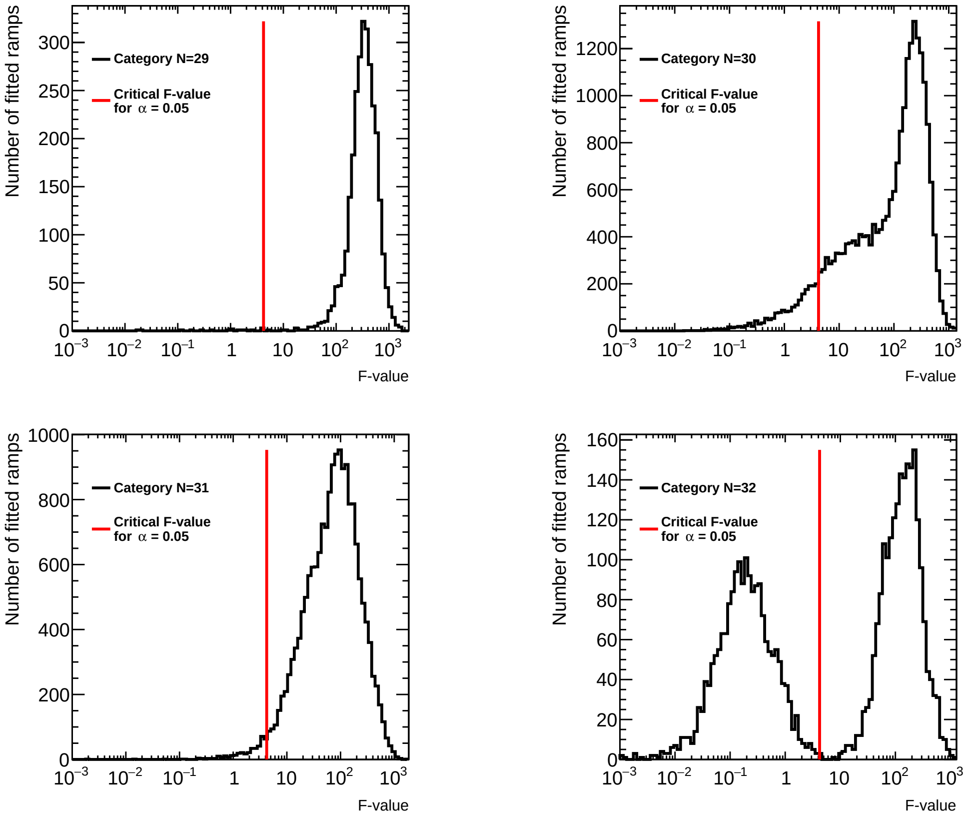

Figure 4.6: Histograms of four categories in which the F-test is run. Ramps with a F-value greater than the critical one pass the F-test within 95% confidence level.

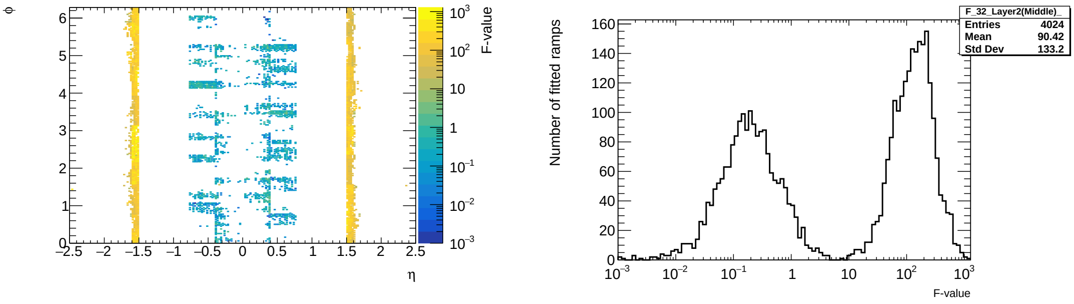

(a) Map in the $\eta - \phi$ space of the second layer of the LAr calorimeter.

(b) Inclusive distribution.

Figure 4.7: F-statistic value computed in the category corresponding to ramps reconstructed with 32 points.

4.2.3 Ramp correction function

After establishing that Eq. 4.1 actually brings a significant improvement to the fit, it can be used to compute a correction to the standard linear ramp used in the official reconstruction. The correction is defined as the relative difference between the two functions:

$$g(x) = \frac{f^{improved}(x) - f^{linear}(x)}{f^{linear}(x)} \tag{4.6}$$

where x can be either ADC or energy, according to whether one wants to look at the correction at ramp-level or at cell-level. [1] A similar correction as a function of the cell energy and as a function of $|\eta|$ was already derived in a previous iteration of this study (Ref.[94]) and it was an average over ϕ, meaning that it had no dependence on the ϕ position of the cell which it was applied to. This kind of correction doesn't take into account the non-negligible spread brought by the ϕ-degeneracy shown in Figure 4.8. Additionally, since it doesn't depend on the sign of η either, it relies on the hypothesis that the two sides of the calorimeter are exactly symmetric from the point of view of the electronic response. In this section, the possible ϕ uniformity and η symmetry of the correction are investigated in detail.

ϕ uniformity and η symmetry

In order to focus on η and ϕ only, the dependency on the energy must be factorized out [2], to do so the average integrated correction must be computed:

$$\langle \text{correction} \rangle = \frac{1}{x_2 - x_1} \int_{x_1}^{x_2} g(x)dx \tag{4.7}$$

In terms of the histogram $G(x_i)$, that has N bins in the interval $[x_1, x_2]$, each of which is Δx wide, the integral in the previous equation is approximated by the sum of the

---

[1] Energy and ADC are related by a conversion factor: $E = F_{DAC \to MeV} \times \left(\frac{M_{phys}}{M_{cali}}\right)^{-1} \times p_1 \times ADC$. (from Eq.3.1)

[2] Note that this is done just to highlight "geometrical" inhomogeneities; in the end the correction will be dependent on the energy.

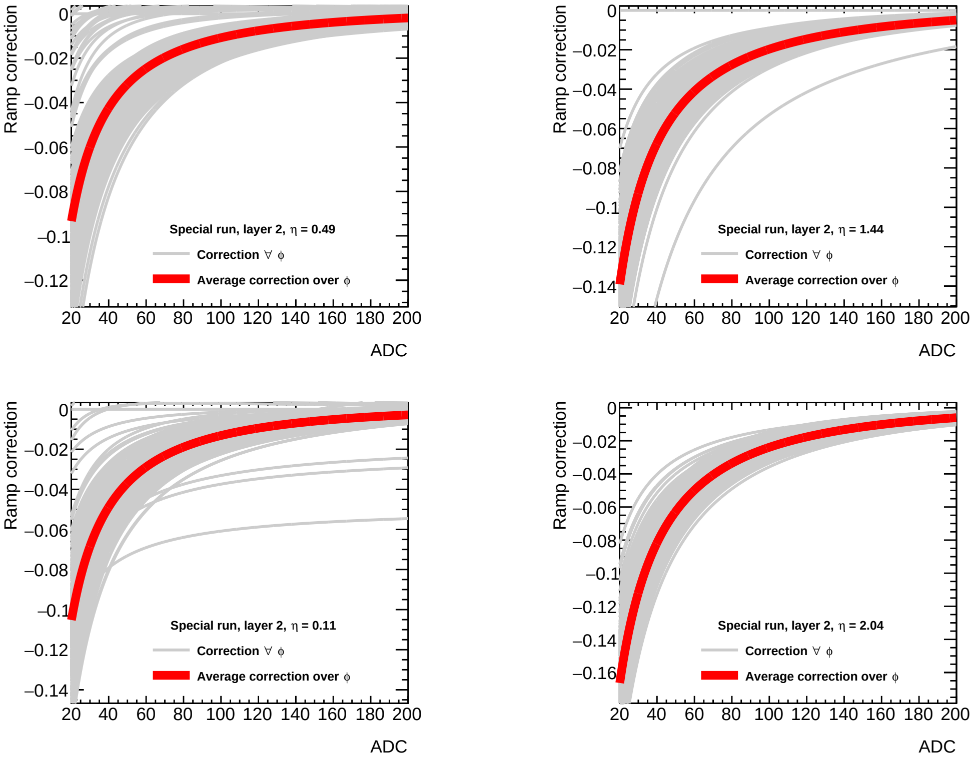

Figure 4.8: Individual correction functions for 256 cells having their center at the same η but at a different ϕ (grey curves) and average correction function for them (red curve).

bin contents:

$$\langle \text{correction} \rangle = \frac{1}{x_{i_2} - x_{i_1}} \sum_{i=i_1}^{i=i_2} G(x_i) \Delta x = \frac{1}{N} \sum_{i=i_1}^{i=i_2} G(x_i) \tag{4.8}$$

where the numerical integration is made with 1000 bins in the interval [5, 60] GeV. From Figure 4.9, which shows a map in the $\eta - \phi$ space of the values of the average correction, one can already see some fluctuations in every column as well as differences between the left side and the right side.

To understand the importance of these fluctuations, the projections of the average correction along the ϕ axis for the barrel and the endcap (side with $\eta > 0$ only) are shown in Figure 4.10 and 4.11. These datapoints are fitted with a zero-degree function to check whether the values are compatible with a constant value within the uncertainty. This is the case only for some of the regions in the barrel (those contained in the interval $0.17 < \eta < 1.20$) while it is not for most of the regions in the endcap.

Another test is performed to more finely probe the possible uniformity of the correction along ϕ. The distribution of the average correction for the cells with the same position in η is investigated. Since there are 256×200 ($\phi - \eta$) cells in L2, 200 histograms each with 256 entries are built. If the origin of the fluctuations encountered before is of statistical nature, then a normal distribution is expected so each histogram is fitted with a Gaussian. Some examples of these fitted distributions are shown in Figure 4.12 while an overview of the results of the fits is given in Figure 4.13. The values of the reduced χ^2 obtained from the fits are roughly distributed around 1 with a tail towards higher values. These bad values are localized in the transition region between barrel and endcap as well as in the central part of the barrel.

The possible symmetry of the average correction with respect to the sign of η is tested as well. This is done by comparing pair by pair the 200 histograms previously built, checking whether the mean of the histogram corresponding to a given η position (i.e. $\eta = 2.41$) is significantly different from the one of the histogram corresponding to the η position with opposite sign (i.e. $\eta = -2.41$). The Student's t-test can answer this kind of question, because it lets one compare the populations from which two separate sets of independent and identically distributed samples are obtained:

1. Consider two sets of data: set p (for positive η) and set n (for negative η);
2. Compute the t-statistic:
$$t = \frac{\bar{X}_p - \bar{X}_n}{\sqrt{\frac{s_p^2}{N_p} + \frac{s_n^2}{N_n}}} \tag{4.9}$$
where $\bar{X}_{i=p,n}$ is the sample mean, $s^2_{i=p,n}$ is the unbiased estimator of the variance of each of the two samples with $N_{i=p,n}$ number of data points (which is equal to 256 for both);
3. Under the hypothesis that the two populations have equal means, t will have a Student's t-distribution with $N_p + N_n - 2$ degrees of freedom;
4. This hypothesis is rejected if the t value calculated from data is greater than the critical value of the Student's t-distribution for some desired false-rejection probability α (in this study, $\alpha = 0.05$).

The t-test is run for every pair and the obtained t-value is compared to the critical value each time. The choice of α to be equal to 0.05 means that a pair passing the t-test by chance is only 5% (or less) likely to happen. Some examples of these pairs of distributions are shown in Figure 4.14 while an overview of the results of the tests is given in Figure 4.15. The majority of the pairs has not passed the t-test, meaning that the difference between the sample means is compatible within statistical fluctuations. On the other hand, the pairs that have passed the test (those having a t-value greater than the critical one) are pretty much localized in the region with $|\eta| > 1.8$. This is enough to conclude that the average correction is found to be η symmetric in the barrel while it is not between the two endcap sides.

4.2.4 Application of the derived correction to LAr cells

In the previous section, some arguments were given to motivate the use of a *cell-by-cell correction* in place of a *ϕ-η-averaged correction.*

The cell-by-cell correction implies the use of 200×256 functions of the form $g_{\eta,\phi}(E)$, each of which implements the correction introduced in Eq.4.6 for a given L2 cell having its center in (η, ϕ). This choice should in principle avoid the propagation of bad fit results due to problematic cells to the whole ramp-correction.

The difference between these two ramp-correction methods is considered as a potential source of systematic uncertainty on the measurement of the gain miscalibration factors, as described in Section 4.4.5.

Before performing the analysis described in Section 4.4, the ramp-correction is applied at cell-level to the events of the special run and the standard run datasets following this procedure. For each electron in an event:

- Get its cluster;

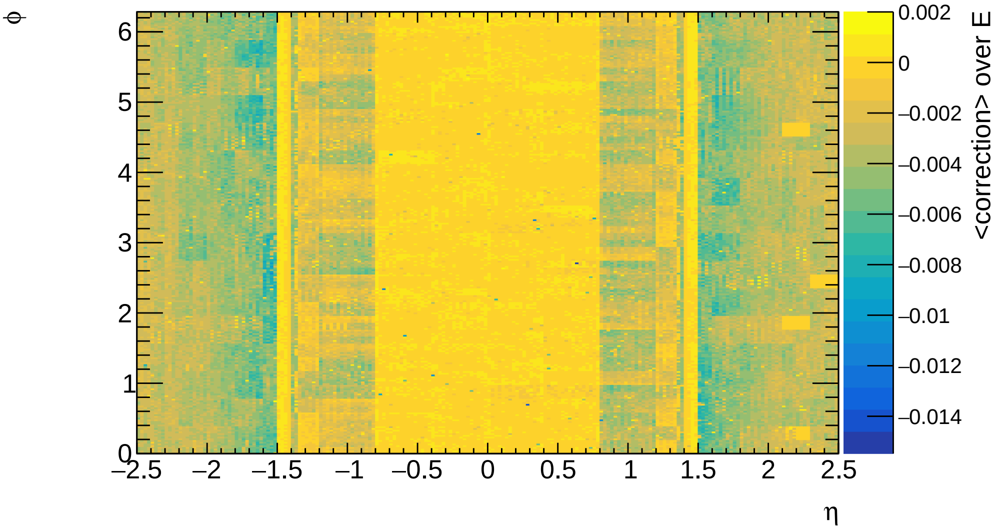

Figure 4.9: Map of the values given by Eq. 4.8.

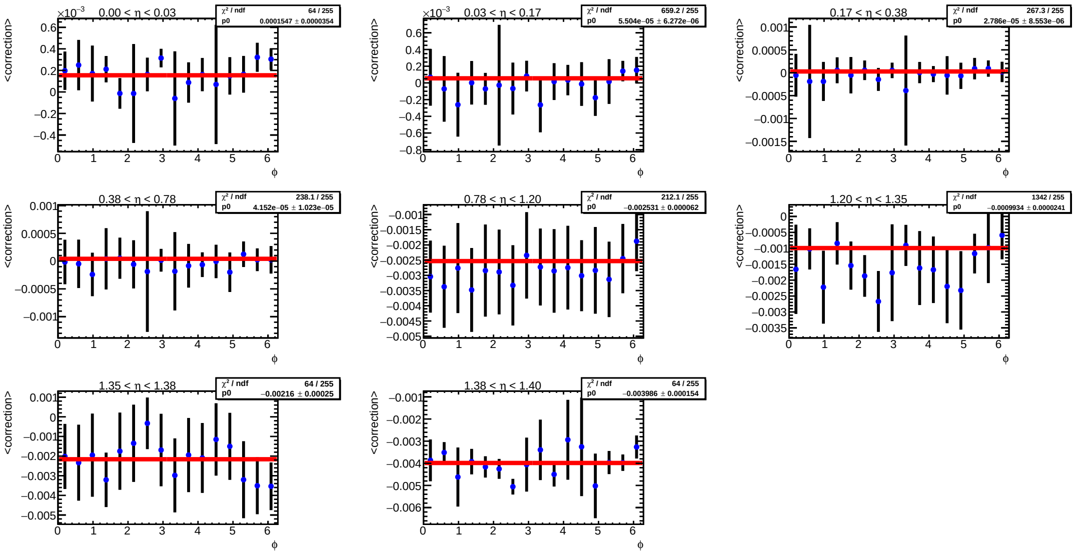

Figure 4.10: Values of the average correction projected along the ϕ axis in 8 η regions defined in the barrel. Error bars are the RMS of the average correction along the η axis in that region. The red line is the result of a fit to a constant.

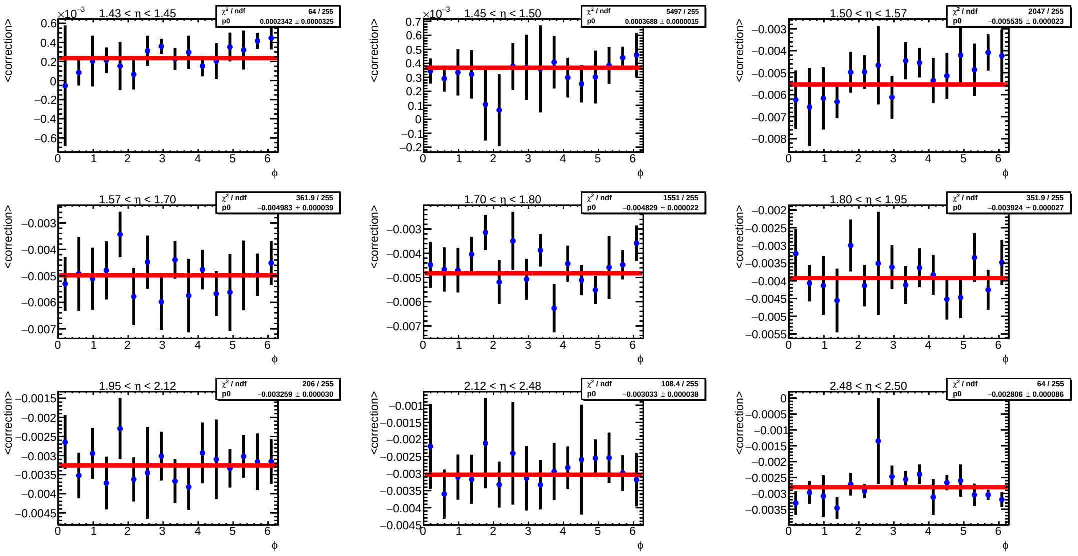

Figure 4.11: Values of the average correction projected along the ϕ axis in 9 η regions defined in the endcap. Error bars are the RMS of the average correction along the η axis in that region. The red line is the result of a fit to a constant.

- If the cluster contain at least a LAr Middle cell reconstructed using the medium gain, apply the ramp correction to its energy;
- Re-compute the energy E_2 associated to Middle cells in the cluster;
- Re-compute the $\frac{E_1}{E_2}$ correction;
- Re-apply the MVA calibration to the corrected cluster energies.

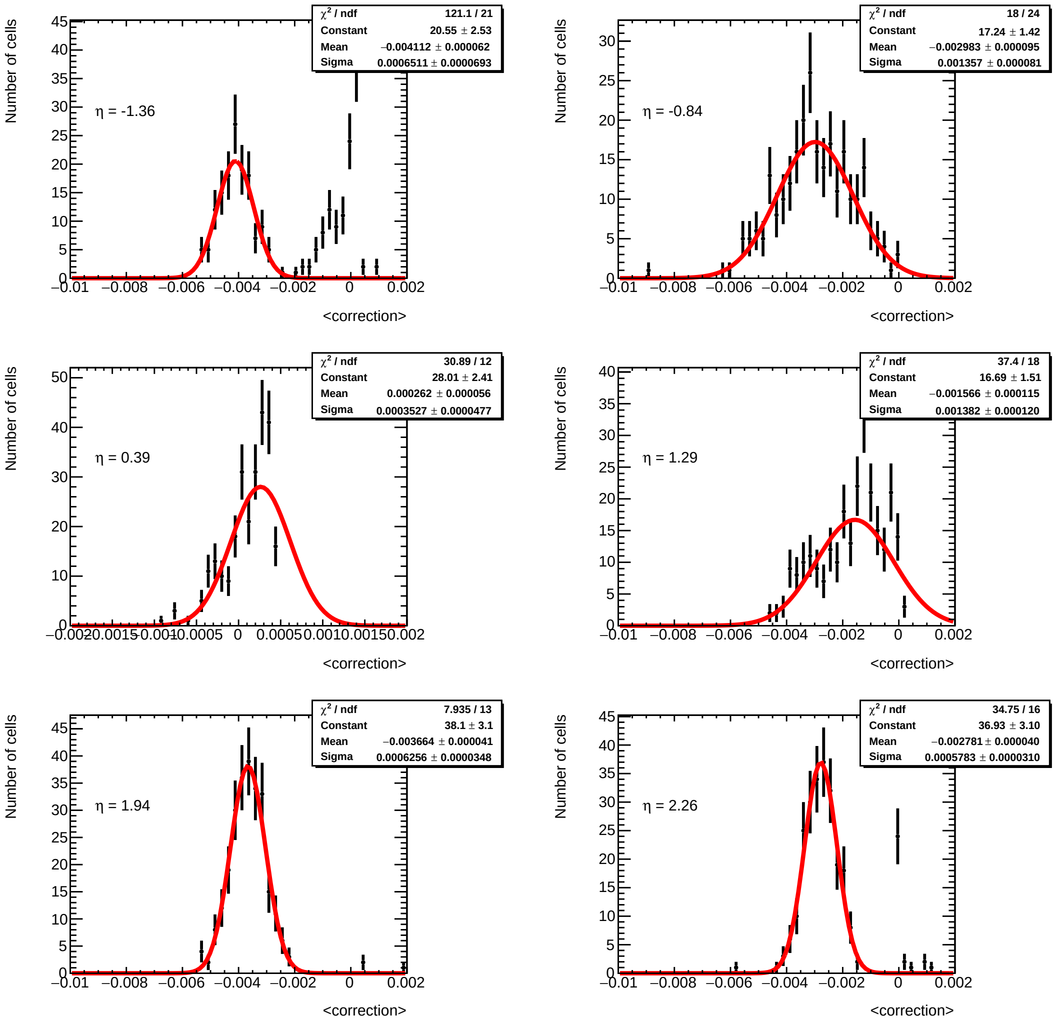

Figure 4.12: Six distributions of the average correction for those cells having the same position in η. The red line is the result of a gaussian fit.

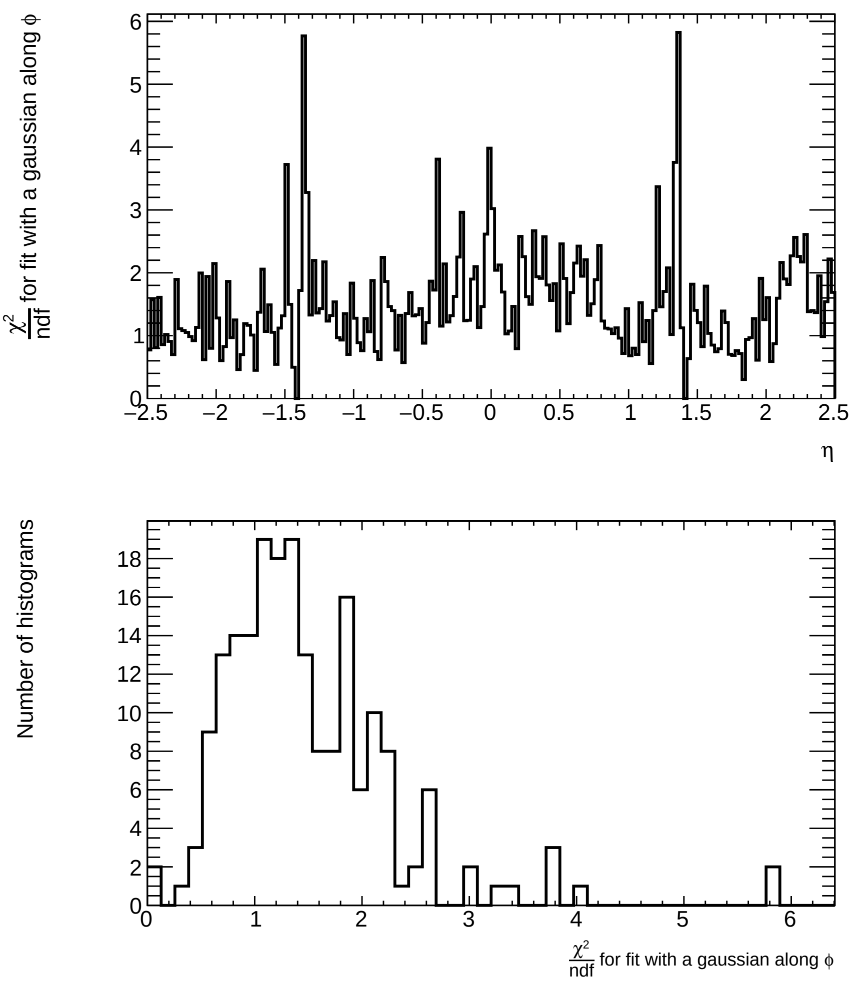

Figure 4.13: Distribution of the reduced χ^2 obtained from all the 200 gaussian fits (bottom plot). Values of the reduced χ^2 in function of η (top plot).

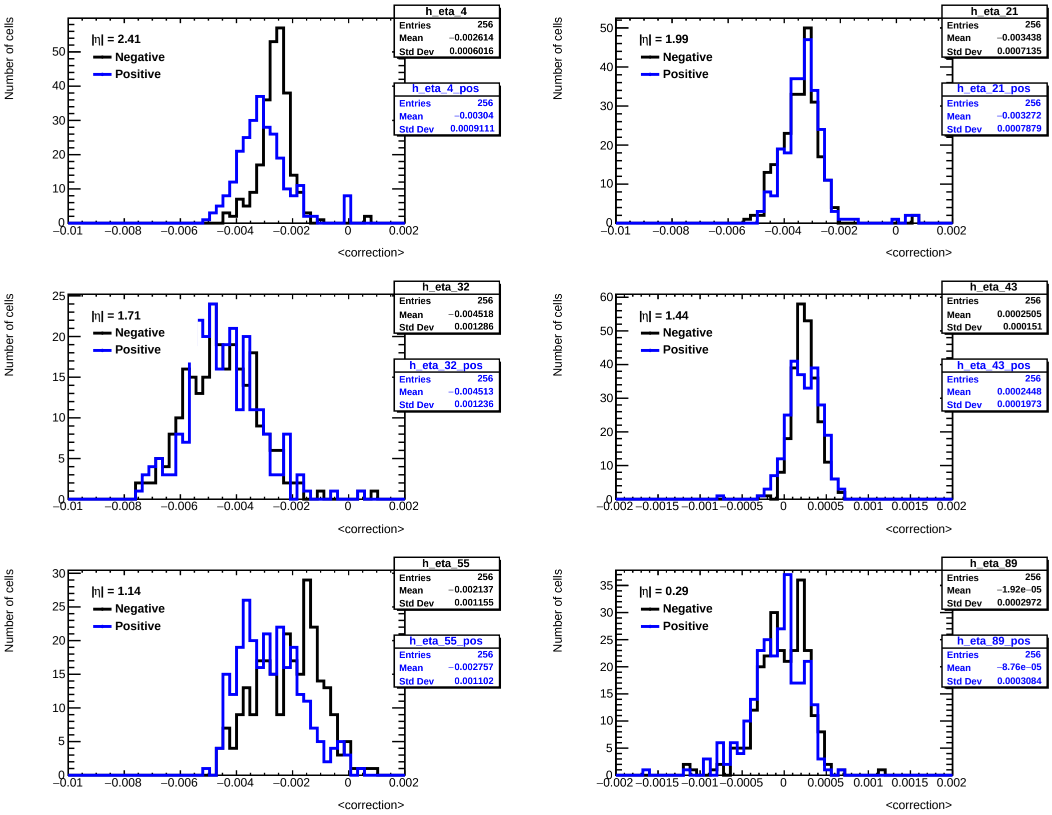

Figure 4.14: Six pairs of distributions of the average correction for cells with the same position in $|\eta|$. The black line corresponds to negative η while the blue line to positive η.

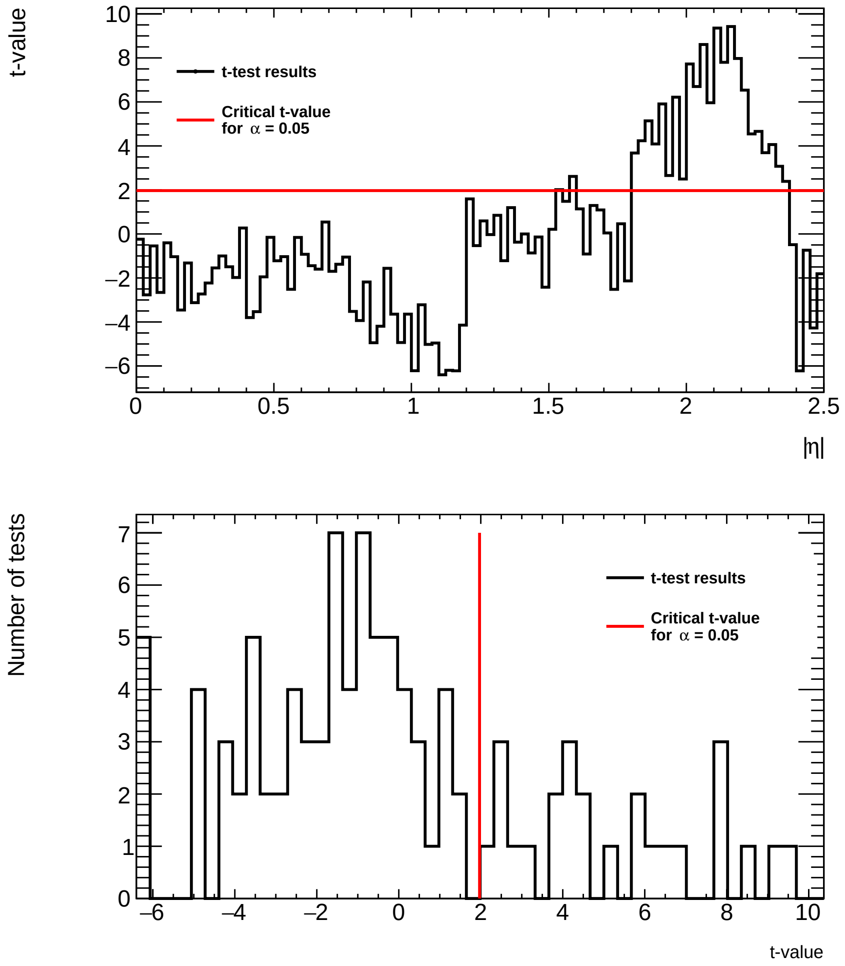

Figure 4.15: Distribution of the computed t-statistic from all the 100 tests (bottom plot). Values of the t-statistic as a function of $|\eta|$ (top plot). Pairs with a t-value greater than the critical one pass the t-test within 95% confidence level.

4.3 Study of the calibration board offset

4.3.1 Ramp fit intercept parameter as a proxy for the calibration board offset

Each calibration board line has distinctive non-zero offsets, corresponding to an injected charge delivered to the calibration lines when the line output DAC value is set to 0. These offsets were measured in the board production phase, for a subset of the calibration boards installed on the ATLAS LAr calorimeters [98]. Unfortunately, the values are not available for all boards (e.g. some values are missing for the boards serving the EMB calorimeter, and no offset value is available for those serving the EMEC calorimeters). On the other hand, it was previously observed that these offsets correlate with the intercept parameters of the ramp fits [99]. In this respect the ramp intercept parameter could be a good proxy for measuring the impact of the board offset, especially for those boards for which a direct measurement is not available, and correct for its effect on medium gain signals, since the standard LAr reconstruction assumes the ramp intercept in medium gain effectively accounts for non-linear behavior of the electronics, and is thus corrected for. While this assumption is at least partially correct, the contribution to the ramp intercept associated to the board offset should not be corrected for or, conversely, should be subtracted to the existing medium gain reconstruction that uses the full intercept value as a correction to the energy.

Fig. 4.16 shows the correlation between the available measurements of the LAr calibration board offsets and the corresponding ramp intercept parameter, $X[0]$, as obtained from the high gain fits. Similar results are obtained when using medium gain ramp data, but with a worse precision because of a larger spread of the intercept parameter $X[0]$. The results are compatible with what was observed in Ref. [99]. The correlation regressions in the two regions $\eta < 0.8$ and $\eta > 0.8$ provide compatible results, and indicate that a common global parametrization can be used to estimate the offset from $X[0]$.

Assuming a common single parametrization for all gains and detector regions, we observe a non-zero value of the global $X[0]$ parameter for a null offset, corresponding to 1.285 ± 0.009 DAC (Figure 4.16a). This value can be associated a genuine non-linearity of the readout electronics, that the linear ramp fit tries to accommodate with its fit. If the ramp fit intercept parameter is to be used as proxy to correct for the board offset, this value will have to be subtracted from the correction to allow the reconstruction to accommodate for genuine non-linearity.

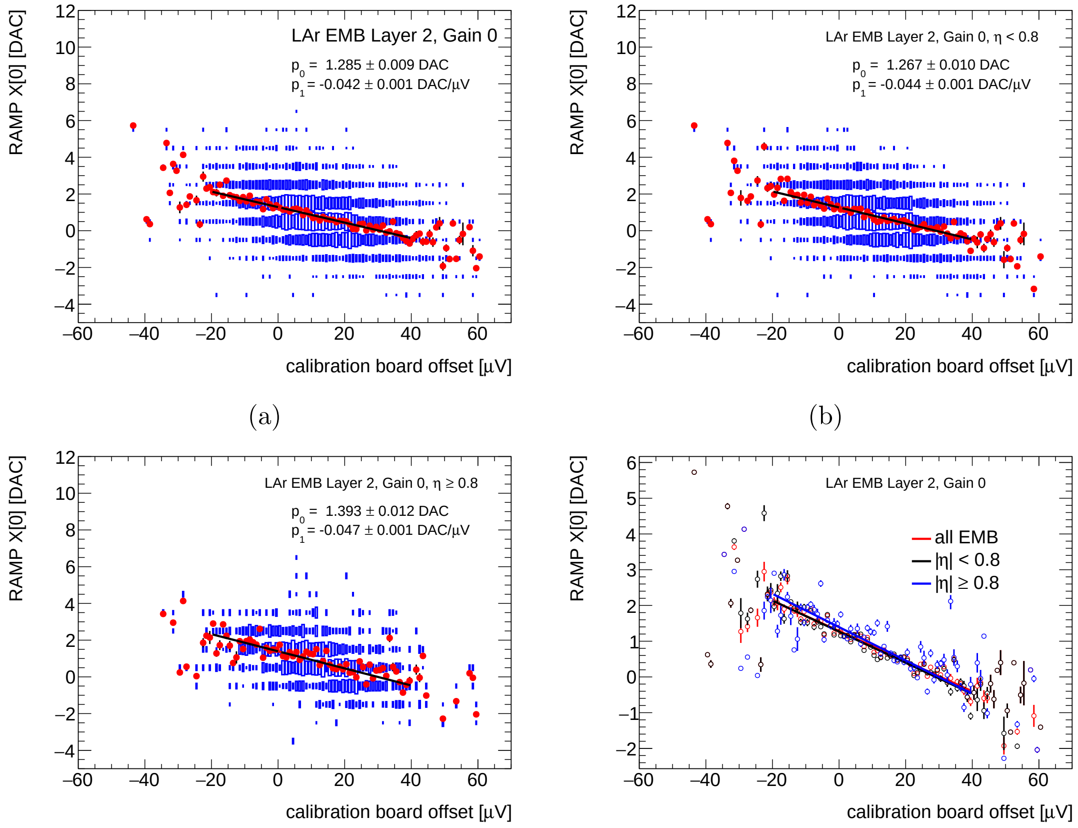

(a) (b) (c) (d)

Figure 4.16: Correlation between the available measurements of the LAr calibration board offsets and the corresponding ramp intercept parameter $X[0]$. (a) All available data, most of LAr EMB; (b) LAr EMB $\eta < 0.8$; (c) LAr EMB $\eta \geq 0.8$; (d) comparison between correlation regression in the various regions.

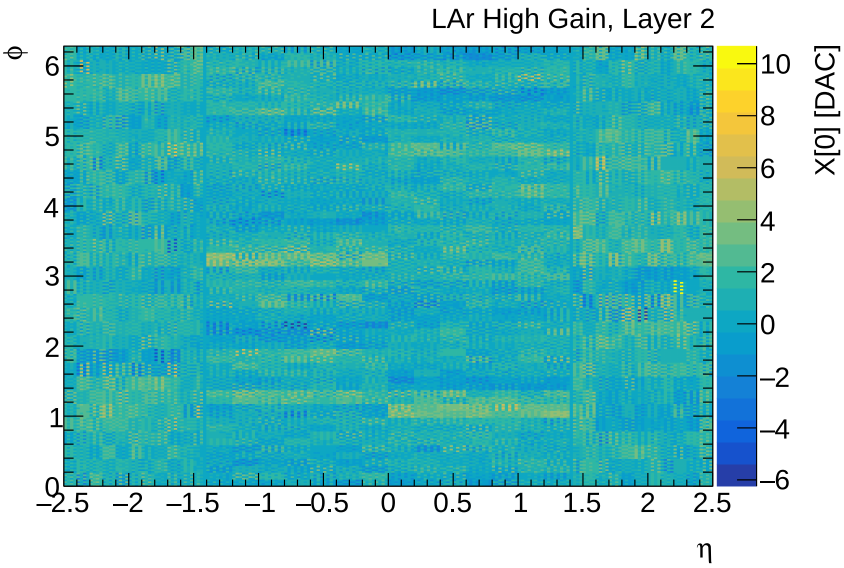

Figure 4.17: Map of the value of the ramp intercept parameter $X[0]$ in high gain for the layer 2 cells.

4.3.2 Energy corrections from ramp fit intercept parameter

Fig. 4.17 shows the map of the value of the ramp intercept parameter $X[0]$ in high gain for the layer 2 cells. Localized patterns can be observed, associated to a single calibration line pulsing eight layer 2 cells at the same time. This property can be exploited to reduce the statistical fluctuations affecting the $X[0]$ parameter on a single ramp fit, by averaging the eight $X[0]$ values associated to the same calibration line. The result of this procedure is shown in Fig. 4.18, where now each cell show the $\langle X[0]\rangle$ value obtained by averaging the cells served by the same calibration line. Fig. 4.19 show the RMS of the $X[0]$ distributions, while Fig. 4.20 the corresponding pulls. The distributions are usually well-behaved, with relatively small RMS values apart for the crack regions ($1.37 \leq |\eta| < 1.52$) and high-η regions ($|\eta| \geq 2.37$) where larger spreads are observed, and randomly distributed pulls everywhere by the crack and high-η regions.

Fig. 4.21 show the distributions of the pull values of the ramp intercept parameter $X[0]$ distributions in high gain for the layer 2 cells in various region of the calorimeters. While the distributions are quasi-Gaussian in the precision regions of the detector, peaks at ± 1 are observed in the pull distributions in the crack and high-η regions. Extending the crack definition to $\eta = 1.6$ removes the still-visible spikes at ± 1 in EMEC pull distribution. The distributions in the precision regions seem sufficiently well-behaved to use the $\langle X[0]\rangle$ values as a correction in these regions, while we expect the impact of the corrections on the crack and high-η region to be negligible with respect to the large uncertainties expected in these regions.

Fig. 4.22, 4.23, 4.24 and 4.25 respectively show the energy equivalent ΔE correction as computed from the ramp intercept parameter $X[0]$ in high gain for the layer 2 cells, and the corresponding averages, RMS and pulls obtained when considering cells served by the same calibration line. Fig. 4.26 shows the distributions in various regions of the LAr EM calorimeters of the ΔE energy correction values averaged over layer 2 cells served by the same calibration line. The energy equivalents of the ramp intercept are relatively small, reaching on average values ranging from 10 to 80 MeV depending

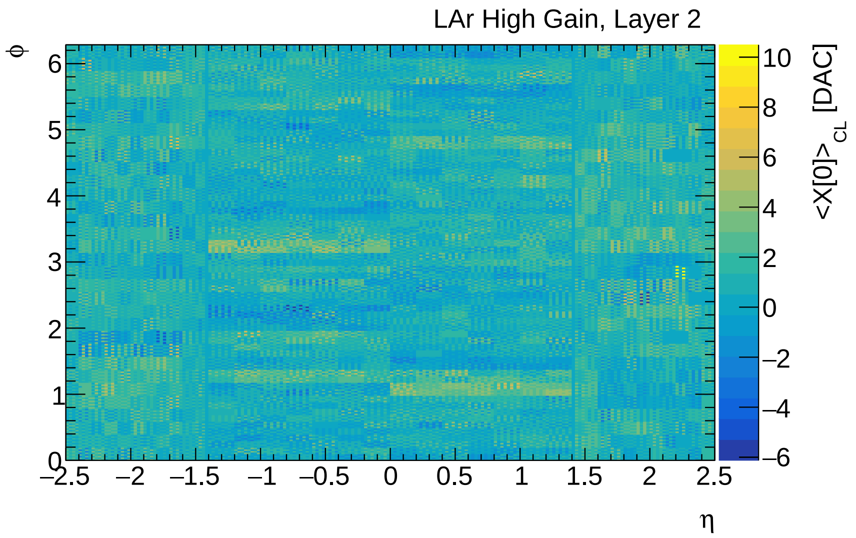

Figure 4.18: Map of the average values of the ramp intercept parameter $X[0]$ distributions in high gain for the layer 2 cells, as obtained from cells served by the same calibration line.

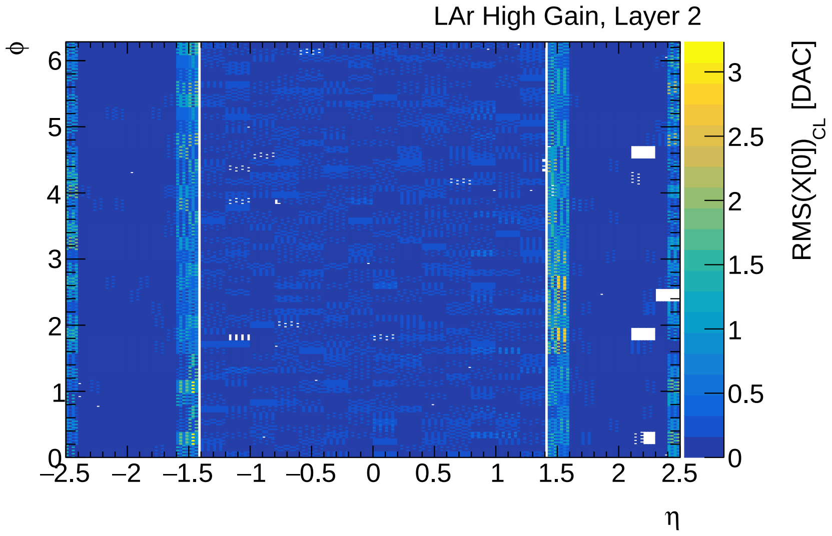

Figure 4.19: Map of the RMS values of the ramp intercept parameter $X[0]$ distributions in high gain for the layer 2 cells, as obtained from cells served by the same calibration line.

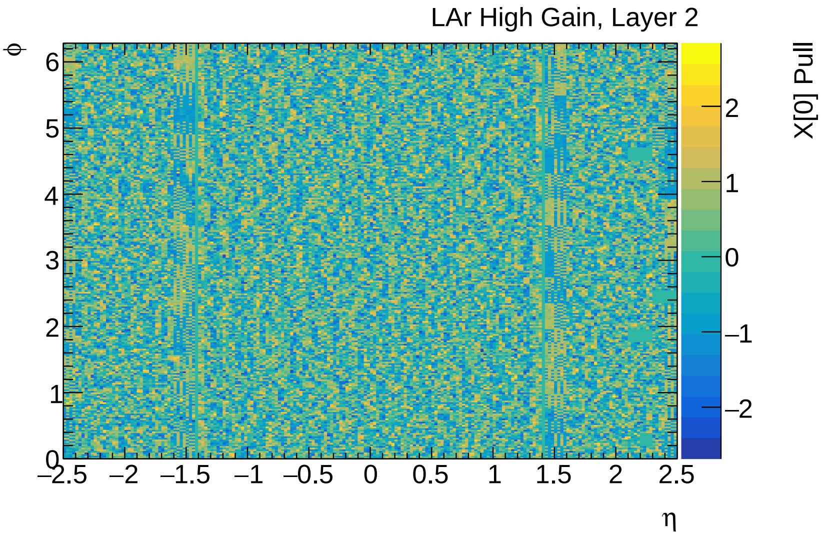

Figure 4.20: Map of the pull values of the ramp intercept parameter $X[0]$ distributions in high gain for the layer 2 cells, as obtained from cells served by the same calibration line.

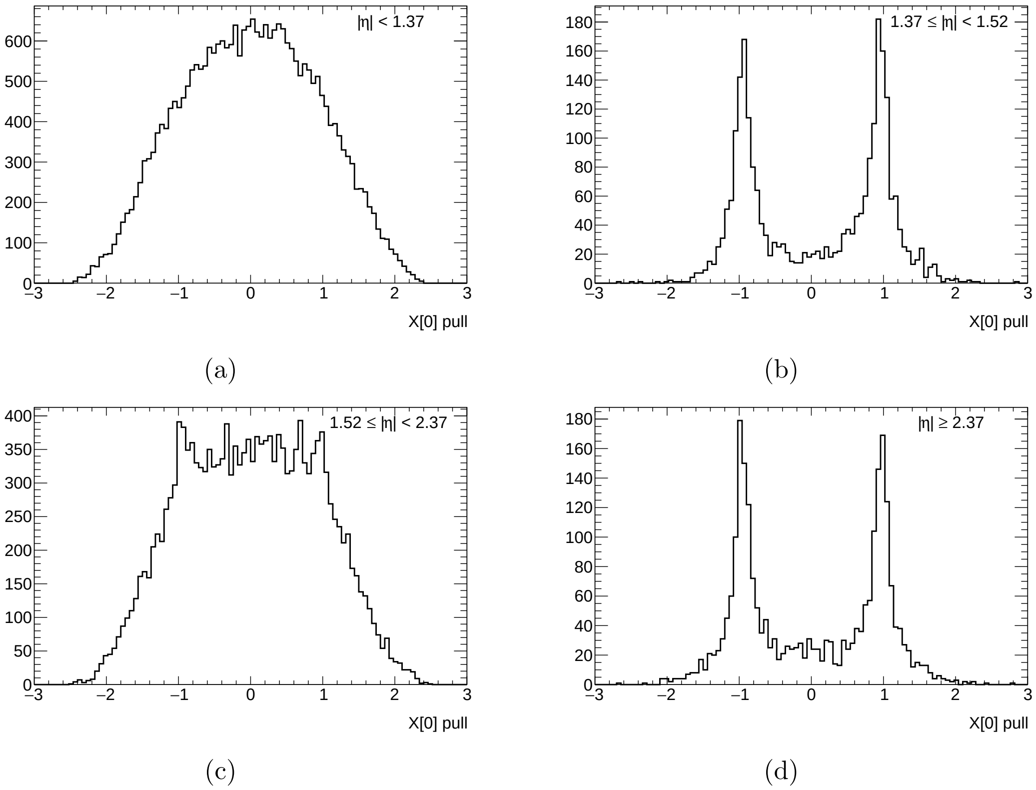

(a) (b)

(c) (d)

Figure 4.21: Distributions in various regions of the calorimeter of the pull values of the ramp intercept parameter $X[0]$.

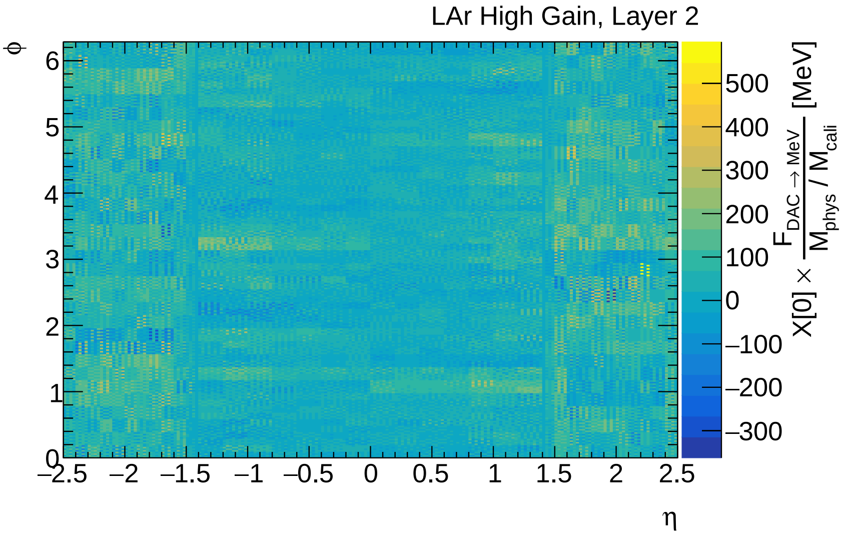

Figure 4.22: Map of ΔE energy correction as computed from the ramp intercept parameter $X[0]$ in high gain for the layer 2 cells.

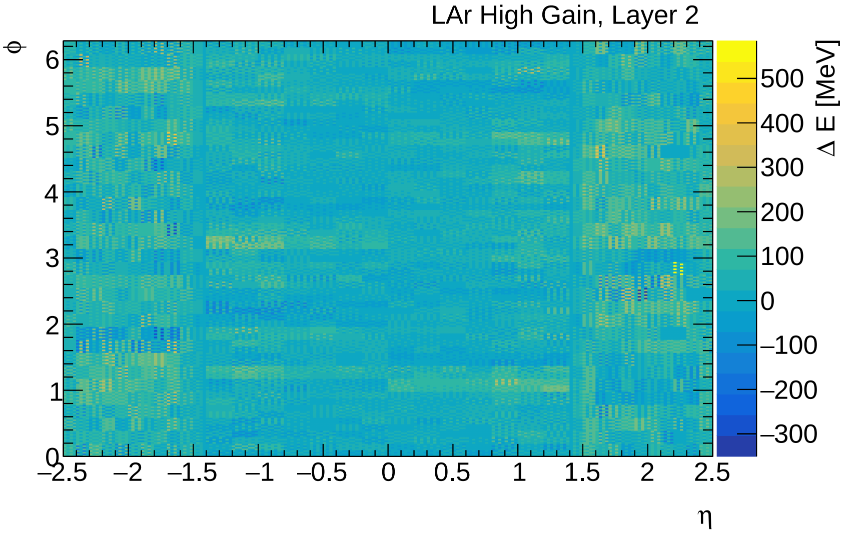

Figure 4.23: Map of average ΔE energy correction as computed from the ramp intercept parameter $X[0]$ in high gain for the layer 2 cells, considering cells served by the same calibration line.

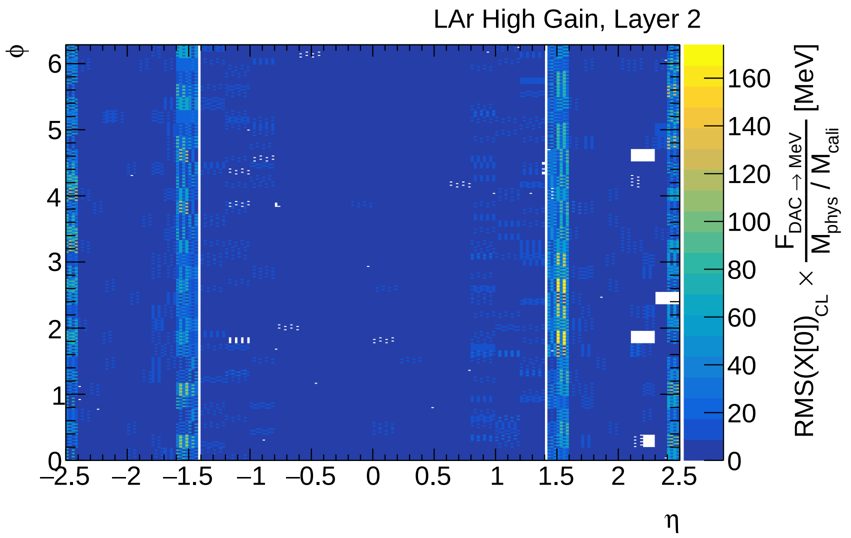

Figure 4.24: Map of the ΔE energy correction RMS as computed from the ramp intercept parameter $X[0]$ in high gain for the layer 2 cells, considering cells served by the same calibration line.

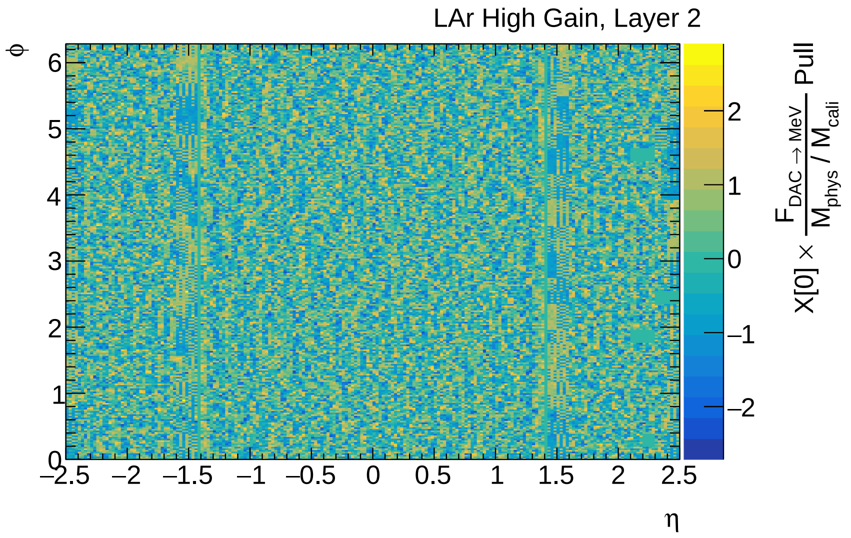

Figure 4.25: Map of the ΔE energy correction pull values as computed from the ramp intercept parameter $X[0]$ in high gain for the layer 2 cells, considering cells served by the same calibration line.

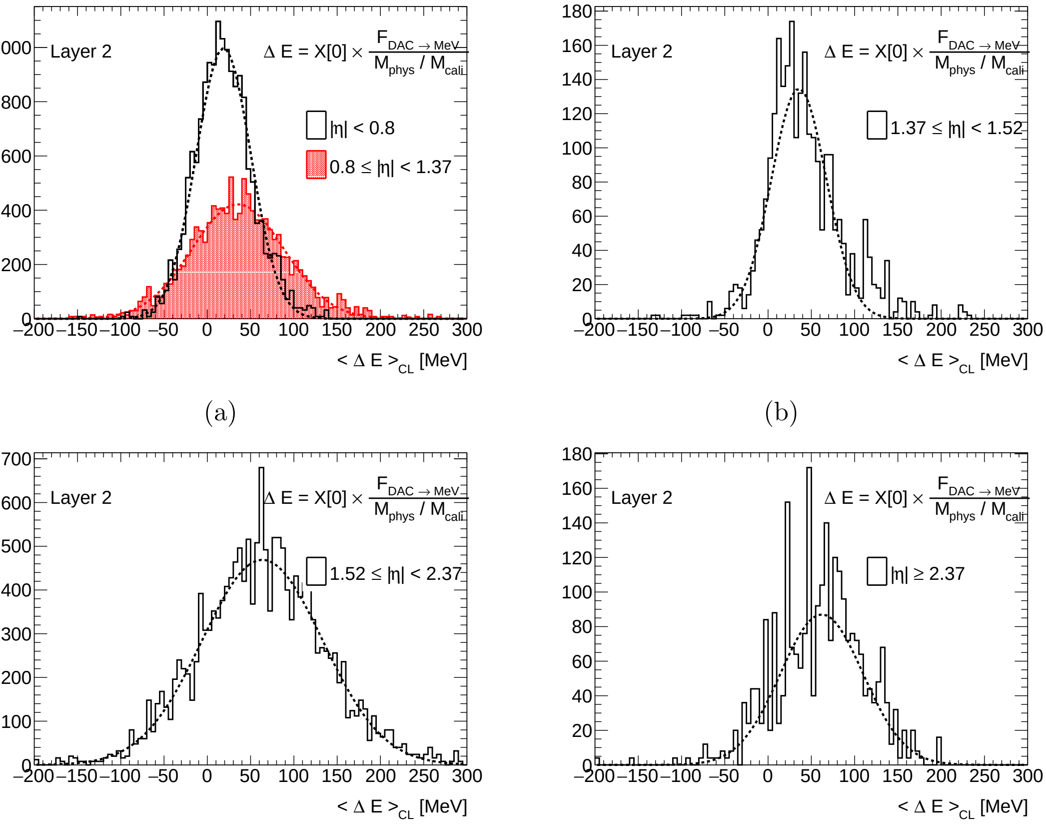

(a) (b)

(c) (d)

Figure 4.26: Distributions in various regions of the LAr EM calorimeters of the ΔE energy correction values averaged over layer 2 cells served by the same calibration line.

on the detector region. Even considering the largest values in the distributions, the correction is never larger than 200-300 MeV: we therefore expect a small impact on the energy of the $Z \to ee$ electrons considered by the analysis discussed in Section 4.4.

It should also be noted that the corrections discussed above represent an upper limit to the bias induced by the calibration board offsets. In fact, ss discussed in Section 4.3.1, the full magnitude of the ramp intercept $X[0]$ parameter can not be attributed to the calibration board offset, and part of it corresponds to a genuine non-linearity of the readout electronics. The average amount of this bias is estimated in Section 4.3.1, and should be *subtracted*[3] from the $X[0]$ values before computing the ΔE equivalent. The result of such a bias correction is shown in Fig. 4.27 for the averaged $X[0]$ values, and in Fig. 4.28 for the corresponding ΔE corrections.

The impact of the corrections discussed above, addressing the calibration board offsets on the intercalibration of the high and medium gains, is discussed in Section 4.4.

---

[3] If the calibration board offset is positive (i.e. a positive injected current when the calibration line DAC is set to 0), then the standard medium gain calibration underestimates the energy. For a positive calibration offset value, the intercept of the DAC vs ADC fit is negative, so the correction for the offset should consist in subtracting the corresponding bias evaluated from the $X[0]$ intercept. This is consistent with the ramp intercept being anti-correlated with the calibration board offsets.

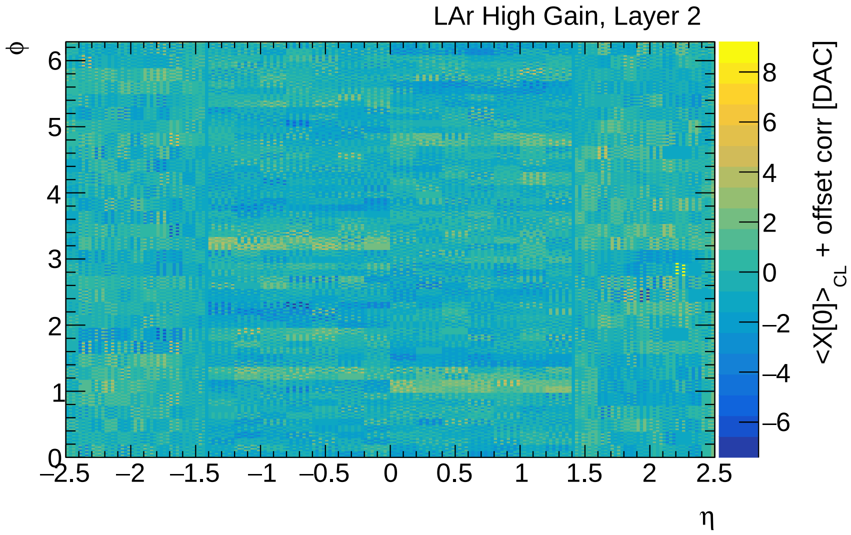

Figure 4.27: Map of the average $X[0]$ values in high gain for the layer 2 cells, after correcting them for the genuine non-linearity effect obtained by the analysis of the correlation with the calibration board offset values.

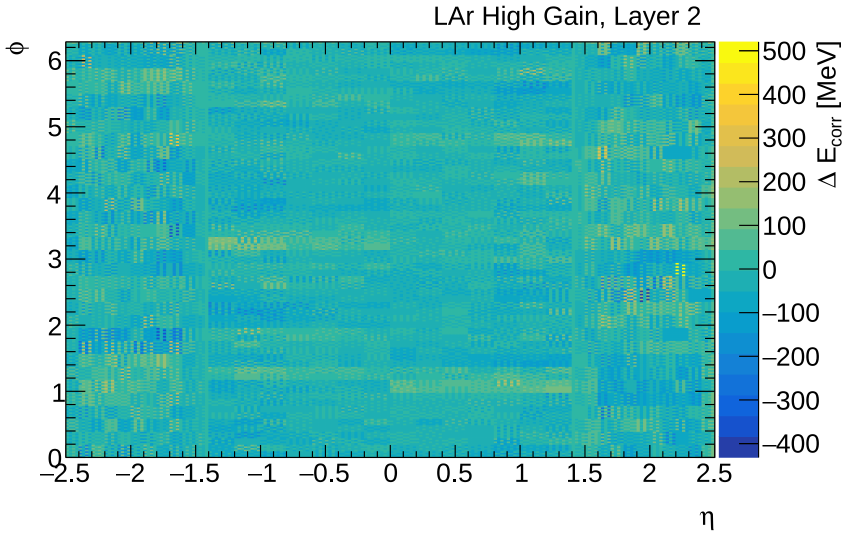

Figure 4.28: Map of the average ΔE correction values obtained from high gain ramps for the layer 2 cells, after correcting them for the genuine non-linearity effect obtained by the analysis of the correlation with the calibration board offset values.

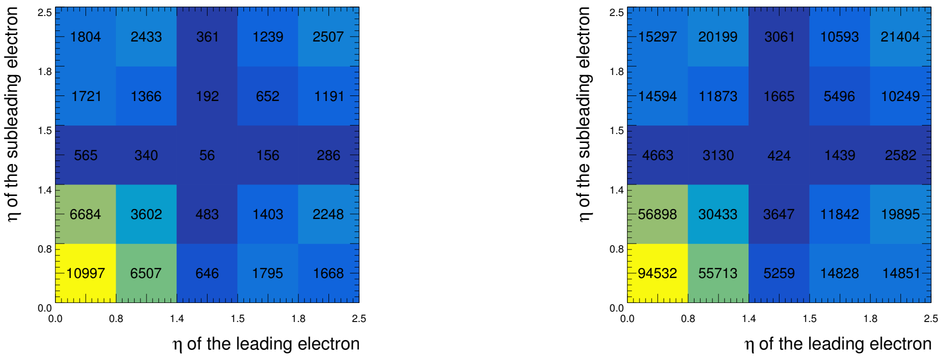

(a) Special run: 124 pb^{-1}.　　(b) Standard runs: 1081 pb^{-1}.

Figure 4.29: Number of events passing the $Z \to e^+e^-$selection.

4.4 Analysis of special $Z \to e^+e^-$ runs

4.4.1 Overview

The special run with lower MG/HG threshold (same threshold as for the 2017 special run) that is analyzed in this study was taken in June 2018 during a toroid off period and it amounts to 124 pb^{-1} of p-p collision data. It is compared to 450 pb^{-1}, 109 pb^{-1} and 522 pb^{-1} of standard physics runs with the normal threshold that were also taken in the same period.
The energy mis-calibration is defined as the difference in response between special run data and standard run data, and at first order is parametrized as follows:

$$E^{\text{spec}} = (1 + \alpha_i)E^{\text{stand}} \tag{4.10}$$

The energy scale factors α_i, where i corresponds to 5 different regions in $|\eta|$ (0-0.8, 0.8-1.37, 1.37-1.50, 1.5-1.8 and 1.8-2.47) are derived by comparing the e^+e^- invariant mass distributions. The idea behind this analysis is that one can gain information about the scale factors by estimating the displacement between the two peaks of $m_{e^+e^-}$. The event selection is done by requiring the presence of at least two electrons with opposite charge. The two with highest p_T are always chosen (leading and subleading, in the following) and must have a p_T greater than 27 GeV, $|\eta| < 2.47$ and must pass the medium likelihood ID test. An overview of the available statistics in the two run types in function of the electrons' pseudorapidity is provided in Figure 4.29.

In order to check the effect of the ramp correction, and especially to quantify the energy difference between the two proposed methods, the distribution of the transverse momentum of the individual electron candidates is shown in Figure 4.30 and 4.31.

A total of 15 $|\eta|$ regions have been defined according to the pseudorapidity value of the two electrons, then the invariant mass of the di-electron system has been built in each region, as shown in Figure 4.32. In the following, η_i (η_j) is the pseudorapidity value of the leading (subleading) electron.

4.4.2 Extraction of the scale factors

To extract the values of the energy scale factors α_i the lineshape method has been used. It consists of two steps: first, the $Z \to e^+e^-$ mass distribution in each of the 15

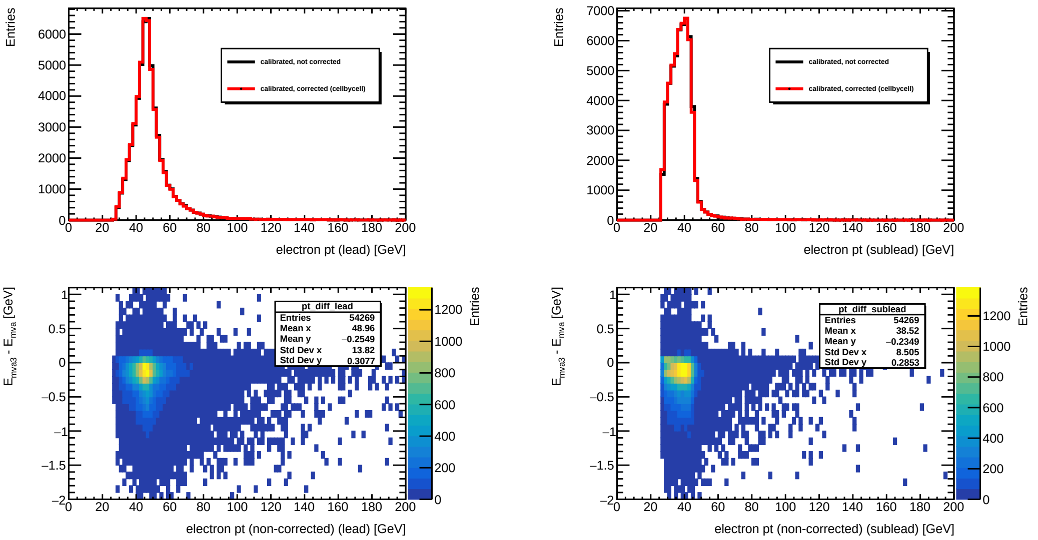

Figure 4.30: Transverse momenta of the two electron candidates when the ramp correction "cellbycell" is applied (Red curve) and when it is not (Black curve). The bottom panels show the energy difference per event between the corrected energy (E_{mva3}) and the uncorrected energy (E_{mva}) of the particle. (Special run data).

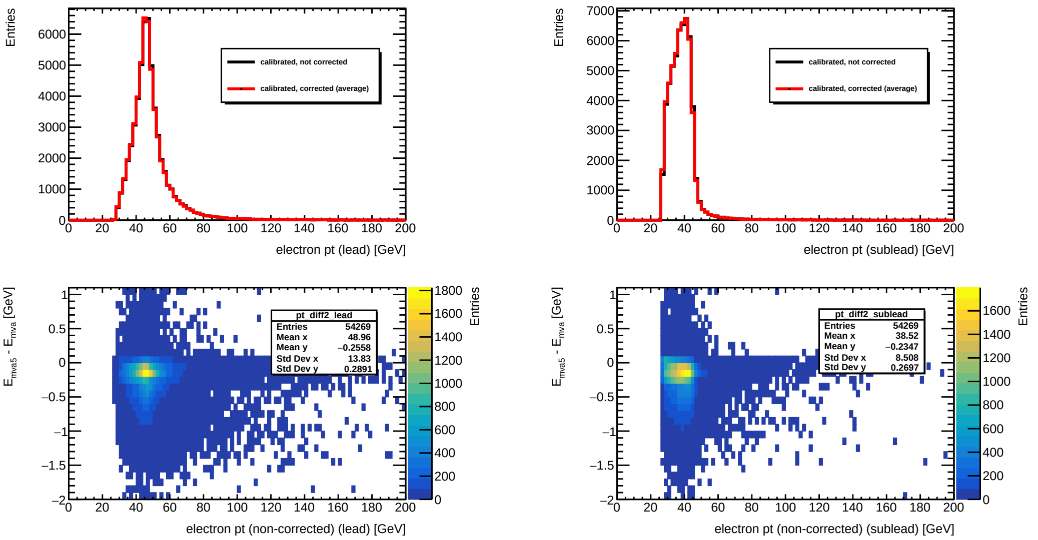

Figure 4.31: Transverse momenta of the two electron candidates when the ramp correction "average" is applied (Red curve) and when it is not (Black curve). The bottom panels show the energy difference per event between the corrected energy (E_{mva5}) and the uncorrected energy (E_{mva}) of the particle. (Special run data).

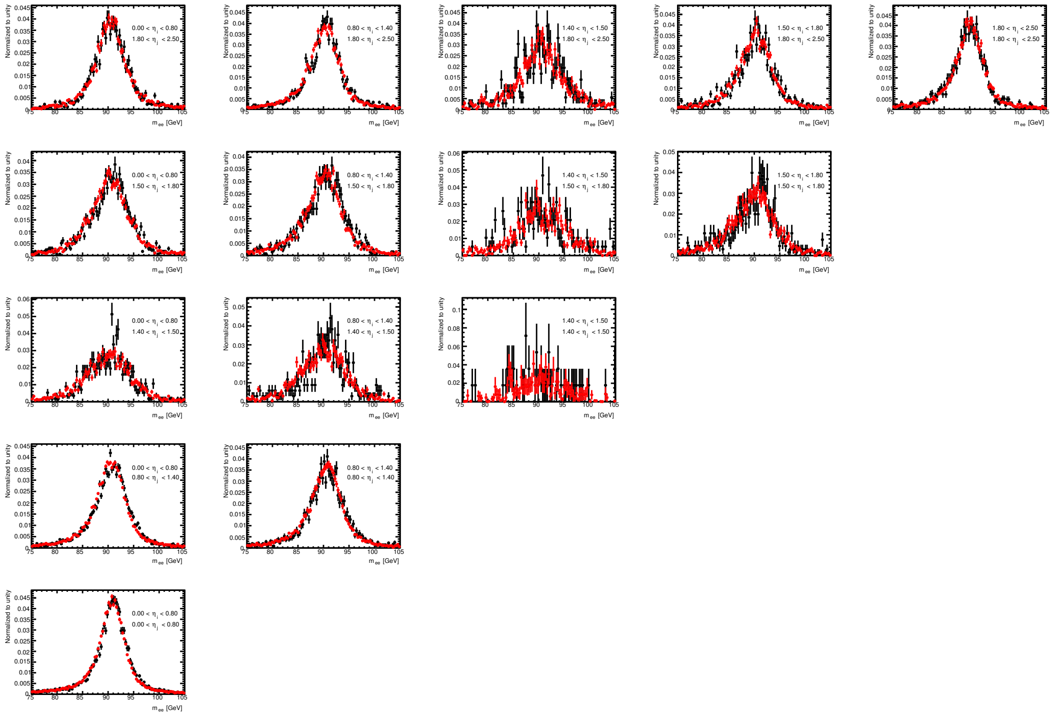

Figure 4.32: Invariant mass distributions for special run data (Black) and standard run data (Red) in the 15 $|\eta|$ regions.

$|\eta|$ bins is parametrized by the **lineshape pdf** function. For this study, the lineshape pdf is chosen to be a sum of three Gaussian functions:

$$P(m_{ee}) = N_1 G_1(m_{ee}; \mu_1, \sigma_1) + N_2 G_2(m_{ee}; \mu_2, \sigma_2) + N_3 G_3(m_{ee}; \mu_3, \sigma_3) \tag{4.11}$$

The parameters of Eq. 4.11 are fixed by fitting the lineshape to the standard run data in each η bin. Examples of this step are shown in Figure 4.33.

Then, during the second step of this method, the parameters of the obtained linehape are re-expressed in terms of the energy scale factors:

$$\mu'_k = \mu_k \sqrt{(1+\alpha_i)(1+\alpha_j)} \tag{4.12}$$

$$\sigma'_k = \sigma_k \sqrt{(1+\alpha_i)(1+\alpha_j)} \qquad k = 1, 2, 3 \tag{4.13}$$

These α_i are finally determined from a simultaneous fit to the special run data in all the $|\eta|$ bins. Examples of this step are shown in Figure 4.34.

All the fits have been performed in the mass range [75, 105] GeV and the number of bins in this interval is 200; only those $|\eta|$ bins with more than 100 events and the maximum of the standard run distribution between 80 and 100 GeV have been used for the fit; additionally, all the three Gaussian functions are required to have $\sigma_k > 1$ GeV in order to avoid fitting any statistical fluctuation in the data.

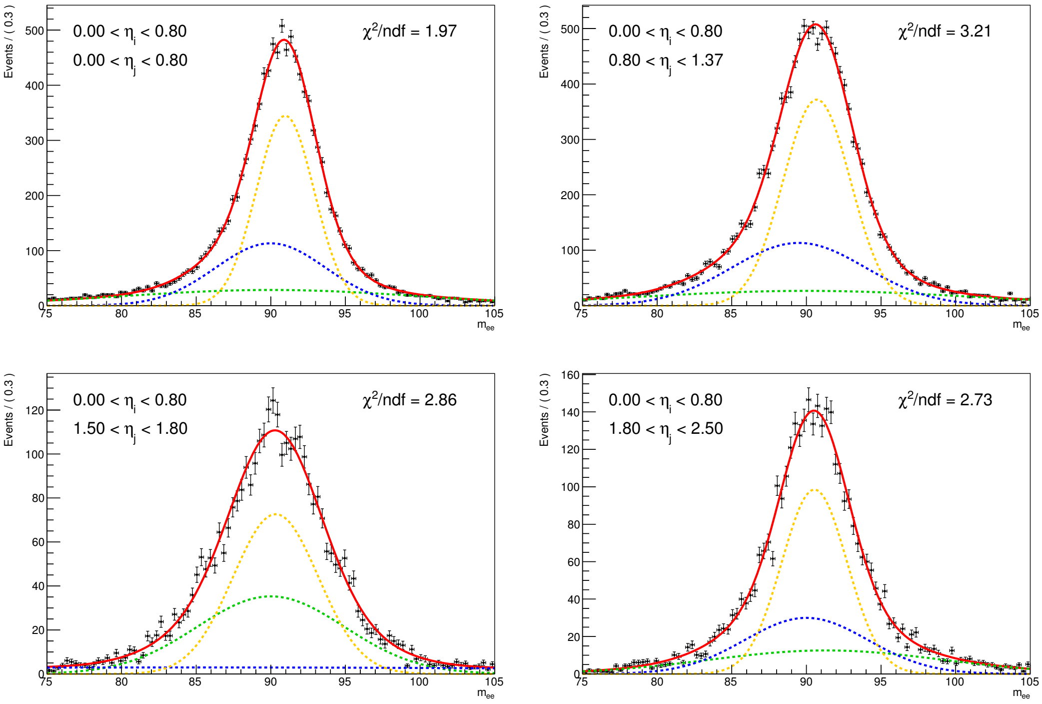

Figure 4.33: Standard run data distributions fitted by the total lineshape pdf (Red curve) in 4 of the 15 $|\eta|$ bins. The three Gaussian components of the pdf are also shown (dashed curves).

4.4.3 Pile-up dependency

As shown in Figure 4.35, the pile-up (PU) distributions of the standard and special runs are very different. Before applying the procedure described in Section 4.4.2, the standard run events are reweighted in order to match the PU distribution of the special run. This configuration will be referred to as the nominal one in the following.

In order to investigate any possible dependency of the α_i on the PU, three categories of events are defined according to the number of collisions per brunch crossing μ:

- $\mu < 33.6$
- $33.6 \leq \mu < 37.6$
- $\mu \geq 37.6$

After the PU reweighting step, the extraction of the scale factors is done independently in each category. Their values and the nominal one are shown in Figure 4.36. The different obtained values in a given bin are compatible with statistical fluctuations around the nominal value, therefore no dependency of the α_i on the PU is retained.

4.4.4 Bootstrap

The statistical uncertainty of the standard runs is propagated to the value of the extracted α_i through bootstrapping. Starting from the original $m_{e^+e^-}$histogram of the standard run data, one can generate N new samples[4] by assigning to each data point a random weight distributed according to the Poisson distribution with $\lambda = 1$. For each sample the extraction of the scale factors is repeated and so N sets of α_i are

---

[4] In this case N is chosen to be 100.

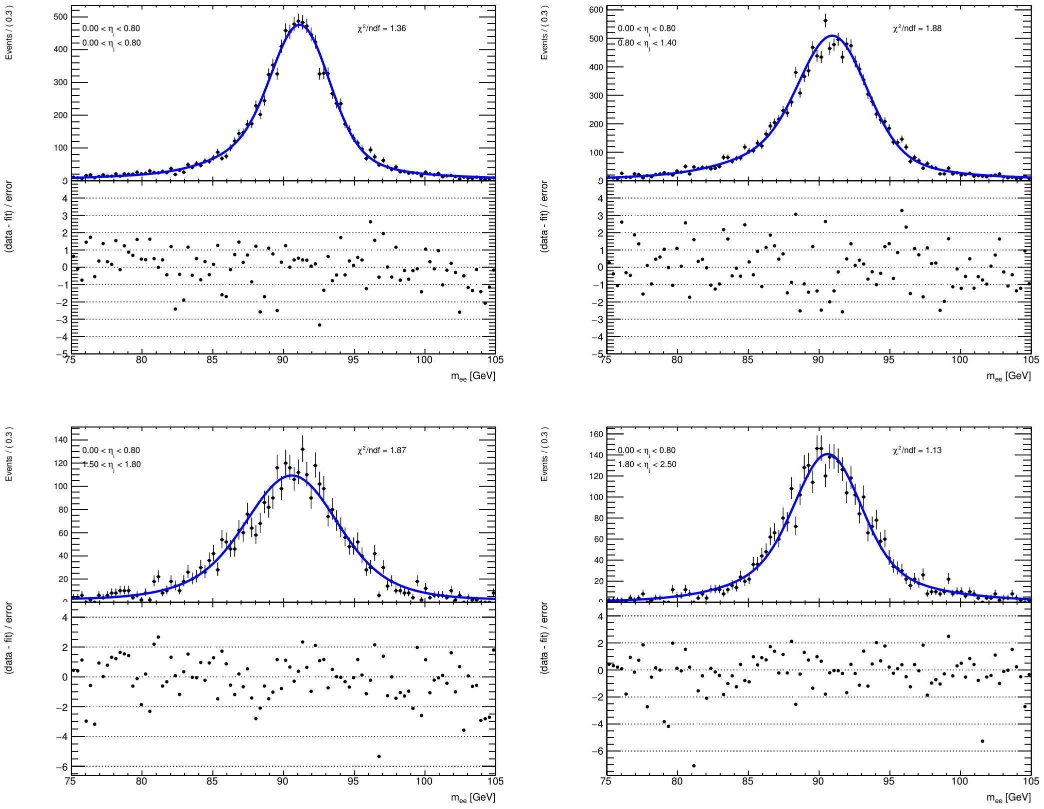

Figure 4.34: Special run data distributions and corresponding lineshape (Blue curve) after the re-parametrization step and the extraction of the scale factors in 4 of the 15 $|\eta|$ bins. Bottom panels show the relative difference between the data and the pdf.

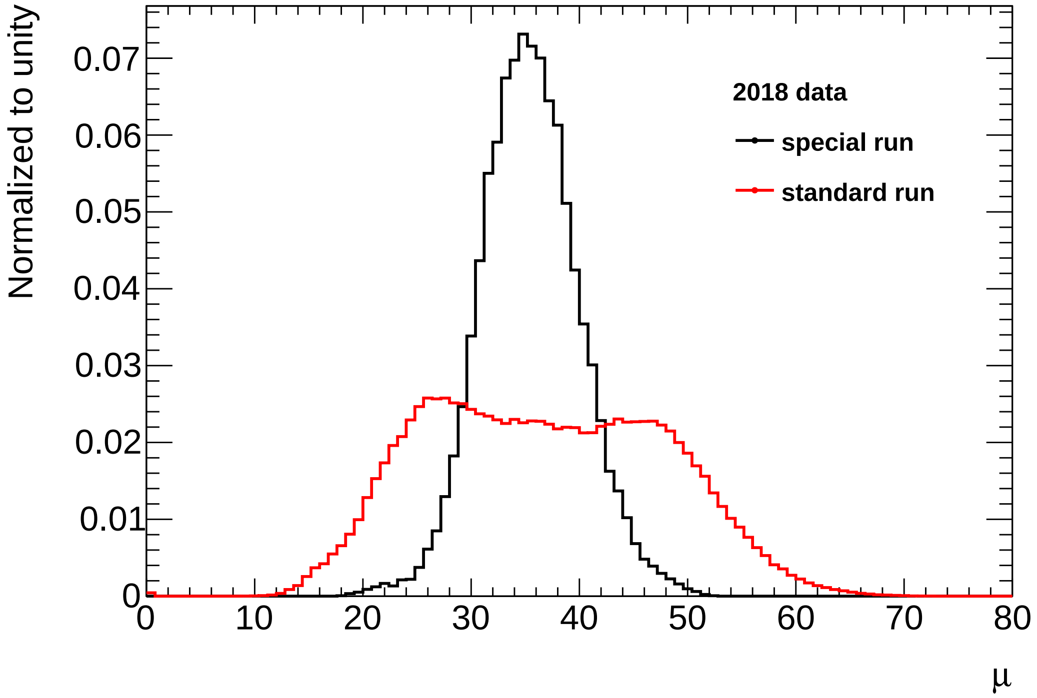

Figure 4.35: Pile-up profiles of the standard run data (Red) and special run data (Black).

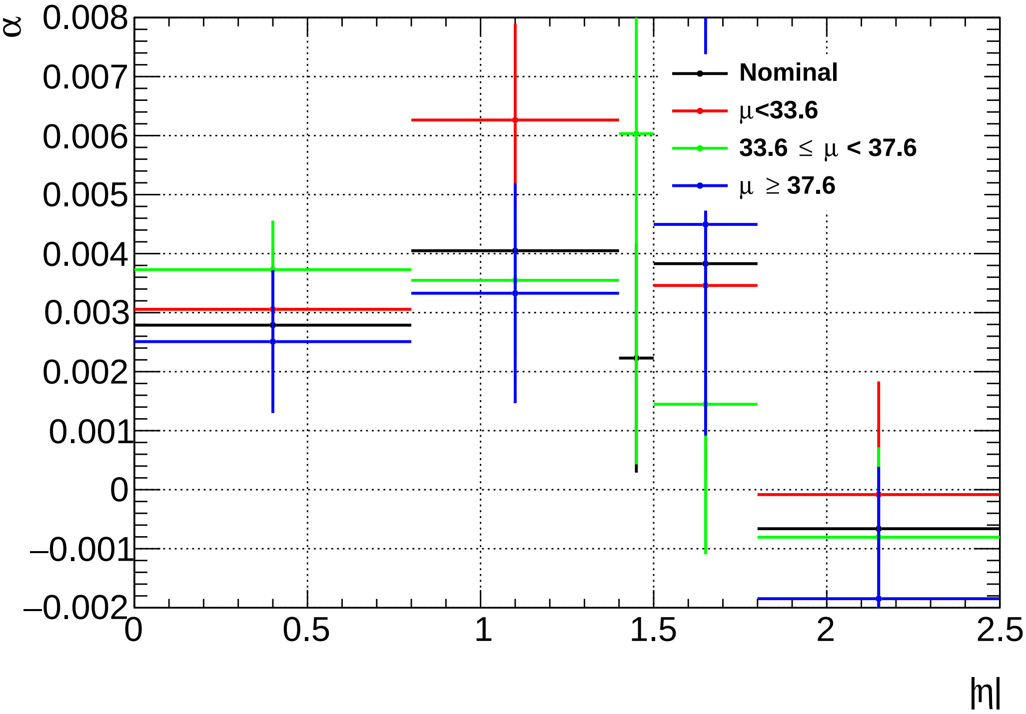

Figure 4.36: Values of the scale factors in the 5 $|\eta|$ bins for the nominal case and the three categories of μ.

produced, whose distributions are shown in Figure 4.37. The standard deviation of the α_i distribution is taken as an additional component of the total statistical uncertainty on its central value:

$$\sigma_{tot}^{stat} = \sqrt{\sigma_{bootstrap}^2 + \sigma_{fit}^2} \tag{4.14}$$

where $\sigma_{bootstrap}$ is an estimate of the statistical uncertainty of the standard run while instead σ_{fit} is the error on the fitted parameter (from the lineshape method) and it estimates the statistical uncertainty of the special run.

Figure 4.38 shows how much the statistical error on scale factors increases for the effect of the bootstrap component.

4.4.5 Systematic uncertainties

In this section, several effects that could introduce systematic uncertainties are investigated and an overview is given. This is always done by extracting the α_i with a variation of the nominal configuration according to the effect under investigation:

- **Electron identification (ID)**: both electron candidates must pass the loose likelihood ID test (instead of the medium likelihood ID, as in the nominal case);
- **Ramp correction**: the "average" ramp correction is applied to the cell energy in L2 (instead of the "cell-by-cell" ramp correction, as in the nominal case);
- **Fit range**: the $m_{e^+e^-}$ mass interval when doing the fit is [85, 95] GeV (instead of [75, 105] GeV, as in the nominal case);
- **Bias correction**: the bias correction (from calibration board offset) is applied (instead of no correction, as in the nominal case).

The difference in the value of the α_i for the four variations, which are plotted in Figure 4.39, are compatible with statistical fluctuations around the nominal value, therefore any systematics related to these effects would be negligible with respect to the total statistical uncertainty. To support this statement, the size of each of the possible systematic variations is compared in detail to the one of the statistical uncertainties in all of the 5 $|\eta|$ bins in Table 4.2.

4.4.6 Purity of the special and standard runs

The analysis presented in this chapter is based on the assumption that the special run represents a sample of events where both electrons coming from the Z decay are reconstructed in MG, i.e. the cluster associated to each of them has at least one of its cells recorded using MG readout. A similar assumption is made for the standard run events, which are supposed to be reconstructed in HG, i.e. with no cells recorded using MG readout. In reality, one has to take into account that the special and standard runs are not 100% pure in MG and HG, respectively. Figure 4.40 shows that the level of "contamination" from HG events in the special run is about 10% and the standard run is composed of almost 6% of MG events. Additionally, by looking at the composition of the two runs in terms of number of MG cells in the clusters and $|\eta|$ position of the clusters plotted in Figure 4.41, the $|\eta|$ regions with the highest fraction of contaminated electrons are detected: in the region $1.4 < |\eta| < 1.5$ there are about 2% of the special run events having the leading electron cluster with 0 cells in MG, while the highest fraction of special run events where the subleading electron cluster has no cells in MG (being about 3%) is in $0.8 < |\eta| < 1.4$; for the standard run, the region with the highest fraction of events (more than 10%) having a cluster containing at least one MG cell is $1.8 < |\eta| < 2.5$, for both the leading and the subleading ones.

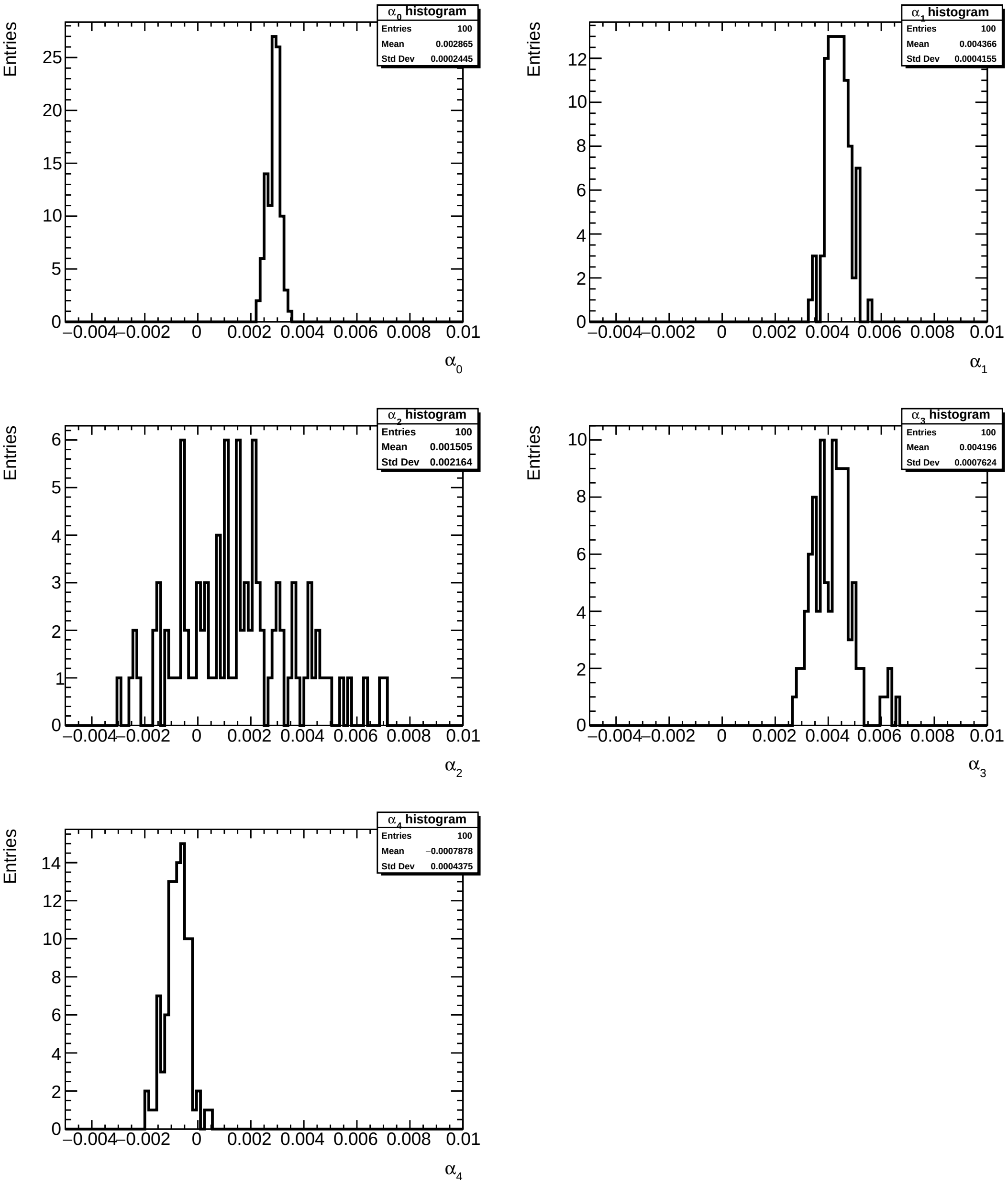

Figure 4.37: α_i histograms obtained through the bootstrap corresponding to the five $|\eta|$ regions.

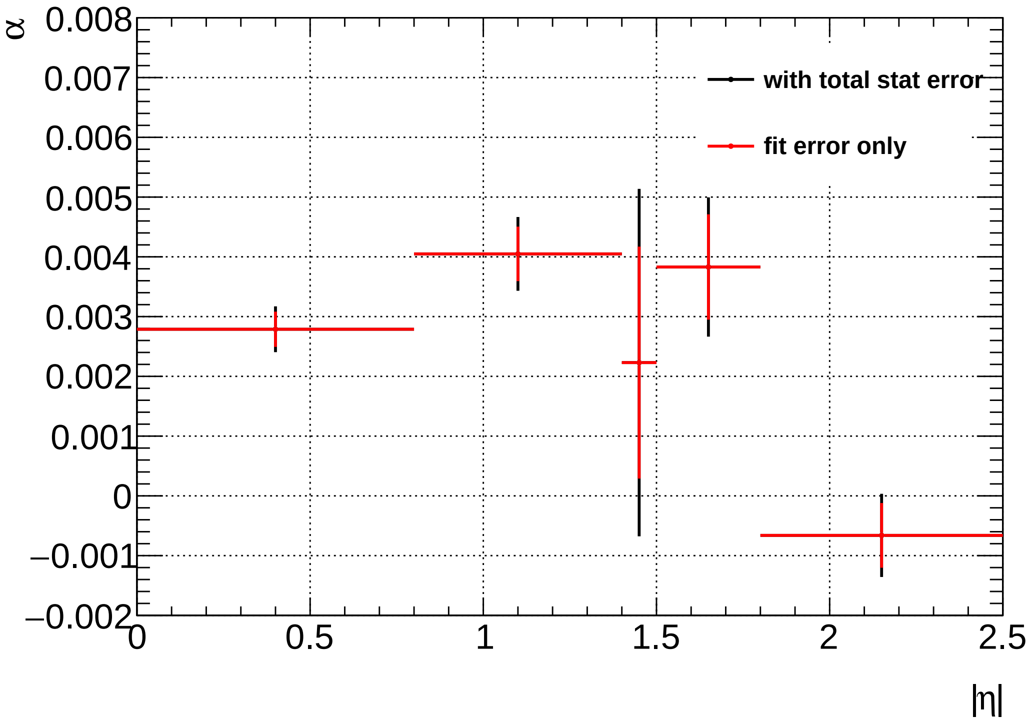

Figure 4.38: Values of the scale factors in the 5 $|\eta|$ bins with and without the addition of the boostrap component to the uncertainty.

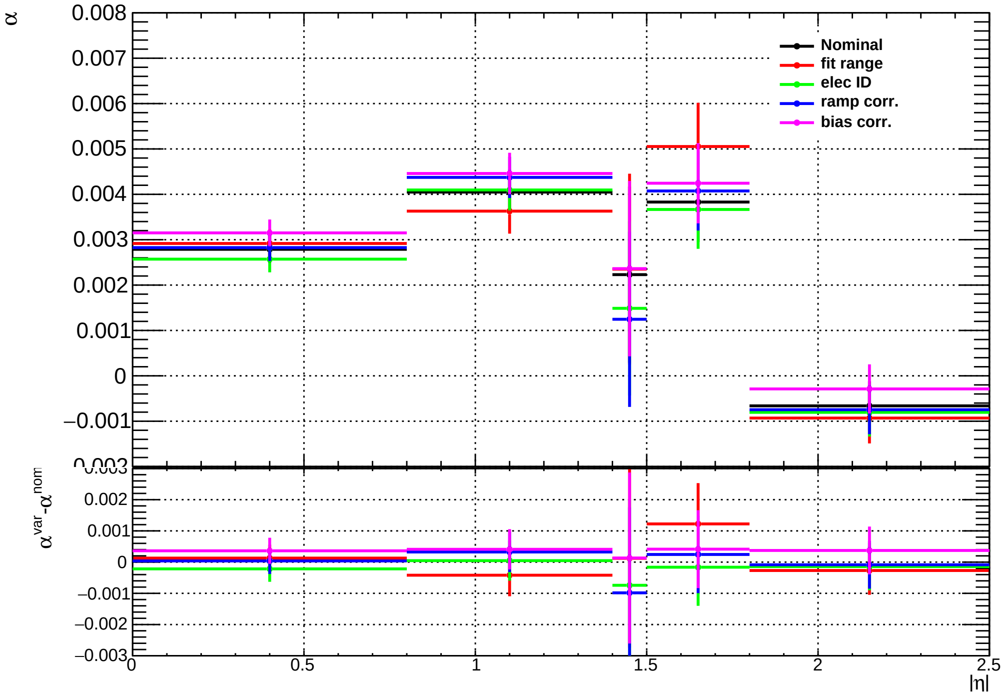

Figure 4.39: Values of the scale factors in the 5 $|\eta|$ bins for the nominal case and the four variations. The bottom panel shows the difference with respect to the nominal. (Error bars don't include the bootstrap component).

		$\lvert\alpha^{var} - \alpha^{nom}\rvert$	$\sigma^{stat}(\alpha^{var})$	$\sigma^{stat}(\alpha^{nom})$	$\sigma^{stat}_{tot}(\alpha^{nom})$
$0.00 < \lvert\eta\rvert < 0.80$	bias corr.	3.62e-04	2.95e-04	2.95e-04	3.83e-04
	fit range	1.29e-04	3.11e-04	2.95e-04	3.83e-04
	elec. ID	2.17e-04	2.90e-04	2.95e-04	3.83e-04
	ramp corr.	3.79e-05	2.94e-04	2.95e-04	3.83e-04
$0.80 < \lvert\eta\rvert < 1.40$	bias corr.	4.10e-04	4.57e-04	4.56e-04	6.17e-04
	fit range	4.20e-04	4.96e-04	4.56e-04	6.17e-04
	elec. ID	4.70e-05	4.50e-04	4.56e-04	6.17e-04
	ramp corr.	3.24e-04	4.54e-04	4.56e-04	6.17e-04
$1.40 < \lvert\eta\rvert < 1.50$	bias corr.	1.32e-04	1.93e-03	1.94e-03	2.91e-03
	fit range	1.21e-04	2.10e-03	1.94e-03	2.91e-03
	elec. ID	7.42e-04	1.92e-03	1.94e-03	2.91e-03
	ramp corr.	9.84e-04	1.93e-03	1.94e-03	2.91e-03
$1.50 < \lvert\eta\rvert < 1.80$	bias corr.	4.15e-04	8.85e-04	8.81e-04	1.17e-03
	fit range	1.22e-03	9.63e-04	8.81e-04	1.17e-03
	elec. ID	1.64e-04	8.67e-04	8.81e-04	1.17e-03
	ramp corr.	2.44e-04	8.71e-04	8.81e-04	1.17e-03
$1.80 < \lvert\eta\rvert < 2.50$	bias corr.	3.73e-04	5.41e-04	5.41e-04	6.96e-04
	fit range	2.69e-04	5.59e-04	5.41e-04	6.96e-04
	elec. ID	1.43e-04	5.33e-04	5.41e-04	6.96e-04
	ramp corr.	8.54e-05	5.40e-04	5.41e-04	6.96e-04

Table 4.2: Comparison table between uncertainties in the 5 $\lvert\eta\rvert$ bins. The first column shows the absolute difference between the variation and the nominal; the second and third columns show the statistical uncertainty (fit component only) of the variation and the nominal, respectively; the fourth column shows the size of the total statistical uncertainty (including the one induced by the bootstrap) in that $\lvert\eta\rvert$ bin.

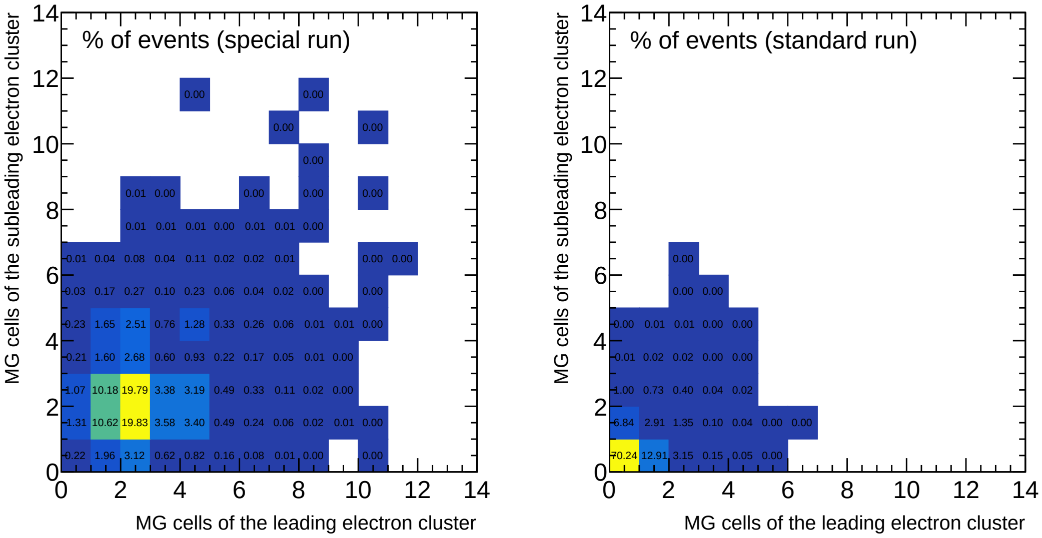

Figure 4.40: Fraction of events in the special (left plot) and standard (right plot) runs as a function of the number of MG cells that are contained in the leading electron cluster (x-axis) and the subleading electron cluster (y-axis).

One may then be tempted to remove all the HG events from the special run and all the MG events from the standard run and perform the extraction of the scale factors using two "pure" samples. However, this cut would introduce a kinematic bias [5] and its consequences are shown in Figures 4.42 and 4.43: although the effects of such a cut are contained for the special run, there is a clear distortion of the p_T spectra of the electrons in some $|\eta|$ regions for the standard run. In conclusion, since it would be very likely to reconstruct a non-physical Z mass using this configuration, the systematic related to this effect can not be estimated through the approach described in Section 4.4.5. Instead, it is done by injecting a known 1% energy change in the MG cell and computing the change in the final electron energy [94].

4.4.7 Comparison with 2017 data

In this section, the results obtained using special run data taken in 2018 are compared to those obtained during the previous year using two different datasets. Special runs 325030 (28 pb^{-1}) and 325558 (27 pb^{-1}) were taken in June 2017 during period A4 and are compared to standard runs 325713 (83 pb^{-1}) and 325790 (47 pb^{-1}) taken shortly after; special run 331466 (105 pb^{-1}) was taken in August 2017 during period D4 and is compared to standard runs 331462 (170 pb^{-1}) and 331479 (114 pb^{-1}) taken shortly before and after. Similarly to the procedure exposed in Section 4.4.3, the pile-up distributions of each standard run is reweighted to the pile-up distribution of its corresponding special run: standard run 2017 A4 is reweighted to special run 2017 A4 and so on. The cut $\mu > 14$ is additionally applied to 2017 A4 data. Plots of the pile-up profiles for the 2017 runs are in Figure 4.44.

After the PU reweighting step, the scale factors are extracted and their values are shown in Figure 4.45. The scale factors derived from August 2017 data are in agreement

---

[5] Since the HG clusters will always be of lower energy, they are more likely to come from the low mass tail of the Breit-Wigner while the MG clusters from the high mass one.

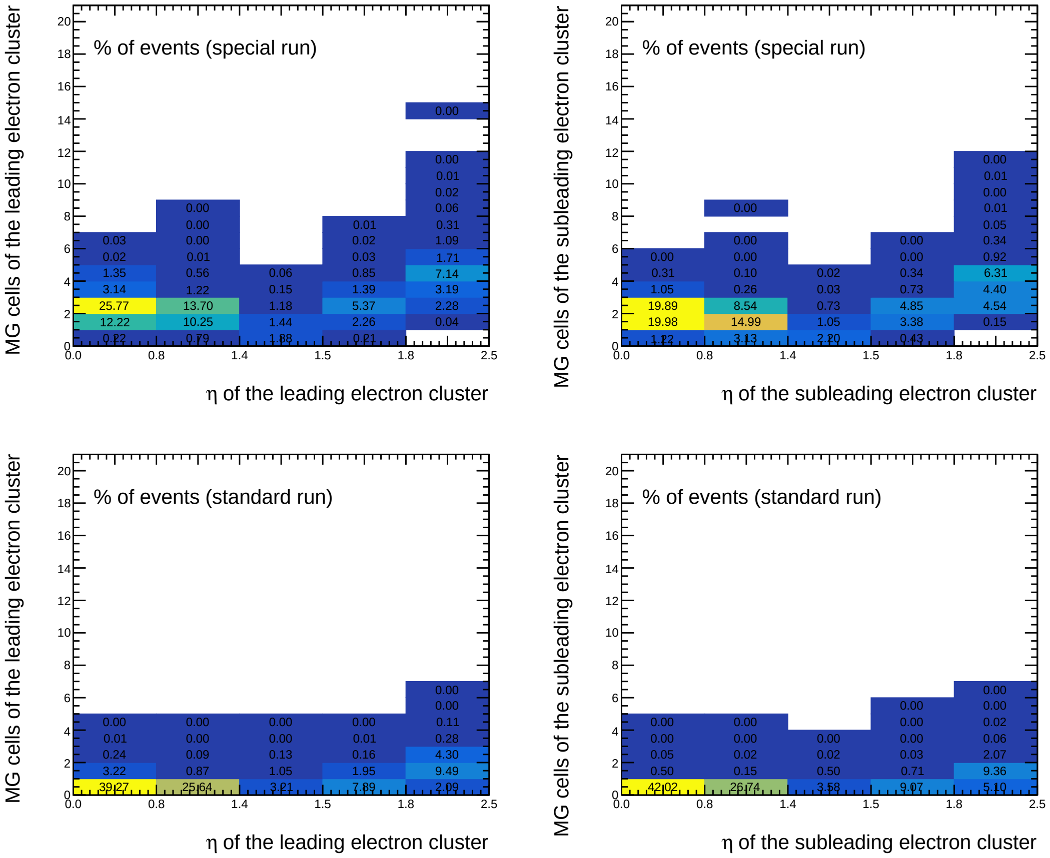

Figure 4.41: Fraction of events in the special (top plots) and standard (bottom plots) runs as a function of the number of MG cells that are contained in the cluster (y-axis) and the position of that cluster (x-axis), for both the leading (left plots) and the subleading (right plots) electrons.

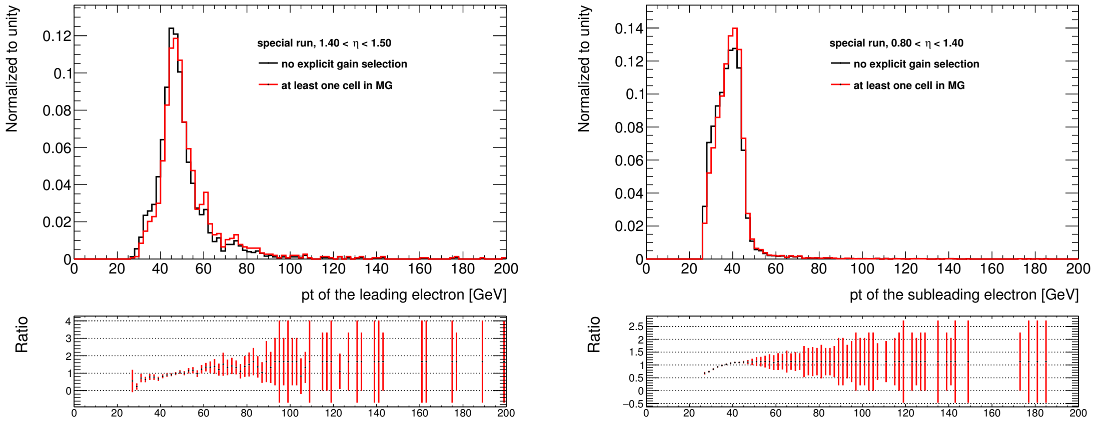

(a) Leading electron.

(b) Subleading electron.

Figure 4.42: p_T distributions of the electrons in the special run for the two $|\eta|$ regions with the highest fraction of contaminated electrons. The nominal case (black line) is compared to the configuration where the special run is composed only by events reconstructed in MG (red line). Bottom panels show the ratio between the two distributions.

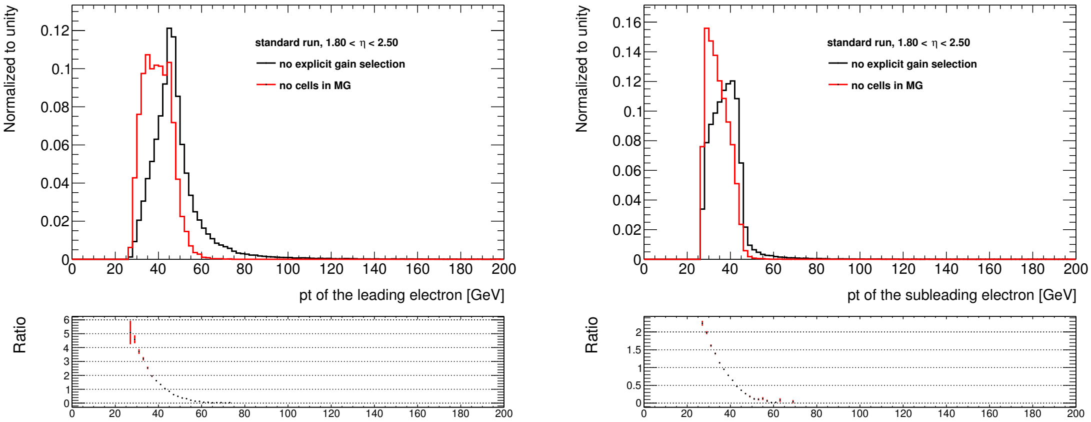

(a) Leading electron.

(b) Subleading electron.

Figure 4.43: p_T distributions of the electrons in the standard run for the two $|\eta|$ regions with the highest fraction of contaminated electrons. The nominal case (black line) is compared to the configuration where the standard run is composed only by events reconstructed in HG (red line). Bottom panels show the ratio between the two distributions.

Bin	Central value	Stat error	Syst error	Tot error
1	0.0024	0.0002	0.0003	0.0003
2	0.0041	0.0004	0.0005	0.0007
3	0.0034	0.0019	0.0012	0.0023
4	0.0033	0.0008	0.0013	0.0015
5	0.0004	0.0005	0.0003	0.0006

Table 4.3: Breakdown of the final values of the scale factors and their uncertainties per η bin.

with the results obtained using 2018 data except for the region $1.8 < |\eta| < 2.47$ where a significant difference is observed; Regarding June 2017 results, the disagreement with both the other two datasets is very large in the region $1.37 < |\eta| < 1.8$ while elsewhere there is still a minimum level of compatibility. In conclusion, the values of the scale factors obtained in the Barrel region ($|\eta| < 1.37$) seem to confirm what was found in previous similar studies, while the results obtained in the other regions of the calorimeter, especially in $1.5 < |\eta| < 1.8$, are not completely understood and further investigation is needed.

4.4.8 Results

Figure 4.46 shows the final values of the scale factors obtained by this study: 2017 and 2018 data-sets are combined to increase the statistical precision, while the systematic uncertainties are computed using only the 2018 data and assumed to be the same for 2017. The total error is computed as the quaratic sum of the statistical component (improved by the bootstrap) and the systematic contributions from all the sources. A more detailed breakdown of the final values and their uncertainties is given in Table 4.3.

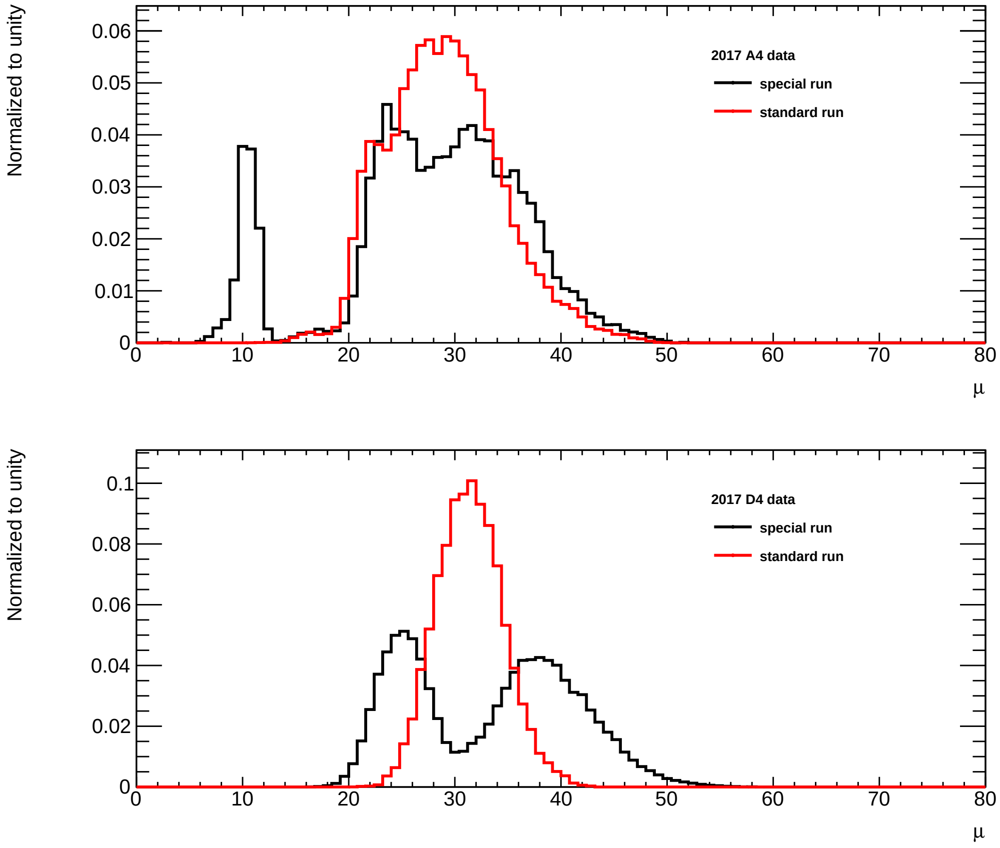

Figure 4.44: Pile-up profiles of the standard run data (Red) and special run data (Black) for the two datasets taken in 2017.

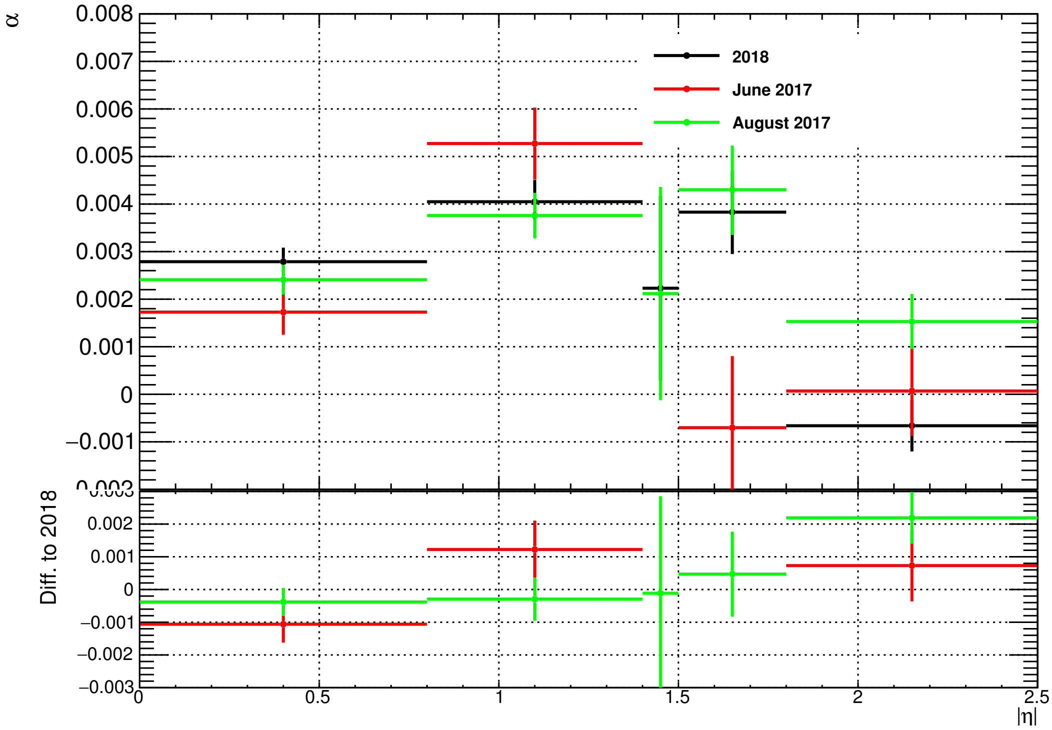

Figure 4.45: Values of the scale factors in the 5 $|\eta|$ bins using 2018 data and 2017 data. The bottom panel shows the difference with respect to 2018 data.

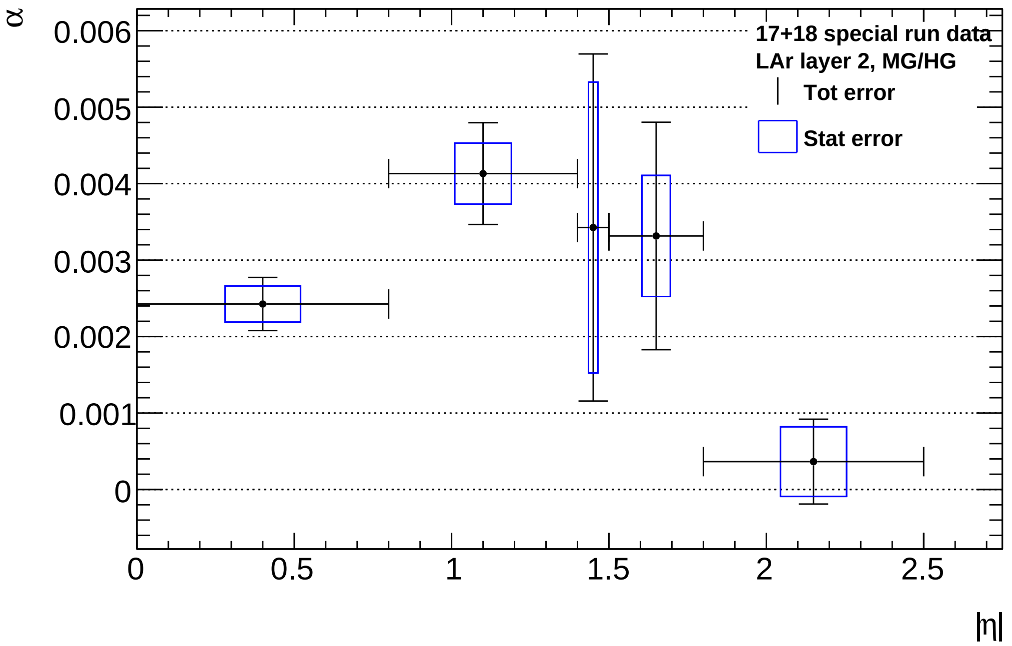

Figure 4.46: Values of the SFs and their uncertainty.

4.5 Study of ADC non-linearity

In Eq.3.1 it was shown that the energy reconstruction in a calorimeter cell is done with a linear conversion from ADC counts. In practice, the energy response of each cell is fitted during dedicated electronic calibration runs (ramp runs) using a linear function. The fits to the calibration ramps show non-zero residuals (Figure 4.47), caused by an intrinsic non-linear behaviour of the electronics. This effect was partially taken into account in the gain intercalibration analysis, where a correction to the linear ramp was derived in order to properly model the non-linear response in MG when the DAC switching threshold was artificially lowered. In this section, a new approach to correct the electronic non-linearities in both HG and MG is presented, as well as a revisited version of the gain intercalibration analysis which profits from it.

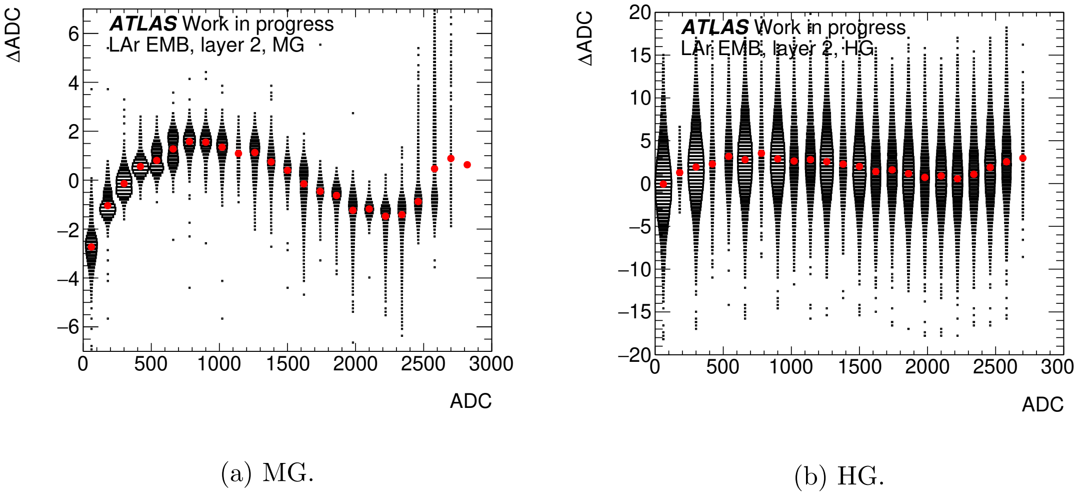

(a) MG.

(b) HG.

Figure 4.47: Residuals of the ramp fits for the L2 cells in the Barrel reconstructed using MG (left) and HG (right).

4.5.1 Definition of the ADC correction

Since the fit residuals can be considered as a measurement of the non-linearity of the electronic response for a given cell, their distribution is parametrized in order to get a continuous analytic function which will be used as a correction. The residuals are fitted using a 5-degree polynomial (alternative parametrizations are investigated in Section 4.5.3), so that it is flexible enough to capture the shape of their distribution. In Figure 4.48, an example of polynomial fit of the residuals is shown. When this polynomial is added to the linear ramp, a modulated ramp is obtained, which results in a better description of the electronic response for that cell.

$$f_{\text{mod}}(ADC) = f_{\text{lin}}(ADC) + f_{\text{pol}}(ADC) = l_0 + l_1 ADC + p_0 + \sum_{i=1}^{5} p_i ADC^i \tag{4.15}$$

where l_0 and l_1 are the intercept and the slope fitted in the standard reconstruction, p_i are the parameters of the polynomial fitted on the residuals. For the HG case, $p_0 = 0$ to be consistent with the fact that $E = 0$ when $ADC = 0$. Then, following the definition given in Eq.4.6, the ADC correction is defined as

$$correction = \frac{f_{\text{mod}} - f_{\text{lin}}}{f_{\text{lin}}} = \frac{f_{\text{pol}}}{f_{\text{lin}}} \tag{4.16}$$

This relative multiplicative correction effectively replaces the ramp-correction described in Section 4.2 and is defined for MG and HG as well. In Figures 4.49 and 4.50, 2-D maps of the correction are shown, both for the MG and HG component.

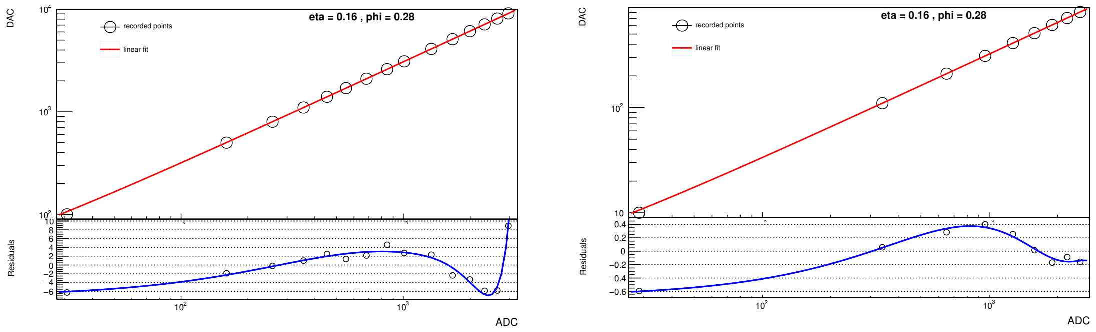

(a) MG.

(b) HG.

Figure 4.48: (Top) Recorded standard ramp fitted by a linear function (red line) for the cell whose center has coordinates $\eta = 0.16$ and $\phi = 0.28$. (Bottom) Residuals of the fit, fitted by a 5-degree polynomial (blue line).

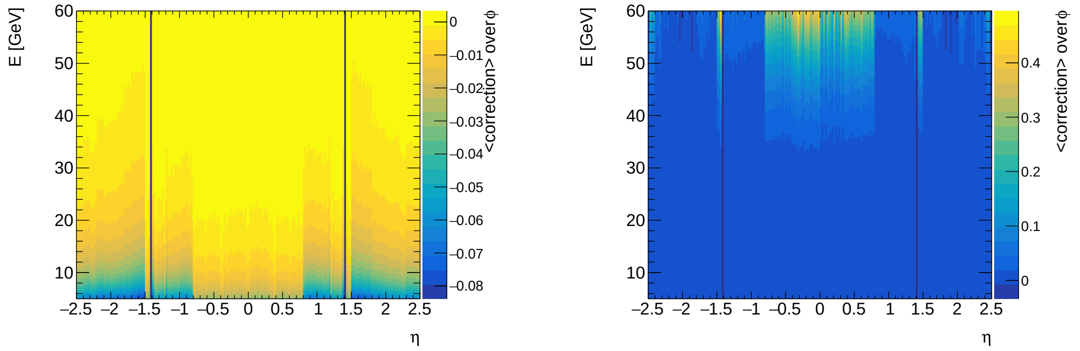

(a) MG.

(b) HG.

Figure 4.49: Map of the correction in the $E - \eta$ space of the second layer of the LAr calorimeter.

4.5.2 Gain intercalibration analysis using ADC correction

The analysis presented in Section 4.4 is repeated here, with the only exception that the $Z \to e^+e^-$runs are reconstructed using the new ADC correction (both for MG and HG) instead of the MG ramp-correction described in Section 4.2. The reader can find a detailed description of the analysis in its dedicated section. The results obtained with the new configuration are shown in Figure 4.51: the values of the HG/MG scale factors (SFs) in the first two η bins are reduced by about a factor 2 with respect to the ones obtained using the nominal ramp-correction, proving that the ADC linearity is at the origin of a large fraction of the shift in calibration between the two electronic gains; additionally, the plot shows that correcting also the energy of the cells in HG, instead of correcting only those in MG, has a significant impact on the final result.
SFs are extracted using this method also from 2017 special runs data and combined

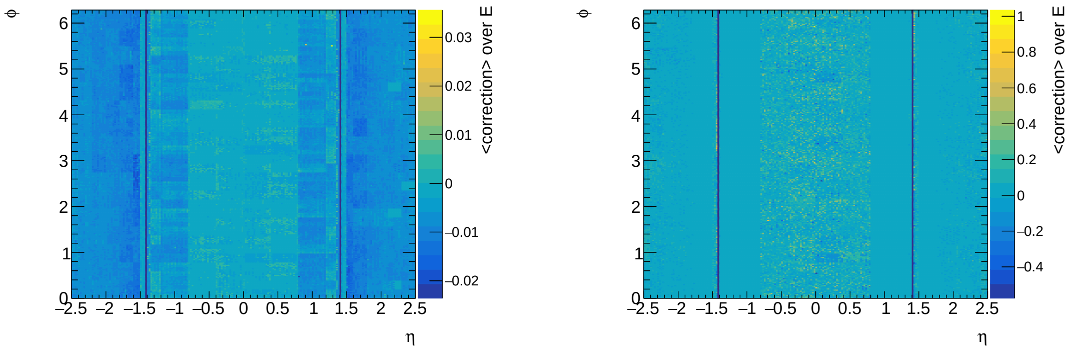

(a) MG. (b) HG.

Figure 4.50: Map of the correction in the $\eta - \phi$ space of the second layer of the LAr calorimeter.

with 2018 ones to obtain the most accurate estimate of the HG/MG miscalibration, as reported in Figure 4.52.

4.5.3 Further checks

In this section, several effects are investigated with the aim of quantifying any possible contribution to the uncertainty of the SFs or, more generally, to estimate a possible systematic error associated to the ADC linearity correction. The impact of each effect is estimated by comparing every time the nominal SFs[6] with the ones obtained when considering the effect under investigation. All the studied effects show small deviations from the nominal case, which are compatible with the size of the statistical uncertainties.

Use of special electronic calibration runs

The ADC linearity correction described in Section 4.5.1 is derived using standard calibration runs. Special calibration runs were taken specifically to populate more the low DAC region and thus provide more information for the modeling of the MG ramp-correction. Figure 4.53 shows the different amount of recorded points between a special ramp and a standard ramp for an example cell. Figure 4.54 shows the SF results for the different configurations: using special ramps (more points in the ramp) instead of standard ramps to derive the MG component of the ADC-linearity correction doesn't impact the results of the gain intercalibration analysis. Indeed, the 5-degree polynomial is able to correctly fit the distribution of the residuals already when it is populated by the standard amount of points.

Alternative parametrizations

The ADC linearity correction described in Section 4.5.1 is derived fitting a 5-degree polynomial to the residuals of the linear ramp fit. Other choices of parametrization can potentially bring a better modelization of the residuals, so the fits of the residuals are repeated using either a 4-degree polynomial or 6-degree polynomial, as an alternative

---

[6] All the checks are performed using 2018 data only.

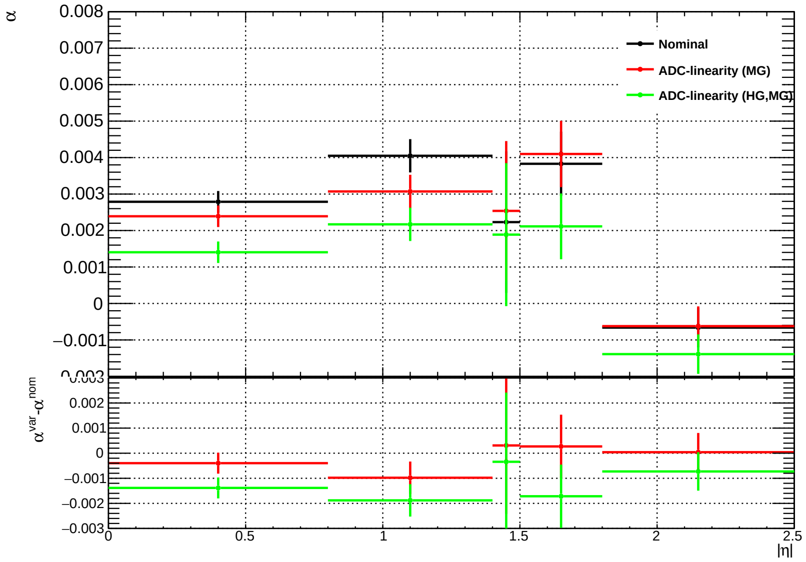

Figure 4.51: Values of the SFs in the 5 η bins when using the nominal ramp-correction (black points), the MG component of the ADC-linearity correction (red points) and both the MG and HG components (green points). The bottom panel shows the difference with respect to the nominal values (2018 data only).

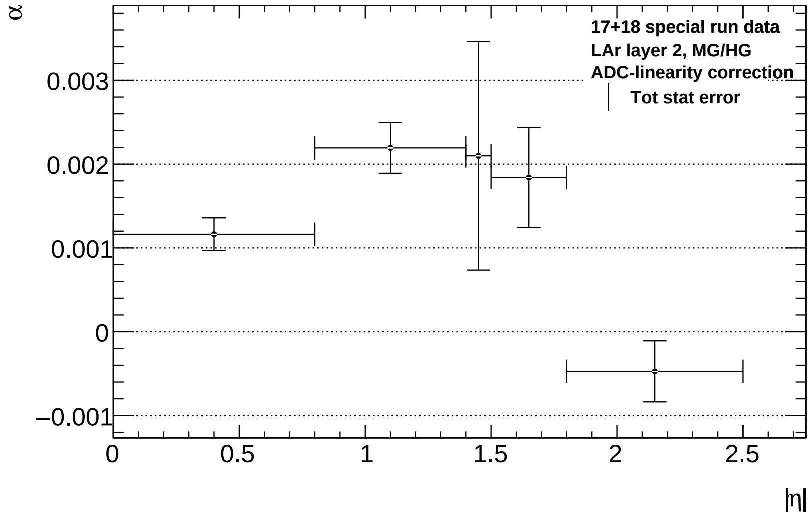

Figure 4.52: Values of the SFs after the application of the ADC-linearity correction. The error bars on this plot are only statistical.

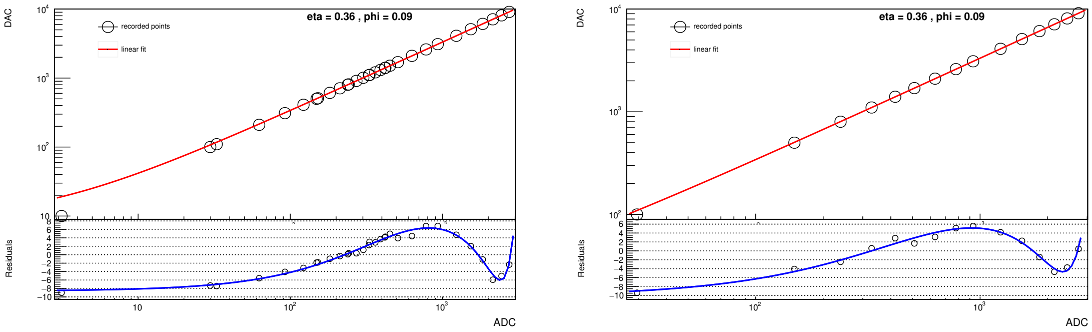

(a) Special calibration ramp.

(b) Standard calibration ramp.

Figure 4.53: Special ramps are recorded on average with twice as many points as the standard ramps in the low DAC region.

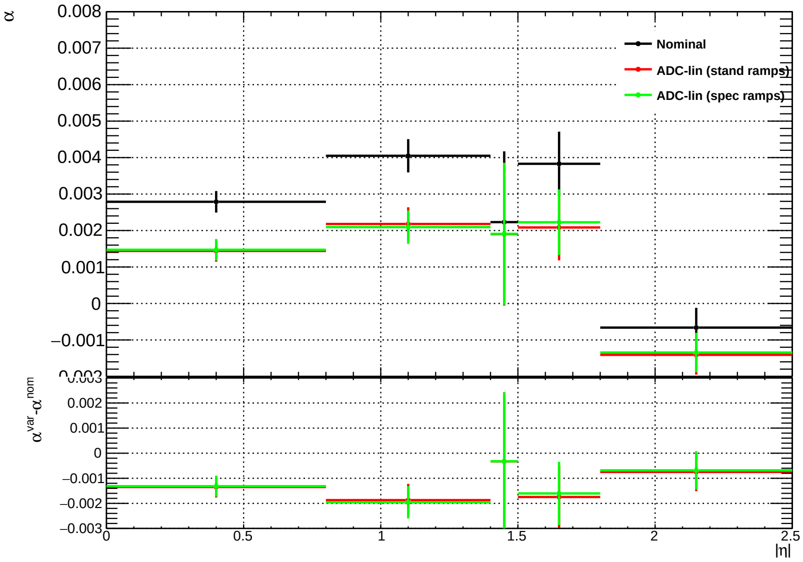

Figure 4.54: Comparison between the results obtained using an ADC linearity correction based on standard ramps (red points) and another based on special ramps (green points). Nominal results (black points) are shown for reference.

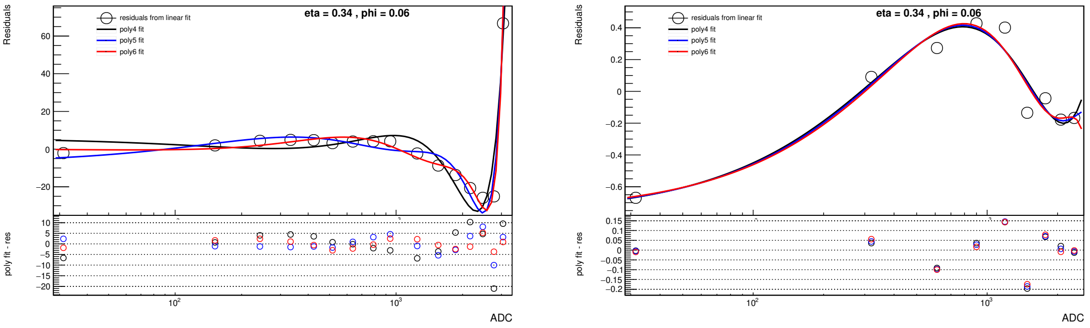

(a) MG.

(b) HG.

Figure 4.55: (Top) Residuals of the linear ramp fit, fitted by 4-degree (black line), 5-degree (blue line) and 6-degree (red line) polynomials for the cell whose center has coordinates $\eta = 0.34$ and $\phi = 0.06$. (Bottom) Residuals of the polynomial fit, for each of the three cases.

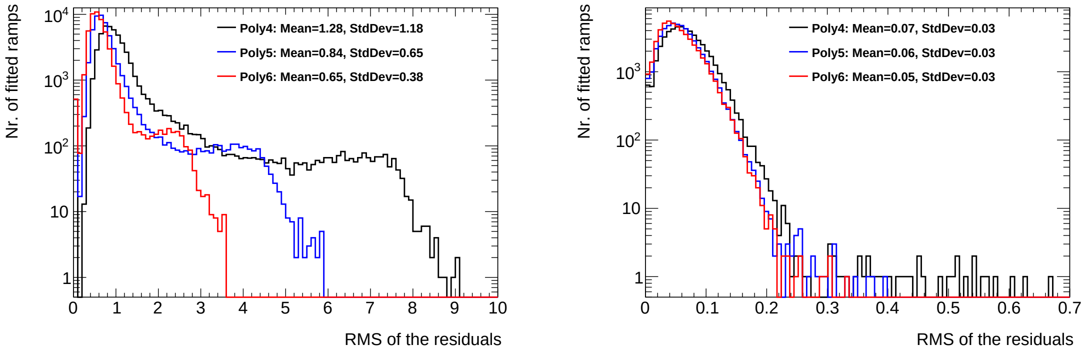

(a) MG.

(b) HG.

Figure 4.56: Distributions of the RMS of the residuals of the 4-degree (black line), 5-degree (blue line) and 6-degree (red line) polynomial fits.

(Figure 4.55). Figure 4.56 shows that the RMS of the residuals[7] of a 6-degree polynomial fit is smaller on average with respect to that of a 5-degree polynomial, which in turn has a smaller one compared to a 4-degree polynomial. This is not surprising because by definition a function with more degrees of freedom can adapt better to a given dataset. However, Figure 4.57 shows that the SF results obtained with different parametrizations are equivalent among themselves within the uncertainties. This is taken as an indication that a more complex parametrization of the residuals is not necessary in the context of the gain intercalibration analysis.

Impact of the average correction

The ADC linearity correction described in Section 4.5.1 is based on individual fits of all 200 × 256 cells in L2. Alternatively, the ADC linearity correction can be derived using fits of the profile distributions of the residuals in five η regions (0-0.8, 0.8-1.37, 1.37-1.50, 1.5-1.8 and 1.8-2.47), as shown in Figure 4.58. In this way, the polynomial

---

[7] Here the RMS of the residuals of the fit is taken as a goodness-of-fit metric, because it is correlated to the χ^2.

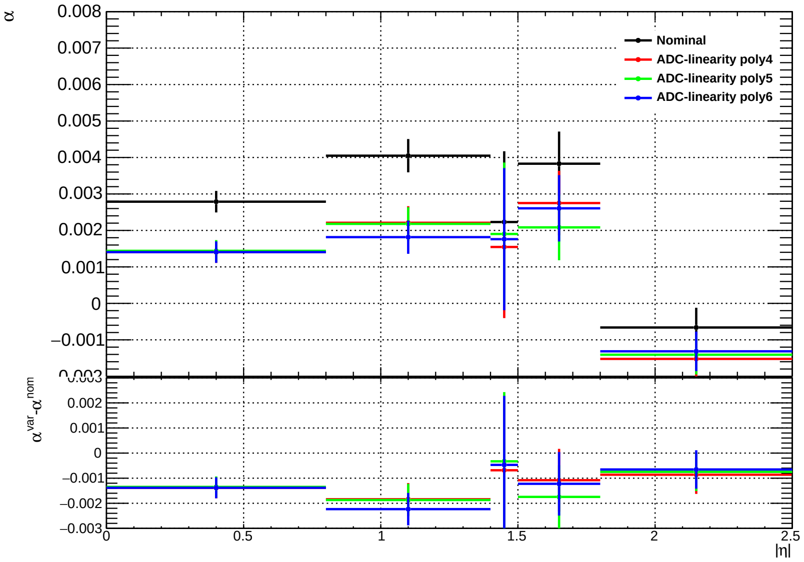

Figure 4.57: Comparison between the results obtained using an ADC linearity correction based on 4-degree (red points), 5-degree (green points) and 6-degree polynomials (blue points). Nominal results (black points) are shown for reference.

parametrization is the same for cells having same η position but different ϕ, and also for those cells belonging to the same η region. In this sense, the spread of the residuals around the fit is not taken into account by this method. Two-dimensional maps of this average correction are shown in Figures 4.59, 4.60. Figure 4.61 shows the SFs obtained with a cell-by-cell ADC correction and an average one. Results are compatible within the uncertainties everywhere but the last η bin where a small discrepancy between the two methods is observed.

Propagation of uncertainty from fit of the residuals

The ADC linearity correction described in Section 4.5.1 is computed using the fitted values of the p_i parameters of the polynomial fit. The uncertainty associated to these

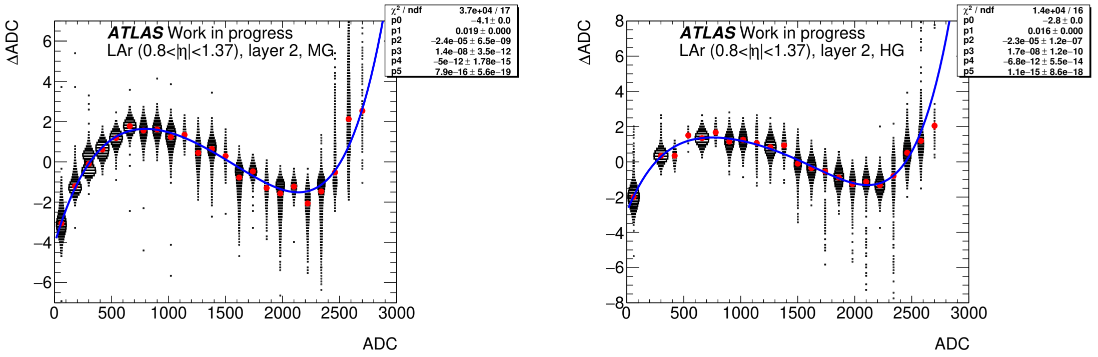

(a) MG. (b) HG.

Figure 4.58: Polynomial fit of the profile distribution of the residuals in the region $0.8 < |\eta| < 1.37$.

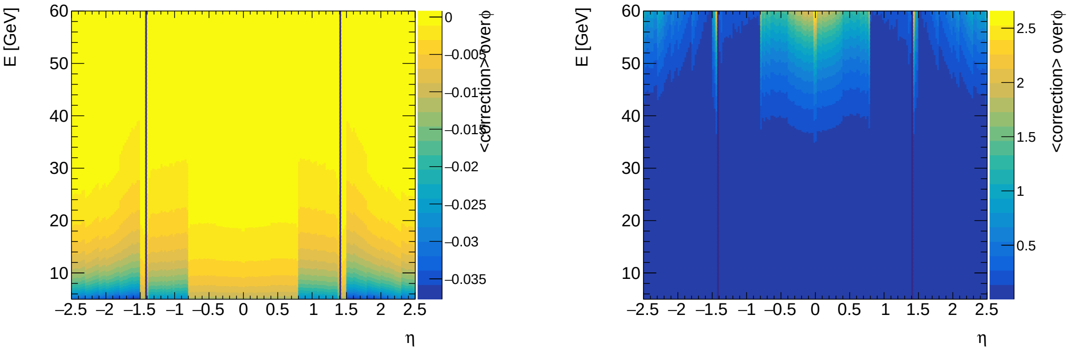

(a) MG.

(b) HG.

Figure 4.59: Map of the average correction in the $E-\eta$ space of the second layer of the LAr calorimeter.

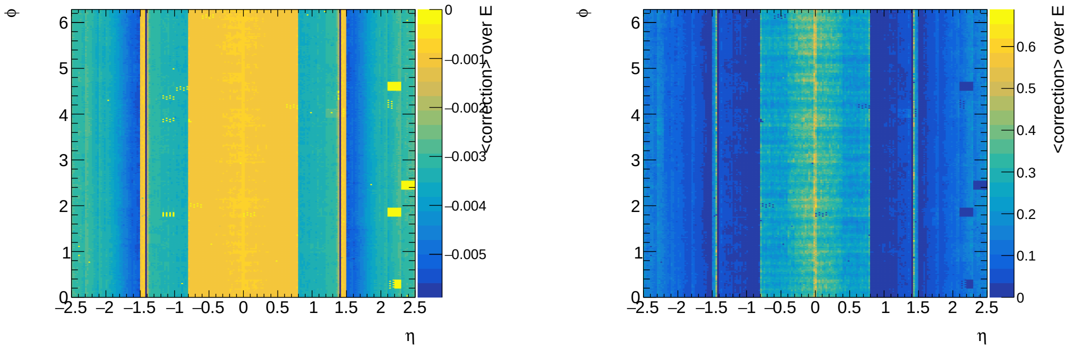

(a) MG.

(b) HG.

Figure 4.60: Map of the average correction in the $\eta-\phi$ space of the second layer of the LAr calorimeter.

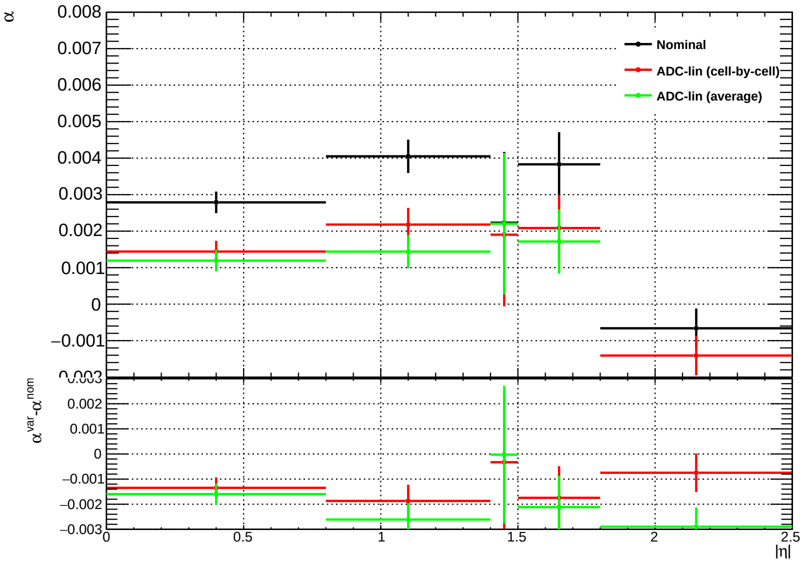

Figure 4.61: Comparison between the results obtained using an ADC linearity correction based on cell-by-cell (red points) and average (green points) methods. Nominal results (black points) are shown for reference.

parameters can be propagated down to the SFs extracted by the gain intercalibration analysis. After performing the nominal 5-degree polynomial fit, every p_i parameter has its 1σ error added (subtracted) and the resulting polynomials are then used to compute up (down) variations of the correction, as shown in Figure 4.62. The 1σ variations computed in such a way are not very accurate, because the correlations among the parameters are not taken into account, but it is sufficient to estimate the maximum size of the propagated uncertainty. Comparison between SF results obtained when using the nominal ADC correction and the variations is given in Figure 4.63.

4.5.4 Perspectives

The correction method presented in this chapter will be included in the next round of the ATLAS recommendations for the energy calibration of electrons and photons (EGamma). A preliminary estimate of the impact of the new gain calibration on the upcoming measurement of the Higgs boson mass in the diphoton decay channel is given here, based on the expected results of the analysis currently being finalized by the collaboration [100]:

$$m_H = 125.09 \pm 0.123(\text{stat}) \pm 0.259(\text{syst})\text{GeV} \tag{4.17}$$

With respect to the measurement shown in Section 1.5, this result exploits the full Run 2 dataset of pp collisions (corresponding to 139fb^{-1}) and the strategy for the categorization of diphoton events is re-optimized. The breakdown of the contributions from different groups of systematic sources to the total uncertainty is given in Table 4.4, where the “LAr cell non-linearity” one is ranked third. Contrary to the previous recommendations, which consisted of using the full size of the measured HG/MG miscalibration as a systematic, the scale factors of Figure 4.52 will be used to correct the energy of electrons and photons and their error bars will be the size of the new gain systematic. As a consequence, the value of the systematic associated to the gain

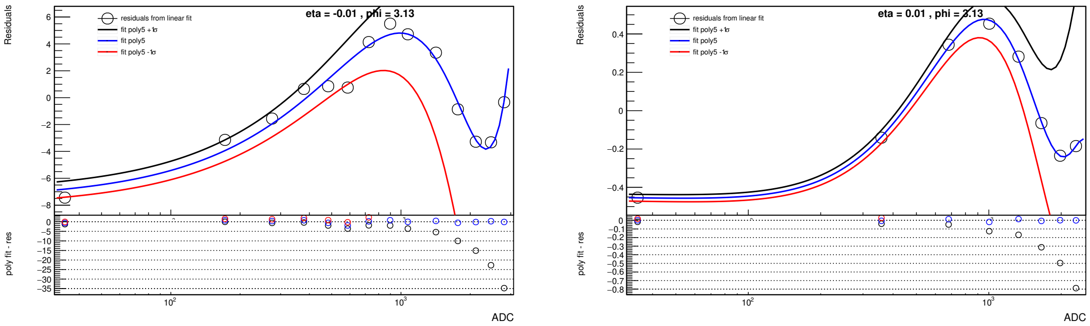

(a) MG.

(b) HG.

Figure 4.62: (Top) Residuals of the linear ramp fit, fitted by a 5-degree polynomial (blue line) and its up (black line) and down (red line) variations. (Bottom) Residuals of each of the three polynomials.

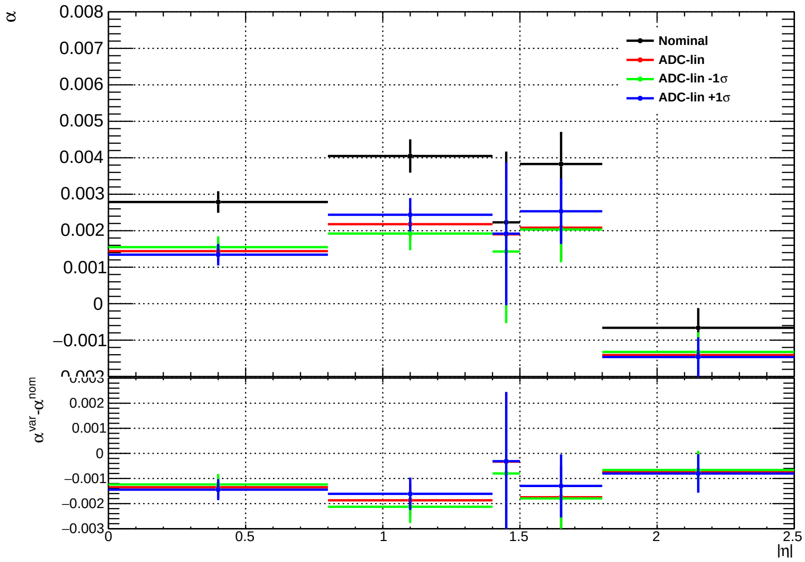

Figure 4.63: Comparison between the results obtained using the central ADC linearity correction(red points) and its up (green points) and down (blue points) variations. Nominal results (black points) are shown for reference.

Systematic group	Impact on m_H (MeV) Down	 Up
Layer calibration	144	160
Lateral shower shape	112	124
LAr cell non-linearity	99	114
Other material (not ID)	78	79
$Z \to ee$ calibration	64	65
Conversion reconstruction	50	51
ID material	25	25
Resolution	8	4
Luminosity	0	0

Table 4.4: Main sources of systematic uncertainties on $m_H^{\gamma\gamma}$, before the application of the new gain calibration.

miscalibration will roughly decrease by a factor 10 in the barrel region. Under the assumption that the impact of "LAr cell non-linearity" scales in the same way as the value of the gain systematic (i.e. by a factor 10), the total systematic uncertainty on m_H can be re-computed leaving all the other contributions unchanged:

$$m_H = 125.09 \pm 0.123(\text{stat}) \pm 0.234(\text{syst})\text{GeV} \tag{4.18}$$

which corresponds to a 10% reduction with respect to the number given in Eq. 4.17. The actual improvement to the mass analysis brought by the gain intercalibration studies, along with other studies targeting the other main systematic sources, can be quantified more precisely after the release of the updated EGamma recommendations.

Chapter 5

Measurements of the Higgs production cross sections in the diphoton decay channel

The content of this chapter is mostly inspired by Ref.[101]. I personally contributed to the analysis effort in the optimization of the categorization (Sections 5.4.1 and 5.5) as well as the cross-check of the results presented in Section 5.9 with an independent statistical framework.

5.1 Introduction

This chapter reports measurements of Higgs boson production cross sections in the diphoton channel, using the full data set of proton-proton collisions at $\sqrt{s} = 13$ TeV collected by the ATLAS experiment during the Run 2 of the LHC. The integrated luminosity of this data set is 139 fb^{-1} [102, 103], a roughly four-fold increase compared to the data set used in the previous version of these measurements in the diphoton channel published by ATLAS [65]. While the performance of the reconstruction and selection is generally better for objects used in these measurements, the most significant improvement in the sensitivity comes from a redesigned and refined data analysis compared to Ref. [65].

The analysis is designed and optimized to measure the production cross-sections in the Stage 1.2 STXS fiducial *regions*[1], which are defined at the particle level. These are defined in the range $|y_H| < 2.5$ of the Higgs boson rapidity y_H, separately for mutually exclusive Higgs boson production processes: the $gg \rightarrow H$ process, which includes both ggF production and $gg \rightarrow ZH$ production followed by a hadronic decay of the Z boson; the electroweak $qq' \rightarrow Hqq'$ process, encompassing both VBF production and $q\bar{q}' \rightarrow VH$ production followed by a hadronic decay of the vector boson; the VH process, corresponding to $pp \rightarrow VH$ production followed by a leptonic decay of the vector boson (in the case of ZH, including both decays to charged leptons and to neutrinos); and the top-associated ttH and tH productions. The Higgs boson decay information is not used in the definition of STXS regions. For each process, non-overlapping fiducial regions are defined based on the kinematics of the Higgs boson and of the associated jets, leptons and top quarks, as well as the number of jets and leptons. Jets are reconstructed from all stable particles with a lifetime greater than 10 ps, excluding the decay products of the Higgs boson and leptons from W and Z boson decays, using the anti-k_t algorithm with a jet radius parameter $R = 0.4$, and must have a transverse momentum larger than 30 GeV.

The measurement regions for the analysis follow the Stage 1.2 definitions with the following modifications:

- The bbH production mode is experimentally difficult to separate from $gg \rightarrow H$, and the two modes are therefore measured as a single process, with each STXS region of the combined process corresponding to the sum of $gg \rightarrow H$ and bbH contributions.
- $gg \rightarrow ZH$ and $q\bar{q} \rightarrow ZH$ production with a leptonic Z decay similarly cannot be distinguished by the analysis selections, and are therefore considered as a single $pp \rightarrow ZH$ process.
- tH production is split into separate $pp \rightarrow tHW$ and $pp \rightarrow tHqb$ contributions, since the two processes have different acceptances for the analysis selections. The s-channel $pp \rightarrow tHb$ process is neglected because of its small cross-section.
- The $p_{\mathrm{T}}^{H} > 200$ GeV region of the electroweak $qq' \rightarrow Hqq'$ process is split into two regions of the invariant mass m_{jj} of the leading jets, $350 < m_{jj} < 700$ GeV and $m_{jj} > 700$ GeV. STXS measurements for these regions are not shown due to limited analysis sensitivity, but the splitting allows the inclusion of this analysis into combined measurements with other Higgs measurements in which these regions can be determined more precisely.

The resulting 44 STXS regions are listed in Figure 5.1. Additionally, the analysis is also expected to be sensitive to the cross sections of Higgs boson production in modes such as

---

[1] See Section 1.7 for more details about the STXS framework.

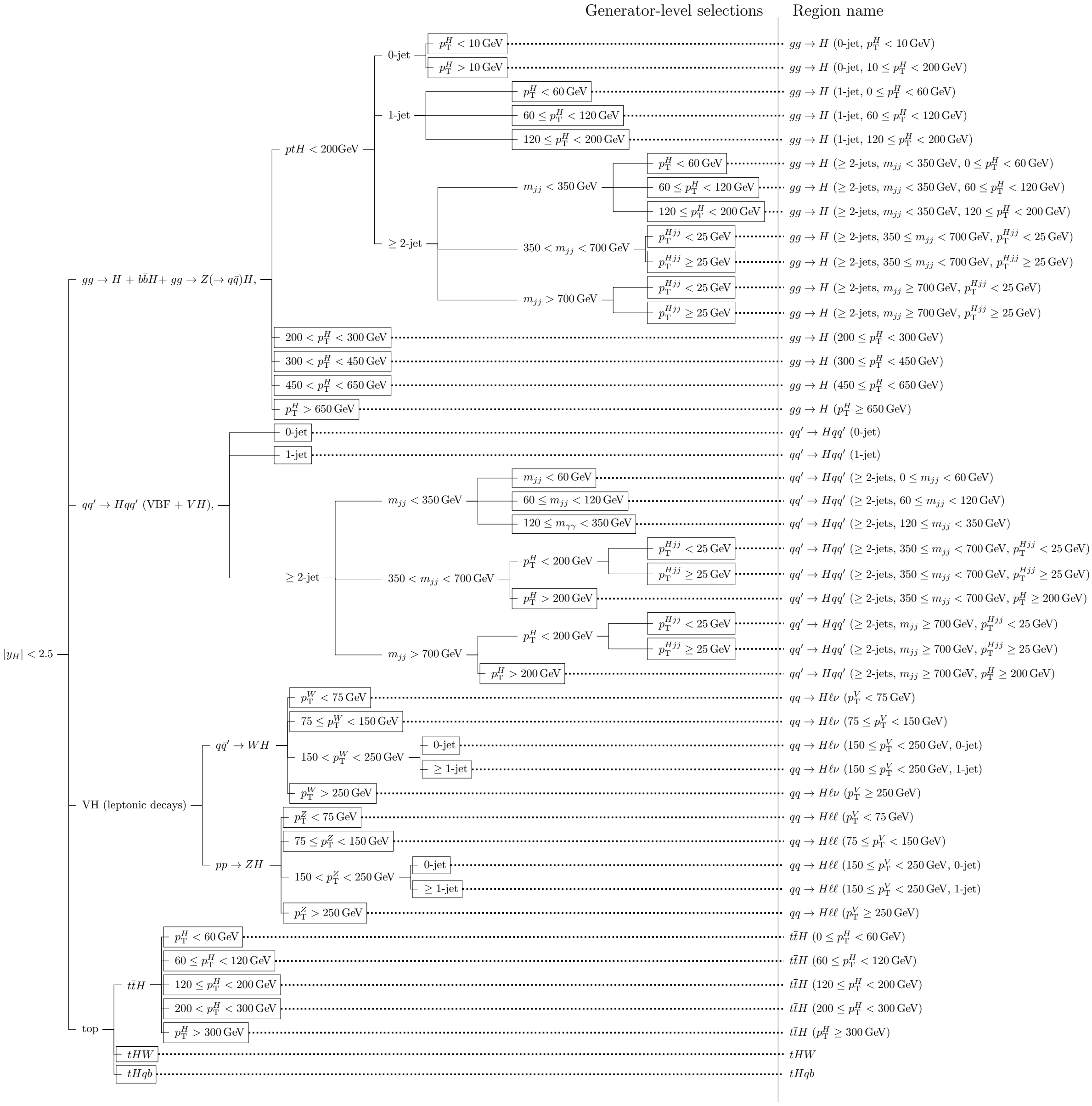

Figure 5.1: Summary of the STXS measurement regions considered in the analysis. The left part of the plot shows the selections applied on the generator-level quantities of simulated signal events, with the selections applied sequentially along the branches of the graph. The final selection for each region is indicated by a box, and the name of each region, used in the rest of this chapter, is shown on the right.

gluon-gluon fusion (ggF), vector-boson fusion (VBF), and associated production with a vector boson (VH where $V = W$ or Z), or a top quark pair (ttH), by considering combinations of STXS regions associated to each mode. A measurement of the total Higgs boson production cross-section in $|y_H| < 2.5$ is also reported using the same method.

The basic measurement parameters of the analysis are the products $(\sigma_i \times B_{\gamma\gamma})$ of the production cross-section σ_i in each STXS region i (or production mode i) and the branching ratio $B_{\gamma\gamma}$ of the $H \to \gamma\gamma$ decay.

5.1.1 Fit strategy

The signature of the Higgs boson in the diphoton final state is a narrow resonance with a width consistent with detector resolution rising above a smooth background in the diphoton invariant mass ($m_{\gamma\gamma}$) distribution. The diphoton mass resolution for such a resonance is typically between 1 GeV and 2 GeV, depending on the details of the photon reconstruction. The event rate of the Higgs boson signal can be extracted through fits of the $m_{\gamma\gamma}$ distribution.

The $m_{\gamma\gamma}$ distribution in each category is described by an extended probability density function (PDF) in which the signal and background shapes are analytic functions of $m_{\gamma\gamma}$, which are defined over the range of $105 \text{ GeV} < m_{\gamma\gamma} < 160 \text{ GeV}$. The likelihood function of the analysis is constructed by a simultaneous fit of the $m_{\gamma\gamma}$ distributions to their PDFs in the categories defined in Section 5.4. Systematic uncertainties related to signal yield and shape, as well as background modeling, are incorporated into the likelihood model as nuisance parameters. For each systematic nuisance parameter, a Gaussian or log-normal constraint PDF of the nuisance parameter is included in the likelihood function. The Gaussian constraint PDF is used for uncertainties relative to background modeling, as well as on the peak position of the signal $m_{\gamma\gamma}$ distribution. A log-normal constraint PDF is used for other uncertainties, including multiplicative uncertainties on expected signal yields and on the $m_{\gamma\gamma}$ mass resolution. An asymmetric log-normal form is used when the corresponding uncertainties are themselves asymmetric. The Higgs boson cross sections are parameters of the signal components in the likelihood model and can be determined by a maximum likelihood fit. The Higgs boson mass m_H is assumed to be 125.09 ± 0.24 GeV, as measured in Ref. [47].

In each category i, the normalization of the signal PDF is expressed as

$$N_i = \sum_t (\sigma_t \times B_{\gamma\gamma})\epsilon_{it}\mathcal{L}K_i(\theta_{\text{yield}}) + N_i^{\text{spur}}\theta_{\text{spur}} \tag{5.1}$$

where the sum runs over targeted truth regions, $(\sigma_t \times B_{\gamma\gamma})$ is the measurement parameter for region t, ϵ_{it} describes the efficiency for events from region t to be reconstructed in category i and it's computed using MC samples, and $\mathcal{L}$ is the integrated luminosity of the fitted sample. The factor $K_i(\theta_{\text{yield}})$ corresponds to multiplicative corrections to the signal yields from systematic effects detailed in Section 5.8, as a function of nuisance parameters collectively denoted by θ_{yield}; N_i^{spur} is the value of the background modeling uncertainty described in Section 5.7 below, implemented as an additive correction to the signal yield proportional to the nuisance parameter θ_{spur}.

5.2 Data and MC samples

5.2.1 Data

The study presented in this chapter uses a data set of $\sqrt{s} = 13$ TeV proton-proton collisions recorded by the ATLAS detector during the Run 2 period of the LHC. After data quality requirements [104] are applied to ensure the good working condition of all detector components, the data set amounts to an integrated luminosity of $139.0 \pm 2.4\,\text{fb}^{-1}$ [102, 103]. The mean number of interactions per bunch crossing was on average $\langle\mu\rangle = 33.7$ during Run 2. Events are selected by a diphoton trigger with transverse energy thresholds of 35 GeV and 25 GeV for the leading and subleading photon candidates, respectively [105], with photon identification selections based on calorimeter shower shape variables. In 2015–2016, a loose photon identification requirement was used in the trigger, and in 2017–2018, this requirement was tightened to cope with a higher instantaneous luminosity. On average, the trigger efficiency is greater than 98% for events that pass the diphoton event selection described in Section 5.3.

5.2.2 Monte Carlo simulation

Signal events for the ggF, VBF, and VH production modes are generated using Powheg [106–114], with the PDF4LHC15 PDF set [115], and interfaced to Pythia8 [116, 117] for parton showering, hadronization and underlying event using the AZNLO set of parameters that are tuned to data [118]. The ggF simulation achieves NNLO accuracy for arbitrary inclusive $gg \to H$ observables by reweighting the Higgs boson rapidity spectrum in Hj-MiNLO [112, 119, 120] to that of HNNLO [121]. The transverse momentum spectrum of the Higgs boson obtained with this sample is found to be compatible with the fixed-order HNNLO calculation and the Hres2.3 calculation [122, 123] performing resummation at next-to-next-to-leading-logarithm accuracy matched to a NNLO fixed-order calculation (NNLL+NNLO).

The ttH and bbH processes are modeled using the PowhegBox v2 [107–109, 114, 124] generator which provides matrix elements at next-to-leading order (NLO) in the strong coupling constant $\alpha_s$in the five-flavour scheme with the `NNPDF3.0nlo` [125] PDF set. For the ttH sample, the functional form of the renormalization and factorization scale is set to $\sqrt[3]{m_{\mathrm{T}}(t) \cdot m_{\mathrm{T}}(\bar{t}) \cdot m_{\mathrm{T}}(H)}$[2]. The generator is interfaced to Pythia8 .230 [117] using the A14 tune [126] and the `NNPDF2.3lo` [125] PDF set. The decays of bottom and charm hadrons are simulated using the EvtGen v1.6.0 program [127].

The $tHqb$ (tWH) samples are produced with MadGraph5_aMC@NLO in the four-flavour (five-flavour) scheme with the `NNPDF3.0nnlo` PDF [125]. The same flavour assumption is used in the matrix element calculation and the PDF. The top and W boson decays are handled by MadSpin [128] for the correct treatment of the spin correlations of the decay products. In the case of tWH the overlap of this process with ttH at NLO was removed following a diagram removal technique [129, 130]. The simulation of the parton shower, hadronization and underlying event is then performed by Pythia8 with the A14 set of tuned parameters [126] for both the $tHqb$ and tWH samples.

Alternative Higgs boson samples are also generated in order to estimate systematic uncertainties related to the modeling of the signal processes. For the ggF, VBF, and VH samples, after matrix element generation, events are also showered with Herwig 7.1.3 [131]. For the ttH process, the alternative parton showering is done with Herwig 7.0.4 [132]. The ggF process was also generated with MadGraph5_aMC@NLO. This simulation is accurate at NLO QCD for zero, one and two additional partons merged with the FxFx merging scheme [133, 134]. The events are showered using Pythia8 with the A14 tune.

All Higgs boson signal events are generated with a m_{H} (Higgs boson mass) of 125 GeV. The generated signal events are passed through a simulation of the ATLAS detector [135] using the Geant4 toolkit [136]. The cross-sections of Higgs production processes are reported for a center-of-mass energy of $\sqrt{s} = 13$ TeV and a Higgs boson with mass $m_H = 125.09$ GeV [47]. These cross-sections [25, 29, 31, 33, 42, 77, 130, 137–165], along with the Higgs boson branching ratio to diphotons (0.227%) [42, 166–171], are used to normalize the simulated signal events.

---

[2] m_{T} denotes the transverse mass of a particle, defined as $m_{\mathrm{T}} = \sqrt{M^2 + p_{\mathrm{T}}^2}$ where M and p_{T} are respectively its mass and transverse momentum.

Process	Generator	Showering	PDF set	σ [pb] $\sqrt{s} = 13$ TeV	Order of σ calculation
ggF	NNLOPS	Pythia8	PDF4LHC15	48.52	$\mathrm{N^3LO(QCD)+NLO(EW)}$
VBF	PowhegBox	Pythia8	PDF4LHC15	3.78	approximate-NNLO(QCD)+NLO(EW)
WH	PowhegBox	Pythia8	PDF4LHC15	1.37	NNLO(QCD)+NLO(EW)
$qq/qg \to ZH$	PowhegBox	Pythia8	PDF4LHC15	0.76	NNLO(QCD)+NLO(EW)
$gg \to ZH$	PowhegBox	Pythia8	PDF4LHC15	0.12	NLO(QCD)
ttH	PowhegBox	Pythia8	PDF4LHC15	0.51	NLO(QCD)+NLO(EW)
bbH	PowhegBox	Pythia8	PDF4LHC15	0.49	NNLO(QCD)
$tHqb$	MG5_aMC@NLO	Pythia8	`NNPDF3.0nnlo`	0.07	NLO(QCD)
tWH	MG5_aMC@NLO	Pythia8	`NNPDF3.0nnlo`	0.02	NLO(QCD)
$\gamma\gamma$	Sherpa	Sherpa	`NNPDF3.0nnlo`		
$V\gamma\gamma$	Sherpa	Sherpa	`NNPDF3.0nnlo`		
$t\bar{t}\gamma\gamma$	MG5_aMC@NLO	Pythia8	`NNPDF2.3lo`		

Table 5.1: Event generators and PDF sets used to model signal and background processes. The cross sections of Higgs production processes [25, 33, 42, 137, 143, 150–152, 154, 158–165, 186, 187] are reported for a center of mass energy of $\sqrt{s} = 13$ TeV and a SM Higgs with mass 125.09 GeV. The order of the calculated cross section is reported in each case. The cross sections for the background processes are omitted, because the background normalization is determined in fits to the data.

Prompt diphoton production ($\gamma\gamma$) is simulated with the Sherpa v2.2.4 [172] generator. In this setup, NLO-accurate matrix elements for up to one parton, and LO-accurate matrix elements for up to three partons are calculated with the Comix [173] and OpenLoops 1 [174–176] libraries. They are matched with the Sherpa parton shower [177] using the MEPS@NLO prescription [178–181] with a dynamic merging cut [182] of 10 GeV. Photons are required to be isolated according to a smooth-cone isolation criterion [183]. Samples are generated using the `NNPDF3.0nnlo` PDF set [125], along with the dedicated set of tuned parton-shower parameters developed by the Sherpa authors.

The production of $V\gamma\gamma$ events is simulated with the Sherpa v2.2.4 [172] generator. QCD LO-accurate matrix elements for up to one additional parton emission are matched and merged with the Sherpa parton shower based on the Catani-Seymour dipole factorization [173, 177] using the MEPS@LO prescription [178–181]. Samples are generated using the same PDF set and parton-shower parameters as the $\gamma\gamma$ sample.

The production of $t\bar{t}\gamma\gamma$ events is modelled using the MadGraph5_aMC@NLO v2.3.3 [133] generator at LO with the `NNPDF2.3lo` [125] parton distribution function (PDF). The treatment of parton showering and underlying event is the same as that of the ttH simulation.

The effect of multiple interactions in the same and neighboring bunch crossings (pileup) is modelled by overlaying simulated inelastic proton–proton (pp) events generated with Pythia8 .1 using the `NNPDF2.3lo` set of parton distribution functions (PDF) [184] and the A3 tune [185] over the original hard-scattering event.

A summary of the simulated signal and background samples is shown in Table 5.1.

5.3 Event selection

Events are selected by first requiring at least two photons[3] satisfying the *loose* identification preselection criteria. The two highest-p_{T} preselected photons are designated as the candidates for the diphoton system, and all other photon candidates are

---

[3] See Section 2.2.3 for more details on the reconstruction of photons and other physics objects.

discarded. The direction of these two photons, along with the reconstructed vertex information in the event, are used as inputs to a neural-network algorithm trained on simulation to determine the correct primary vertex [188]. This algorithm is shown to select the correct primary vertex (within 0.3 mm of the true vertex) in simulated gluon-fusion signal events 76% of the time. Its performance was validated using $Z \rightarrow ee$ events in data and simulation, ignoring the track information of the electrons and treating them as photon candidates [189]. The algorithm efficiency is in particular weakly dependent on the event pileup, and its residual dependence is well described by simulation. The two preselected photon candidates are required to satisfy the *tight* identification criteria and the isolation selection described above. Finally, the leading and subleading photon candidates are required to satisfy $p_{\mathrm{T}}/m_{\gamma\gamma} > 0.35$ and 0.25, respectively. Events that fail the tight identification or the isolation selection are used as control sample for background estimation and modeling purposes.

The trigger, object and event selection described above are used to define the events that are selected for further analysis for Higgs boson properties. In total, about 1.2 million events are selected in this data set with a diphoton invariant mass between 105 and 160 GeV. The predicted efficiency for a SM Higgs boson signal with $|y_H| < 2.5$, is 39%.

The background in the selected diphoton sample consists of the dominant continuum $\gamma\gamma$ production, γj and jj production where one or more jets in the event are misidentified as photons. These three types of processes are shown in Figure 5.2. Figure 5.3 shows the purity of the selected diphoton sample, defined as the fraction of $\gamma\gamma$ events, as a function of the mean number of interactions per bunch crossing, μ, using the method described in Section 5.7.

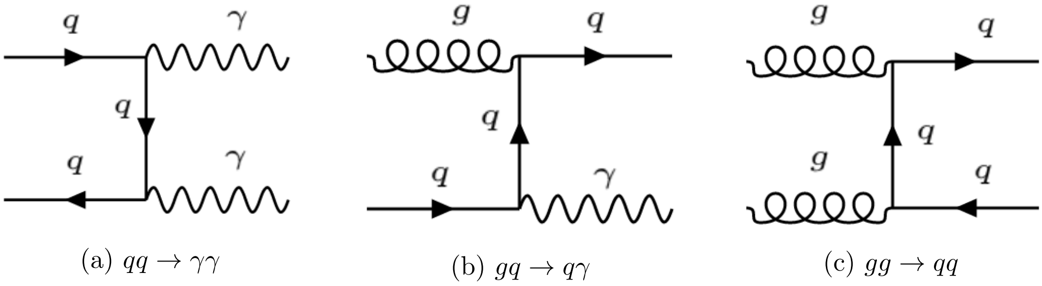

(a) $qq \rightarrow \gamma\gamma$ (b) $gq \rightarrow q\gamma$ (c) $gg \rightarrow qq$

Figure 5.2: Some Feynman diagrams at LO of the SM processes contributing to the diphoton background: (5.2a) two photons non-resonant production; (5.2b) a photon and a jet faking a photon in the final state; (5.2c) two jets that may fake photons in the detector.

5.4 Categorization

The events passing the selection described in Section 5.3 are classified into mutually exclusive event categories, each targeting a particular STXS region, using a technique covering all processes simultaneously and designed to maximize a global criterion of sensitivity to STXS parameters.

The technique proceeds in several steps. First, a multi-class boosted decision tree (BDT) is trained to separate signal events from different STXS regions using simulation samples of the Higgs boson events. This multiclass BDT classifier outputs one discriminant value for each STXS region. Then, the output discriminant values are

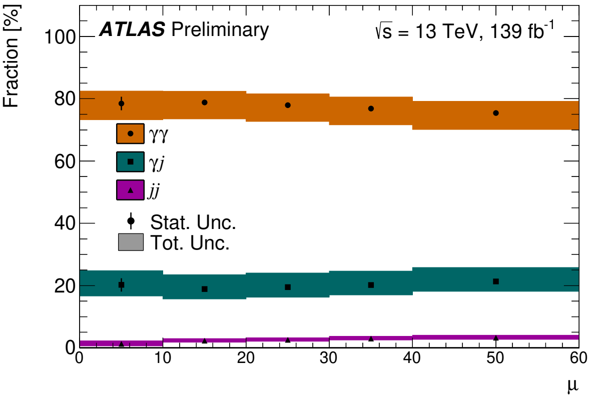

Figure 5.3: The purity of selected diphoton events, measured in bins of μ (the mean number of interactions per bunch crossing). The fraction of $\gamma\gamma$, γj and jj events in each μ region is measured using the procedure described in Section 5.7.

used to assign signal events into different *classes*. Each detector-level class is targeting events of an STXS region at the particle level. Finally, each class of events is further divided into multiple *categories* based on a binary BDT classifier. This binary BDT is trained to separate signal from continuum background in each class.

The inputs to all the BDTs are variables describing the kinematic and identification properties of the reconstructed particles presented in Section 2.2.3: the kinematics of the diphoton system; the number of reconstructed jets, b-jets, electrons, muons and top quarks; the kinematics of the system composed of the two photons and one or more jets, if jets are present, and of the system composed of the two leading jets in the event, if at least two jets are present; the kinematics of the reconstructed leptons and top quarks; the reconstruction score of the top quarks, computed from a BDT as described in Ref. [190], and other event quantities such as the missing transverse momentum. In order to avoid biases to the $m_{\gamma\gamma}$ distributions used in the statistical analysis, any variable found to have a linear correlation coefficient of 5% or more with $m_{\gamma\gamma}$ in the signal or background training samples is removed from the list of inputs. The training variables used in the analysis are summarized in Table 5.2.

The multiclass BDT used in the initial step of the classification is trained on a dataset obtained by merging the ggF, VBF, VH, ttH and tH signal samples described in Section 5.2.2. A weight is applied to the events in each STXS region so that the regions have equal event yields in the training sample. This configuration improves the performance of the discrimination. For each event, the output of the BDT consists of a set of class discriminants y_i, where the index i runs over the 44 STXS regions defined in the previous section. This output is then normalized into the parameters $z_i = \exp(y_i)/\sum_j \exp(y_j)$, a procedure also known as a softmax layer. The training is performed by minimizing the cross-entropy of the z_i with respect to the true STXS region assignments, using the LightGBM package [191].

To classify selected diphoton events, a set of per-class weights w_i are first optimized. Starting from the initial values $w_i = 1$, the weights are iteratively updated, using the following procedure: for a given set of w_i, events in each of the simulated signal samples listed above are assigned to an STXS class corresponding to the maximum value of

STXS regions	Multi-class BDT	STXS regions	Binary BDT
$gg \to H$	di-photon p_{T} and absolute rapidity; di-jet p_{T}, mass, Δy, $\Delta\phi$, $\Delta\eta$ between the 2 jets; p_{T}, mass of $\gamma\gamma + j$ and $\gamma\gamma + jj$, Δy, $\Delta\phi$ between $\gamma\gamma$ and jj, minimum ΔR between jets and photons, mass of the sum of all jets; di-lepton p_{T}, di-e or di-μ mass, E_{T}^{miss}, p_{T} of lepton + E_{T}^{miss}; p_T, η, ϕ, mass of top candidates; Number of jets, barrel jets ($\lvert\eta\rvert < 2.5$), b-jets and leptons; leading jet p_T, sum p_{T} of all jets $\sum E^{\mathrm{T}}$, E_{T}^{miss} significance; Average interaction per crossing, number of primary vertices	individual STXS regions from $gg \to H$ or $qq' \to Hqq'$	Multi-class BDT variables, and $\Delta\phi$, $\Delta\eta$ between the 2 photons ($\Delta\phi_{\gamma\gamma}$, $\Delta\eta_{\gamma\gamma}$); Number of electrons and muons; E_{T}^{miss}, $\sum E^{\mathrm{T}}$, E_{T}^{miss} significance, and E_{T}^{miss} azimuthal angle computed from hardest vertex; $\gamma\gamma$ $\vec{p}_{\mathrm{T}}$ projected to its thrust axis ($p_{\mathrm{Tt}}^{\gamma\gamma}$); Half difference between di-photon η and sum η of leading 2 jets (η^{Zepp}); $\phi^*_{\gamma\gamma} = \tan(\frac{\pi - \lvert\Delta\phi_{\gamma\gamma}\rvert}{2})\sqrt{1 - \tanh^2(\frac{\Delta\eta_{\gamma\gamma}}{2})}$ $\cos\theta^*_{\gamma\gamma} = \lvert\frac{(E^{\gamma_1}+p_z^{\gamma_1})\cdot(E^{\gamma_2}-p_z^{\gamma_2})-(E^{\gamma_1}-p_z^{\gamma_1})\cdot(E^{\gamma_2}+p_z^{\gamma_2})}{m_{\gamma\gamma}+\sqrt{(m_{\gamma\gamma}^2+(p_{\mathrm{T}}^{\gamma\gamma})^2)}}\rvert$
$qq' \to Hqq'$			
$qq \to H\ell\nu$		WH STXS regions combined	$p_{\mathrm{T}}/m_{\gamma\gamma}$, η, ϕ of 2 leading photons; p_{T}, η, ϕ of 2 leading leptons; E_{T}^{miss}, E_{T}^{miss} significance, E_{T}^{miss} azimuthal angle; Whether or not the E_{T}^{miss} built from di-photon vertex is larger than that built from the hardest vertex by more than 30 GeV; di-lepton mass, and transverse mass of lepton + E_{T}^{miss}
$qq \to H\ell\ell$		ZH STXS regions combined	
$t\bar{t}H$		$t\bar{t}H$ STXS regions combined	p_{T}, η, ϕ of 2 leading photons; p_{T}, η, ϕ and B-tagging scores of 6 leading jets; E_{T}^{miss}, E_{T}^{miss} significance, E_{T}^{miss} azimuthal angle; Top reconstruction BDT scores
tH		tWH, $tHqb$	

Table 5.2: List of training variables used for the multiclass BDT and the binary BDTs.

$w_i z_i$. A simulated dataset is then produced for each region by mixing the events from each signal sample in the proportions of their SM production cross sections, together with a sample of simulated continuum background events normalized to data in the control region $95 < m_{\gamma\gamma} < 105$ GeV. A simplified statistical model approximating the full model used to get the final results is then used to obtain the covariance matrix C of the measured event yields in each region. The weights are then adjusted until the determinant $|C|$ is minimized. This *D-optimality* (determinant) criterion leads in particular to a reduction of the measurement uncertainties, and is suggested by the fact that $|C|^{-1}$ is a known measure of the information provided by the measurement [192]. The final set of weights w_i are used to classify events as originating from STXS region i if that classification provides the maximum value of $w_i z_i$. This procedure results in one detector-level class of events for each STXS region.

Figure 5.4 shows the multiclass discriminant distributions for four representative STXS classes. Compared to the simple selection based on the z_i alone, the selection based on the $w_i z_i$ provides a higher purity for classes associated with rare processes such as tH , ttH, VH and VBF, as well as for production at high values of p_{T}^H or m_{jj}.

This multiclass training allows the selection of target process events that otherwise would fail a requirement based on detector level quantities corresponding to the STXS region definition. For example, in the STXS region $gg \to H$ (1-jet, $p_{\mathrm{T}}^H < 60$ GeV), detector-level events that are from the target process but have no reconstructed jets would fail requirements defined by the number of jets and p_{T}^H, however, those events could be selected by the multiclass discriminant. For this STXS region, 20% of events from the target process have no reconstructed jets. The recovery of these results leads a reduction of about 6% in the measurement uncertainty. It is also robust against pileup in the determination of jet multiplicity in $gg \to H$. This leads to measurements with generally smaller uncertainties and lower correlations.

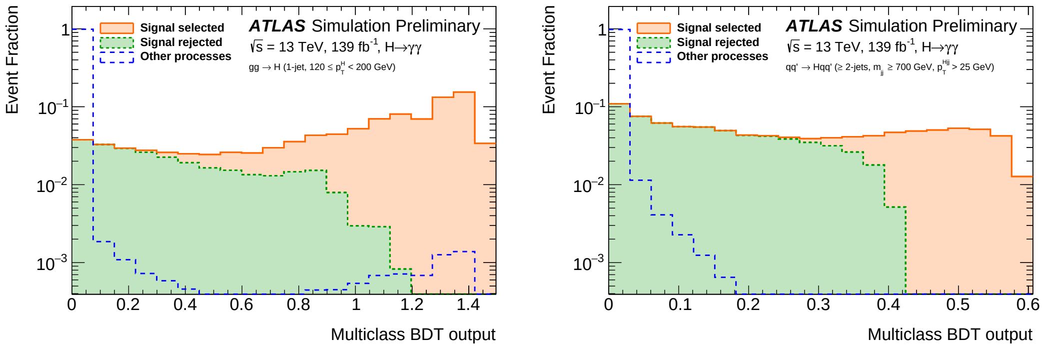

(a) $gg \to H$ (1-jet, $120 \le p_{\mathrm{T}}^{H} \le 200$ GeV) (b) $qq' \to Hqq'$ ($\geq$ 2-jets, $m_{jj} > 700$ GeV, $p_{\mathrm{T}}^{Hjj} > 25$ GeV)

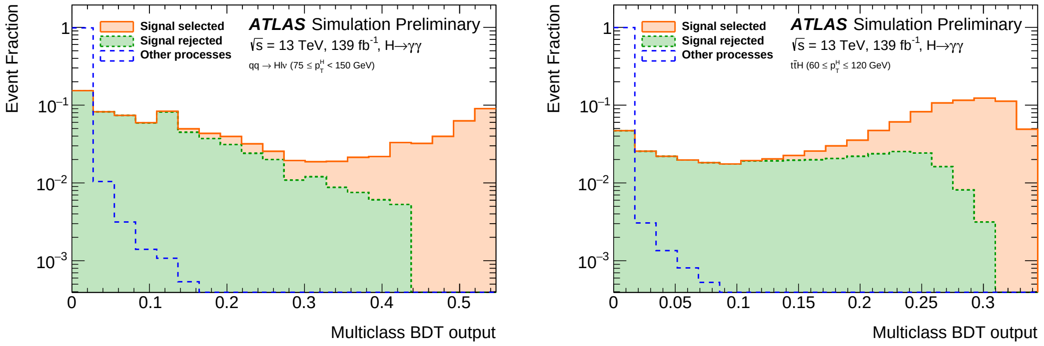

(c) $qq \to H\ell\nu$ ($75 \le p_{\mathrm{T}}^{H} < 150$ GeV) (d) ttH ($60 \le p_{\mathrm{T}}^{H} < 120$ GeV)

Figure 5.4: Multiclass discriminant output distributions for four representative STXS classes. In each plot, the multiclass discriminant distribution is shown separately for events corresponding to the target STXS region (solid line) and events in other STXS regions (long-dashed). The target STXS region is further broken down into the subset of events passing the multiclass selection at detector level (orange-solid), and the subset of events that fail this selection (green-dashed). The orange-solid component is stacked on top of the dashed component.

After the classes are defined, binary BDT classifiers are then trained and used to further divide each class into multiple categories, to improve the measurement sensitivity. For each of the classes targeting $gg \to H$ and $qq' \to Hqq'$ processes, a binary BDT classifier is trained between simulated signal events of the corresponding STXS region and both simulated continuum background events and Higgs boson events from other STXS regions. The remaining classes are split into two groups: one targeting WH and ZH processes and the other targeting ttH and tH processes. For each of these two class groups, a single binary BDT classifier is trained between simulated signal events of the corresponding production process and background events. This merging of classes is only implemented for the binary BDT training and is needed to improve the statistics of the background training sample. The background training samples for these two binary classifiers are taken from a data control region defined by reversing the photon identification and/or isolation requirement.

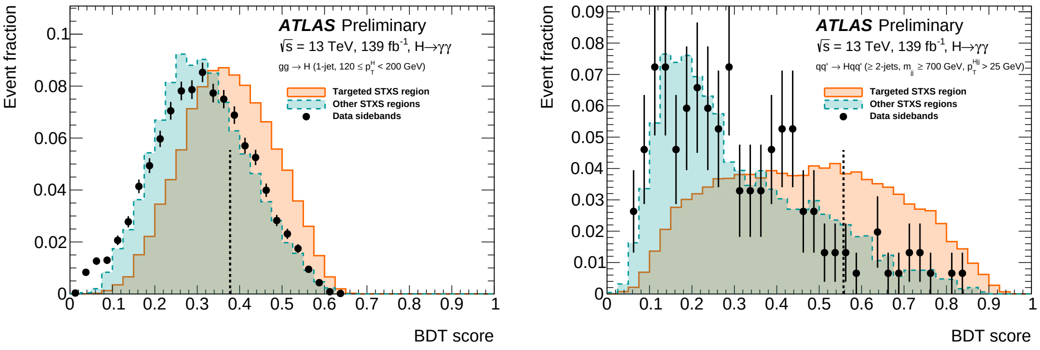

(a) $gg \to H$ (1-jet, $120 \leq p_{\mathrm{T}}^{H} < 200$ GeV) (b) $qq' \to Hqq'$ ($\geq$ 2-jets, $m_{jj} > 700$ GeV, $p_{\mathrm{T}}^{Hjj} > 25$ GeV)

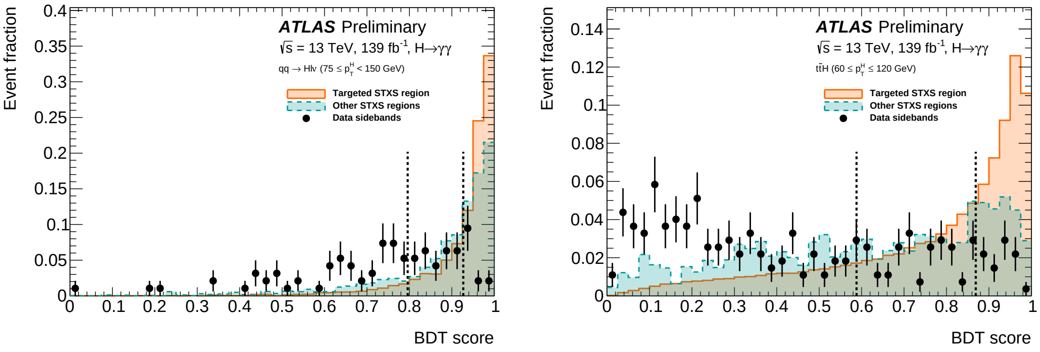

(c) $qq \to H\ell\nu$ ($75 \leq p_{\mathrm{T}}^{H} < 150$ GeV) (d) ttH ($60 \leq p_{\mathrm{T}}^{H} < 120$ GeV)

Figure 5.5: Binary BDT discriminant distributions in four representative STXS classes. For each class, the binary BDT discriminant distribution is shown for the target STXS region (solid), other STXS regions (dashed), and background (dots) represented by the events in the diphoton mass sidebands ($105 < m_{\gamma\gamma} < 120$ GeV or $130 < m_{\gamma\gamma} < 160$ GeV). The vertical lines delimit categories used in the analysis for each class.

In each class, events are then classified into categories corresponding to ranges of binary BDT output values. Up to three categories are defined in this way, depending on the targeted STXS region. The boundary positions in the BDT output are determined by scanning over all possible values and finding the set that maximizes the sum in quadrature of the expected significance values in all categories. The expected

Category	S	B	f	Z
$gg \to H$ (0-jet, $p_{\mathrm{T}}^{H} < 10$ GeV)	730	24000	0.03	4.6
$gg \to H$ (0-jet, $10 \leq p_{\mathrm{T}}^{H} < 200$ GeV)	2200	66000	0.03	8.4
$gg \to H$ (1-jet, $p_{\mathrm{T}}^{H} < 60$ GeV)	550	16000	0.03	4.4
$gg \to H$ (1-jet, $60 \leq p_{\mathrm{T}}^{H} < 120$ GeV)	470	10000	0.04	4.7
$gg \to H$ (1-jet, $120 \leq p_{\mathrm{T}}^{H} < 200$ GeV), High-purity	37	250	0.13	2.3
$gg \to H$ (1-jet, $120 \leq p_{\mathrm{T}}^{H} < 200$ GeV), Med-purity	50	620	0.07	2.0
$gg \to H$ ($\geq$ 2-jets, $m_{jj} < 350$ GeV, $p_{\mathrm{T}}^{H} < 60$ GeV), High-purity	39	1200	0.03	1.1
$gg \to H$ ($\geq$ 2-jets, $m_{jj} < 350$ GeV, $p_{\mathrm{T}}^{H} < 60$ GeV), Med-purity	120	5300	0.02	1.6
$gg \to H$ ($\geq$ 2-jets, $m_{jj} < 350$ GeV, $p_{\mathrm{T}}^{H} < 60$ GeV), Low-purity	490	19000	0.03	3.6
$gg \to H$ ($\geq$ 2-jets, $m_{jj} < 350$ GeV, $60 \leq p_{\mathrm{T}}^{H} < 120$ GeV), High-purity	36	370	0.09	1.8
$gg \to H$ ($\geq$ 2-jets, $m_{jj} < 350$ GeV, $60 \leq p_{\mathrm{T}}^{H} < 120$ GeV), Med-purity	110	2300	0.05	2.2
$gg \to H$ ($\geq$ 2-jets, $m_{jj} < 350$ GeV, $60 \leq p_{\mathrm{T}}^{H} < 120$ GeV), Low-purity	230	7000	0.03	2.7
$gg \to H$ ($\geq$ 2-jets, $m_{jj} < 350$ GeV, $120 \leq p_{\mathrm{T}}^{H} < 200$ GeV), High-purity	44	220	0.17	2.9
$gg \to H$ ($\geq$ 2-jets, $m_{jj} < 350$ GeV, $120 \leq p_{\mathrm{T}}^{H} < 200$ GeV), Med-purity	70	830	0.08	2.4
$gg \to H$ ($\geq$ 2-jets, $350 \leq m_{jj} < 700$ GeV, $p_{\mathrm{T}}^{Hjj} < 25$ GeV), High-purity	4.1	17	0.19	0.9
$gg \to H$ ($\geq$ 2-jets, $350 \leq m_{jj} < 700$ GeV, $p_{\mathrm{T}}^{Hjj} < 25$ GeV), Med-purity	15	110	0.12	1.4
$gg \to H$ ($\geq$ 2-jets, $350 \leq m_{jj} < 700$ GeV, $p_{\mathrm{T}}^{Hjj} < 25$ GeV), Low-purity	16	380	0.04	0.8
$gg \to H$ ($\geq$ 2-jets, $350 \leq m_{jj} < 700$ GeV, $p_{\mathrm{T}}^{Hjj} \geq 25$ GeV), High-purity	5.7	40	0.12	0.9
$gg \to H$ ($\geq$ 2-jets, $350 \leq m_{jj} < 700$ GeV, $p_{\mathrm{T}}^{Hjj} \geq 25$ GeV), Med-purity	20	270	0.07	1.2
$gg \to H$ ($\geq$ 2-jets, $350 \leq m_{jj} < 700$ GeV, $p_{\mathrm{T}}^{Hjj} \geq 25$ GeV), Low-purity	22	930	0.02	0.7
$gg \to H$ ($\geq$ 2-jets, $m_{jj} \geq 700$ GeV, $p_{\mathrm{T}}^{Hjj} < 25$ GeV), High-purity	4.4	9.0	0.33	1.4
$gg \to H$ ($\geq$ 2-jets, $m_{jj} \geq 700$ GeV, $p_{\mathrm{T}}^{Hjj} < 25$ GeV), Med-purity	14	40	0.26	2.1
$gg \to H$ ($\geq$ 2-jets, $m_{jj} \geq 700$ GeV, $p_{\mathrm{T}}^{Hjj} < 25$ GeV), Low-purity	16	150	0.10	1.3
$gg \to H$ ($\geq$ 2-jets, $m_{jj} \geq 700$ GeV, $p_{\mathrm{T}}^{Hjj} \geq 25$ GeV), High-purity	5.1	33	0.14	0.9
$gg \to H$ ($\geq$ 2-jets, $m_{jj} \geq 700$ GeV, $p_{\mathrm{T}}^{Hjj} \geq 25$ GeV), Med-purity	14	150	0.09	1.1
$gg \to H$ ($\geq$ 2-jets, $m_{jj} \geq 700$ GeV, $p_{\mathrm{T}}^{Hjj} \geq 25$ GeV), Low-purity	16	380	0.04	0.8
$gg \to H$ ($200 \leq p_{\mathrm{T}}^{H} < 300$ GeV), High-purity	7.2	11	0.40	2.0
$gg \to H$ ($200 \leq p_{\mathrm{T}}^{H} < 300$ GeV), Med-purity	28	84	0.25	2.9
$gg \to H$ ($200 \leq p_{\mathrm{T}}^{H} < 300$ GeV), Low-purity	28	210	0.12	1.9
$gg \to H$ ($300 \leq p_{\mathrm{T}}^{H} < 450$ GeV), High-purity	1.7	1.8	0.49	1.1
$gg \to H$ ($300 \leq p_{\mathrm{T}}^{H} < 450$ GeV), Med-purity	7.1	10	0.41	2.0
$gg \to H$ ($300 \leq p_{\mathrm{T}}^{H} < 450$ GeV), Low-purity	17	63	0.21	2.1
$gg \to H$ ($450 \leq p_{\mathrm{T}}^{H} < 650$ GeV), High-purity	1.9	1.4	0.58	1.4
$gg \to H$ ($450 \leq p_{\mathrm{T}}^{H} < 650$ GeV), Med-purity	2.1	7.5	0.22	0.7
$gg \to H$ ($p_{\mathrm{T}}^{H} \geq 650$ GeV), High-purity	0.72	1.0	0.42	0.7
$gg \to H$ ($p_{\mathrm{T}}^{H} \geq 650$ GeV), Med-purity	0.21	1.1	0.17	0.2
$qq' \to Hqq'$ (0-jet), High-purity	0.32	3.9	0.08	0.2
$qq' \to Hqq'$ (0-jet), Med-purity	0.60	8.1	0.07	0.2
$qq' \to Hqq'$ (1-jet), High-purity	1.9	2.3	0.45	1.1
$qq' \to Hqq'$ (1-jet), Med-purity	2.4	4.8	0.33	1.0
$qq' \to Hqq'$ (1-jet), Low-purity	4.9	33	0.13	0.8
$qq' \to Hqq'$ ($\geq$ 2-jets, $m_{jj} < 60$ GeV), High-purity	0.61	1.8	0.25	0.4
$qq' \to Hqq'$ ($\geq$ 2-jets, $m_{jj} < 60$ GeV), Med-purity	2.0	8.1	0.20	0.7
$qq' \to Hqq'$ ($\geq$ 2-jets, $m_{jj} < 60$ GeV), Low-purity	5.9	52	0.10	0.8
$qq' \to Hqq'$ ($\geq$ 2-jets, $60 \leq m_{jj} < 120$ GeV), High-purity	5.3	6.1	0.46	1.9
$qq' \to Hqq'$ ($\geq$ 2-jets, $60 \leq m_{jj} < 120$ GeV), Med-purity	6.9	32	0.18	1.2
$qq' \to Hqq'$ ($\geq$ 2-jets, $120 \leq m_{jj} < 350$ GeV), High-purity	0.91	3.0	0.23	0.5
$qq' \to Hqq'$ ($\geq$ 2-jets, $120 \leq m_{jj} < 350$ GeV), Med-purity	14	87	0.14	1.4
$qq' \to Hqq'$ ($\geq$ 2-jets, $120 \leq m_{jj} < 350$ GeV), Low-purity	27	380	0.07	1.4
$qq' \to Hqq'$ ($\geq$ 2-jets, $350 \leq m_{jj} < 700$ GeV, $p_{\mathrm{T}}^{Hjj} < 25$ GeV), High-purity	3.1	3.0	0.51	1.6
$qq' \to Hqq'$ ($\geq$ 2-jets, $350 \leq m_{jj} < 700$ GeV, $p_{\mathrm{T}}^{Hjj} < 25$ GeV), Med-purity	12	51	0.19	1.6
$qq' \to Hqq'$ ($\geq$ 2-jets, $350 \leq m_{jj} < 700$ GeV, $p_{\mathrm{T}}^{Hjj} \geq 25$ GeV), High-purity	1.3	1.8	0.42	0.9
$qq' \to Hqq'$ ($\geq$ 2-jets, $350 \leq m_{jj} < 700$ GeV, $p_{\mathrm{T}}^{Hjj} \geq 25$ GeV), Med-purity	0.42	4.7	0.08	0.2
$qq' \to Hqq'$ ($\geq$ 2-jets, $m_{jj} \geq 700$ GeV, $p_{\mathrm{T}}^{Hjj} < 25$ GeV), High-purity	9.0	1.8	0.83	4.5
$qq' \to Hqq'$ ($\geq$ 2-jets, $m_{jj} \geq 700$ GeV, $p_{\mathrm{T}}^{Hjj} < 25$ GeV), Med-purity	18	22	0.45	3.5
$qq' \to Hqq'$ ($\geq$ 2-jets, $m_{jj} \geq 700$ GeV, $p_{\mathrm{T}}^{Hjj} \geq 25$ GeV), High-purity	1.5	1.7	0.47	1.0
$qq' \to Hqq'$ ($\geq$ 2-jets, $m_{jj} \geq 700$ GeV, $p_{\mathrm{T}}^{Hjj} \geq 25$ GeV), Med-purity	2.4	3.4	0.42	1.2
$qq' \to Hqq'$ ($\geq$ 2-jets, $m_{jj} \geq 700$ GeV, $p_{\mathrm{T}}^{Hjj} \geq 25$ GeV), Low-purity	6.5	20	0.24	1.4
$qq' \to Hqq'$ ($\geq$ 2-jets, $350 \leq m_{jj} < 700$ GeV, $p_{\mathrm{T}}^{H} \geq 200$ GeV), High-purity	1.6	1.3	0.55	1.2
$qq' \to Hqq'$ ($\geq$ 2-jets, $350 \leq m_{jj} < 700$ GeV, $p_{\mathrm{T}}^{H} \geq 200$ GeV), Med-purity	0.55	2.0	0.22	0.4
$qq' \to Hqq'$ ($\geq$ 2-jets, $m_{jj} \geq 700$ GeV, $p_{\mathrm{T}}^{H} \geq 200$ GeV), High-purity	8.1	1.6	0.83	4.3
$qq' \to Hqq'$ ($\geq$ 2-jets, $m_{jj} \geq 700$ GeV, $p_{\mathrm{T}}^{H} \geq 200$ GeV), Med-purity	7.6	11	0.42	2.1
Other $qq \to H\ell\nu$	7.7	210	0.04	0.5
$qq \to H\ell\nu$ ($0 \leq p_{\mathrm{T}}^{V} < 75$ GeV), High-purity	2.3	3.5	0.40	1.1
$qq \to H\ell\nu$ ($0 \leq p_{\mathrm{T}}^{V} < 75$ GeV), Med-purity	6.3	39	0.14	1.0
$qq \to H\ell\nu$ ($75 \leq p_{\mathrm{T}}^{V} < 150$ GeV), High-purity	3.7	1.8	0.67	2.2
$qq \to H\ell\nu$ ($75 \leq p_{\mathrm{T}}^{V} < 150$ GeV), Med-purity	1.3	4.8	0.21	0.6
$qq \to H\ell\nu$ ($150 \leq p_{\mathrm{T}}^{V} < 250$ GeV, 0-jet)	1.8	1.9	0.48	1.1
$qq \to H\ell\nu$ ($150 \leq p_{\mathrm{T}}^{V} < 250$ GeV, 1-jet)	2.2	2.3	0.49	1.3
$qq \to H\ell\nu$ ($p_{\mathrm{T}}^{V} \geq 250$ GeV)	1.5	1.2	0.56	1.2
Other $qq \to H\ell\ell$	11	280	0.04	0.6
$qq \to H\ell\ell$ ($0 \leq p_{\mathrm{T}}^{V} < 75$ GeV)	0.9	1.8	0.32	0.6
$qq \to H\ell\ell$ ($75 \leq p_{\mathrm{T}}^{V} < 150$ GeV), High-purity	3.2	3.9	0.45	1.4
$qq \to H\ell\ell$ ($75 \leq p_{\mathrm{T}}^{V} < 150$ GeV), Med-purity	5.6	21	0.21	1.2
$qq \to H\ell\ell$ ($150 \leq p_{\mathrm{T}}^{V} < 250$ GeV, 0-jet)	1.6	2.1	0.42	1.0
$qq \to H\ell\ell$ ($150 \leq p_{\mathrm{T}}^{V} < 250$ GeV, 1-jet)	1.7	3.2	0.35	0.9
$qq \to H\ell\ell$ ($p_{\mathrm{T}}^{V} \geq 250$ GeV)	1.8	2.0	0.47	1.1
Other tH or ttH	11	120	0.08	1.0
ttH ($p_{\mathrm{T}}^{H} < 60$ GeV), High-purity	3.2	5.0	0.39	1.3
ttH ($p_{\mathrm{T}}^{H} < 60$ GeV), Med-purity	3.5	15	0.18	0.8
ttH ($60 \leq p_{\mathrm{T}}^{H} < 120$ GeV), High-purity	5.1	4.3	0.54	2.1
ttH ($60 \leq p_{\mathrm{T}}^{H} < 120$ GeV), Med-purity	3.7	10	0.26	1.1
ttH ($120 \leq p_{\mathrm{T}}^{H} < 200$ GeV), High-purity	6.1	3.8	0.62	2.6
ttH ($120 \leq p_{\mathrm{T}}^{H} < 200$ GeV), Med-purity	3.1	8.1	0.28	1.0
ttH ($200 \leq p_{\mathrm{T}}^{H} < 300$ GeV)	4.6	1.7	0.73	2.7
ttH ($p_{\mathrm{T}}^{H} \geq 300$ GeV)	3.6	1.0	0.78	2.6
tHW	0.80	2.4	0.25	0.5
$tHqb$	0.88	2.7	0.24	0.5

Table 5.3: For each event category, values of the expected signal (S) and background (B) yields within the smallest mass window containing 90% of signal events, and corresponding estimates of the signal purity $f = S/(S+B)$ and the expected significance $Z = \sqrt{2((S+B)\log(1+S/B)-S)}$. S includes contribution from all Higgs boson events.

significance is computed as $Z = \sqrt{2((S+B)\ln(1+S/B)-S)}$, where S and B are the expected signal of the targeted STXS region and background yields in a range of $m_{\gamma\gamma}$ around the expected Higgs boson signal peak. The background B includes contributions from continuum background and Higgs boson events from other STXS regions. The continuum background is computed from the $m_{\gamma\gamma}$ distribution in simulation, normalized to the data control region $95 < m_{\gamma\gamma} < 105$ GeV. A class is split into two categories if it leads to an improvement of more than 5% in the expected significance, and into three categories if a further improvement of at least 5% with respect to the two-category configuration can be achieved. Figure 5.5 shows binary BDT discriminant distributions as well as category boundaries for four representative STXS classes.

In this process, some events may fail to enter the final categories and are grouped into three *unselected* categories, corresponding to events from $qq \to H\ell\nu$and $pp \to ZH$; ttH; and tH classes. These categories only contribute weakly to the overall sensitivity, but the separation leads to higher signal purity in the other VH, ttH and tH categories.

The procedure results in the definition of 88 categories in total. The expected signal and background yields of these categories are summarized in Table 5.3. The expected signal purity, defined as the expected signal yield over the expected yield from both signal and background processes, in a $m_{\gamma\gamma}$ window containing 90% of signal events, ranges from 3% to 83%. The contribution of each STXS region to the expected event yields in each category are presented in Figure 5.6.

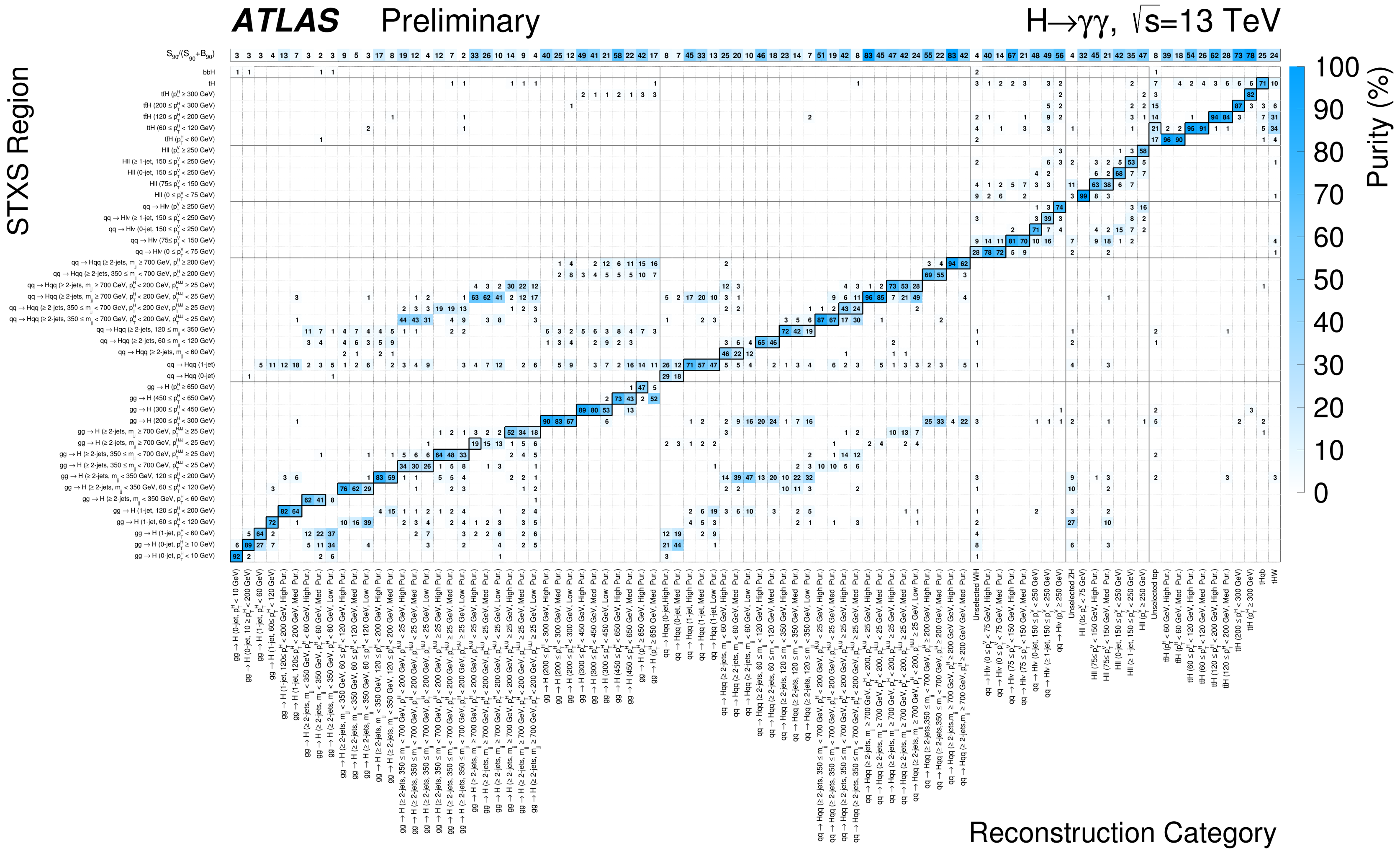

Figure 5.6: Contribution of STXS regions in the expected event yields to each reconstruction category. The top row corresponds to the value of $S_{90}/(S_{90}+B_{90})$ in each category, where S_{90} and B_{90} are respectively the total number of signal (including all STXS regions) and background events expected in the smallest $m_{\gamma\gamma}$ range containing 90% of the signal yield. Other entries correspond to the percentage fraction for the contribution of a given STXS region (on the y-axis) to the Higgs boson signal yield in a given reconstruction category (on the x-axis). Entries for the STXS regions targeted by each reconstruction category are outlined in black if the corresponding value is above 15%. Entries with a value below 1% are not shown. The entries in each column, corresponding to the same reconstruction category, sum up to 100 (%), except for rounding effects and values below 1%.

5.4.1 Photon performance and category resolution

In the current categorization, photon η and photon conversion status are not explicitly used to define categories with simple cuts. In the past iteration of the analysis [193], two categories, "ggH 0J CEN" and "ggH 0J FWD", are explicitly defined according to the η of the two photons: central photons (both photons $|\eta| < 0.95$) or forward photons (at least one photon $|\eta| > 0.95$), respectively. The goal of this separation was to improve the sensitivity in the ggH zero-jet truth bin. In this section, I verify whether a similar improvement in sensitivity is actually achieved by the binary BDT of the current categorization, which indeed is able to learn how to select events with a better diphoton invariant mass resolution starting from the available input variables.

Binary BDT behavior

In this section the "true" diphoton relative invariant mass resolution is defined as:

$$\frac{m_{\gamma\gamma}^{\text{Reco}} - m_{\gamma\gamma}^{\text{Truth}}}{m_{\gamma\gamma}^{\text{Truth}}} \tag{5.2}$$

where $m_{\gamma\gamma}^{\text{Reco}}$ and $m_{\gamma\gamma}^{\text{Truth}}$ are the invariant mass of the two photons at Reco-level and at Truth-level, respectively.

Figure 5.7 plots the standard deviation of the relative invariant mass resolution for all the categories[4]. It clearly shows how the binary BDTs separate events coming from the same STXS bin into two (or more) reco categories with improving resolution: tight categories (marked with `__0`) (almost) always have a smaller standard deviation with respect to the loose or very loose categories (marked with `__1` or `__2`) of the same kind. The behavior of the binary BDT in this respect is then well understood: it orders events coming from the same physics process (e.g. same STXS bin) in a way similar to an explicit η separation.

Comparison with an explicit cut-based categorization

One could wonder how the baseline categorization for the analysis compares in terms of resolution with respect to a similar categorization where simple cuts are applied to define a tight/loose selection in place of the binary BDT output. Three possible scenarios have been investigated:

- **η-based cuts:** if both photons have $|\eta| < 0.95$, the event is classified in the Central category, otherwise in the Forward category;
- **Conversion-based cuts:** if both photons are unconverted, the event is classified in the Unconverted category, otherwise in the Converted category;
- **η-conversion-based cuts:** both the Central/Forward and the Unconverted/Converted selections are applied in sequence.

These alternative categorizations are implemented in the simple case where the simple cuts are applied to the reco categories targeting the ggH 0-jets process only: all the other categories and the multiclass pre-selection step are the same as the baseline.

The comparison in resolution between the categorizations is shown in Figure 5.8. The resolution of the binary BDT tight categories is at the same level of the one

---

[4] The study presented in this section was performed with an early version of the categories, which don't correspond exactly to the 88 categories used in the final analysis. However, since the optimization method is the same, the conclusions of this study still hold.

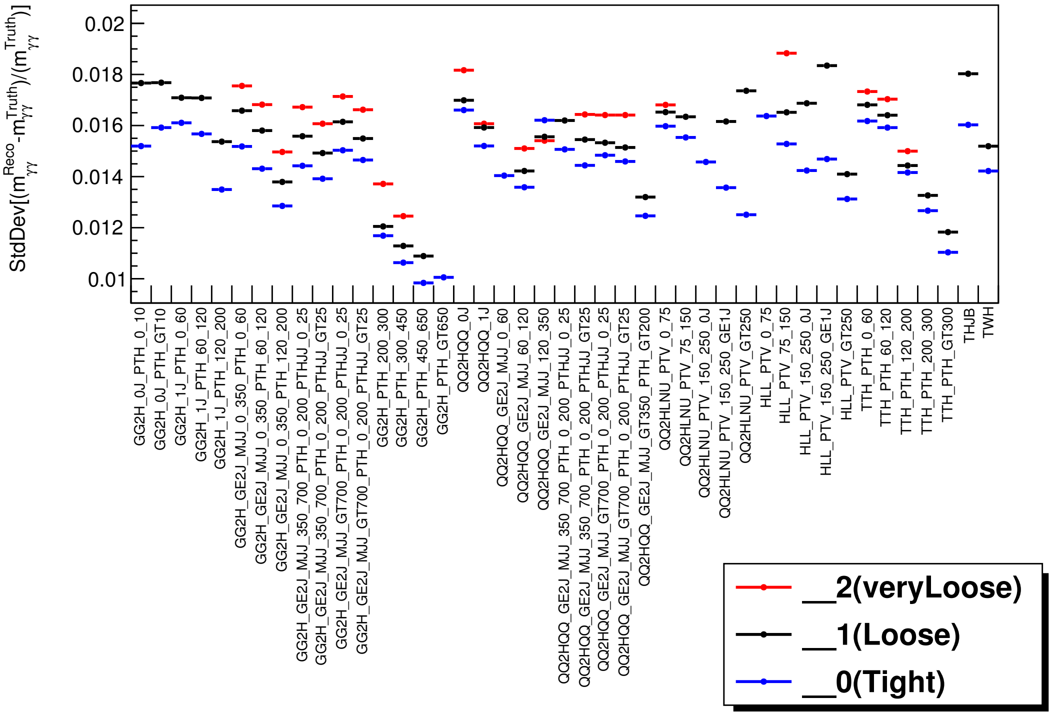

Figure 5.7: Relative invariant mass resolution as a function of the categorization.

	Stat-only error on μ			
	Baseline	wEtaCuts	wConvCuts	wEtaConvCuts
ggH	7.85e-02	7.68e-02	7.84e-02	7.60e-02
VBF	1.69e-01	1.70e-01	1.70e-01	1.70e-01
WH	4.08e-01	4.10e-01	4.10e-01	4.10e-01
ZH	6.34e-01	6.36e-01	6.35e-01	6.33e-01
top	2.50e-01	2.53e-01	2.52e-01	2.51e-01

Table 5.4: All 5 POIs floating.

obtained if using simple cuts; the gap in resolution is larger with Central/Forward or Unconverted/Converted selection than with binary BDT selection.

In order to obtain a more quantitative comparison, these categorizations have been used to perform a statistical-only fit to an Asimov dataset [194] generated under the SM hypothesis ($\mu = 1$). The results of the fit with a 5 POI scheme (i.e. five production modes: ggH, VBF, WH, ZH and top) are shown in Table 5.4 and in Table 5.5, while those obtained with only μ_{ggH} allowed to float are in Table 5.6 and in Table 5.7.

The sensitivity to ggH is improved by +3.18% when using the alternative categorization with a combination of η and conversion cuts, at little expenses of the other POIs with μ_{VBF} being the most penalized one -0.59%. When all other POIs are fixed to 1, thus fitting only ggH, the ggH improvement is +3.55%. The potential sensitivity gain on the ggH POI if an explicit η-conversion categorization was used is therefore relatively minor. The categorization based on binary BDTs is retained as the baseline categorization of the analysis.

	Relative difference wrt Baseline		
	wEtaCuts	wConvCuts	wEtaConvCuts
ggH	+2.17%	+0.13%	+3.18%
VBF	-0.59%	-0.59%	-0.59%
WH	-0.49%	-0.49%	-0.49%
ZH	-0.32%	-0.16%	+0.16%
top	-1.20%	-0.80%	-0.40%

Table 5.5: All 5 POIs floating.

	Stat-only error on μ			
	Baseline	wEtaCuts	wConvCuts	wEtaConvCuts
ggH	7.61e-02	7.34e-02	7.50e-02	7.36e-02

Table 5.6: Only μ_{ggH} floating.

5.5 Alternative categorization for EWqqH and ggH events

An alternative categorization which aims to target electroweak qqH and ggH STXS regions has been developed and is presented in this section. This classification method was designed to be applied within the sequential approach already used in Ref.[193]. Events not satisfying the selection requirements of the ttH, tH or VH-leptonic categories but passing the baseline diphoton selections are processed by this method which strongly relies on Deep Learning. First, a multiclassification is performed by a Recurrent Neural Network (RNN) in order to split the events into reco categories matching the targeted STXS scheme. Then, in each reco category defined in the previous step, a significance scan is performed over the RNN output score in order to further split the events into a ”loose” category and a ”tight” category of the same kind. Results contained in this section are obtained using the Stage 1.0 definition of the STXS bins in the strong merging scheme, they only serve as a proof of principle for this method. Therefore, the 8 target classes are: GGH_0j, GGH_1j_PTH_0_60, GGH_1j_PTH_60_120, GGH_1j_PTH_120_200, GGH_2j, GGH_BSM, QQ2HQQ, QQ2HQQ_BSM. In addition, to give a more complete view of the global result, the categories defined for the $80 fb^{-1}$ analysis are used to target the remaining two STXS bins: top and VHlep.

5.5.1 Multiclassification with a Recurrent Neural Network

The architecture of the RNN used in the multiclassification step consists in two LSTM layers (*Long Short-Term Memory*, a special type of recurrent layer [195]) and three Dense layers stacked in sequence one after the other, for a total of about 35000 trainable weights. Recurrent layers represent a smart way to deal with variable length inputs, i.e. events with a variable number of jets, because they transform the matrix of

	Relative difference wrt Baseline		
	wEtaCuts	wConvCuts	wEtaConvCuts
ggH	+3.55%	+1.45%	+3.29%

Table 5.7: Only μ_{ggH} floating.

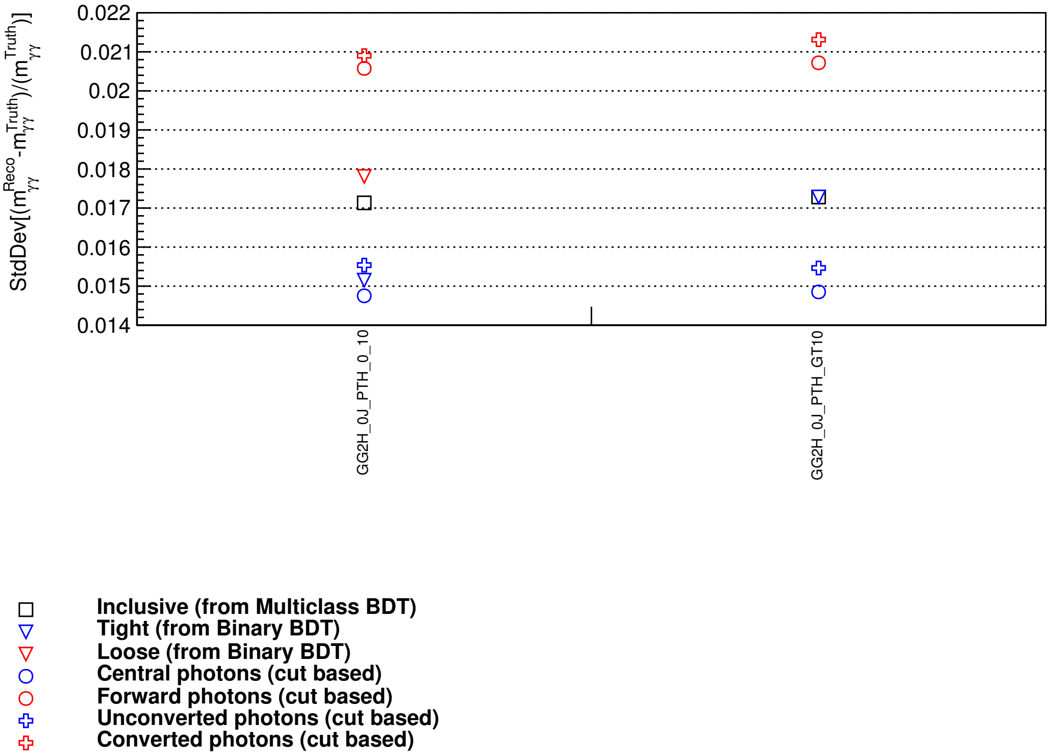

Figure 5.8: Relative invariant mass resolution of the baseline categorization (triangles), multiclass BDT (squares), the alternative categorization with η cuts (circles) and with conversion cuts (crosses).

input features into a **sequence** of matrices. The limit of this sequence is set to be 2 (i.e. up to 2 objects in the event are processed [5]) and it is applied through a technique known as *Padding and masking*: during the pre-processing, sequences whose length is shorter than the chosen limit are "padded" with a dummy value to be masked (skipped) by the network, while longer sequences are just shortened accordingly. The net effect of this procedure is that the events with less than or equal to 2 jets are processed taking into account only the features of the jets that are present, while for all the other events only the features of the first 2 (p_T leading) jets are considered. It was checked that inserting an additional jet to the sequence does not bring additional improvement to the RNN performance. This allows to keep all the information in the dataset without having to select the events according to the number of jets, as it is done by other algorithms.

The scheme of a classic recurrent layer is shown in Figure 5.9.

- x_t is the input at step t, x_1 could correspond, for example, to the p_T of the second jet in the sequence;
- U, V, W are the tunable parameters of the network and are the same across all steps, because the task to perform is the same at each step, just with different inputs;
- s_t is the hidden state at step t and is calculated based on the previous hidden state and the input at the current step: $s_t = f(Ux_t + Ws_{t-1})$, where f is the

---

[5] Objects in the sequence can still be either photons or jets, but since the diphoton selection already restricts the number of photons to be 2, it mainly acts over the number of jets.

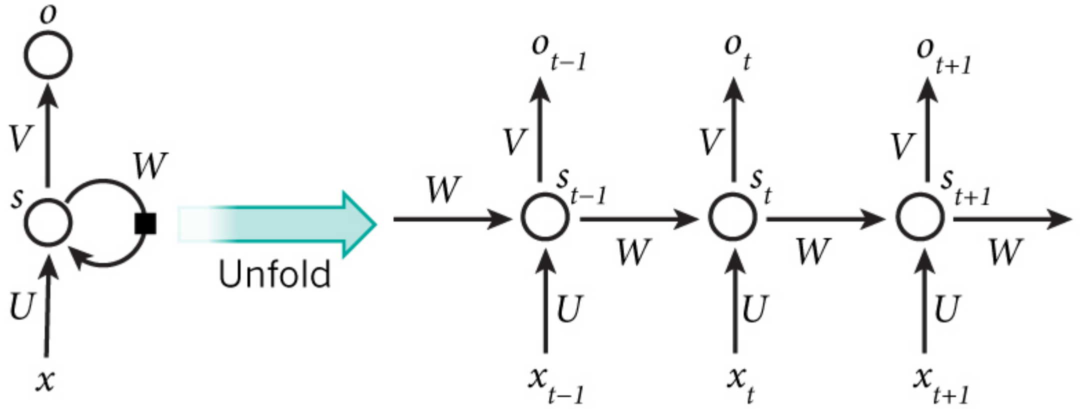

Figure 5.9: Schematic representation of a recurrent layer and its unfolding into a sequence of dense layers.

activation function of the layer. s_{-1}, which is required to calculate the first hidden state, is typically initialized to all zeroes;

- $o_t = f(Vs_t)$ is the output at step t. The RNN presented in this section doesn't have outputs at each step, but only one final output at the end of the sequence.

The input features of the RNN are p_T, η and ϕ of the jets and the photons in the event. Figure 5.10 shows the distributions for some of these variables for different truth targets in the training set. The activation function of the nodes in the hidden layers is ReLu (Figure 5.11a),

$$f(z) = max(0, z), \tag{5.3}$$

while the output layer uses SoftMax (Figure 5.11b),

$$f(z_i) = \frac{exp(z_i)}{\sum_j exp(z_j)}, \tag{5.4}$$

so that the 8 output scores can be interpreted as probabilities of being classified as one of the 8 target classes. The multiclass assignment is done using the RNN output score with the highest value, i.e. an event is classified to the reco category which corresponds to the STXS bin for which the RNN has predicted the highest probability. The network is trained with MC samples of the processes ggF, VBF, $WH$and ZH(mc16a/d/e campaigns) using about 3.5 millions events and the input samples are weighted with MC weights. At first order, the ratio between the yield of two target classes in the training is the ratio between the cross sections of the corresponding STXS bins. Normalizing the yields to the same sum of weights has also been attempted, but it lead to poor results. The loss function used in the training is *Categorical Cross Entropy* and it has been optimized with the *Adam* algorithm for 100 epochs.

5.5.2 Significance scan

An additional categorization step is performed after the multiclassification to increase the overall sensitivity. Within each of the 8 reco categories built by the RNN, sub-categories are defined by cutting on the output score for a given target class. The cut is always chosen by maximizing the significance $\frac{S}{\sqrt{B}}$ of the resulting category. As an example, Fig 5.12 shows the distributions of two output scores. An overall picture

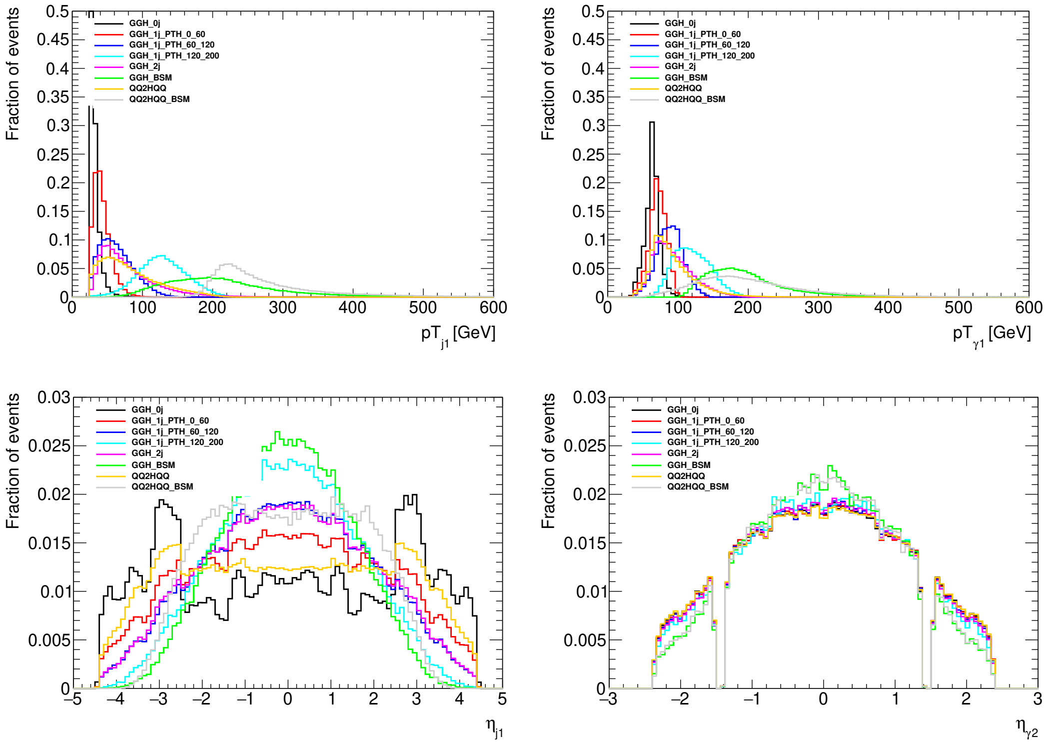

Figure 5.10: Distributions of 4 training variables for different STXS bins (different colors): transverse momentum of the leading jet (top left) and of the leading photon (top right); pseudorapidity of the leading jet (bottom left) and of the subleading photon (bottom right).

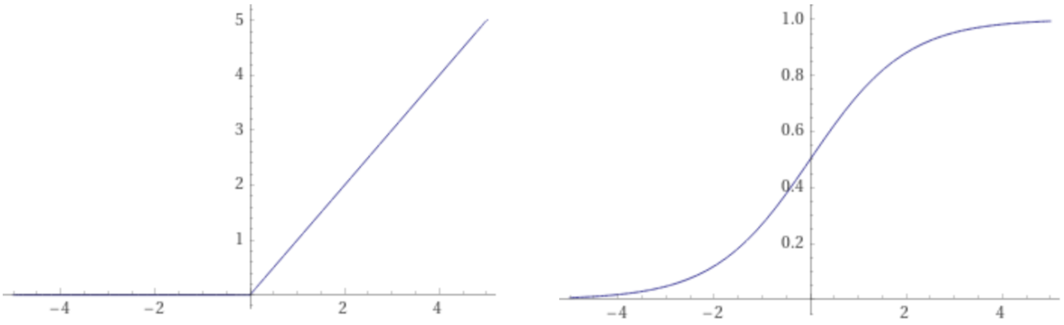

(a) ReLu activation function.

(b) Logistic activation function (SoftMax is a generalization to multiple dimensions).

Figure 5.11

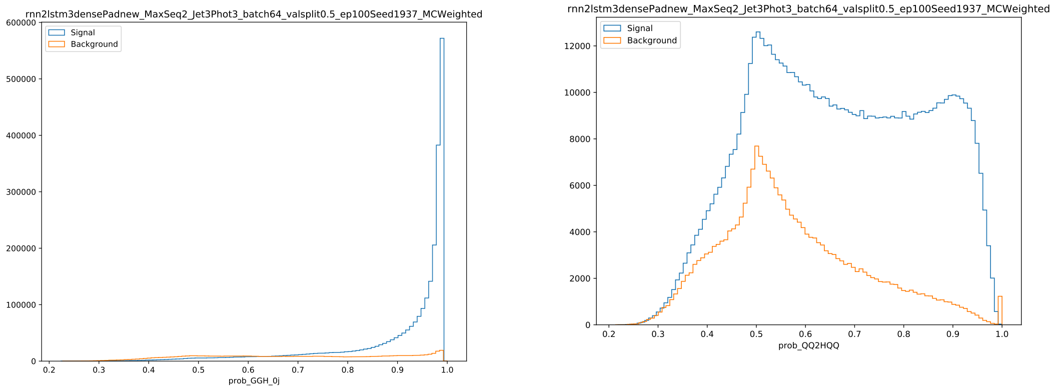

(a) GGH_0j

(b) QQ2HQQ

Figure 5.12: Distributions of the RNN output score for the GGH_0j and QQ2HQQ events. In each case the targeted bin is treated as signal while all others represent the background. The QCD diphoton background is not considered.

of the resulting categorization is given by Figure 5.13 where the purities of all the categories with respect to the targeted STXS regions are shown.

5.5.3 Evaluation of the performance

The performance of a classifier can be evaluated by considering how much the statistical precision of a measurement, i.e. errors and correlations of the parameters of interest (POIs), would improve if using it as part of the analysis. To evaluate this metric for a given classification method, a *counting experiment* has to be performed: Data ($139fb^{-1}$) and MC events are assigned to categories using the method under examination[6]; in each of these categories, a Double Sided Crystal Ball is fitted over signal events and the bounds of the S_{90} region are computed (S_{90} is the smallest region that contains 90% of the signal and it's extracted from the fitted pdf). The signal efficiencies are computed in the S_{90} region ($\epsilon_{S_{90}}$) and the background yield ($B_{S_{90}}$) is computed integrating a pdf fitted on the $m_{\gamma\gamma}$ data side-bands. The function used is an exponential of a second order polynomial for all categories.

Given the signal efficiencies for each STXS bin and the background yields in each category in its S_{90} region, a simple counting likelihood can be built with the yields of the various categories modelled as

$$N^c = B^c_{S_{90}} + \sum_t \mu_t \cdot L \cdot \sigma_t^{\gamma\gamma} \cdot \epsilon^{ct}_{S_{90}}, \tag{5.5}$$

where $\epsilon^{ct}_{S_{90}}$ is the efficiency for the t-th truth bin in S_{90} region of the c-th category. The likelihood can measure the signals strengths μ_t related to the STXS bins used to train the classifier. From this likelihood, which does not contain any shape information, an Asimov dataset is generated, fixing the signal strengths for each process to the predicted SM value ($\mu_t = 1$). Fitting the Asimov is enough to obtain the values of the errors and correlations among the POIs.

A counting experiment has been run using the categorization described in this section,

---

[6] This is done according to the procedure described in Sections 5.5.1 and 5.5.2, when evaluating the performance of the RNN.

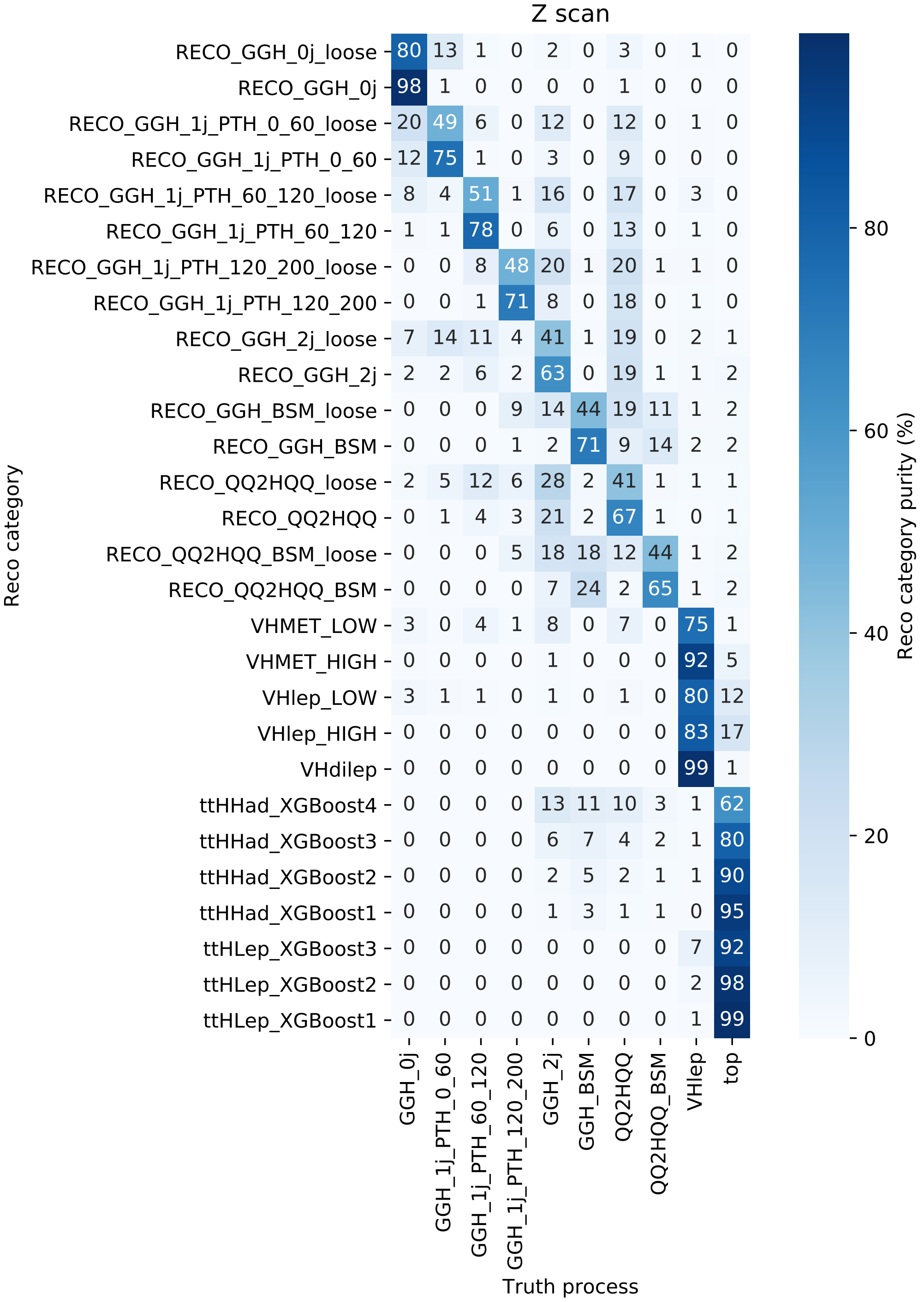

Figure 5.13: Relative content of each reco category (y-axis) in terms of the targeted STXS regions (x-axis).

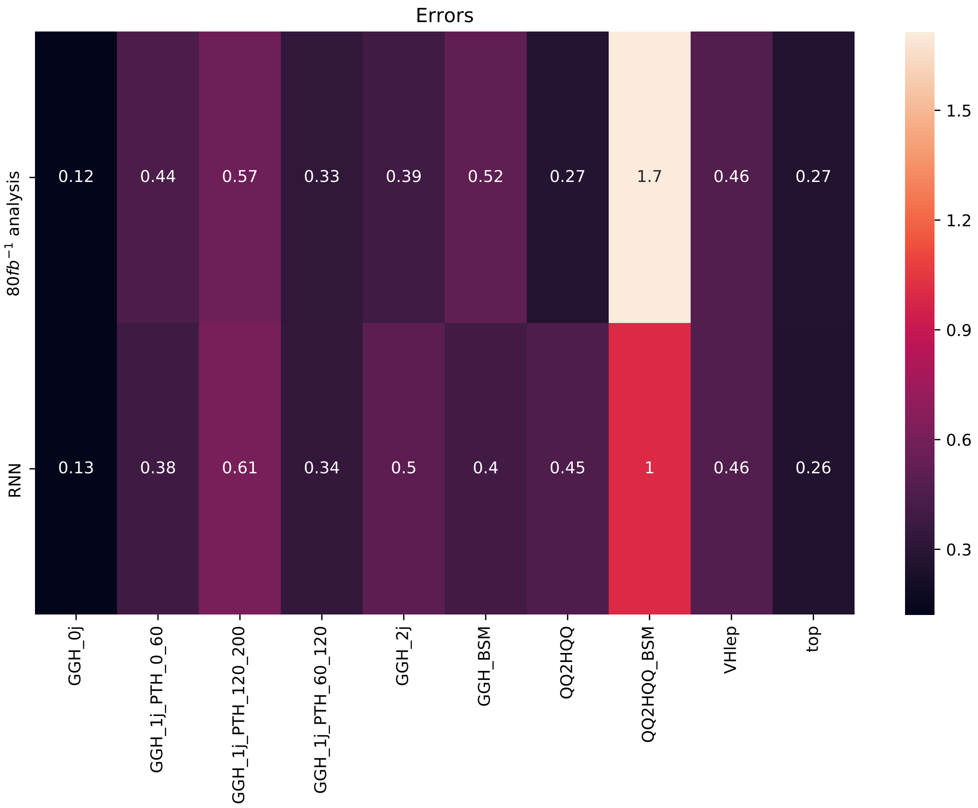

Figure 5.14: Errors on the 10 fitted POIs obtained using the categorization proposed in this section. The same values are also reported for the categorization used for the $80fb^{-1}$ analysis.

for which the obtained errors and correlations of the fitted POIs are shown in Figures 5.14 and 5.15. For comparison, errors and correlations obtained with the full categorization used for the $80fb^{-1}$ analysis are also shown in Figures 5.14 and 5.15. The proposed categorization based on a RNN shows no global improvement with respect to the baseline: for some of the POIs errors and correlations are reduced, while for others they are at the same level if not worse. As a result, this method was found to be not very competitive and the categorization presented in Section 5.4 was actually used in the final version of the analysis.

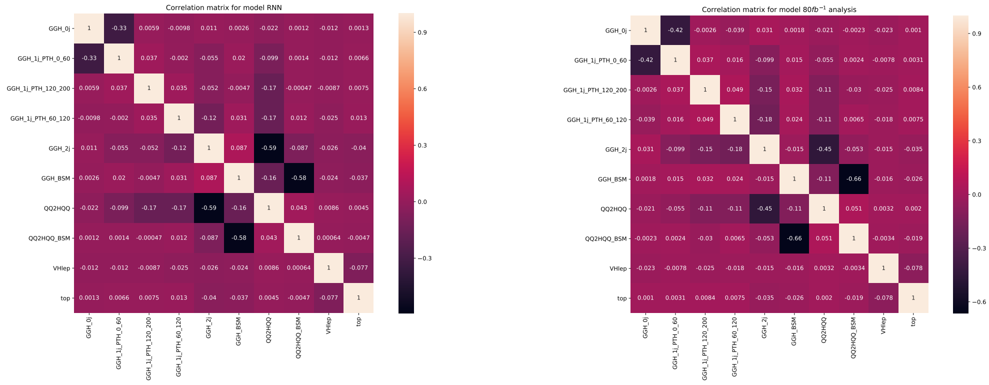

	GGH_0j	GGH_1j_PTH_0_60	GGH_1j_PTH_120_200	GGH_1j_PTH_60_120	GGH_2j	GGH_BSM	QQ2HQQ	QQ2HQQ_BSM	VHlep	top
GGH_0j	1	-0.33	0.0059	-0.0098	0.011	0.0026	-0.022	0.0012	-0.012	0.0013
GGH_1j_PTH_0_60	-0.33	1	0.037	-0.002	-0.055	0.02	-0.099	0.0014	-0.012	0.0066
GGH_1j_PTH_120_200	0.0059	0.037	1	0.035	-0.052	-0.0047	-0.17	-0.00047	-0.0087	0.0075
GGH_1j_PTH_60_120	-0.0098	-0.002	0.035	1	-0.12	0.031	-0.17	0.012	-0.025	0.013
GGH_2j	0.011	-0.055	-0.052	-0.12	1	0.087	-0.59	-0.087	-0.026	-0.04
GGH_BSM	0.0026	0.02	-0.0047	0.031	0.087	1	-0.16	-0.58	-0.024	-0.037
QQ2HQQ	-0.022	-0.099	-0.17	-0.17	-0.59	-0.16	1	0.043	0.0086	0.0045
QQ2HQQ_BSM	0.0012	0.0014	-0.00047	0.012	-0.087	-0.58	0.043	1	0.00064	-0.0047
VHlep	-0.012	-0.012	-0.0087	-0.025	-0.026	-0.024	0.0086	0.00064	1	-0.077
top	0.0013	0.0066	0.0075	0.013	-0.04	-0.037	0.0045	-0.0047	-0.077	1

(a) RNN

	GGH_0j	GGH_1j_PTH_0_60	GGH_1j_PTH_120_200	GGH_1j_PTH_60_120	GGH_2j	GGH_BSM	QQ2HQQ	QQ2HQQ_BSM	VHlep	top
GGH_0j	1	-0.42	-0.0026	-0.039	0.031	0.0018	-0.021	-0.0023	-0.023	0.001
GGH_1j_PTH_0_60	-0.42	1	0.037	0.016	-0.099	0.015	-0.055	0.0024	-0.0078	0.0031
GGH_1j_PTH_120_200	-0.0026	0.037	1	0.049	-0.15	0.032	-0.11	-0.03	-0.025	0.0084
GGH_1j_PTH_60_120	-0.039	0.016	0.049	1	-0.18	0.024	-0.11	0.0065	-0.018	0.0075
GGH_2j	0.031	-0.099	-0.15	-0.18	1	-0.015	-0.45	-0.053	-0.015	-0.035
GGH_BSM	0.0018	0.015	0.032	0.024	-0.015	1	-0.11	-0.66	-0.016	-0.026
QQ2HQQ	-0.021	-0.055	-0.11	-0.11	-0.45	-0.11	1	0.051	0.0032	0.002
QQ2HQQ_BSM	-0.0023	0.0024	-0.03	0.0065	-0.053	-0.66	0.051	1	-0.0034	-0.019
VHlep	-0.023	-0.0078	-0.025	-0.018	-0.015	-0.016	0.0032	-0.0034	1	-0.078
top	0.001	0.0031	0.0084	0.0075	-0.035	-0.026	0.002	-0.019	-0.078	1

(b) 80fb^{-1}analysis categories

Figure 5.15: Correlations among the 10 fitted POIs obtained using the categorization proposed in this section (a) and the categorization used for the $80fb^{-1}$ analysis (b).

5.6 Signal modeling

The signal component in each category corresponds to the sum of the contributions from each STXS region, which are all assumed to follow the same $m_{\gamma\gamma}$ distribution within a given analysis category. The shape is described using a double-sided Crystal Ball (DSCB) function [196, 197], consisting of a Gaussian distribution in the region around the peak position, continued by power-law tails at lower and higher $m_{\gamma\gamma}$ values.

The Gaussian core of the DSCB is parameterized by the peak position $(m_H + \Delta\mu_{\mathrm{CB}})$ and the width (σ_{CB}). The non-Gaussian contributions to the mass resolution arise mostly from converted photons $\gamma \to e^+e^-$ with at least one electron losing a significant fraction of its energy through bremsstrahlung in the inner detector material. The parametric form for a given reconstructed category i, where the Higgs boson mass is m_H , can be written as:

$$
\begin{aligned}
&f_i^{sig}(m_{\gamma\gamma}; \Delta\mu_{\mathrm{CB,i}}, \sigma_{\mathrm{CB,i}}, \alpha^{\pm}_{\mathrm{CB,i}}, n^{\pm}_{\mathrm{CB,i}}) = \\
&= N_c \begin{cases}
e^{-\frac{t^2}{2}} & -\alpha^{-}_{\mathrm{CB,i}} \leq t \leq \alpha^{+}_{\mathrm{CB,i}} \\
\left(\frac{n^{-}_{\mathrm{CB,i}}}{|\alpha^{-}_{\mathrm{CB,i}}|}\right)^{n^{-}_{\mathrm{CB,i}}} e^{-\frac{|\alpha^{-}_{\mathrm{CB,i}}|^2}{2}} \left(\frac{n^{-}_{\mathrm{CB,i}}}{|\alpha^{-}_{\mathrm{CB,i}}|} - \alpha^{-}_{\mathrm{CB,i}} - t\right)^{-n^{-}_{\mathrm{CB,i}}} & t < -\alpha^{-}_{\mathrm{CB,i}} \\
\left(\frac{n^{+}_{\mathrm{CB,i}}}{|\alpha^{+}_{\mathrm{CB,i}}|}\right)^{n^{+}_{\mathrm{CB,i}}} e^{-\frac{|\alpha^{+}_{\mathrm{CB,i}}|^2}{2}} \left(\frac{n^{+}_{\mathrm{CB,i}}}{|\alpha^{+}_{\mathrm{CB,i}}|} - \alpha^{+}_{\mathrm{CB,i}} - t\right)^{-n^{+}_{\mathrm{CB,i}}} & t > \alpha^{+}_{\mathrm{CB,i}}
\end{cases}
\end{aligned}
\tag{5.6}
$$

where $t = (m_{\gamma\gamma} - m_H - \Delta\mu_{\mathrm{CB,i}})/\sigma_{\mathrm{CB,i}}$, and N_c is a normalization factor. The non-Gaussian parts are parametrized by $\alpha^{\pm}_{\mathrm{CB,i}}$ and $n^{\pm}_{\mathrm{CB,i}}$ separately for the low-mass $(-)$ and the high-mass $(+)$ tails.

The potential bias in the estimate of signal yield due to an intrinsic shape difference between the DSCB function and signal $m_{\gamma\gamma}$ distribution is found to be negligible [82].

The parameters of the DSCB in each category are obtained by a fit to a mixture of the ggF, VBF, VH, ttH and tH samples described in Section 5.2.2, in the proportion of their SM cross-sections. A shift of 0.09 GeV is applied to the position of the signal peak to account for the difference between the reference Higgs boson mass used in

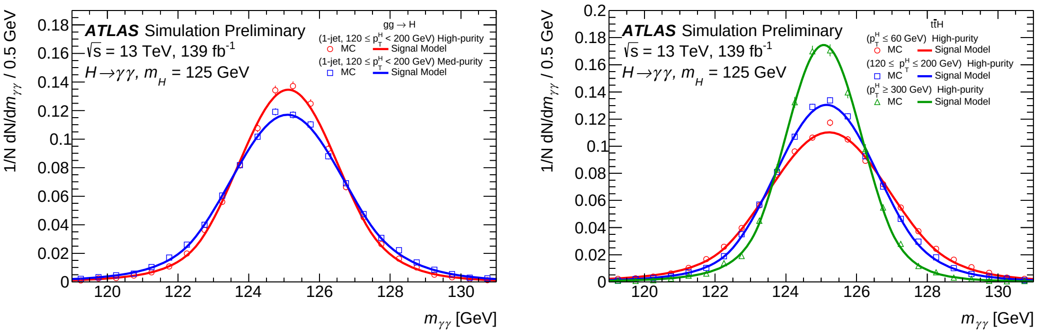

(a) $gg \rightarrow H$ (1-jet, $120 \leq p_{\mathrm{T}}^{H} < 200$ GeV)

(b) ttH

Figure 5.16: Shape of the signal $m_{\gamma\gamma}$ distribution for two groups of categories. 5.16a compares the signal $m_{\gamma\gamma}$ shapes for two categories targeting the same STXS region with different purities. 5.16b compares the signal $m_{\gamma\gamma}$ shapes for three "high-purity" categories targeting different p_{T}^{H} regions of the ttH process.

this analysis ($m_H = 125.09$ GeV) and the one for which the samples were generated ($m_H = 125$ GeV).

Simulated signal $m_{\gamma\gamma}$ distributions and their corresponding DSCB functions are shown for two groups of categories in Figure 5.16.

5.7 Background modeling

The procedure for the modeling of the continuum background involves two main steps: first, a background $m_{\gamma\gamma}$ template is constructed from a combination of simulation samples and data control samples; second, a background function is selected from a number of candidate functions, using a test known as the *spurious signal test*, with the goal of identifying an analytic function that is flexible enough to fit the $m_{\gamma\gamma}$ distribution in data and results in a small potential bias compared to the statistical uncertainty.

In $gg \rightarrow H$ and $qq' \rightarrow Hqq'$ categories, the template is defined as a combination of the $\gamma\gamma$, γj, and jj processes defined in Section 5.3, each of which is weighted according to its fractions in the selected analysis category. The fractions of these processes are determined by a data-driven method, known as the double two-dimensional sideband method [188], which uses control regions in data in which one or both of the identification and isolation criteria of each photon are reversed. For these categories, the fraction of total background events due to $\gamma\gamma$ process ranges between 75% and 95%, the fraction of γj process is between 2% and 25%, and the fraction of jj process is smaller than 6%.

While a simulation sample is used to model the $\gamma\gamma$ process in this study, it is computationally prohibitive to generate sufficiently large samples of γj and jj processes passing analysis selections because of the high jet rejection performance of the ATLAS photon identification algorithms. To avoid this issue, the $m_{\gamma\gamma}$ shapes of the γj or jj components are obtained from the data control samples described above, inverting the identification and isolation requirement of one (for the γj process) or both (for the jj process) photons. The ratio of the $m_{\gamma\gamma}$ shape of the γj and jj components to that of the simulated $\gamma\gamma$ sample is fitted to a linear function of $m_{\gamma\gamma}$. The function is then applied as a reweighting procedure to the $\gamma\gamma$ sample to obtain the final template. Changing the fraction of the γj and jj components within the uncertainties of their determination is found to have a negligible impact on the spurious signal test described below.

For categories targeting STXS regions of the VH, ttH, or tH production processes, the background template is constructed from the simulated $\gamma\gamma$ process alone: the contribution from γj and jj processes is small, and neglecting it does not significantly change the background shape. Because of the categorization selection, the $\gamma\gamma$ events in these categories are primarily from $V\gamma\gamma$ production or $t\bar{t}\gamma\gamma$ production. As such, the $V\gamma\gamma$ and $t\bar{t}\gamma\gamma$ samples described in Section 5.2.2 are used to construct the background templates in corresponding categories.

The background templates constructed for four example categories targeting the $gg \to H$, $qq' \to Hqq'$, VH and ttH processes are shown in Figure 5.17.

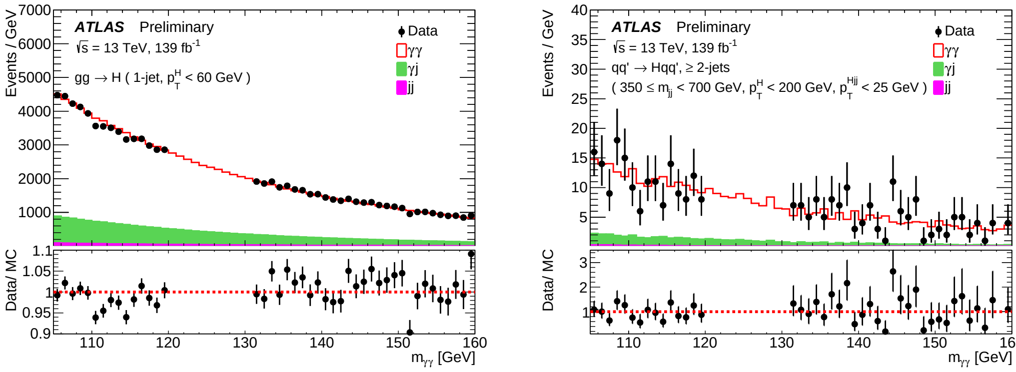

(a) $gg \to H$ (1-jet, $p_{\mathrm{T}}^{H} < 60$ GeV) (b) $qq' \to Hqq'$ ($\geq$ 2-jets, $350 \leq m_{jj} < 700$ GeV, $p_{\mathrm{T}}^{H} < 200$ GeV, $p_{\mathrm{T}}^{Hjj} < 25$ GeV)

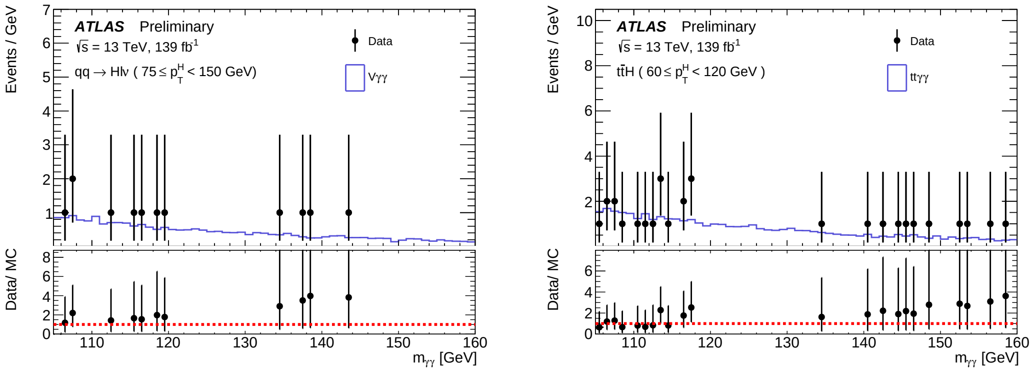

(c) $qq \to H\ell\nu$ ($75 \leq p_{\mathrm{T}}^{H} < 150$ GeV) (d) ttH ($60 \leq p_{\mathrm{T}}^{H} < 120$ GeV)

Figure 5.17: Distribution of the diphoton invariant mass $m_{\gamma\gamma}$ in four representative STXS categories in data (black points) and continuum background simulation (histograms). The data are shown excluding the region $120 < m_{\gamma\gamma} < 130$ GeV containing the signal. In categories 5.17a and 5.17b, the $\gamma\gamma$ (red), γj (green) and jj (magenta) background contributions are shown stacked and colored differently.

Three families of analytic functions are tested as candidates to model the $m_{\gamma\gamma}$ distribution for a given analysis category. They include power law functions, Bernstein polynomials [198], and exponential functions of a polynomial. These functions and the number of degrees of freedom tested are summarized in Table 5.8. The coefficients of these functions are considered to be independent across categories, regardless of the functions chosen, and in all cases are treated as free parameters in the fits to data.

Type	Function	N_{pars}	Acronym
Power law	$m_{\gamma\gamma}^{a}$	1	`PowerLaw`
Exponential	$\exp(am_{\gamma\gamma})$	1	`Exp`
Exponential of second-order polynomial	$\exp(a_1 m_{\gamma\gamma} + a_2 m_{\gamma\gamma}^2)$	2	`ExpPoly2`
Exponential of third-order polynomial	$\exp(a_1 m_{\gamma\gamma} + a_2 m_{\gamma\gamma}^2 + a_3 m_{\gamma\gamma}^3)$	3	`ExpPoly3`
Bernstein polynomial	$(1-x)^n + a_1 nx(1-x)^{n-1} + \cdots + a_n x^n$	$n = 1$–5	`Bern1`–`Bern5`

Table 5.8: Summary of the functions used for the modeling of the continuum background component. N_{pars} denotes the number of free parameters used to define the function shape. For the definition of the Bernstein polynomials, $x = (m_{\gamma\gamma} - m_{\text{min}})/(m_{\text{max}} - m_{\text{min}})$, where $m_{\text{min}} = 105$ GeV and $m_{\text{max}} = 160$ GeV are respectively the lower and upper bounds of the fitted $m_{\gamma\gamma}$ range.

The main criterion used to select the functional form in each category is a bias test performed by fitting the background template using a model with free parameters for both the signal and the background event yields. The potential bias due to the mis-modeling of background $m_{\gamma\gamma}$ distribution is estimated from the fitted signal yield (the *spurious* signal). This test is performed for m_H from 121 GeV to 129 GeV, with a step of 1 GeV. In order to avoid accidentally small bias values at the nominal Higgs boson mass of $m_H = 125.09$ GeV, the maximum absolute value of fitted signal yield $|S_{\text{spur}}|$ over the range $121 < m_H < 129$ GeV, is considered as the potential bias.

For categories with at least 100 data events in the sideband regions defined as $105 < m_{\gamma\gamma} < 120$ GeV or $130 < m_{\gamma\gamma} < 160$ GeV, the background functions are selected to result in a $|S_{\text{spur}}|$ that is smaller than either 10% of the total expected Higgs boson signal event (S_{exp}) or 20% of the statistical uncertainty of the fitted signal yield (σ_{exp}). The fit of the analytic function to the background template is required to yield a χ^2 probability of at least 1% [7].

If multiple functions pass the requirements, the one with the smallest number of degrees of freedom is chosen. If no function passes, the spurious signal requirement is relaxed to $||S_{\text{spur}}| - 20\%\,\sigma_{\text{exp}}| < 2\sigma_{\text{tm}}$ or $||S_{\text{spur}}| - 10\%\,S_{\text{exp}}| < 2\sigma_{\text{tm}}$, where σ_{tm} is the uncertainty on the signal yield arising from the size of the sample used to build the template. For 28 out of the 88 categories, these relaxed conditions were used.

For categories with fewer than 100 data events in the sideband regions, candidate background functions are limited to `Exp`, `ExpPoly2` and `ExpPoly3` (as defined in Table 5.8), in order to avoid unphysical fits due to large statistical fluctuations in the sidebands. The function is chosen using a Wald test: first the quantity $q_{12} = -2\log L_1/L_2$ is computed from the maximum likelihood values L_1 and L_2 of background-only fits to the data sideband regions using respectively the `Exp` and `ExpPoly2` descriptions of the backgrounds. The `ExpPoly2` model is chosen if the p-value computed from q_{12} is less than 0.05, assuming that q_{12} follows a χ^2 distribution with one degree of freedom. Similarly, the `ExpPoly3` form is chosen over `ExpPoly2` if the p-value for the corresponding Wald test is 0.05 or less. For 45 out of the 88 categories, the Wald-test-based condition was used.

In all cases, $|S_{\text{spur}}|$ of the selected background function provides an estimate of the possible bias in the fitted signal yield introduced by the intrinsic difference between the background $m_{\gamma\gamma}$ shape and the selected function, and is used as the systematic

---

[7] The χ^2 is computed with a background template uniformly binned over 105 GeV $< m_{\gamma\gamma} <$ 160 GeV. The number of bins is 22, and the degrees of freedom used in the computation is 21 - N_{pars}, the number of free function parameters. The normalization of the template removes one degree of freedom.

Category	σ_{68} (GeV)	Function
$gg \to H$		
0-jet, $p_{\mathrm{T}}^{H} < 10$ GeV	1.95	`ExpPoly2`
0-jet, $p_{\mathrm{T}}^{H} \geq 10$ GeV	1.94	`ExpPoly2`
1-jet, $p_{\mathrm{T}}^{H} < 60$ GeV	1.89	`ExpPoly2`
1-jet, $60 \leq p_{\mathrm{T}}^{H} < 120$ GeV	1.84	`ExpPoly2`
1-jet, $120 \leq p_{\mathrm{T}}^{H} < 200$ GeV , High-purity	1.50	`ExpPoly2`
1-jet, $120 \leq p_{\mathrm{T}}^{H} < 200$ GeV , Med-purity	1.73	`PowerLaw`
$\geq$ 2-jets, $m_{jj} < 350$ GeV, $p_{\mathrm{T}}^{H} < 60$ GeV , High-purity	1.76	`ExpPoly2`
$\geq$ 2-jets, $m_{jj} < 350$ GeV, $p_{\mathrm{T}}^{H} < 60$ GeV , Med-purity	1.91	`ExpPoly2`
$\geq$ 2-jets, $m_{jj} < 350$ GeV, $p_{\mathrm{T}}^{H} < 60$ GeV , Low-purity	1.99	`ExpPoly2`
$\geq$ 2-jets, $m_{jj} < 350$ GeV, $60 \leq p_{\mathrm{T}}^{H} < 120$ GeV , High-purity	1.65	`ExpPoly2`
$\geq$ 2-jets, $m_{jj} < 350$ GeV, $60 \leq p_{\mathrm{T}}^{H} < 120$ GeV , Med-purity	1.80	`ExpPoly2`
$\geq$ 2-jets, $m_{jj} < 350$ GeV, $60 \leq p_{\mathrm{T}}^{H} < 120$ GeV , Low-purity	1.87	`Exp`
$\geq$ 2-jets, $m_{jj} < 350$ GeV, $120 \leq p_{\mathrm{T}}^{H} < 200$ GeV , High-purity	1.52	`ExpPoly2`
$\geq$ 2-jets, $m_{jj} < 350$ GeV, $120 \leq p_{\mathrm{T}}^{H} < 200$ GeV , Med-purity	1.66	`PowerLaw`
$\geq$ 2-jets, $350 \leq m_{jj} < 700$ GeV, $p_{\mathrm{T}}^{Hjj} < 25$ GeV , High-purity	1.62	`PowerLaw`
$\geq$ 2-jets, $350 \leq m_{jj} < 700$ GeV, $p_{\mathrm{T}}^{Hjj} < 25$ GeV , Med-purity	1.74	`Exp`
$\geq$ 2-jets, $350 \leq m_{jj} < 700$ GeV, $p_{\mathrm{T}}^{Hjj} < 25$ GeV , Low-purity	1.93	`Exp`
$\geq$ 2-jets, $350 \leq m_{jj} < 700$ GeV, $p_{\mathrm{T}}^{Hjj} \geq 25$ GeV , High-purity	1.50	`Exp`
$\geq$ 2-jets, $350 \leq m_{jj} < 700$ GeV, $p_{\mathrm{T}}^{Hjj} \geq 25$ GeV , Med-purity	1.68	`ExpPoly2`
$\geq$ 2-jets, $350 \leq m_{jj} < 700$ GeV, $p_{\mathrm{T}}^{Hjj} \geq 25$ GeV , Low-purity	1.82	`Exp`
$\geq$ 2-jets, $m_{jj} \geq 700$ GeV, $p_{\mathrm{T}}^{Hjj} < 25$ GeV , High-purity	1.67	`Exp`
$\geq$ 2-jets, $m_{jj} \geq 700$ GeV, $p_{\mathrm{T}}^{Hjj} < 25$ GeV , Med-purity	1.79	`Exp`
$\geq$ 2-jets, $m_{jj} \geq 700$ GeV, $p_{\mathrm{T}}^{Hjj} < 25$ GeV , Low-purity	1.95	`PowerLaw`
$\geq$ 2-jets, $m_{jj} \geq 700$ GeV, $p_{\mathrm{T}}^{Hjj} \geq 25$ GeV , High-purity	1.63	`PowerLaw`
$\geq$ 2-jets, $m_{jj} \geq 700$ GeV, $p_{\mathrm{T}}^{Hjj} \geq 25$ GeV , Med-purity	1.77	`Exp`
$\geq$ 2-jets, $m_{jj} \geq 700$ GeV, $p_{\mathrm{T}}^{Hjj} \geq 25$ GeV , Low-purity	1.89	`PowerLaw`
$200 \leq p_{\mathrm{T}}^{H} < 300$ GeV , High-purity	1.27	`Exp`
$200 \leq p_{\mathrm{T}}^{H} < 300$ GeV , Med-purity	1.35	`Exp`
$200 \leq p_{\mathrm{T}}^{H} < 300$ GeV , Low-purity	1.52	`PowerLaw`
$300 \leq p_{\mathrm{T}}^{H} < 450$ GeV , High-purity	1.09	`Exp`
$300 \leq p_{\mathrm{T}}^{H} < 450$ GeV , Med-purity	1.18	`PowerLaw`
$300 \leq p_{\mathrm{T}}^{H} < 450$ GeV , Low-purity	1.33	`PowerLaw`
$450 \leq p_{\mathrm{T}}^{H} < 650$ GeV , High-purity	1.07	`Exp`
$450 \leq p_{\mathrm{T}}^{H} < 650$ GeV , Med-purity	1.12	`Exp`
$p_{\mathrm{T}}^{H} \geq 650$ GeV , High-purity	1.00	`Exp`
$p_{\mathrm{T}}^{H} \geq 650$ GeV , Med-purity	1.09	`Exp`
$qq' \to Hqq'$		
0-jet , High-purity	1.70	`Exp`
0-jet , Med-purity	1.91	`Exp`
1-jet , High-purity	1.65	`Exp`
1-jet , Med-purity	1.68	`Exp`
1-jet , Low-purity	1.84	`PowerLaw`
$\geq$ 2-jets, $m_{jj} < 60$ GeV , High-purity	1.62	`Exp`
$\geq$ 2-jets, $m_{jj} < 60$ GeV , Med-purity	1.59	`Exp`
$\geq$ 2-jets, $m_{jj} < 60$ GeV , Low-purity	1.62	`Exp`
$\geq$ 2-jets, $60 \leq m_{jj} < 120$ GeV , High-purity	1.49	`Exp`
$\geq$ 2-jets, $60 \leq m_{jj} < 120$ GeV , Med-purity	1.55	`PowerLaw`
$qq' \to Hqq'$		
$\geq$ 2-jets, $120 \leq m_{jj} < 350$ GeV , High-purity	1.69	`Exp`
$\geq$ 2-jets, $120 \leq m_{jj} < 350$ GeV , Med-purity	1.67	`Exp`
$\geq$ 2-jets, $120 \leq m_{jj} < 350$ GeV , Low-purity	1.67	`PowerLaw`
$\geq$ 2-jets, $350 \leq m_{jj} < 700$ GeV, $p_{\mathrm{T}}^{Hjj} < 25$ GeV , High-purity	1.65	`Exp`
$\geq$ 2-jets, $350 \leq m_{jj} < 700$ GeV, $p_{\mathrm{T}}^{Hjj} < 25$ GeV , Med-purity	1.77	`Exp`
$\geq$ 2-jets, $350 \leq m_{jj} < 700$ GeV, $p_{\mathrm{T}}^{Hjj} \geq 25$ GeV , High-purity	1.69	`Exp`
$\geq$ 2-jets, $350 \leq m_{jj} < 700$ GeV, $p_{\mathrm{T}}^{Hjj} \geq 25$ GeV , Med-purity	1.88	`Exp`
$\geq$ 2-jets, $m_{jj} \geq 700$ GeV, $p_{\mathrm{T}}^{Hjj} < 25$ GeV , High-purity	1.65	`Exp`
$\geq$ 2-jets, $m_{jj} \geq 700$ GeV, $p_{\mathrm{T}}^{Hjj} < 25$ GeV , Med-purity	1.81	`PowerLaw`
$\geq$ 2-jets, $m_{jj} \geq 700$ GeV, $p_{\mathrm{T}}^{Hjj} \geq 25$ GeV , High-purity	1.65	`Exp`
$\geq$ 2-jets, $m_{jj} \geq 700$ GeV, $p_{\mathrm{T}}^{Hjj} \geq 25$ GeV , Med-purity	1.63	`Exp`
$\geq$ 2-jets, $m_{jj} \geq 700$ GeV, $p_{\mathrm{T}}^{Hjj} \geq 25$ GeV , Low-purity	1.76	`Exp`
$\geq$ 2-jets, $350 \leq m_{jj} < 700$ GeV, $p_{\mathrm{T}}^{H} \geq 200$ GeV , High-purity	1.38	`Exp`
$\geq$ 2-jets, $350 \leq m_{jj} < 700$ GeV, $p_{\mathrm{T}}^{H} \geq 200$ GeV , Med-purity	1.49	`Exp`
$\geq$ 2-jets, $m_{jj} \geq 700$ GeV, $p_{\mathrm{T}}^{H} \geq 200$ GeV , High-purity	1.38	`Exp`
$\geq$ 2-jets, $m_{jj} \geq 700$ GeV, $p_{\mathrm{T}}^{H} \geq 200$ GeV , Med-purity	1.44	`Exp`
$qq \to H\ell\nu$		
Other	1.88	`Exp`
$0 \leq p_{\mathrm{T}}^{V} < 75$ GeV , High-purity	1.64	`Exp`
$0 \leq p_{\mathrm{T}}^{V} < 75$ GeV , Med-purity	1.87	`Exp`
$75 \leq p_{\mathrm{T}}^{V} < 150$ GeV , High-purity	1.64	`Exp`
$75 \leq p_{\mathrm{T}}^{V} < 150$ GeV , Med-purity	1.87	`Exp`
$150 \leq p_{\mathrm{T}}^{V} < 250$ GeV, 0-jet	1.60	`Exp`
$150 \leq p_{\mathrm{T}}^{V} < 250$ GeV, 1-jet	1.52	`Exp`
$p_{\mathrm{T}}^{V} \geq 250$ GeV	1.35	`Exp`
$qq \to H\ell\ell$		
Other	2.15	`Exp`
$0 \leq p_{\mathrm{T}}^{V} < 75$ GeV	1.85	`Exp`
$75 \leq p_{\mathrm{T}}^{V} < 150$ GeV , High-purity	1.73	`Exp`
$75 \leq p_{\mathrm{T}}^{V} < 150$ GeV , Med-purity	1.78	`Exp`
$150 \leq p_{\mathrm{T}}^{V} < 250$ GeV, 0-jet	1.60	`Exp`
$150 \leq p_{\mathrm{T}}^{V} < 250$ GeV, 1-jet	1.58	`Exp`
$p_{\mathrm{T}}^{V} \geq 250$ GeV	1.36	`Exp`
ttH		
Other (including tH)	1.74	`Exp`
$p_{\mathrm{T}}^{H} < 60$ GeV , High-purity	1.81	`Exp`
$p_{\mathrm{T}}^{H} < 60$ GeV , Med-purity	1.90	`Exp`
$60 \leq p_{\mathrm{T}}^{H} < 120$ GeV , High-purity	1.72	`Exp`
$60 \leq p_{\mathrm{T}}^{H} < 120$ GeV , Med-purity	1.86	`Exp`
$120 \leq p_{\mathrm{T}}^{H} < 200$ GeV , High-purity	1.54	`Exp`
$120 \leq p_{\mathrm{T}}^{H} < 200$ GeV , Med-purity	1.66	`Exp`
$p_{\mathrm{T}}^{H} \geq 200$ GeV	1.37	`Exp`
$p_{\mathrm{T}}^{H} \geq 300$ GeV	1.17	`Exp`
tHW	1.59	`Exp`
$tHqb$	1.63	`Exp`

Table 5.9: For each event category, size of the smallest mass window containing 68% of the integral of the signal $m_{\gamma\gamma}$ distribution (σ_{68}) and type of function used to model the background $m_{\gamma\gamma}$ distribution.

uncertainty for the background modeling. The chosen functional form for each category is shown in Table 5.9.

5.8 Systematic uncertainties

Systematic uncertainties considered in this analysis can be grouped into two types: experimental uncertainties, acting both on the signal yield and shape, and theoretical uncertainties, which can cause migrations between the different analysis bins. These systematic uncertainties are incorporated into the likelihood model of the measurement as nuisance parameters. More detail on these the uncertainties is provided in this section.

5.8.1 Experimental uncertainties

The modeling of the signal $m_{\gamma\gamma}$ distribution is subject to experimental uncertainties on the energy scale and energy resolution of photon candidates, as well as the uncertainty on the Higgs boson mass. The photon energy scale uncertainties are broken down to 40 independent sources, and are propagated to the peak position of the signal DSCB shape. The overall effect is usually less than 0.3% relative to the peak position value, depending on the category. The photon energy resolution uncertainties are broken down to nine independent sources, and they are propagated to the Gaussian width of the signal DSCB shape, with a relative impact between 1% and 8%, depending on the category. The estimate and implementation of the photon energy scale and resolution uncertainties follow the procedure outlined in Ref. [78].

The measurement assumes a Higgs boson mass of 125.09 GeV, as reported in Ref. [47]. The total uncertainty on the measured Higgs boson mass, 0.24 GeV, is considered as an additional uncertainty of the peak position of the signal DSCB shape.

The modeling of the background $m_{\gamma\gamma}$ distribution with an analytic function can introduce a potential bias to the fitted signal yield. An uncertainty on the modeling of the background is included as an additive contribution to the signal yield in each category, as discussed in Section 5.7. The uncertainty is considered to be uncorrelated between different categories. The uncertainty values in each category range from 10% to 99% of the statistical uncertainty on the measured event yield in the category.

Experimental uncertainties affecting the expected signal yields include: the efficiency of the diphoton trigger [105], the photon identification efficiencies [78], the photon isolation efficiencies, the impact of the photon energy scale and resolution uncertainties on the selection efficiency [78], the modeling of pileup in the simulation, which is evaluated by varying by ± 9% the value of the visible inelastic cross-section used to reweight the pileup distribution in the simulation to that in the data, the jet energy scale and resolution [85], the efficiency of the jet vertex tagger, the efficiency of the b-tagging algorithm [84], the electron [78] and muon [86] reconstruction, identification and isolation efficiencies, the electron [78] and muon [86] energy and momentum scale and resolution, as well as the contribution to $E_{\mathrm{T}}^{\mathrm{miss}}$from charged-particle tracks that are not associated with high-p_{T}electrons, muons, jets, or photons [88]. The uncertainty on the combined 2015–2018 integrated luminosity is 1.7% [102], obtained using the LUCID-2 detector [103] for the primary luminosity measurements.

Among these, the uncertainties with the largest variations in signal yields are the pileup modeling uncertainty (up to 7%), jet flavor tagging uncertainty (up to 5%), and jet energy resolution uncertainty (up to 4%).

5.8.2 Theoretical uncertainties

Theory modeling uncertainties enter into the measurements through their effect on the efficiency factors ϵ_{it}, as defined in Eq. 5.1, which are used to obtain the cross-section values from the event yields. Measurements in regions spanning multiple STXS region, such as those of the total and production mode cross-sections, depend on the fraction of the cross-section assigned to each region and therefore on the theory modeling uncertainties.

For the production mode and simplified template cross section measurements, the main theory uncertainties arise from missing higher-order terms in the perturbative QCD calculations, the modeling of parton shower, and choices of the parton distribution functions and value of α_{S}. For measurements of ttH and tH related regions, the modeling of heavy flavor quark production in the ggF, VBF, and VH processes is also important.

Uncertainties due to missing higher-order terms in the perturbative QCD calculations, are estimated by varying the renormalization and factorization scales. These uncertainties are derived from event migration between STXS regions within a given production process. The QCD scale uncertainties are implemented in the likelihood function in a way so that only correlated variations in the acceptances of STXS regions are introduced. For the $gg \to H$ processes, four sources [42, 199–201] account for modeling uncertainties on bins of the jet multiplicity; four sources cover the modeling of the Higgs boson p_{T} distribution; two sources [202, 203] account for the uncertainty on the distribution of the p_{T}^{Hjj} variable; four sources account for the uncertainty on the distribution of the m_{jj} variable. In addition, a comparison of the acceptance and efficiency factors between the nominal ggF sample and the alternative sample generated from MadGraph5_aMC@NLO, as described in Section 5.2.2, is made. The differences are considered as additional modeling uncertainties for the ggF process and can reach values of up to 20% in high Higgs boson p_{T} regions.

QCD scale uncertainties are also estimated for VBF and VH processes. For each of the WH, $qq/qg \to ZH$, and $gg \to ZH$ processes, one overall source of scale uncertainty, four sources of p_{T}^{V} modeling uncertainty, and two sources of jet multiplicity modeling uncertainty, are estimated. For $qq' \to Hqq'$ processes, a similar set of uncertainty sources is identified: one for overall variation, two for modeling of jet multiplicity as well as p_{T}^{Hjj} distributions, one for migration between $p_{\mathrm{T}}^{H} < 200$ GeV and $p_{\mathrm{T}}^{H} > 200$ GeV, and six for the modeling of m_{jj} distribution.

For the ttH process, the QCD scale uncertainties include one overall variation, as well as six covering modeling of the p_{T}^{H} distribution.

For all processes, variations of acceptances and efficiencies of STXS regions in individual categories are estimated and treated as uncertainties. The variations due to these uncertainties range from 5% to 25%.

The modeling of the parton shower, underlying event, and hadronization, assessed by comparing the acceptance times efficiency of simulated signal samples showered with Pythia8 to that of samples showered with Herwig7 . The uncertainties estimated by these variations typically do not exceed 10%.

Uncertainties arising from the choice of parton distribution functions and the value of α_{S} are estimated using the PDF4LHC15 recommendations [115]. Their effects are usually small compared to those of the previous two sources of theory uncertainty.

In categories targeting the ttH and tH processes, the predicted ggF, VBF and VH yields are each assigned a conservative 100% uncertainty (correlated between categories), which is due to the theoretical uncertainty on the radiation of additional heavy-flavor jets in these Higgs boson production modes. This is supported by measurements using $H\to ZZ^{*}\to 4\ell$ [204], $t\bar{t}b\bar{b}$ [205], and Vb [206, 207] events. The impact of this uncertainty on the results is generally negligible compared to the statistical uncertainties, since the contributions from non-ttH processes are generally low.

The uncertainties of Higgs boson production cross section, as well as the $H \to \gamma\gamma$ decay branching ratio are obtained for the presentation of the SM prediction and are not used in the measurements. The $H \to \gamma\gamma$ decay branching ratio has an uncertainty of 1.6%, based on calculations from the HDECAY [166–168] and PROPHECY4F [169–171] programs.

5.9 Results

Results are presented in terms of several descriptions of Higgs boson production: a single overall production cross-section, separate cross-sections for the main Higgs boson production modes (Section 5.9.1), and cross-sections in a set of merged STXS regions defined in each production process (Section 5.9.2).

In each case, the measurement is performed by expressing the event yields in each event category in terms of the measurement parameters, and fitting the model to the data. Best-fit values are reported along with uncertainties corresponding to 68% CL intervals obtained from a profile likelihood technique [194]. In some cases, uncertainties are presented as a decomposition into separate components: the *statistical* component is obtained from a fit in which the nuisance parameters associated with systematic uncertainties are fixed to their best-fit values; the *systematic* component, corresponding to the combined effect of systematic uncertainties, is computed by subtracting in quadrature the statistical component from the total uncertainty. Finer splits into uncertainty components corresponding to groups of nuisance parameters are obtained by iteratively fixing the parameters in each group and subtracting in quadrature the uncertainties obtained in this configuration from those obtained when the parameters are profiled.

Expected results for the SM are obtained from a fit to an Asimov data set built from the best-fit values of the model parameters in a fit to the observed data under the SM hypothesis. Compatibility with the Standard Model is computed from the value of the profile likelihood ratio of the model in data under the SM hypothesis; a p-value quantifying compatibility with the SM is computed under the assumption that this quantity follows a χ^2 distribution with a number of degrees of freedom equal to the number of parameters of interest [194].

5.9.1 Total and production mode cross-sections

The overall rate of Higgs boson production at $\sqrt{s} = 13$ TeV is probed by measuring a single parameter of interest, the product of the Higgs boson production cross section and the $H \to \gamma\gamma$ branching ratio $(\sigma \times B_{\gamma\gamma})$, which scales the expected yields in all the categories. The total Higgs boson production cross section corresponds to the region $|y_H| < 2.5$, where y_H is the Higgs boson rapidity.

The product $(\sigma \times B_{\gamma\gamma})$, treated as a single parameter of interest in the likelihood function, is measured by simultaneously fitting the $m_{\gamma\gamma}$ distributions of the 88 analysis categories. Figure 5.18 shows the $m_{\gamma\gamma}$ distribution from the inclusive diphoton sample. The events in each category are weighted by $\ln(1 + S/B)$, where S and B are the expected signal and background yields in this category within the smallest $m_{\gamma\gamma}$ window containing 90% of the signal events. This choice of event weight is designed to enhance the contribution of events from categories with higher signal-to-background ratio in a way that approximately matches the impact of these events in the categorized analysis of the data.

The Higgs boson production cross section times $H \to \gamma\gamma$ branching ratio is measured to be

$$(\sigma \times B_{\gamma\gamma})_{\text{obs}} = 127 \pm 10\,\text{fb} = 127 \pm 7\ (\text{stat.}) \pm 7\ (\text{syst.})\,\text{fb} \tag{5.7}$$

with an SM expectation of

$$(\sigma \times B_{\gamma\gamma})_{\text{exp}} = 116 \pm 5\,\text{fb}. \tag{5.8}$$

The mechanism of Higgs boson production is probed by considering separately the ggF, VBF, WH, ZH and top-associated production processes. The measurement is reported in terms of the $(\sigma \times B_{\gamma\gamma})$ value in each case, with the cross-sections defined in $|y_H| < 2.5$. As in the STXS region definition, the contribution from the bbH process is included in the ggF component. The top-associated production includes both the ttH and tH processes, and the sum of their cross sections are measured. Figure 5.19 shows the weighted $m_{\gamma\gamma}$ distributions for these production cross-section measurements. These distributions are weighted using the same procedure as that of Figure 5.18, except that the signal yield only includes the contribution from the targeted production process and the background yield also includes contributions from other production processes. The observed (expected) significance values for the VBF, WH, and ttH + tH processes

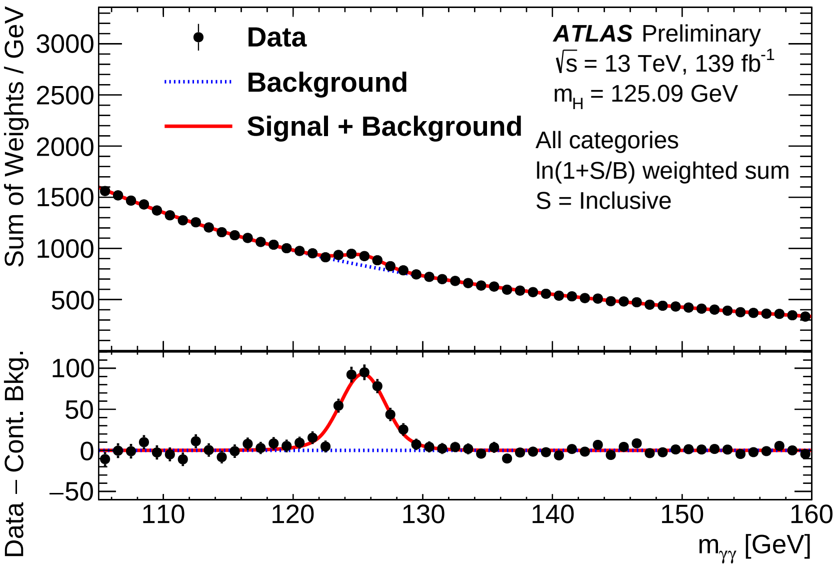

Figure 5.18: The inclusive diphoton invariant mass distribution of events from all analysis categories. The data events (dots) in each category are weighted by $\ln(1+S/B)$, where S and B are the expected signal and background yields in this category within the smallest $m_{\gamma\gamma}$ window containing 90% of the signal events. The fitted signal plus background PDFs from all categories are also weighted and summed, shown as the solid line. The blue dotted line represents the weighted sum of the fitted background functions from all categories.

are 7.5 (6.1) σ, 5.6 (2.8) σ, and 4.7 (5.0) σ, respectively. The expected significance for the ZH process is 1.7 σ, and no excess over its background is observed in data. The best-fit values of the production cross-sections and their uncertainties are summarized in Figure 5.20 and Table 5.10. The correlations between these measurements are shown in Figure 5.21. Compared to Ref. [65], correlations between measurements are reduced, and in particular, the correlation between the ggF and VBF measurements is now 14%, corresponding to a 30% reduction.

The largest systematic uncertainty of a theoretical nature in these measurements arises from the modeling of the parton showering and underlying event, and its impact on the measured cross sections ranges from around 11% for the VBF process to around 2% for the ggF and VH processes. For the $gg \to H$ and VH categories, the leading experimental systematic uncertainty arises from the modeling of background $m_{\gamma\gamma}$ distribution, and it is around 4% for these production processes. For the VBF and ttH processes, the leading experimental uncertainty is related to the measurement of jets, and it can be as large as 6%. Table 5.11 lists the uncertainties of the cross section measurements according to their origins.

The compatibility between the measurement and the SM prediction corresponds to a p-value of 3%, corresponding to a 1.9σ deviation from the SM. The difference is mainly due to a larger than expected yield for the WH process, and a smaller than expected yield for the ZH process. The correlation coefficient between these two measurements is -41%, as shown in Figure 5.21.

If WH and ZH production are considered together as a single VH process, its cross-section is measured to be $\sigma_{VH} = 5.9 \pm 1.4\,\text{fb} = 5.9 \pm 1.4\,\text{(stat.)} \pm 0.4\,\text{(syst.)}$ fb, compared to an expectation of $\sigma_{VH,\text{exp}} = 4.53 \pm 0.12$ fb in the SM. For this measurement,

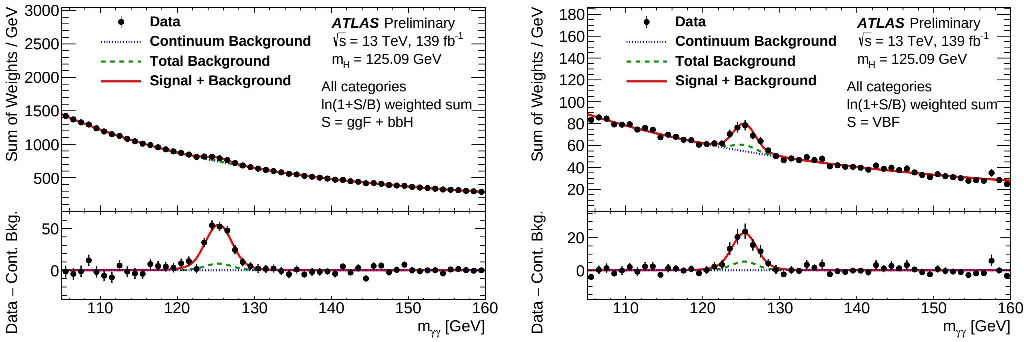

(a) ggF+ bbH (b) VBF

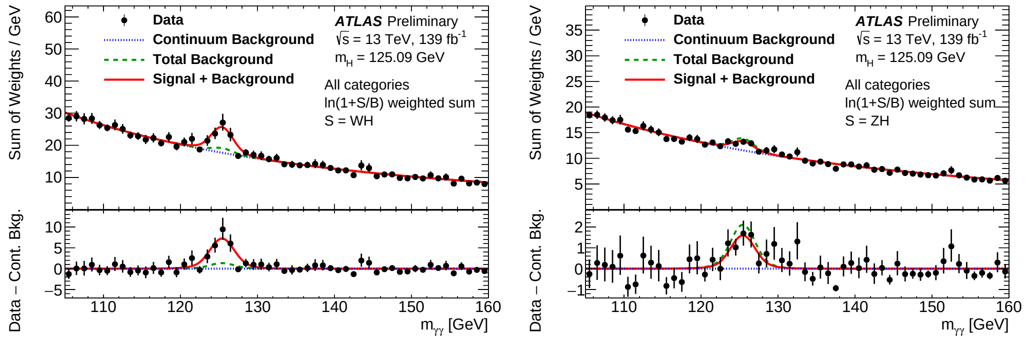

(c) WH (d) ZH

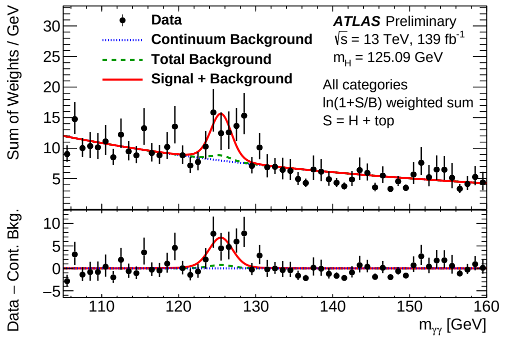

(e) ttH+ tH

Figure 5.19: Combined diphoton invariant mass distributions for categories targeting the same production processes. The data (black dots) is weighted by $\ln(1+S/B)$ where S and B are respectively the expected signal and background yields in the smallest $m_{\gamma\gamma}$ window containing 90% of the signal events. In this calculation, only Higgs boson events from the targeted production processes are considered as signal events. Higgs boson events from other processes as well as the continuum background events are considered as background. The fitted signal plus background PDFs from the relevant categories are also weighted and summed, and represented by a solid line. The blue dotted line represents the weighted sum of the fitted continuum background PDFs, while the dashed line combines the weighted contributions of continuum background and other Higgs boson events.

Table 5.10: Best-fit values and uncertainties for the production cross sections of the Higgs boson times the $H \to \gamma\gamma$ branching ratio. The total uncertainties are decomposed into components for data statistics (Stat.), and systematic uncertainties (Syst.). SM predictions are shown for the cross section of each production process. These are obtained from the total cross-sections and associated uncertainties reported in Ref. [42], multiplied by an acceptance factor for the region $|y_H| < 2.5$ computed using the Higgs boson simulation samples described in Section 5.2.2.

Process	Value	Uncertainty [fb]			SM pred.
($\|y_H\| < 2.5$)	[fb]	Total	Stat.	Syst.	[fb]
ggF + $b\bar{b}H$	104	$^{+11}_{-11}$	$^{+8}_{-8}$	$^{+7}_{-6}$	102 ± 5
VBF	10.7	$^{+2.1}_{-1.9}$	± 1.4	$^{+1.4}_{-1.3}$	8.0 ± 0.2
WH	6.4	$^{+1.5}_{-1.4}$	$^{+1.5}_{-1.3}$	$^{+0.4}_{-0.3}$	2.7 ± 0.1
ZH	-1.2	$^{+1.1}_{-1.0}$	$^{+1.1}_{-1.0}$	± 0.1	$1.8\ ^{+0.1}_{-0.1}$
$t\bar{t}H$+ tH	1.2	$^{+0.4}_{-0.3}$	± 0.3	± 0.1	1.3 ± 0.1

Table 5.11: The contribution of groups of systematic uncertainties to the total error on the observed cross section times branching ratio. This is shown as the uncertainty due to each group of systematic uncertainties ($\Delta\sigma$), as a fraction of the total observed cross section (σ). For each group of uncertainties, asymmetric errors are assigned. Here $\Delta\sigma$ shows the impact of systematic variations on σ.

	ggF+ $b\bar{b}H$	VBF	WH	ZH	$t\bar{t}H$+ tH
Uncertainty source	$\Delta\sigma$[%]	$\Delta\sigma$[%]	$\Delta\sigma$[%]	$\Delta\sigma$[%]	$\Delta\sigma$[%]
Underlying Event and Parton Shower (UEPS)	±2.3	±10	< ±1	±9.6	±3.5
Modeling of Heavy Flavor Jets in non-$t\bar{t}H$ Processes	< ±1	< ±1	< ±1	< ±1	±1.3
Higher-Order QCD Terms (QCD)	±1.6	< ±1	< ±1	±1.9	< ±1
Parton Distribution Function and α_S Scale (PDF+α_S)	< ±1	±1.1	< ±1	±1.9	< ±1
Photon Energy Resolution (PER)	±2.9	±2.4	±2.0	±1.3	±4.9
Photon Energy Scale (PES)	< ±1	< ±1	< ±1	±3.4	±2.2
Jet/$E_{\mathrm{T}}^{\mathrm{miss}}$	±1.6	±5.5	±1.2	±4.0	±3.0
Photon Efficiency	±2.5	±2.3	±2.4	±1.4	±2.4
Background Modeling	±4.1	±4.7	±2.8	±18	±2.4
Flavor Tagging	< ±1	< ±1	< ±1	< ±1	< ±1
Leptons	< ±1	< ±1	< ±1	< ±1	< ±1
Pileup	±1.8	±2.7	±2.1	±3.8	±1.1
Luminosity and Trigger	±2.1	±2.1	±2.3	±1.1	±2.3
Higgs Boson Mass	< ±1	< ±1	< ±1	±3.7	±1.9

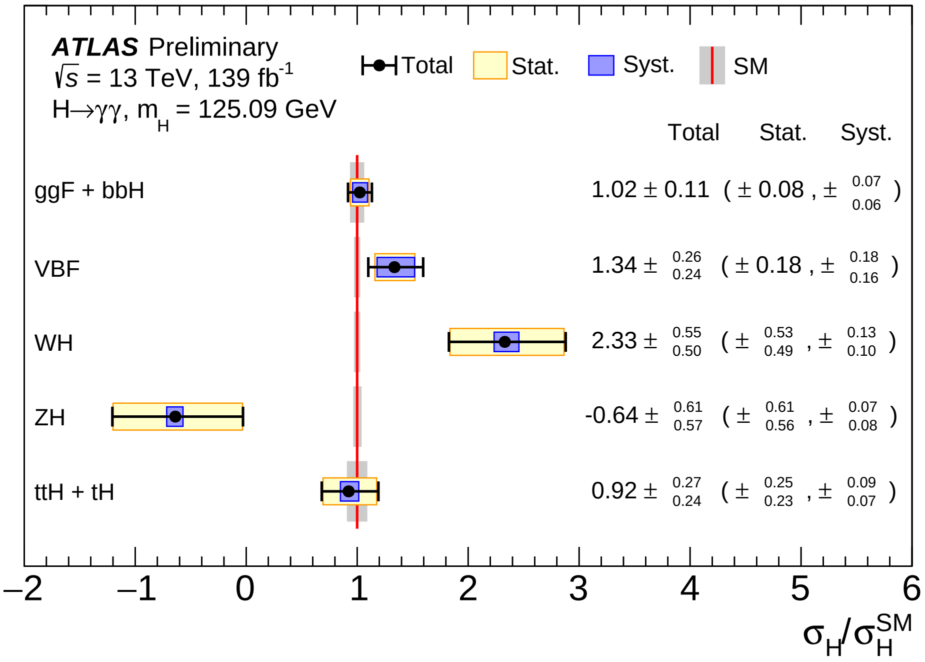

Figure 5.20: Cross sections times branching fraction for ggF+ bbH, VBF, VH and ttH+ tH production, normalized to their SM predictions. The values are obtained from a simultaneous fit to all categories. The black error bars, blue boxes and yellow boxes show the total, systematic, and statistical uncertainties in the measurements, respectively. The gray bands show the theory uncertainties in the predictions, including uncertainties due to missing higher-order terms in the perturbative QCD calculations and choices of parton distribution functions and value of α_{S}.

the compatibility between the observation and the SM prediction corresponds to a p-value of 50%.

An upper limit on the rate of the tH production can be obtained by treating the normalization of other Higgs boson production processes as nuisance parameters. Using the CL_s method [208], this excludes a tH production rate of eight times its SM prediction or greater at 95% CL.

5.9.2 Cross-sections in STXS regions

A measurement of the cross-sections defined in the STXS scheme is performed based on the regions described in Section 5.1. In order to avoid large uncertainties and large absolute correlations between the measurements, some of the regions are merged as follows:

- In the $gg \to H$ process, the four bins in regions of $350 < m_{jj} < 700$ GeV and $m_{jj} > 700$ GeV, are merged into a single region corresponding to $m_{\gamma\gamma} > 350$ GeV. The $p_{\mathrm{T}}^{H} > 650$ GeV bin is also merged with the $450 < p_{\mathrm{T}}^{H} < 650$ GeV bin into a single region corresponding to $p_{\mathrm{T}}^{H} > 450$ GeV.
- In the $qq' \to Hqq'$ process, the 0-jet and 1-jet regions are combined, as well as the regions corresponding to $m_{jj} < 60$ GeV and $120 < m_{jj} < 350$ GeV. The splits at $p_{\mathrm{T}}^{Hjj} = 25$ GeV are removed as for the $gg \to H$ process, and a single $p_{\mathrm{T}}^{H} > 200$ GeV region is also defined by merging together the two regions

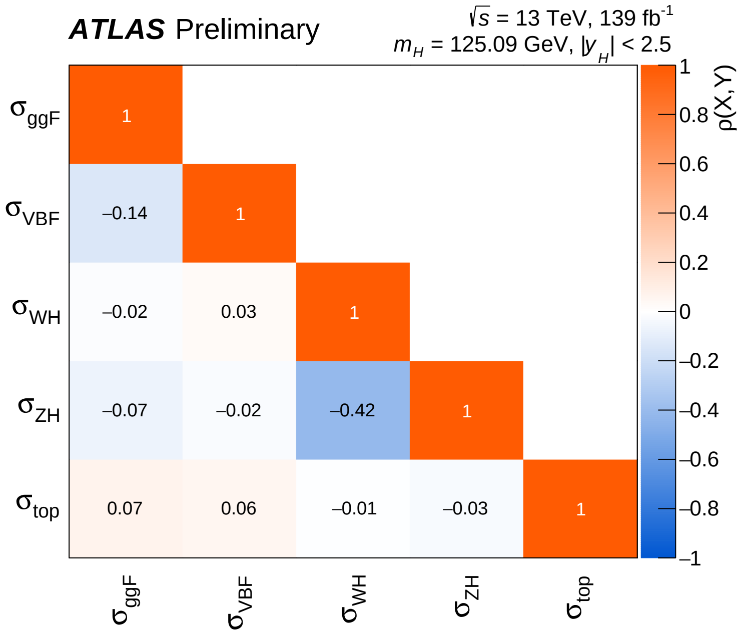

Figure 5.21: Correlation matrix for the measurement of production cross sections of the Higgs boson.

corresponding to $350 < m_{jj} < 700$ GeV and $m_{jj} > 700$ GeV.

- In both the $q\bar{q}' \to WH$ and $pp \to ZH$ processes, only the two regions $p_T^V < 150$ GeV and $p_T^V > 150$ GeV are retained, removing the intermediate splits at $p_T^V = 75$ GeV and $p_T^V = 250$ GeV.
- In the ttH process, a $p_T^H > 200$ GeV region is defined, combining the $200 < p_T^H < 300$ GeV and $p_T^H > 300$ GeV regions.
- the $tHqb$ and tHW regions are merged into a single tH region.

This scheme is defined based on the SM expectation, independently of the observed data. It is illustrated in Figure 5.22.

In each case the acceptance parameters for the combined regions are derived from those of the regions that are merged, assuming SM values for their production rates and including the SM uncertainties on these rates as systematic uncertainties.

Results are shown in Table 5.12 and Figure 5.23. The correlation matrix of the measurements is shown in Figure 5.24. The relative uncertainties on the measurements range from 20% to more than 100%. Smaller uncertainties are associated with the 0-jet and 1-jet regions of $gg \to H$, as well as the $200 < p_T^H < 300$ GeV region of $gg \to H$ and the $m_{jj} > 700$ GeV region of $qq' \to Hqq'$. Larger uncertainties occur in particular in regions of high p_T^H and p_T^V, as well as the low-m_{jj} regions of $qq' \to Hqq'$. The systematic component of uncertainties is everywhere smaller than the statistical component, but reaches similar values for the 0-jet regions of $gg \to H$. No significant deviations from the SM expectation are observed and the compatibility between the measurements and the SM predictions corresponds to a p-value of 60%.

5.10 Conclusion

Higgs boson production is measured in the diphoton channel using 139 fb^{-1} of data, corresponding to the full dataset collected by ATLAS during Run 2 of the LHC. The

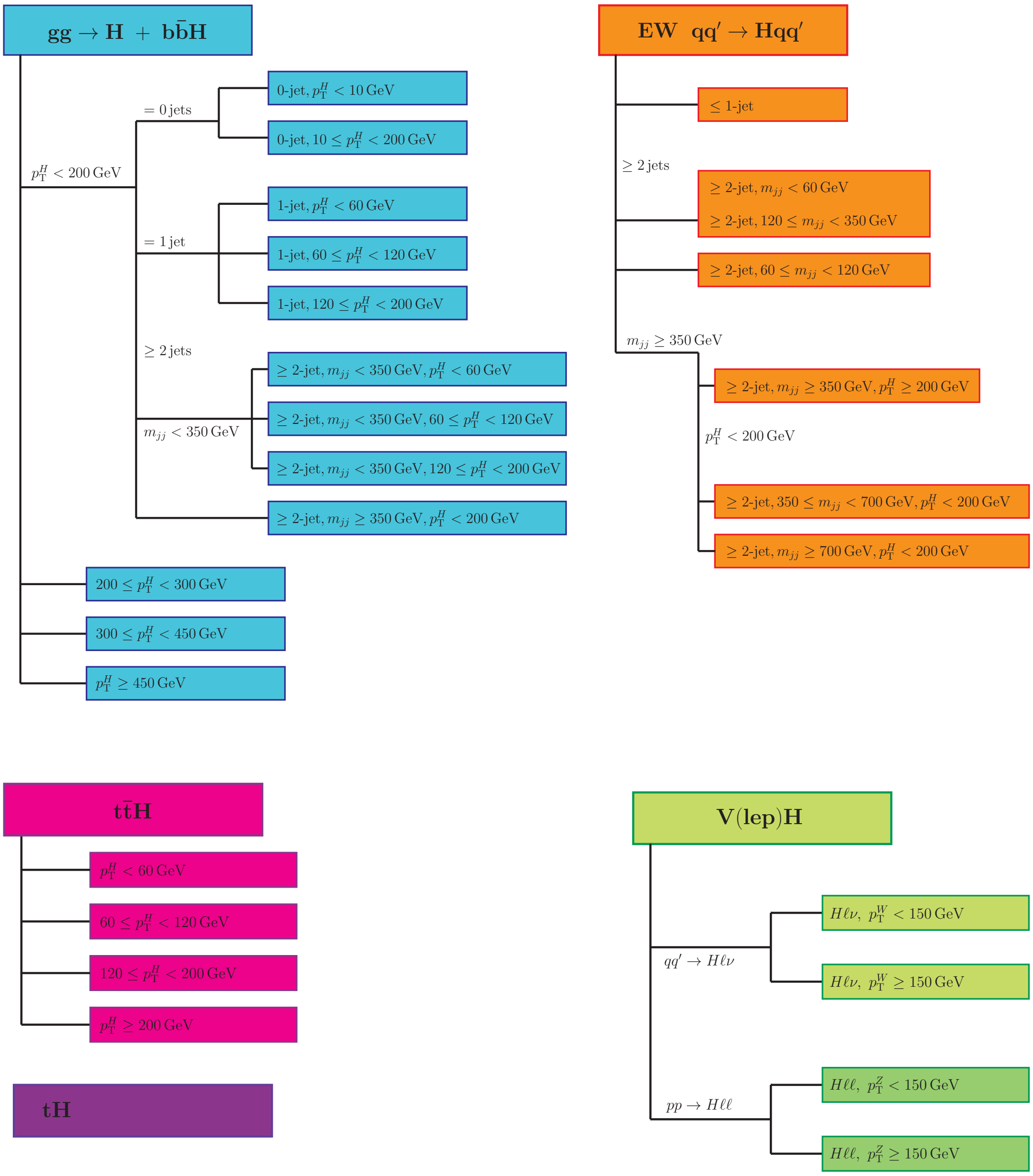

Figure 5.22: Summary of the 27 regions for which STXS measurements are reported.

Table 5.12: Best-fit values and uncertainties for the production cross-section times $H \to \gamma\gamma$ branching ratio ($\sigma_i \times B_{\gamma\gamma}$) in each STXS region. The values for the $gg \to H$ process also include the contributions from bbH production. The total uncertainties are decomposed into components for data statistics (Stat.) and systematic uncertainties (Syst.). SM predictions [42] are also shown for each quantity with their total uncertainties.

STXS region ($\sigma_i \times B_{\gamma\gamma}$)	Value	Uncertainty [fb]			SM prediction
	[fb]	Total	Stat.	Syst.	[fb]
$gg \to H$ (0-jet, $p_{\mathrm{T}}^{H} \leq p_{\mathrm{T}}^{H} < 10\,\mathrm{GeV}$)	11.4	$^{+4.7}_{-4.5}$	$^{+3.9}_{-3.9}$	$^{+2.7}_{-2.4}$	15.0 ± 2.0
$gg \to H$ (0-jet, $p_{\mathrm{T}}^{H} \leq p_{\mathrm{T}}^{H} < 200\,\mathrm{GeV}$)	54.7	$^{+9.4}_{-8.9}$	$^{+7.0}_{-7.0}$	$^{+6.1}_{-5.2}$	$46.8^{+3.5}_{-3.6}$
$gg \to H$ (1-jet, $p_{\mathrm{T}}^{H} \leq p_{\mathrm{T}}^{H} < 60\,\mathrm{GeV}$)	13.4	$^{+6.5}_{-6.3}$	$^{+5.9}_{-5.9}$	$^{+2.8}_{-2.4}$	14.7 ± 2.1
$gg \to H$ (1-jet, $p_{\mathrm{T}}^{H} \leq p_{\mathrm{T}}^{H} < 120\,\mathrm{GeV}$)	12.1	$^{+4.0}_{-3.8}$	$^{+3.8}_{-3.8}$	$^{+1.5}_{-0.6}$	10.2 ± 1.5
$gg \to H$ (1-jet, $p_{\mathrm{T}}^{H} \leq p_{\mathrm{T}}^{H} < 200\,\mathrm{GeV}$)	1.2	$^{+0.9}_{-0.9}$	$^{+0.9}_{-0.9}$	$^{+0.2}_{-0.2}$	1.7 ± 0.3
$gg \to H$ ($\geq$ 2-jets, $m_{jj} < 350\,\mathrm{GeV}$, $60 \leq p_{\mathrm{T}}^{H} < 60\,\mathrm{GeV}$)	1.2	$^{+3.4}_{-3.2}$	$^{+3.1}_{-3.0}$	$^{+1.5}_{-1.0}$	2.6 ± 0.6
$gg \to H$ ($\geq$ 2-jets, $m_{jj} < 350\,\mathrm{GeV}$, $120 \leq p_{\mathrm{T}}^{H} < 120\,\mathrm{GeV}$)	1.1	$^{+2.4}_{-2.4}$	$^{+2.3}_{-2.3}$	$^{+0.5}_{-0.5}$	4.1 ± 0.9
$gg \to H$ ($\geq$ 2-jets, $m_{jj} < 350\,\mathrm{GeV}$, $200 \leq p_{\mathrm{T}}^{H} < 200\,\mathrm{GeV}$)	1.3	$^{+1.0}_{-1.0}$	$^{+0.9}_{-0.9}$	$^{+0.4}_{-0.3}$	2.1 ± 0.6
$gg \to H$ ($\geq$ 2-jets, $m_{jj} \geq 350\,\mathrm{GeV}$, $200 \leq p_{\mathrm{T}}^{H} < 200\,\mathrm{GeV}$)	4.5	$^{+2.0}_{-1.8}$	$^{+1.8}_{-1.7}$	$^{+0.9}_{-0.6}$	2.0 ± 0.25
$gg \to H$ ($200 \leq p_{\mathrm{T}}^{H} < 300\,\mathrm{GeV}$)	1.0	$^{+0.4}_{-0.4}$	$^{+0.4}_{-0.4}$	$^{+0.1}_{-0.1}$	1.04 ± 0.3
$gg \to H$ ($300 \leq p_{\mathrm{T}}^{H} < 450\,\mathrm{GeV}$)	0.05	$^{+0.14}_{-0.12}$	$^{+0.13}_{-0.12}$	$^{+0.03}_{-0.02}$	0.24 ± 0.08
$gg \to H$ ($p_{\mathrm{T}}^{H} \geq 450\,\mathrm{GeV}$)	0.07	$^{+0.06}_{-0.05}$	$^{+0.06}_{-0.05}$	$^{+0.01}_{-0.00}$	0.04 ± 0.02
$qq' \to Hqq'$ ($\leq$ 1-jet)	7.4	$^{+5.9}_{-5.2}$	$^{+5.5}_{-4.9}$	$^{+2.1}_{-1.8}$	$4.8^{+0.1}_{-0.1}$
$qq' \to Hqq'$ ($\geq$ 2-jets, $0 \leq m_{jj} < 60\,\mathrm{GeV}$) + $qq' \to Hqq'$ ($\geq$ 2-jets, $120 \leq m_{jj} < 350\,\mathrm{GeV}$)	5.2	$^{+3.0}_{-2.8}$	$^{+2.8}_{-2.7}$	$^{+1.2}_{-0.9}$	1.65 ± 0.05
$qq' \to Hqq'$ ($\geq$ 2-jets, $60 \leq m_{jj} < 120\,\mathrm{GeV}$)	0.9	$^{+1.1}_{-1.0}$	$^{+1.1}_{-1.0}$	$^{+0.3}_{-0.3}$	1.20 ± 0.04
$qq' \to Hqq'$ ($\geq$ 2-jets, $350 \leq m_{jj} < 700\,\mathrm{GeV}$, $200 \leq p_{\mathrm{T}}^{H} < 200\,\mathrm{GeV}$)	1.0	$^{+0.9}_{-0.8}$	$^{+0.8}_{-0.7}$	$^{+0.5}_{-0.4}$	1.24 ± 0.04
$qq' \to Hqq'$ ($\geq$ 2-jets, $m_{jj} \geq 700\,\mathrm{GeV}$, $200 \leq p_{\mathrm{T}}^{H} < 200\,\mathrm{GeV}$)	1.8	$^{+0.6}_{-0.5}$	$^{+0.5}_{-0.4}$	$^{+0.4}_{-0.3}$	1.67 ± 0.05
$qq' \to Hqq'$ ($\geq$ 2-jets, $m_{jj} \geq 350\,\mathrm{GeV}$, $p_{\mathrm{T}}^{H} <\ \mathrm{GeV}$)	0.5	$^{+0.2}_{-0.2}$	$^{+0.2}_{-0.1}$	$^{+0.07}_{-0.06}$	0.36 ± 0.01
$qq \to H\ell\nu$ ($p_{\mathrm{T}}^{V} < 150\,\mathrm{GeV}$)	1.8	$^{+0.5}_{-0.5}$	$^{+0.5}_{-0.5}$	$^{+0.2}_{-0.2}$	0.76 ± 0.02
$qq \to H\ell\nu$ ($p_{\mathrm{T}}^{V} \geq 150\,\mathrm{GeV}$)	0.3	$^{+0.1}_{-0.1}$	$^{+0.1}_{-0.1}$	$^{+0.02}_{-0.02}$	0.124 ± 0.005
$qq \to H\ell\ell$ ($p_{\mathrm{T}}^{V} < 150\,\mathrm{GeV}$)	-0.5	$^{+0.4}_{-0.4}$	$^{+0.4}_{-0.4}$	$^{+0.1}_{-0.1}$	0.45 ± 0.02
$qq \to H\ell\ell$ ($p_{\mathrm{T}}^{V} \geq 150\,\mathrm{GeV}$)	-0.01	$^{+0.10}_{-0.09}$	$^{+0.10}_{-0.08}$	$^{+0.01}_{-0.02}$	0.092 ± 0.011
$t\bar{t}H$ ($p_{\mathrm{T}}^{H} < 60\,\mathrm{GeV}$)	0.2	$^{+0.2}_{-0.2}$	$^{+0.2}_{-0.2}$	$^{+0.06}_{-0.05}$	0.27 ± 0.04
$t\bar{t}H$ ($60 \leq p_{\mathrm{T}}^{H} < 120\,\mathrm{GeV}$)	0.3	$^{+0.2}_{-0.2}$	$^{+0.2}_{-0.2}$	$^{+0.04}_{-0.03}$	$0.40^{+0.05}_{-0.04}$
$t\bar{t}H$ ($120 \leq p_{\mathrm{T}}^{H} < 200\,\mathrm{GeV}$)	0.3	$^{+0.2}_{-0.2}$	$^{+0.2}_{-0.2}$	$^{+0.05}_{-0.04}$	0.29 ± 0.03
$t\bar{t}H$ ($p_{\mathrm{T}}^{H} \geq 200\,\mathrm{GeV}$)	0.2	$^{+0.09}_{-0.08}$	$^{+0.09}_{-0.08}$	$^{+0.02}_{-0.02}$	0.18 ± 0.02
tH	0.2	$^{+0.6}_{-0.5}$	$^{+0.6}_{-0.4}$	$^{+0.2}_{-0.2}$	$0.19^{+0.01}_{-0.02}$

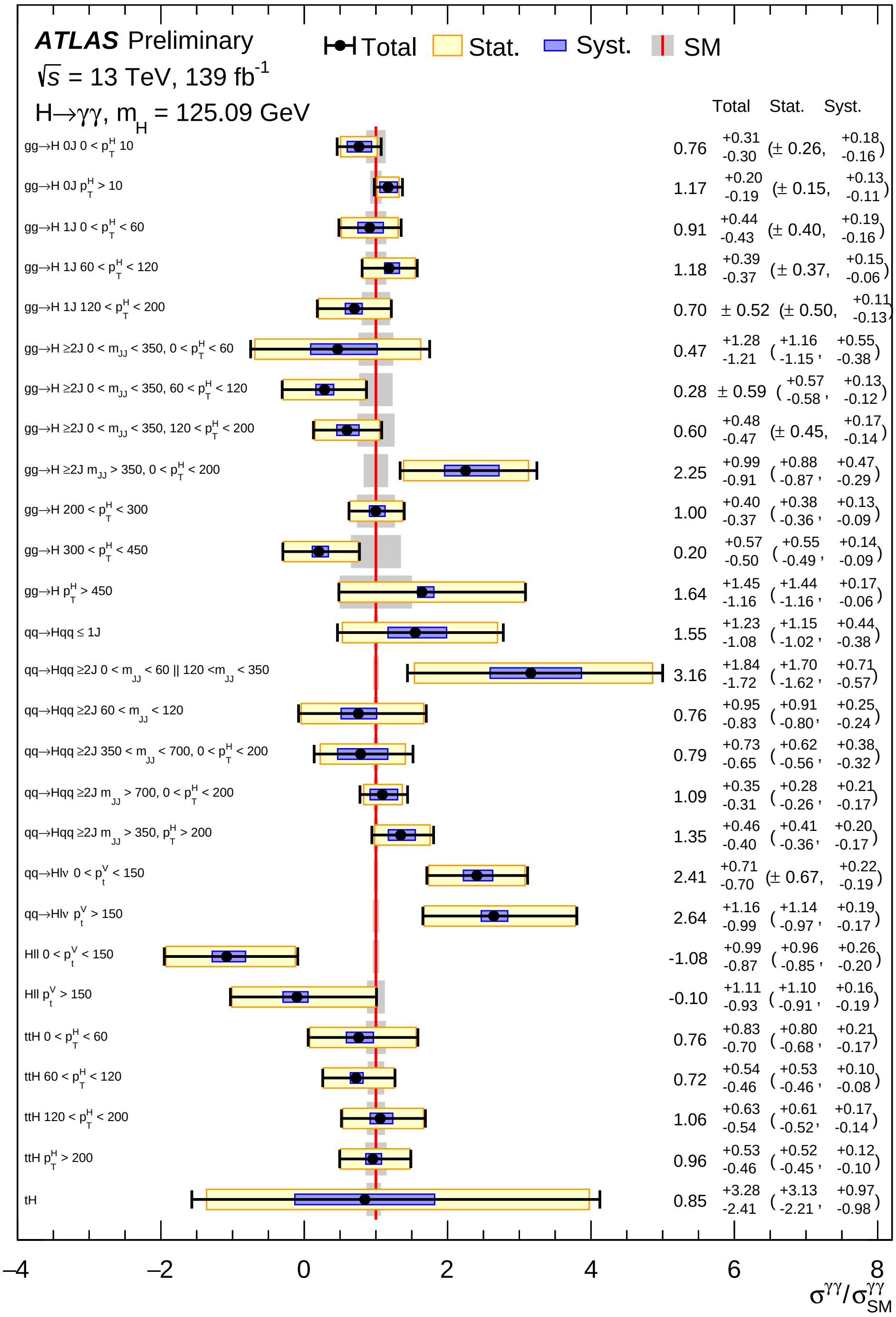

Figure 5.23: Best-fit values and uncertainties for the cross sections in each measurement region, normalized to the SM predictions for the various parameters. The values for the $gg \to H$ process also include the contributions from bbH production. The black error bars, blue boxes and yellow boxes show the total, systematic, and statistical uncertainties in the measurements, respectively. The gray bands show the theory uncertainties in the predictions, including uncertainties due to missing higher-order terms in the perturbative QCD calculations and choices of parton distribution functions and value of α_S.

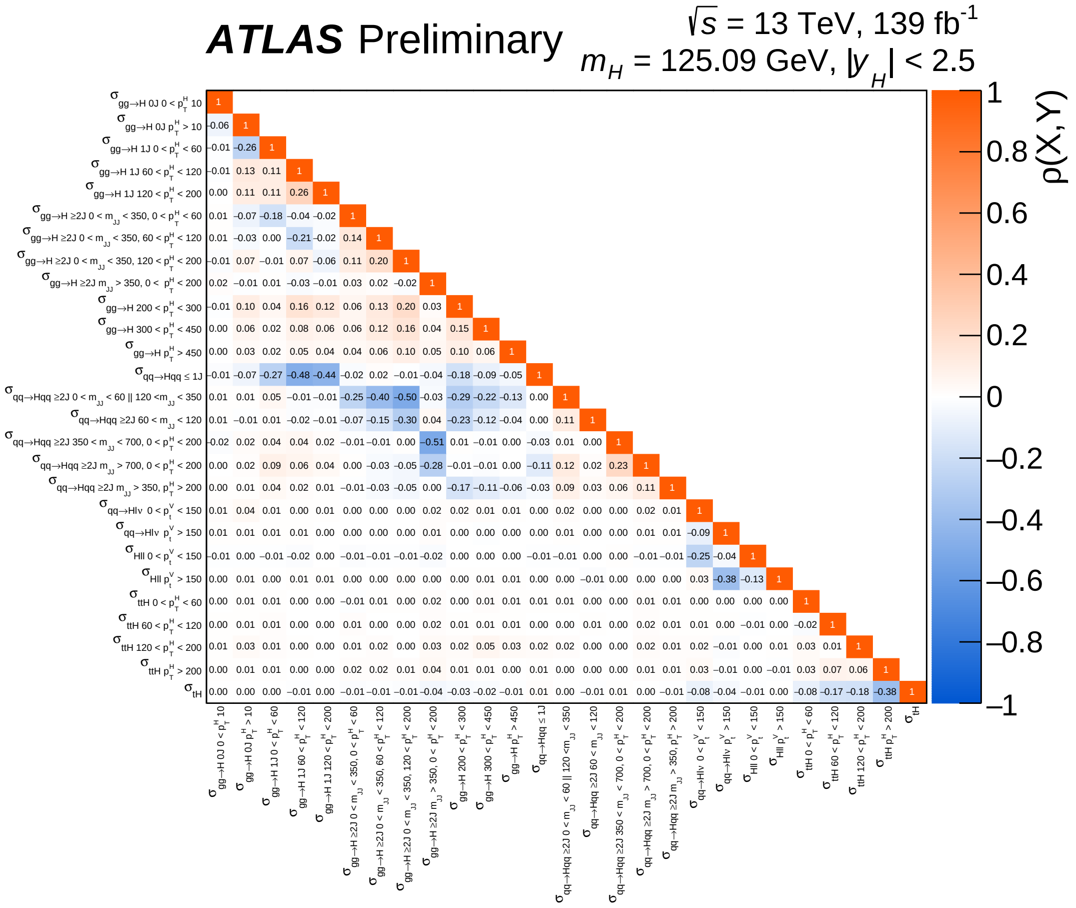

	$\sigma_{gg\to H\ 0J\ 0 < p_T^H\ 10}$	$\sigma_{gg\to H\ 0J\ p_T^H > 10}$	$\sigma_{gg\to H\ 1J\ 0 < p_T^H < 60}$	$\sigma_{gg\to H\ 1J\ 60 < p_T^H < 120}$	$\sigma_{gg\to H\ 1J\ 120 < p_T^H < 200}$	$\sigma_{gg\to H\ \geq 2J\ 0 < m_{JJ} < 350,\ 0 < p_T^H < 60}$	$\sigma_{gg\to H\ \geq 2J\ 0 < m_{JJ} < 350,\ 60 < p_T^H < 120}$	$\sigma_{gg\to H\ \geq 2J\ 0 < m_{JJ} < 350,\ 120 < p_T^H < 200}$	$\sigma_{gg\to H\ \geq 2J\ m_{JJ} > 350,\ 0 < p_T^H < 200}$	$\sigma_{gg\to H\ 200 < p_T^H < 300}$	$\sigma_{gg\to H\ 300 < p_T^H < 450}$	$\sigma_{gg\to H\ p_T^H > 450}$	$\sigma_{qq\to Hqq\ \leq 1J}$	$\sigma_{qq\to Hqq\ \geq 2J\ 0 < m_{JJ} < 60\ \Vert\ 120 < m_{JJ} < 350}$	$\sigma_{qq\to Hqq\ \geq 2J\ 60 < m_{JJ} < 120}$	$\sigma_{qq\to Hqq\ \geq 2J\ 350 < m_{JJ} < 700,\ 0 < p_T^H < 200}$	$\sigma_{qq\to Hqq\ \geq 2J\ m_{JJ} > 700,\ 0 < p_T^H < 200}$	$\sigma_{qq\to Hqq\ \geq 2J\ m_{JJ} > 350,\ p_T^H > 200}$	$\sigma_{qq\to Hl\nu\ 0 < p_t^V < 150}$	$\sigma_{qq\to Hl\nu\ p_t^V > 150}$	$\sigma_{Hll\ 0 < p_t^V < 150}$	$\sigma_{Hll\ p_t^V > 150}$	$\sigma_{ttH\ 0 < p_T^H < 60}$	$\sigma_{ttH\ 60 < p_T^H < 120}$	$\sigma_{ttH\ 120 < p_T^H < 200}$	$\sigma_{ttH\ p_T^H > 200}$	σ_{tH}
$\sigma_{gg\to H\ 0J\ 0 < p_T^H\ 10}$	1																										
$\sigma_{gg\to H\ 0J\ p_T^H > 10}$	−0.06	1																									
$\sigma_{gg\to H\ 1J\ 0 < p_T^H < 60}$	−0.01	−0.26	1																								
$\sigma_{gg\to H\ 1J\ 60 < p_T^H < 120}$	−0.01	0.13	0.11	1																							
$\sigma_{gg\to H\ 1J\ 120 < p_T^H < 200}$	0.00	0.11	0.11	0.26	1																						
$\sigma_{gg\to H\ \geq 2J\ 0 < m_{JJ} < 350,\ 0 < p_T^H < 60}$	0.01	−0.07	−0.18	−0.04	−0.02	1																					
$\sigma_{gg\to H\ \geq 2J\ 0 < m_{JJ} < 350,\ 60 < p_T^H < 120}$	0.01	−0.03	0.00	−0.21	−0.02	0.14	1																				
$\sigma_{gg\to H\ \geq 2J\ 0 < m_{JJ} < 350,\ 120 < p_T^H < 200}$	−0.01	0.07	−0.01	0.07	−0.06	0.11	0.20	1																			
$\sigma_{gg\to H\ \geq 2J\ m_{JJ} > 350,\ 0 < p_T^H < 200}$	0.02	−0.01	0.01	−0.03	−0.01	0.03	0.02	−0.02	1																		
$\sigma_{gg\to H\ 200 < p_T^H < 300}$	−0.01	0.10	0.04	0.16	0.12	0.06	0.13	0.20	0.03	1																	
$\sigma_{gg\to H\ 300 < p_T^H < 450}$	0.00	0.06	0.02	0.08	0.06	0.06	0.12	0.16	0.04	0.15	1																
$\sigma_{gg\to H\ p_T^H > 450}$	0.00	0.03	0.02	0.05	0.04	0.04	0.06	0.10	0.05	0.10	0.06	1															
$\sigma_{qq\to Hqq\ \leq 1J}$	−0.01	−0.07	−0.27	−0.48	−0.44	−0.02	0.02	−0.01	−0.04	−0.18	−0.09	−0.05	1														
$\sigma_{qq\to Hqq\ \geq 2J\ 0 < m_{JJ} < 60\ \Vert\ 120 < m_{JJ} < 350}$	0.01	0.01	0.05	−0.01	−0.01	−0.25	−0.40	−0.50	−0.03	−0.29	−0.22	−0.13	0.00	1													
$\sigma_{qq\to Hqq\ \geq 2J\ 60 < m_{JJ} < 120}$	0.01	−0.01	0.01	−0.02	−0.01	−0.07	−0.15	−0.30	0.04	−0.23	−0.12	−0.04	0.00	0.11	1												
$\sigma_{qq\to Hqq\ \geq 2J\ 350 < m_{JJ} < 700,\ 0 < p_T^H < 200}$	−0.02	0.02	0.04	0.04	0.02	−0.01	−0.01	0.00	−0.51	0.01	−0.01	0.00	−0.03	0.01	0.00	1											
$\sigma_{qq\to Hqq\ \geq 2J\ m_{JJ} > 700,\ 0 < p_T^H < 200}$	0.00	0.02	0.09	0.06	0.04	0.00	−0.03	−0.05	−0.28	−0.01	−0.01	0.00	−0.11	0.12	0.02	0.23	1										
$\sigma_{qq\to Hqq\ \geq 2J\ m_{JJ} > 350,\ p_T^H > 200}$	0.00	0.01	0.04	0.02	0.01	−0.01	−0.03	−0.05	0.00	−0.17	−0.11	−0.06	−0.03	0.09	0.03	0.06	0.11	1									
$\sigma_{qq\to Hl\nu\ 0 < p_t^V < 150}$	0.01	0.04	0.01	0.00	0.01	0.00	0.00	0.00	0.02	0.02	0.01	0.01	0.00	0.02	0.00	0.00	0.02	0.01	1								
$\sigma_{qq\to Hl\nu\ p_t^V > 150}$	0.01	0.01	0.01	0.01	0.00	0.00	0.00	0.00	0.01	0.00	0.00	0.00	0.00	0.01	0.00	0.00	0.01	0.01	−0.09	1							
$\sigma_{Hll\ 0 < p_t^V < 150}$	−0.01	0.00	−0.01	−0.02	0.00	−0.01	−0.01	−0.01	−0.02	0.00	0.00	0.00	−0.01	−0.01	0.00	0.00	−0.01	−0.01	−0.25	−0.04	1						
$\sigma_{Hll\ p_t^V > 150}$	0.00	0.01	0.00	0.01	0.01	0.00	0.00	0.00	0.00	0.00	0.01	0.01	0.00	0.00	−0.01	0.00	0.00	0.00	0.03	−0.38	−0.13	1					
$\sigma_{ttH\ 0 < p_T^H < 60}$	0.00	0.01	0.01	0.00	0.00	−0.01	0.01	0.00	0.02	0.00	0.01	0.01	0.01	0.01	0.00	0.00	0.01	0.01	0.00	0.00	0.00	0.00	1				
$\sigma_{ttH\ 60 < p_T^H < 120}$	0.00	0.01	0.01	0.00	0.00	0.01	0.00	0.00	0.02	0.01	0.01	0.01	0.00	0.00	0.01	0.00	0.02	0.01	0.01	0.00	−0.01	0.00	−0.02	1			
$\sigma_{ttH\ 120 < p_T^H < 200}$	0.01	0.03	0.01	0.00	0.00	0.01	0.02	0.00	0.03	0.02	0.05	0.03	0.02	0.02	0.00	0.00	0.02	0.01	0.02	−0.01	0.00	0.01	0.03	0.01	1		
$\sigma_{ttH\ p_T^H > 200}$	0.00	0.01	0.01	0.00	0.00	0.02	0.02	0.01	0.04	0.01	0.01	0.00	0.01	0.00	0.00	0.00	0.01	0.01	0.03	−0.01	0.00	−0.01	0.03	0.07	0.06	1	
σ_{tH}	0.00	0.00	0.00	−0.01	0.00	−0.01	−0.01	−0.01	−0.04	−0.03	−0.02	−0.01	0.01	0.00	−0.01	0.01	0.00	−0.01	−0.08	−0.04	−0.01	0.00	−0.08	−0.17	−0.18	−0.38	1

Figure 5.24: Correlation matrix for the STXS measurement.

total production cross-section in $|y_H| < 2.5$ is measured to be

$$(\sigma \times B_{\gamma\gamma})_{\text{obs}} = 127 \pm 10\,\text{fb}, \tag{5.9}$$

in good agreement with the SM expectation of 115 ± 5 fb. Cross-sections for the ggF+ bbH, VBF, WH, ZH and ttH+ tH production are also reported, with relative uncertainties ranging from 11% to 58%. Given the large observed correlation between the measurements of WH and ZH cross-sections, a total cross-section for the WH and ZH production processes together is also reported. An upper limit of eight times the SM prediction is set for the associated production of the Higgs boson with a single top quark process. This represents the most stringent experimental constraint on tH production, superseding the result from Ref. [190]. Cross-sections are also presented in 27 regions of Higgs boson production phase space defined in the STXS framework, including additional measurements at high values of p_{T}^{H} and m_{jj} compared to previous analyses.

Chapter 6

Constraint of the Higgs decay width in the diphoton decay channel

The analysis presented in this chapter is currently under development within ATLAS, with its unblinding approval still to be scheduled. My contributions to this analysis range from the production and validation of Monte Carlo samples to the extraction of the final results, and include the parametrization of the signal and interference shape, the optimization of the categorization, the study of the background modeling, the evaluation of the experimental and theoretical systematics, and the implementation of the statistical model.

6.1 Introduction

This chapter presents an analysis aiming at constraining the Higgs decay width using only diphoton events. The main idea is to exploit the interference between the resonant signal $gg \to H \to \gamma\gamma$ and the continuum diphoton background $gg \to \gamma\gamma$ in the channel. As studied in Refs. [57, 58], the presence of such interference term, not taken into account in other $H \to \gamma\gamma$ analyses (e.g. the STXS/couplings of Chapter 5), produces both a shift in the invariant mass of the diphoton system (of the order of 100 MeV) and a reduction of the observed cross section (order of 2% the SM value), as already discussed in Section 1.6.1. These two effects are known to be dependent on the Higgs width Γ_H, therefore sensitive to any possible deviation of its value from the SM prediction Γ_{SM} due to new physics. If the Higgs width differs from the SM prediction, the couplings to gluons and photons should then change accordingly, in order to maintain roughly SM signal yields, as is in reasonable agreement with current measurements at the LHC.
The analysis uses the full Run 2 dataset of proton-proton collisions at $\sqrt{s} = 13$ TeV collected by the ATLAS experiment, amounting to about 139 fb^{-1} of integrated luminosity.

In this analysis, the interference term is separately described from the signal and background terms, using an analytic function of $m_{\gamma\gamma}$, so that its impact on the shape and normalization of the total PDF can be taken into account at the same time. The sensitivity to the interference effects is obtained by exploiting the strong dependence of the Higgs mass peak shift on a lower cut on the Higgs transverse momentum p_T^H illustrated by Figure 1.10, as presented in Ref. [58]: multiple exclusive p_T regions are defined using rectangular cuts on the $p_T^{\gamma\gamma}$ value of the selected events, thus creating at least one low-p_T category targeting a region of the phase-space highly affected by the interference and other high-p_T categories where the mass shift is expected to be negligible, representing reference regions. Using the expanded PDF, $m_{\gamma\gamma}$ distributions of the events in reconstruction categories are simultaneously fitted in order to place an upper limit on the parameter λ, defined as $\lambda = \frac{\Gamma_H}{\Gamma_{SM}}$. The analysis share an approach common to other $H \to \gamma\gamma$ measurements: the event selection and the modeling of signal and background terms are very similar to the ones described in Chapter 5; on the other hand, the MC samples and the modeling of the interference term are exclusive of this analysis and will be described in detail in the following sections.

6.2 MC inputs

The signal and background samples used in this chapter are exactly those described in Section 5.2.2. Since in this analysis we are not interested in measuring the different production modes, the contributions from all the Higgs processes are merged together (according to their cross sections) to form an inclusive Higgs signal sample.

The gg-interference process is modeled using Sherpa v2.2.11 [172], with the settings `HIGGS_INTERFERENCE_MODE=3`, `HIGGS_INTERFERENCE_ONLY=1`. The order of calculation of the matrix elements is NLO in QCD and the parton shower is based on the Catani-Seymour dipole factorization [177]. The samples are generated using the `NNPDF30_nnlo_as_0118_hessian` PDF set [125]. For the purpose of interference modeling studies, several samples with different values of the Higgs decay width have been produced: $\lambda = 1, 5, 10, 50, 100$.

All events are generated with a m_{H} (Higgs boson mass) of 125 GeV. The generated events are passed through a simulation of the ATLAS detector [135] using the GEANT4 toolkit [136].

6.2.1 Detector simulation and resolution

To model the interference process, SHERPA generates weighted events with weights that may be negative and whose absolute value is in general very close to 0. If we denote w the weights, the statistical error on the interference cross section is

$$\frac{\delta\sigma_I}{\sigma_I} = \frac{\sum w^2}{|\sum w|} \tag{6.1}$$

which is finite but requires a lot of events to become small.
A possible compromise to speed up the processing of this high number of events is to use an approximate description of the detector during the simulation stage. In order to estimate the impact on the resolution of such less accurate simulation, two test signal SHERPA samples with partial MC statistics have been produced using two different detector configurations: the full GEANT4 simulation (FullG4) and an alternative configuration where FastCaloSim is used for the calorimeters while GEANT4 is used for the rest (G4FastCalo). The resolution of the variable X can be assessed from the distribution of

$$\frac{X^{\mathrm{Reco}} - X^{\mathrm{Truth}}}{X^{\mathrm{Truth}}} \tag{6.2}$$

where X can be either $m_{\gamma\gamma}$, $pT_{\gamma 1}$ or $pT_{\gamma 2}$. Event distributions of these three variables for the two test samples are shown in Figure 6.1 and they are fitted with a gaussian function. The fitted σ is reported in all cases and its value is compared between the two detector configurations: G4FastCalo has always a larger σ than FullG4, in particular the relative difference of mass resolution is about 20%. Table 6.1 makes a comparison of the time required to produce the test samples in the two configurations. Despite the large computational cost, it was chosen to simulate the complete detector response for each event nonetheless, because using a less accurate description would result in a significant loss of signal resolution.

	Total	Per event average
FullG4	16.8h	48s
G4FastCalo	0.5h	1.8s

Table 6.1: Summary of the wall-time required by the simulation of FullG4 and G4FastCalo. Numbers are based on a 10k events sample.

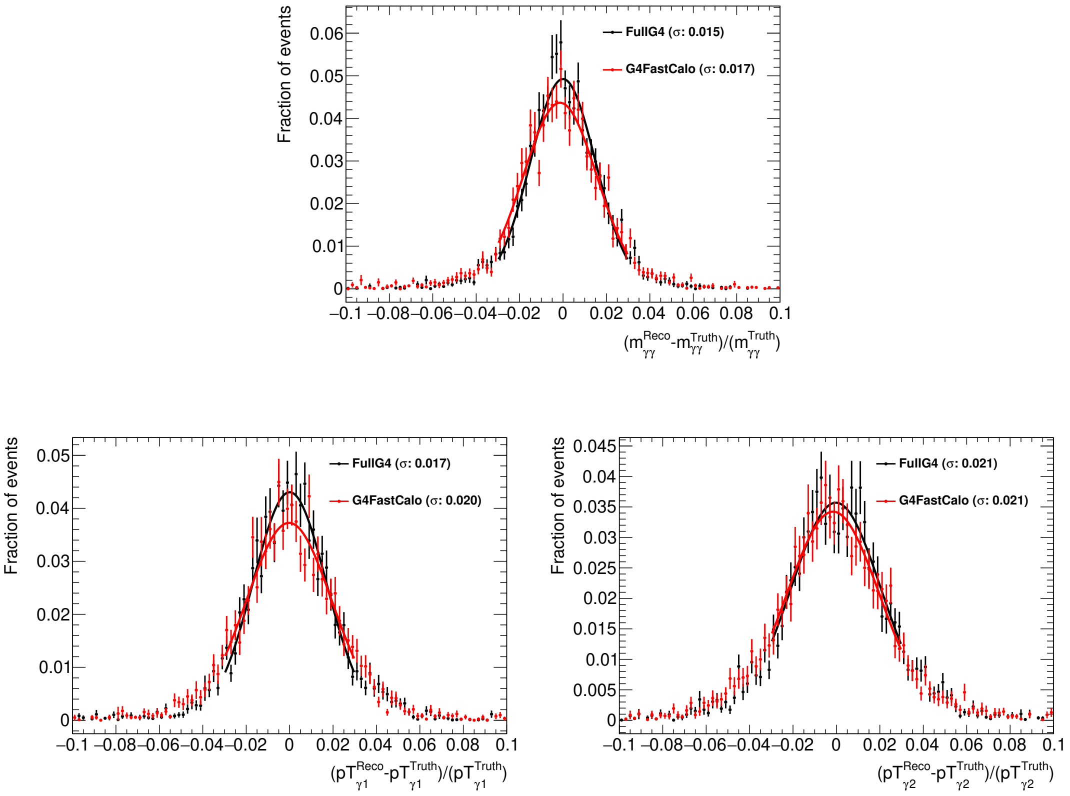

Figure 6.1: Comparison in terms of resolution between the FullG4 (black) and G4FastCalo (red) detector simulations.

6.3 Modeling of the diphoton events

The $m_{\gamma\gamma}$ distribution of the selected events can be described by the sum of the signal (S), background (B) and interference (I) components. The S and B components are very similar to the models defined in Chapter 5 for the STXS/couplings analysis. The I component contributes to the total PDF and it's the key to constrain Γ_H in this approach.

$$f \equiv \mu N_S f_S(m_{\gamma\gamma}; m_H, \boldsymbol{\theta}_{\text{shape}}) + N_I \sqrt{\mu\lambda K_S} f_I(m_{\gamma\gamma}; \lambda, m_H, \boldsymbol{\theta}_{\text{shape}}) + N_B f_B(m_{\gamma\gamma}; \boldsymbol{\theta}_{\text{BS}}) \tag{6.3}$$

where

- $\lambda = \frac{\Gamma_H}{\Gamma_{SM}}$ is the ratio of the observed Higgs width to the SM expectation. It is the parameter of interest (POI) of the model and its (upper) error from the fit will be used to set a(n upper) limit on Γ_H;
- μ is the signal strength. It can be either set to 1 (i.e. perfect agreement with the SM) or, to be more model-independent, can be let free-to-float in the model, thus providing an additional nuisance parameter (NP). Fit results will be provided in both configurations;
- m_H is the Higgs mass. It can be either set to 125.09 GeV (i.e. best mass measurement so far) or, to be more assumption-free, can be let free-to-float in the model, thus providing an additional NP. Fit results will be provided in both configurations;

- f_S is the signal PDF. The parametrization of the shape is obtained by a fit to the signal MC, as described in Section 6.5. This shape is fixed in the fit to the data, except when m_H is free-to-float which can shift the position of the signal peak. NPs associated to the shape systematic uncertainties ($\boldsymbol{\theta}_{\text{shape}}$) can affect the position and the width of the signal peak;
- f_I is the interference PDF. The parametrization of the shape is obtained by a fit to the interference MC, as described in Section 6.6; In the fit to the data the change of shape is controlled by λ. m_H, when it is free-to-float in the fit, can shift the position of the whole lineshape, consistently with f_S. NPs associated to the shape systematic uncertainties ($\boldsymbol{\theta}_{\text{shape}}$) can affect the position and the width of the lineshape, consistently with f_S;
- f_B is the background PDF. The choice of the analytic function describing the shape is obtained by the spurious signal test, as described in Section 6.7. Both the background shape parameters $\boldsymbol{\theta}_{\text{BS}}$ and the background normalization N_B (one parameter per category) are NPs in the fit to the data;
- $K_S = 1.45$ rescales the interference cross section taking into account missing higher order terms in the NLO computation [42].

6.4 Event categorization

The events passing the diphoton selection are first required to have 0 reconstructed leptons and MET < 75 GeV. This lepton-MET veto is needed to ensure that in all the analysis regions the dominant signal is always $gg \rightarrow H \rightarrow \gamma\gamma$. Then, the events are further divided in orthogonal categories in order to maximize the sensitivity to the interference effects and to minimize the contribution of the continuum background at the same time. The first goal is addressed by exploiting the strong dependence of the Higgs mass shift on a lower cut on the Higgs transverse momentum p_T^H illustrated by Figure 1.10, as presented in Ref. [58]: multiple exclusive p_T regions are defined using rectangular cuts on the $p_T^{\gamma\gamma}$ value of the selected events, thus creating at least one low-p_T category targeting a region of the phase-space highly affected by the interference and other high-p_T categories where the mass shift is expected to be negligible, representing reference regions. The $p_T^{\gamma\gamma}$ distributions of the signal and gg-interference samples are shown in Figure 6.2. To increase the signal-to-background ratio, events are further split into a *central* or *forward* region according to the pseudorapidity $|\eta|$ of the two photons: if both photons have $|\eta| < 0.95$, the event is classified as *central*; otherwise if at least one photon has $|\eta| \geq 0.95$, the event is *forward*. The η distributions of the signal and gg-interference samples are shown in Figure 6.3 for both the leading and the subleading photon.

6.4.1 Optimization

Combining the two criteria above results in a two-step selection for the categorization of the events, which is schematically shown in Figure 6.4. The number and the position of the $p_T^{\gamma\gamma}$ cuts have been optimized by evaluating the impact of each categorization on the final result with an approximate method: a simplified version of the model described in Section 6.3 with no systematic uncertainties and preliminary signal, background and interference models has been used to fit an Asimov dataset generated at $\lambda = 1$ and the $+1\sigma$ uncertainty on the λ POI is reported in Table 6.2 for a set of possible categorizations. The categorization named `CenFwd_PTH_10_60` was found to be the optimal compromise in terms of minimal number of total categories and maximal precision of the fit and is therefore chosen as the baseline categorization of the analysis. It is defined by two $p_T^{\gamma\gamma}$ cuts at 10 GeV and 60 GeV with the *central/forward* cut discussed above applied in sequence in each region, resulting in a total of 6 reconstruction event categories. $m_{\gamma\gamma}$ distributions in these categories are shown in Figure 6.5 for the signal and gg-interference samples. The properties of these categories are shown in Table 6.3, where the number of signal (N_S), background (N_B) and interference (N_I) events contained within the $m_{\gamma\gamma}$ window [120, 130] GeV is reported. N_S and N_I are computed directly from the respective MC, while N_B is estimated from a fit to the data sidebands [1]. Values of the purity [2] $P(X) = \frac{N_X}{N_{tot}}$, resolution $R(X) = \text{stdDev}\left[\frac{m_{\gamma\gamma}^{\text{Reco}} - m_{\gamma\gamma}^{\text{Truth}}}{m_{\gamma\gamma}^{\text{Truth}}}\right]$ and efficiency $\epsilon(X) = \frac{N_X^{\text{Reco,selected}}}{N_X^{\text{Truth,all}}}$ of the process X are also reported. As a matter of fact, the absolute value of the number of expected interference events $|N_I|$ is higher in the categories targeting events with $p_T^{\gamma\gamma} < 60$ GeV and lower in the categories targeting events with high $p_T^{\gamma\gamma}$. Moreover, the signal purity $P(S)$ is higher and the signal resolution $R(S)$ is lower [3] in the categories targeting events having central photons than in the forward ones.

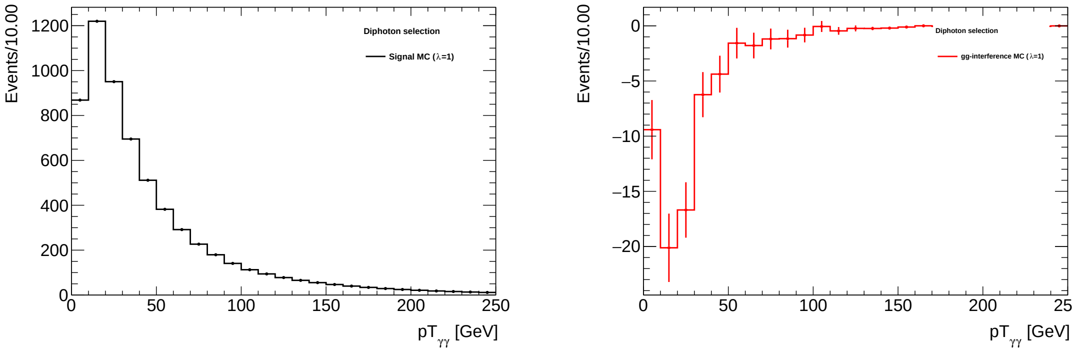

Figure 6.2: Distribution of $p_T^{\gamma\gamma}$ for the signal (black) and gg-interference (red) after the diphoton selection.

---

1. Data sidebands are defined as $105 < m_{\gamma\gamma} < 120$ GeV or $130 < m_{\gamma\gamma} < 160$ GeV.
2. Reported purity values refer to the $m_{\gamma\gamma}$ window [120, 130] GeV.
3. According to its definition, the lower the value of $R(X)$ is, the better the X resolution is.

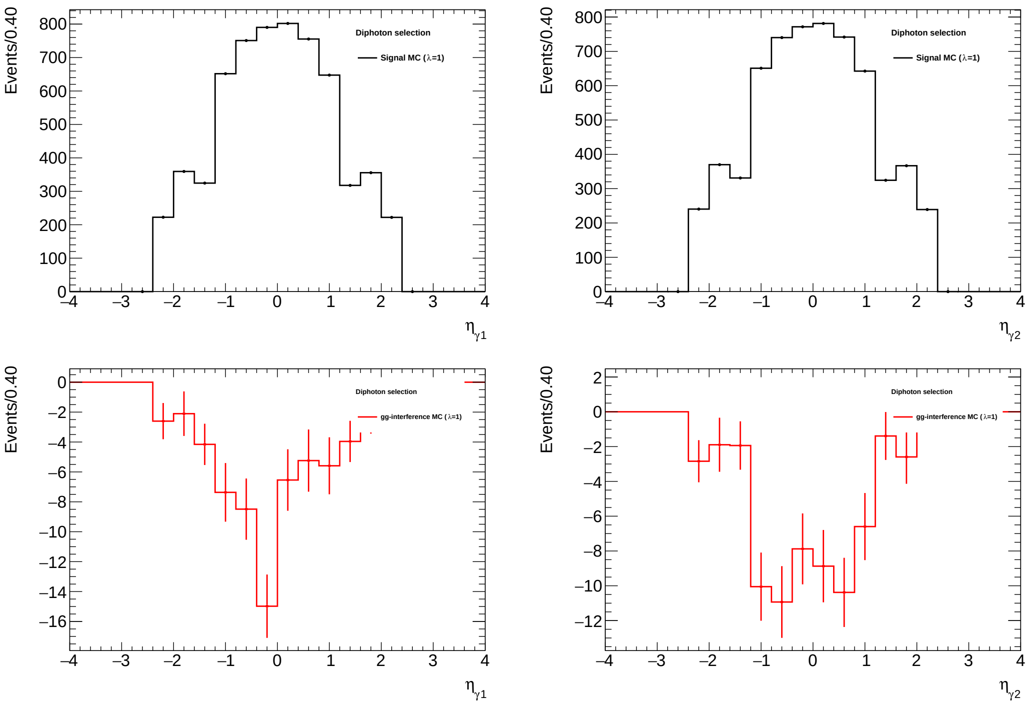

Figure 6.3: Distributions of $\eta_{\gamma 1}$ and $\eta_{\gamma 2}$ for the signal (black) and gg-interference (red) after the diphoton selection.

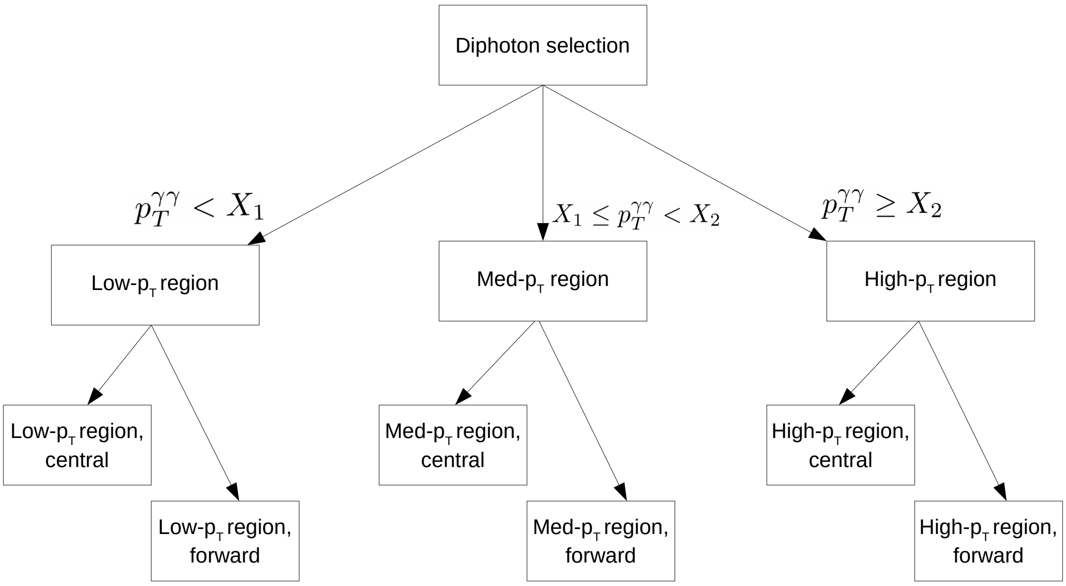

Figure 6.4: Schematic overview of the categorization strategy. In the current analysis, $X_1 = 10$ GeV and $X_2 = 60$ GeV.

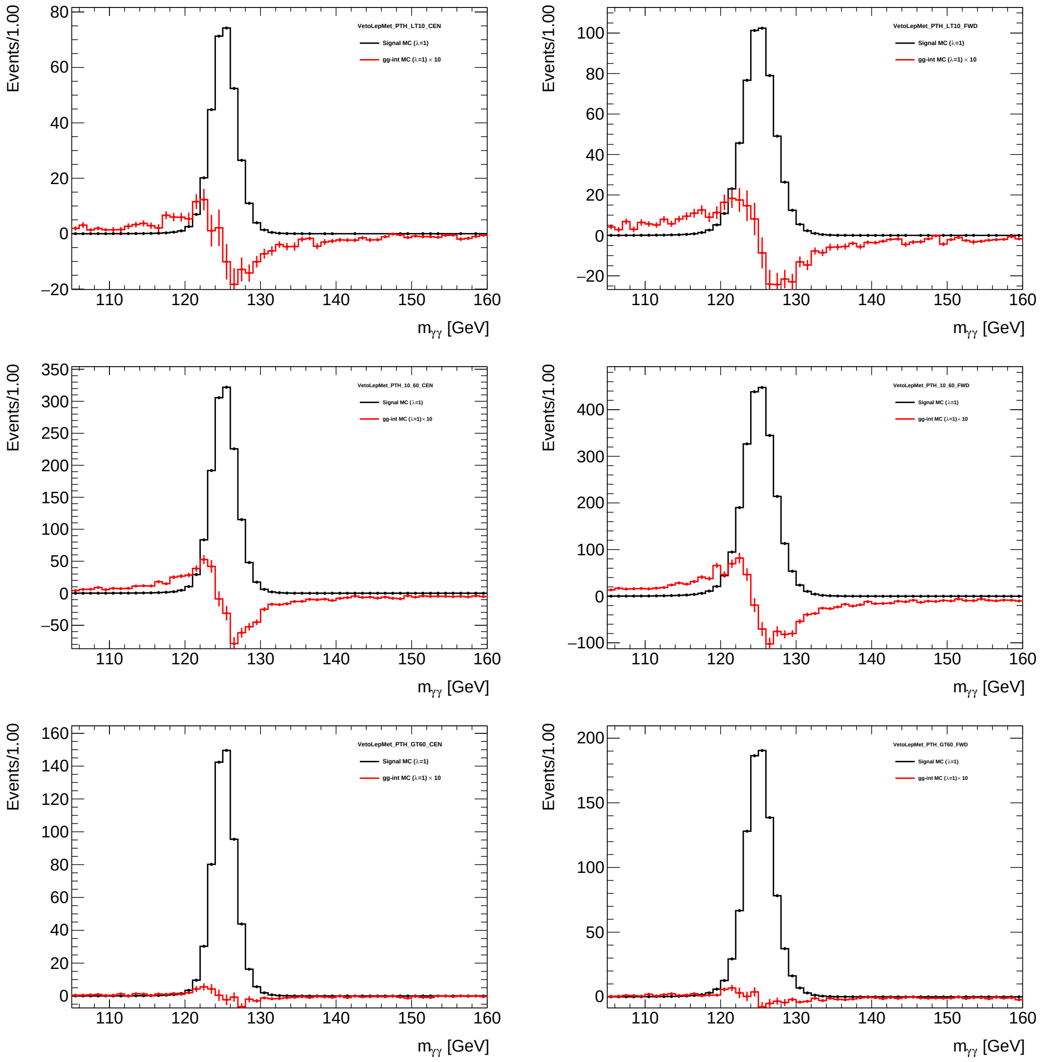

Figure 6.5: Distributions of $m_{\gamma\gamma}$ for the signal (black) and gg-interference (red) in each of the analysis categories. The gg-interference component is re-scaled by a factor 10 for visualization purposes.

Categorization	Nr. categories	Upper error on λ
PTH_10_20_30	8	+15.3
CenFwd_PTH_10_60	6	+12.5
CenFwd_PTH_10_60_120	8	+12.5
CenFwd_PTH_20_40_80	8	+12.7
CenFwd_PTH_10_60_120_200	10	+12.4

Table 6.2: Estimation of the impact on the fit results for each categorization strategy.

Category	N_S	N_B	$\|N_I\|$	$P(S)$	$P(I)$	$R(S)$	$R(I)$	$\epsilon(S)$	$\epsilon(I)$
PTH_LT10_CEN	315.0	10524.3	4.0	0.03	3.72e-03	0.01	0.02	0.06	0.04
PTH_LT10_FWD	526.3	27989.1	3.9	0.02	1.39e-03	0.02	0.02	0.10	0.03
PTH_10_60_CEN	1354.2	40862.1	14.2	0.03	3.36e-03	0.01	0.02	0.39	0.15
PTH_10_60_FWD	2264.3	115192.0	24.0	0.02	2.03e-03	0.02	0.02	0.68	0.21
PTH_GT60_CEN	576.3	10521.5	0.1	0.05	7.50e-06	0.01	0.02	0.59	2.62e-03
PTH_GT60_FWD	883.0	27009.9	0.7	0.03	2.40e-05	0.02	0.02	0.87	0.02

Table 6.3: For each analysis category, the number of signal (N_S), background (N_B) and interference (N_I) events contained within the $m_{\gamma\gamma}$ window [120, 130] GeV is reported. Values of the purity $P(X)$, resolution $R(X)$ and efficiency $\epsilon(X)$ of the process X are also reported.

6.5 Signal model

The modeling of the signal component mostly follows the procedure already described in Section 5.6. The function used to fit the $m_{\gamma\gamma}$ distribution of the signal MC is the Double Sided Crystall Ball (DSCB), whose analytic expression is (5.6). Simulated signal $m_{\gamma\gamma}$ distributions and their corresponding DSCB functions are shown for the 6 categories of the analysis in Figure 6.6.

6.6 Interference model

Because of negative MC weights, the simulated $m_{\gamma\gamma}$ spectrum of the interference goes below 0, as shown in Figure 6.7a. Any analytic function describing this distribution will eventually take negative values when evaluated in the interval $m_{\gamma\gamma} > 125$ GeV, something that is not compatible with the actual definition of a PDF. A possible workaround to overcome this problem is to add a constant value *ped* to all bins of the histogram, resulting in a global translation that will move it upward without distorting its shape, as shown in Figure 6.7b. When *ped* is greater or equal to the minimum value of the histogram, every point of the translated distribution will be ≥ 0 and a proper PDF can be fitted to it[4]. In order to preserve the correct number of events, the same value *ped* is subtracted at a later stage to each bin of the total PDF, by means of the artificial *Pedestal* component.

---

[4] Note that the fit must be binned.

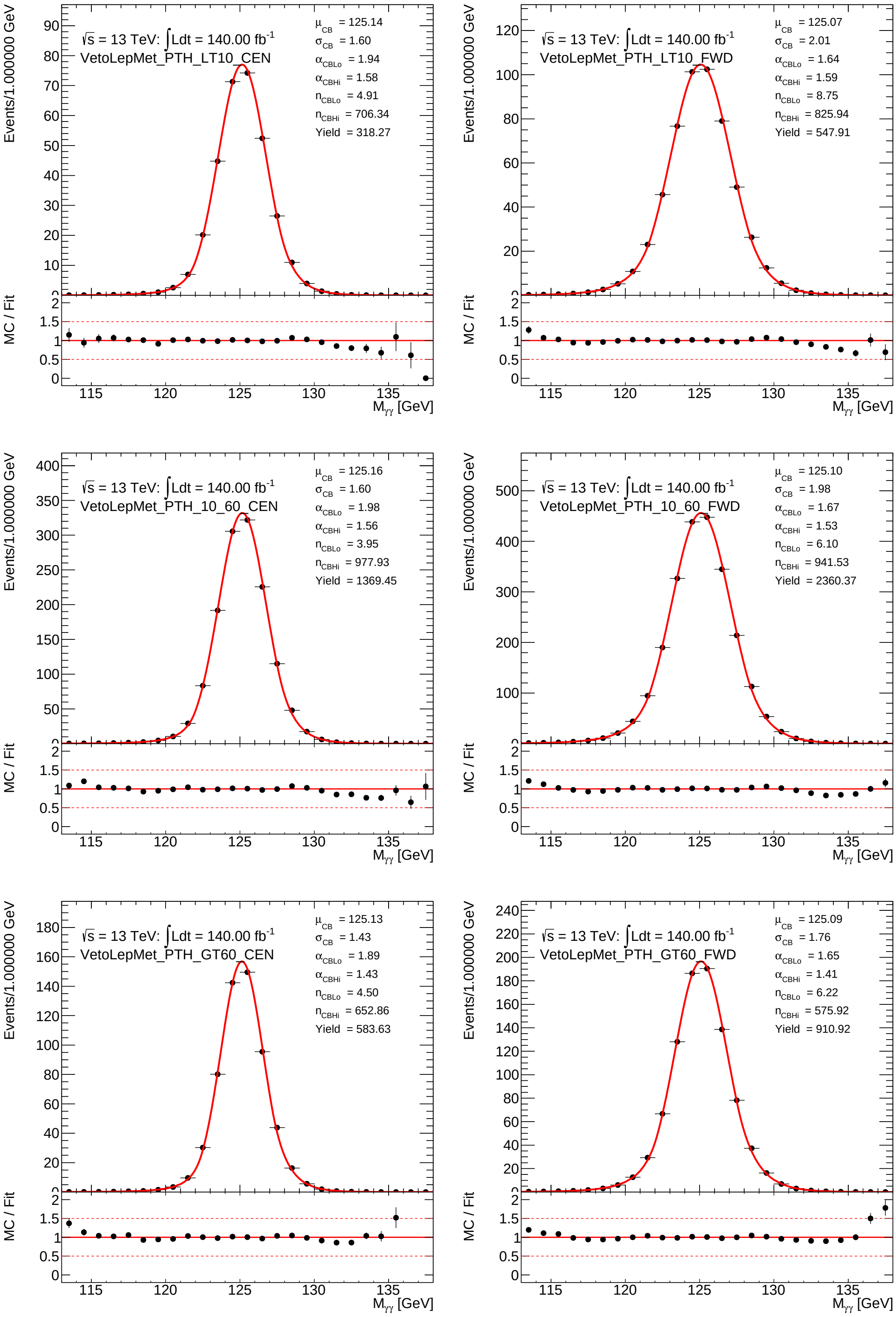

Figure 6.6: Fitted DSCB shapes for all the reconstructed categories of the analysis.

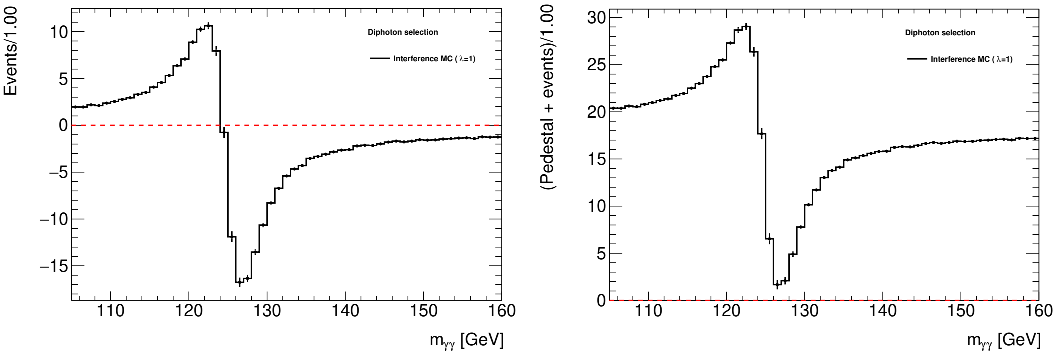

(a) (b)

Figure 6.7: Left: $m_{\gamma\gamma}$ distribution of the interference MC; Right: same distribution after the application of the pedestal term.

6.6.1 Fit function

The analytic function chosen to describe the interference lineshape is the sum of two DSCBs with opposite signs:

$$f_I = ped + N_L f^L_{\text{DSCB}} - N_R f^R_{\text{DSCB}} \tag{6.4}$$

Its number of degrees of freedom is $6 \times 2 - 2 + 2 = 12$, because a single DSCB has 6 free parameters ($m0$, σ, α_{Lo}, n_{Lo}, α_{Hi}, n_{Hi}) and there are 2 of them (L for Left and R for Right), but for consistency the high mass tail of the Left DSCB must be equal to the low mass tail of the Right DSCB, so 2 conditions can be imposed ($\alpha^L_{\text{Hi}} = \alpha^R_{\text{Lo}}$ and $n^L_{\text{Hi}} = n^R_{\text{Lo}}$). Additionally, 2 independent amplitudes (N_L and N_R) are free parameters, while the *ped* value is constant. For each category, these parameters are fitted to the $m_{\gamma\gamma}$ distribution of the interference MC with $\lambda = 1$. Fits of the lineshape per category are shown in Figure 6.8.

6.6.2 λ parametrization

Apart from the $\sqrt{\lambda}$ scale factor in the normalization of the interference PDF, the λ POI should enter the analytic expression of the lineshape as well, to represent the fact that it depends on the Higgs width. Under the hypothesis that an increase in λ generates a shift towards the low (high) mass values of the left (right) DSCB's peak position and a lowering of each of the DSCB's peak height, the parameters $m0^{L(R)}$ and $N^{L(R)}$ are reparametrized:

$$m0^{L(R)} = m0^{L(R)}_{\lambda=1} + p_0^{L(R)} + p_1^{L(R)}(\lambda - 1) + m_H - 125\text{GeV} \tag{6.5}$$

$$N^{L(R)} = N^{L(R)}_{\lambda=1} + p_0^{L(R)} + p_1^{L(R)}(\lambda - 1) \tag{6.6}$$

where $m0^{L(R)}_{\lambda=1}$ and $N^{L(R)}_{\lambda=1}$ are the parameters fitted on the $\lambda = 1$ sample (as explained in Section 6.6.1), $p_0^{L(R)}$ and $p_1^{L(R)}$ are free parameters and the term $m_H - 125$ takes into account the difference between the value of the Higgs boson mass used in the analysis ($m_H = 125.09$ GeV) and the one for which the samples were generated ($m_H = 125$ GeV). The values of the free parameters $p_0^{L(R)}$ and $p_1^{L(R)}$ are extracted from a simultaneous fit to the $m_{\gamma\gamma}$ distribution of the interference at 5 width points: $\lambda =$

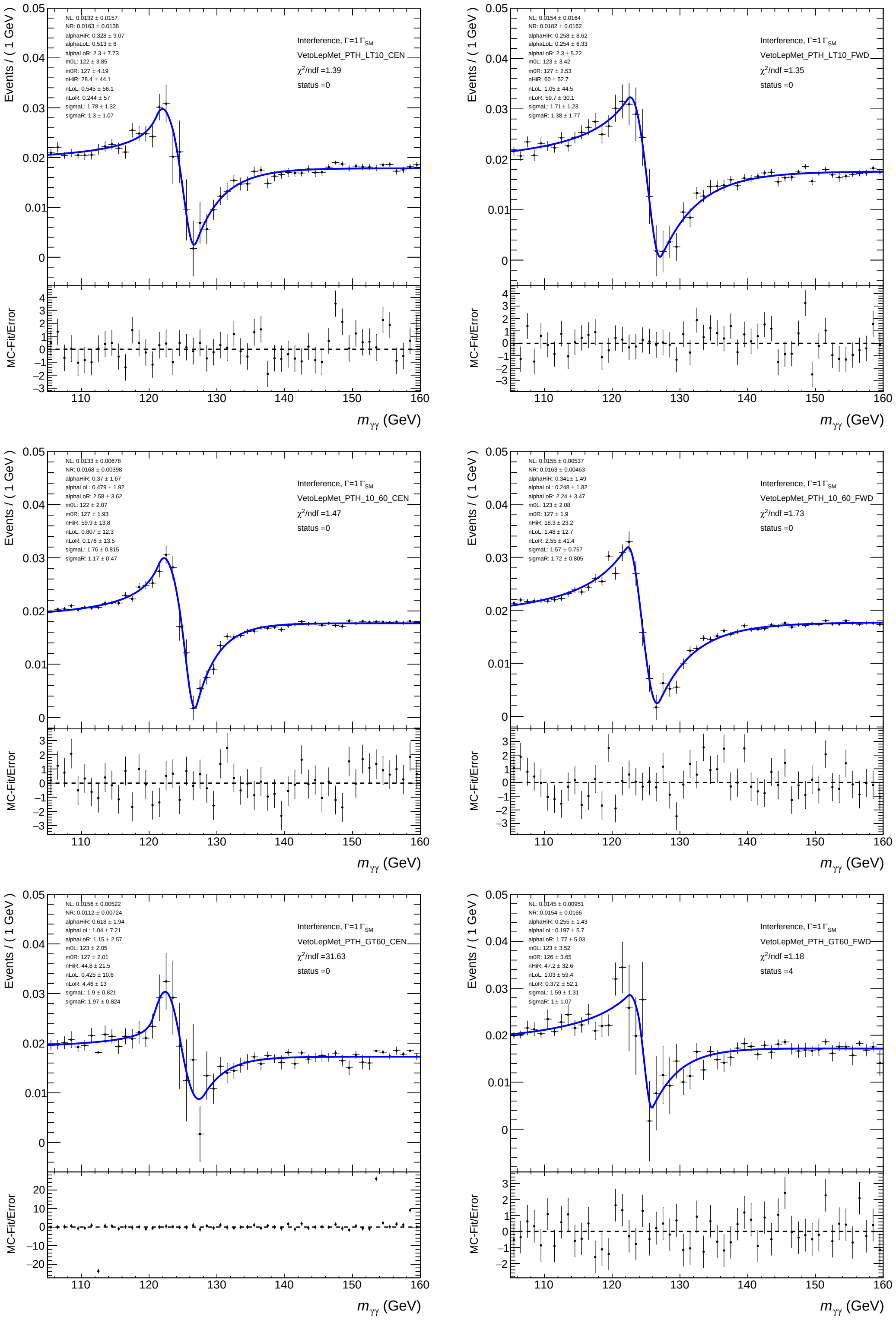

Figure 6.8: Fitted interference shapes for all the reconstructed categories of the analysis.

$1, 5, 10, 50, 100$. The 5 distributions are obtained from MC samples generated at a given λ value. Plots of the simultaneous fit to the 5 templates are shown from Figure 6.9 to 6.14. Figure 6.15 shows how the interference lineshape changes with λ. The dependency of each parameter of the interference PDF on λ is shown from Figure 6.16 to 6.21. For comparison, the values of the parameters from single independent fits are also shown on the same plots. The two approaches (simultaneous fit and independent fits) don't necessarily have to agree: the independent fits give results which are not consistent among the different λ points and it's not possible to derive a meaningful λ parametrization from them; on the other hand, the simultaneous fit automatically adapts the parametrization to all the 5 MC distributions at the same time, as best as possible.

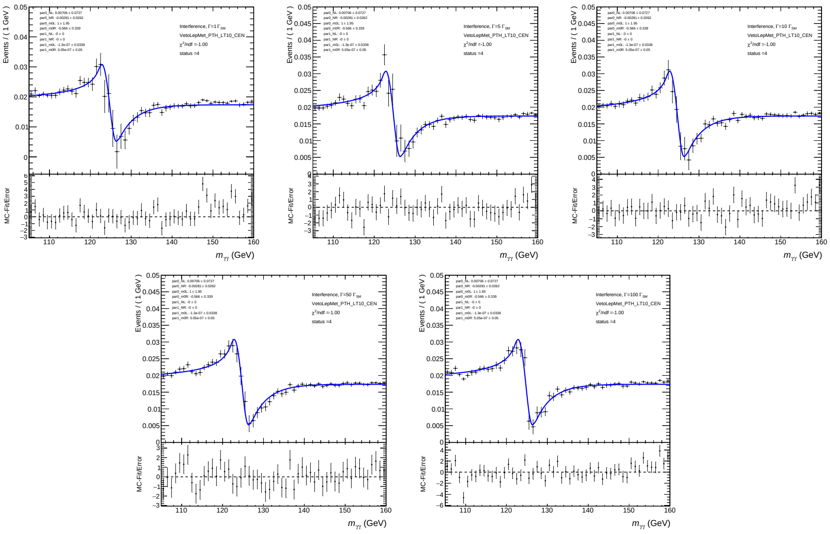

Figure 6.9: Simultaneous fits to the 5 interference MC samples for category 1.

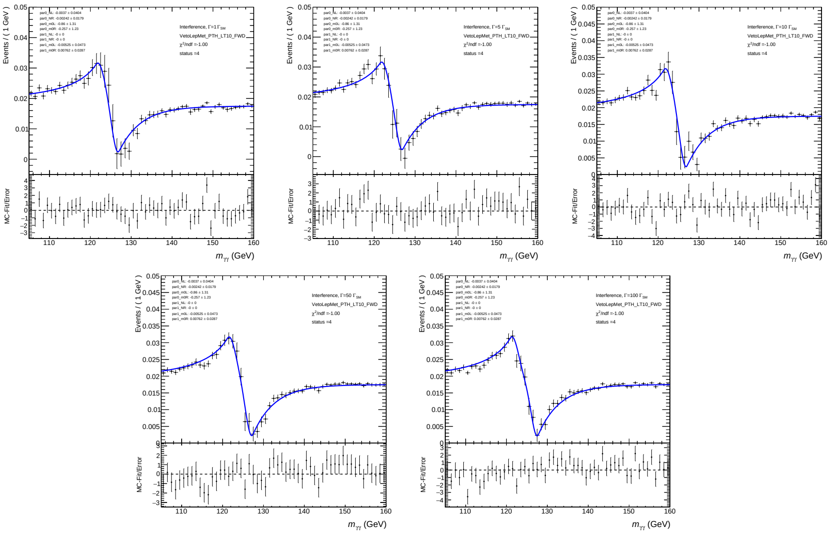

Figure 6.10: Simultaneous fits to the 5 interference MC samples for category 2.

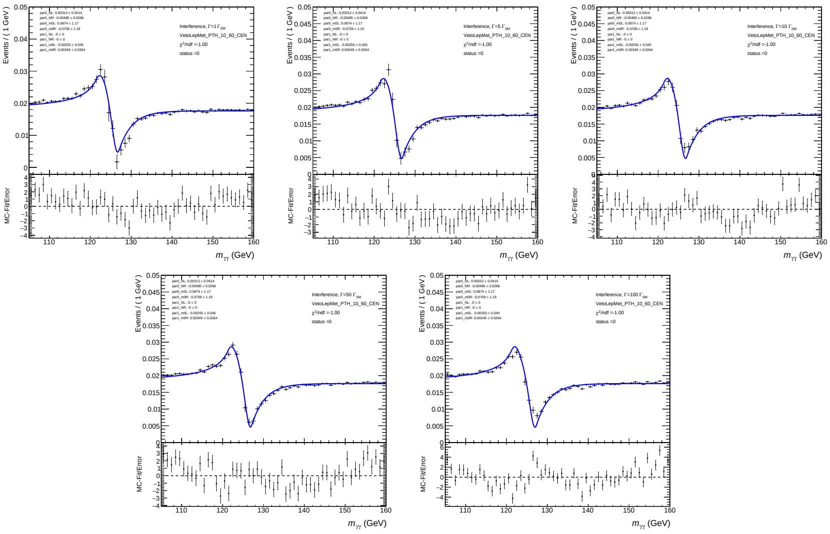

Figure 6.11: Simultaneous fits to the 5 interference MC samples for category 3.

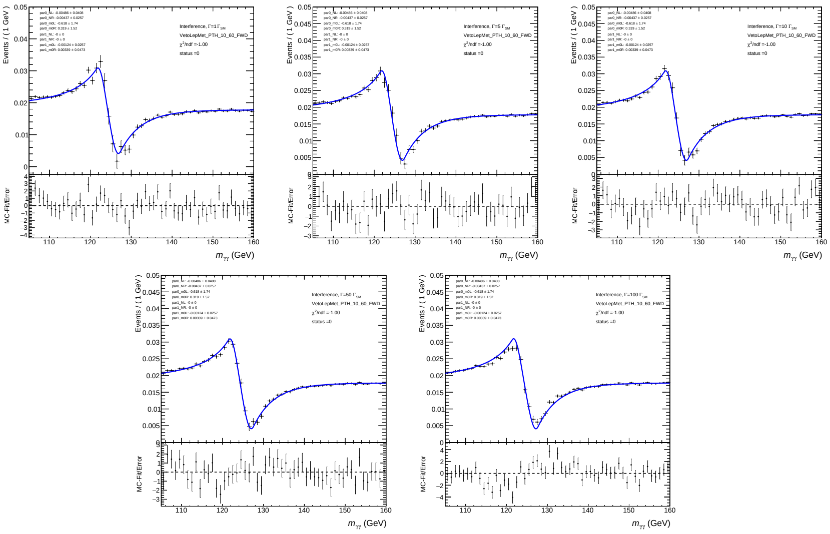

Figure 6.12: Simultaneous fits to the 5 interference MC samples for category 4.

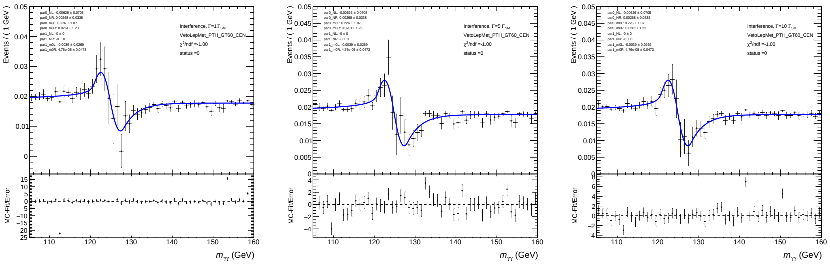

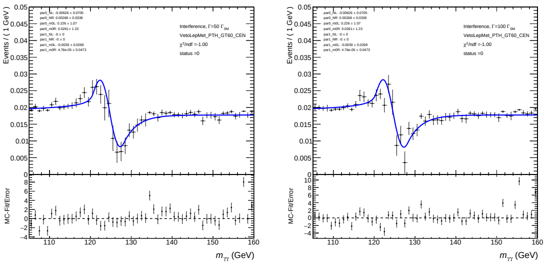

Figure 6.13: Simultaneous fits to the 5 interference MC samples for category 5.

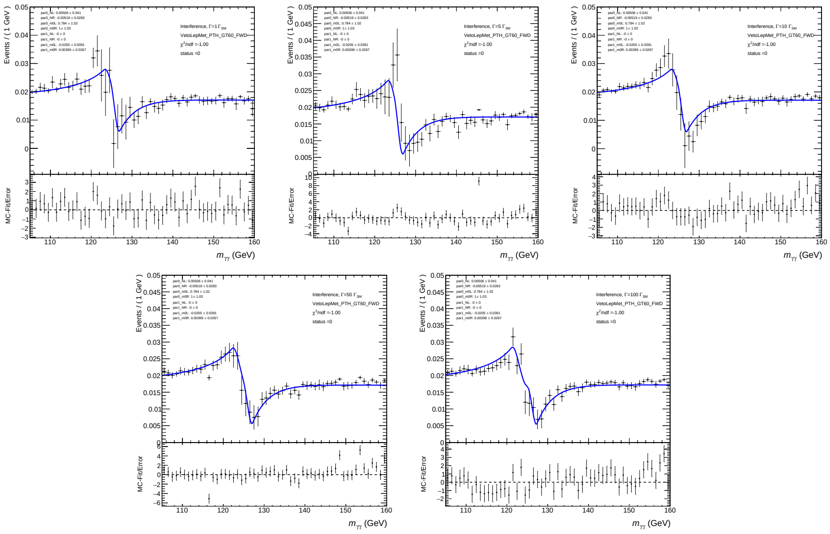

Figure 6.14: Simultaneous fits to the 5 interference MC samples for category 6.

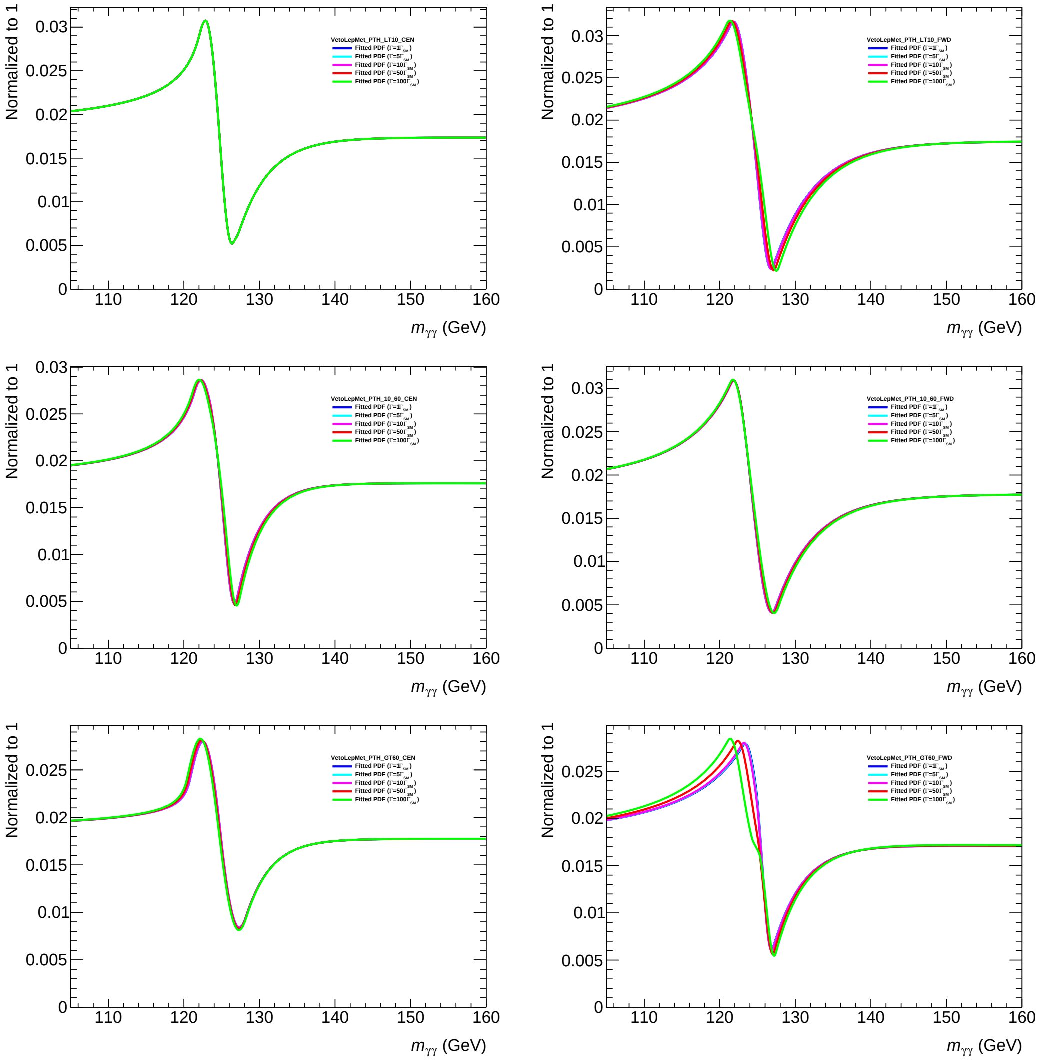

Figure 6.15: Interference lineshape evaluated at different λ points for all the reconstructed categories of the analysis.

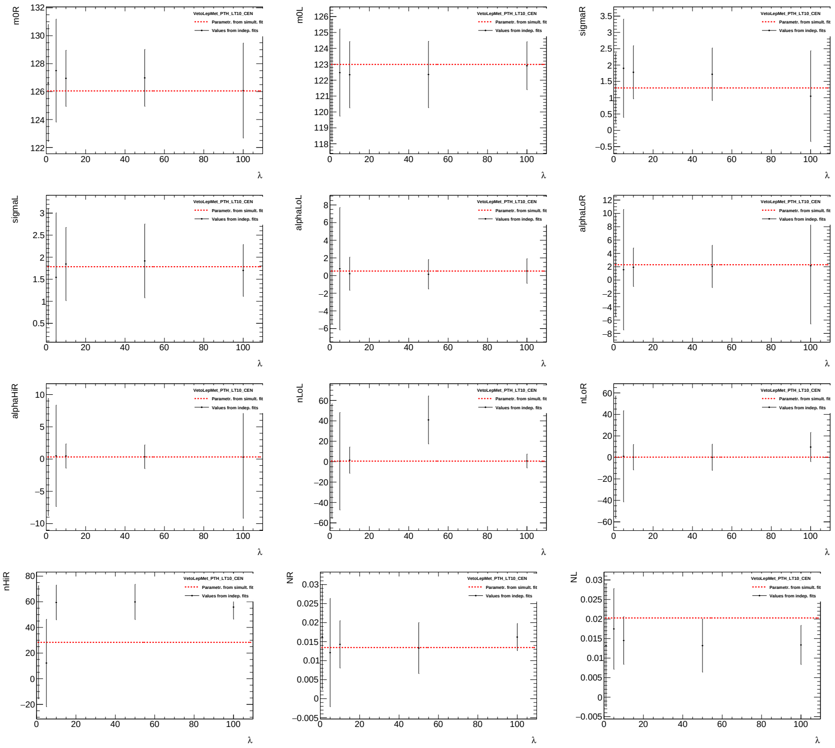

Figure 6.16: Comparison between the parametrization from the simultaneous fit (dotted red line) and the values from the independent fits (black points) for the 12 parameters of the interference function for category 1.

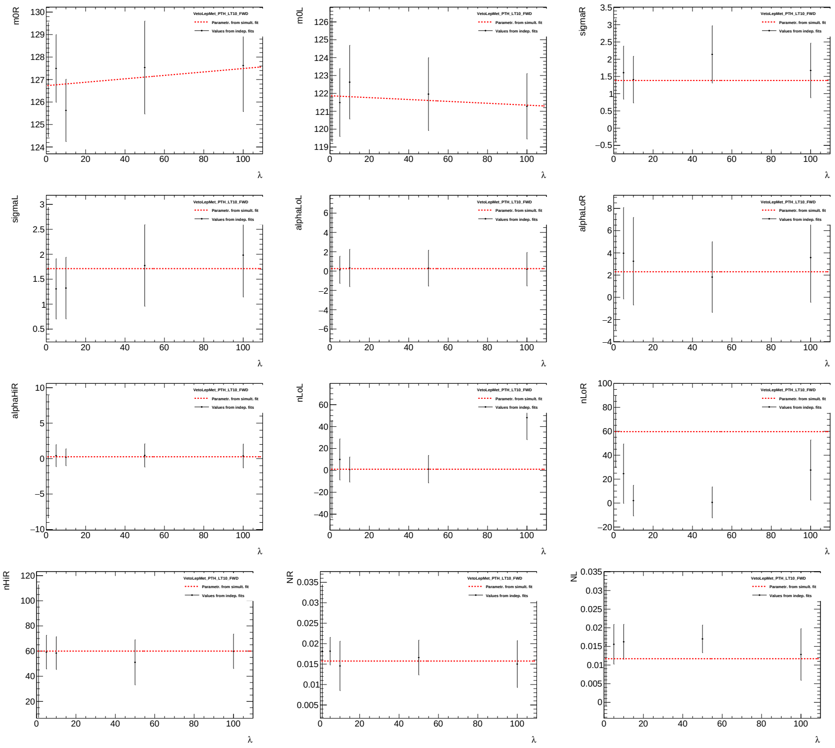

Figure 6.17: Comparison between the parametrization from the simultaneous fit (dotted red line) and the values from the independent fits (black points) for the 12 parameters of the interference function for category 2.

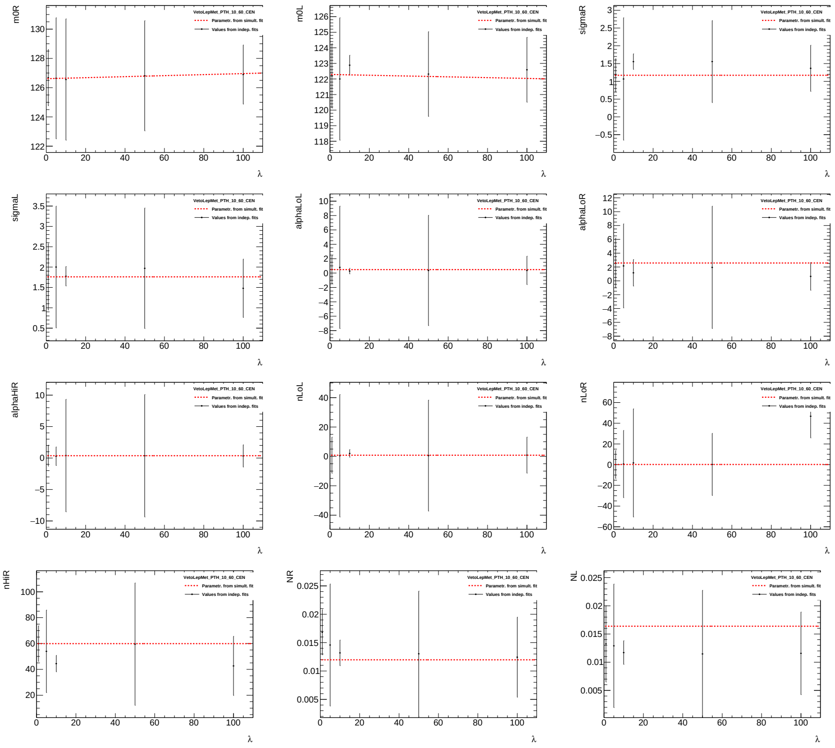

Figure 6.18: Comparison between the parametrization from the simultaneous fit (dotted red line) and the values from the independent fits (black points) for the 12 parameters of the interference function for category 3.

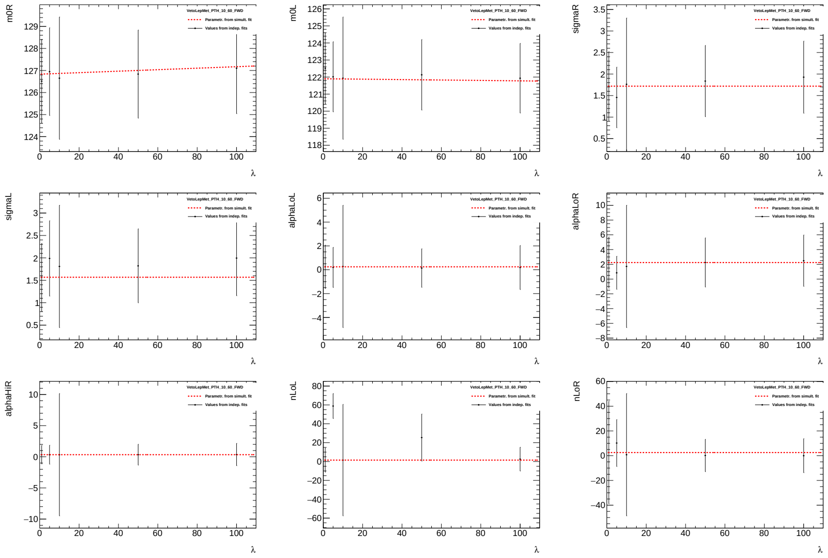

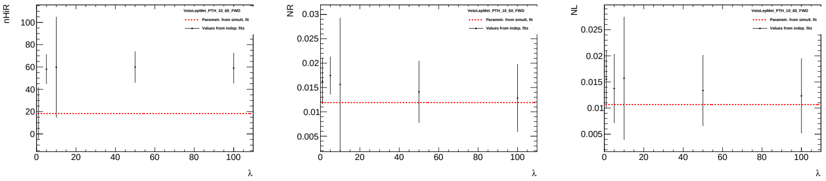

Figure 6.19: Comparison between the parametrization from the simultaneous fit (dotted red line) and the values from the independent fits (black points) for the 12 parameters of the interference function for category 4.

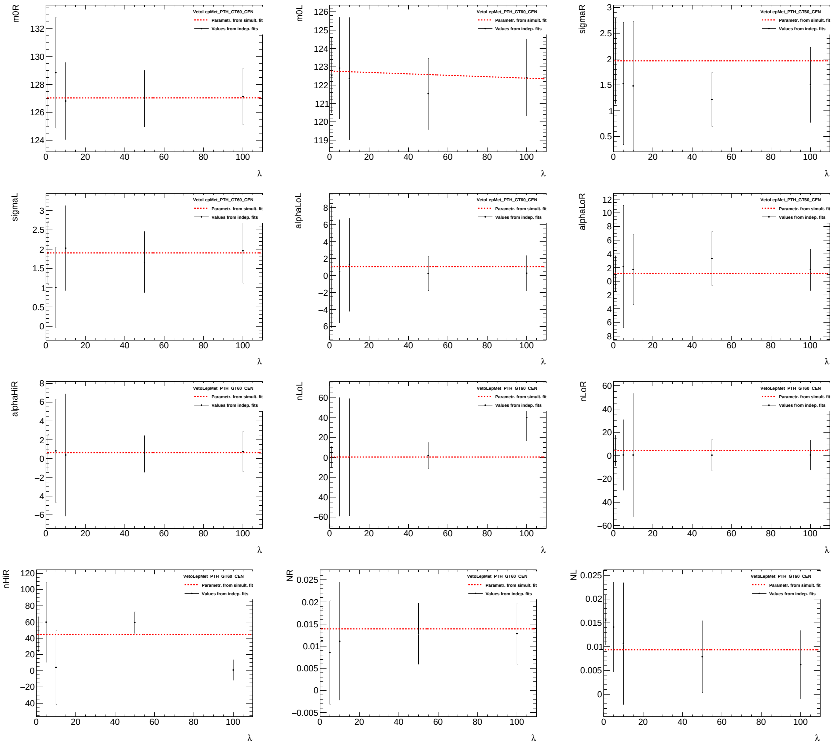

Figure 6.20: Comparison between the parametrization from the simultaneous fit (dotted red line) and the values from the independent fits (black points) for the 12 parameters of the interference function for category 5.

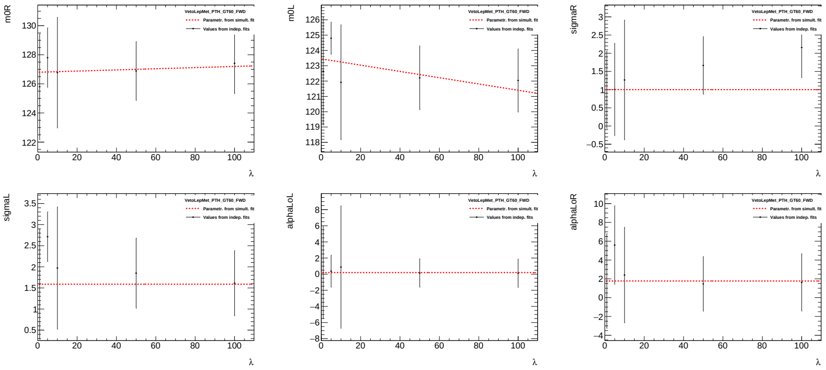

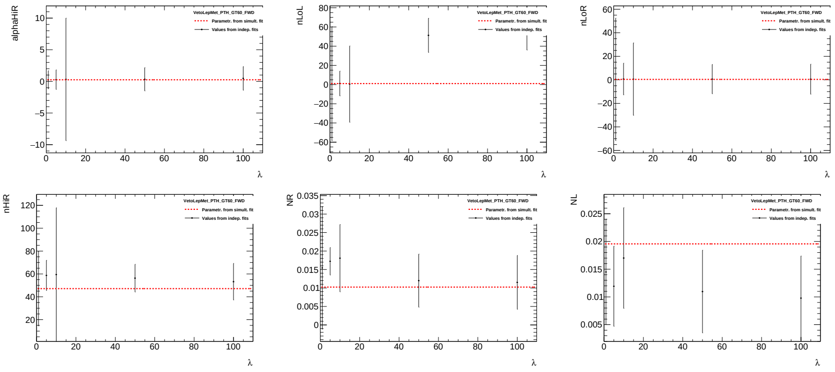

Figure 6.21: Comparison between the parametrization from the simultaneous fit (dotted red line) and the values from the independent fits (black points) for the 12 parameters of the interference function for category 6.

6.6.3 Injection test

The fits to the $m_{\gamma\gamma}$ distributions of the interference MC are not perfect. In some categories, the χ^2/ndf is larger than 1 and this is caused mainly by a mismodeling of the interference lineshape at low or high $m_{\gamma\gamma}$ values. In order to estimate the impact of this mismodeling on the final result, an injection test has been performed. The extraction of the expected results (shown later in Section 6.11.1) has been repeated using an alternative configuration: the interference component of the generated Asimov dataset, which is the PDF fitted in Figure 6.8 evaluated at each point, is replaced with the MC distribution of the interference (injected MC), which is exactly the histogram fitted in Figure 6.8. The original Asimov term and the injected MC are compared in Figure 6.22. The results of a total-PDF fit to the Asimov dataset per category are shown in Figure 6.23 for both the nominal case and the injection test. The size of the mismodeling depends on the category and it is about 10% for most of them. The red points (injection test) don't show a clear bias with respect to the reference value $\lambda = 1$, they rather fluctuate around the horizontal dotted line in agreement with the hypothesis that the difference observed between the simulated interference distribution and its analytic model are compatible within the statistical uncertainty of the MC.

Dependency of the mismodeling on λ

In the previous subsection the mismodeling of the interference lineshape was studied per category for the case $\lambda = 1$. However, its evolution with λ must be investigated as well. The injection test is repeated for 5 width points ($\lambda = 1, 5, 10, 50, 100$), each time performing a simultaneous fit across all the categories of the analysis [5]. The results are given in Figure 6.24. The uncertainty on the bias is estimated with a bootstrap of 101 trials and the distributions of the fitted value of λ for each point are shown in Figure 6.25. The difference between the fitted value and the generated value of λ is compatible with 0 within the error bars for most of the points, except for $\lambda = 5$ where it is about 30%. However, since no clear systematic trend is observed, the bias is considered not significant and thus not propagated to the results of the analysis.

---

[5] Since here we are not interested anymore in measuring a bias per category, it's more useful to have one single number from the fit to compare among different λ points.

	Removing one point		All points	
$\lambda = 50$	Asimov: 49.8	Bias: 21%	Asimov: 50.4	Bias: -5%
	Injection: 39.5		Injection: 52.7	
$\lambda = 10$	Asimov: 9.96	Bias: 16%	Asimov: 9.62	Bias: -3%
	Injection: 8.36		Injection: 10.3	
$\lambda = 5$	Asimov: 4.91	Bias: -33%	Asimov: 4.47	Bias: -35%
	Injection: 6.64		Injection: 6.73	

Table 6.4: Results of the injection test for the alternative parametrizations "Removing one point" and the nominal one with "All points". Results from the fit to the Asimov are provided for reference as well.

Interpolation with less points

The nominal parametrization, as described in section 6.6.2, is built interpolating among 5 width points, $\lambda = 1, 5, 10, 50, 100$. In the previous section, the mismodeling bias was evaluated exactly for the same width points, $\lambda = 1, 5, 10, 50, 100$, which correspond to the available MC samples of the interference. Ideally, if an additional MC sample with $\lambda \neq 1, 5, 10, 50, 100$ was accessible, it could be used to make an injection test on a width point "unknown" to the parametrization. Alternatively, one can build a parametrization using one less point and perform the injection test on the "missing" point that was not used in the interpolation. This simple test allows to check how much the nominal parametrization relies on a given width point and it is performed for $\lambda = 5, 10, 50$. Results of the test are given in Table 6.4: removing one point from the interpolation increases the mismodeling for that point, from 5% to 20% for $\lambda = 50$ and from 3% to 16% for $\lambda = 10$; instead for $\lambda = 5$, where the mismodeling with the nominal parametrization was already at the level of 30%, it is not increased.

Impact of neglecting the qg component of the interference

As explained in section 6.6.2, the interference lineshape is parametrized on the MC samples of the gg-interference only. The subdominant qg contribution, which consists in the interference between the signal and background processes initiated by a quark-gluon pair, is therefore neglected in the nominal parametrization. The impact of this approximation is estimated with an injection test for $\lambda = 1$ where the injected MC contains also the qg component. Results are given in Table 6.5: as a reference, the first column corresponds to the standard injection test for which the injected MC contains the gg-interference only; results in the second column are obtained injecting a MC which is a mixture (according to their cross sections) of the two interferences; for the third column, the two components are combined as well, with the qg cross section scaled by a factor 2, in order to cover for uncertainties in a rough but very conservative way. A bias towards smaller width values is observed on the fitted value of λ, along with a decrease of its uncertainty which results in a more optimistic limit. This is not surprising because the qg-interference contributes with opposite sign (with respect to gg-interference) to the total cross section, as shown in Figure 6.26.

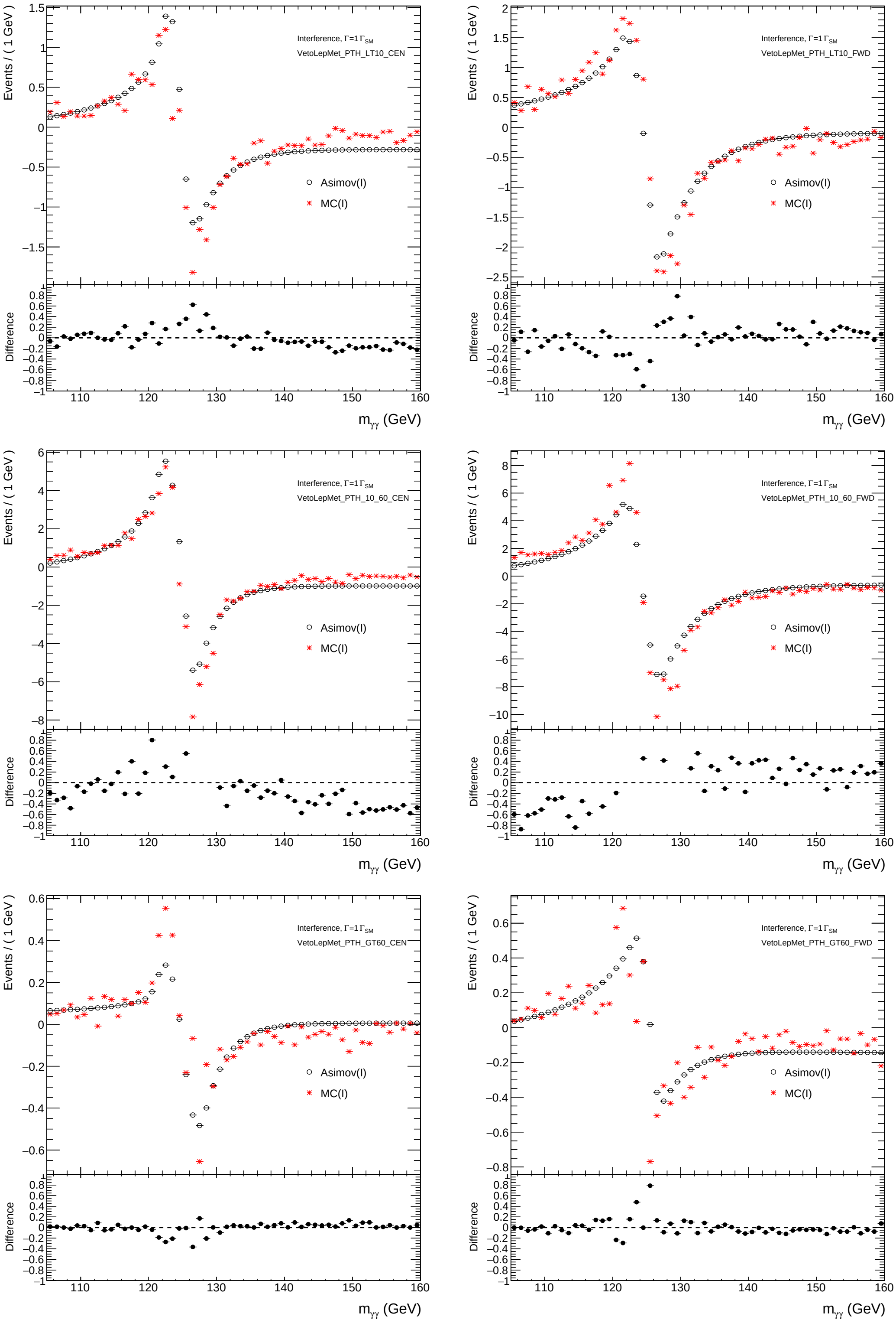

Figure 6.22: Comparison between the Asimov term generated by the interference PDF and the injected MC distribution for all the reconstructed categories of the analysis.

	Int-gg only	Int-gg+Int-qg	Int-gg+2*Int-qg
Fitted λ	1.05	0.64	0.33
Limit on λ (stat-only)	40	38	36
Limit on λ (total unc.)	80	77	74

Table 6.5: Results of the injection test for which the injected MC contains the gg-interference only, the combination of gg and qg-interference and the combination with a factor 2 in front of the qg-interference.

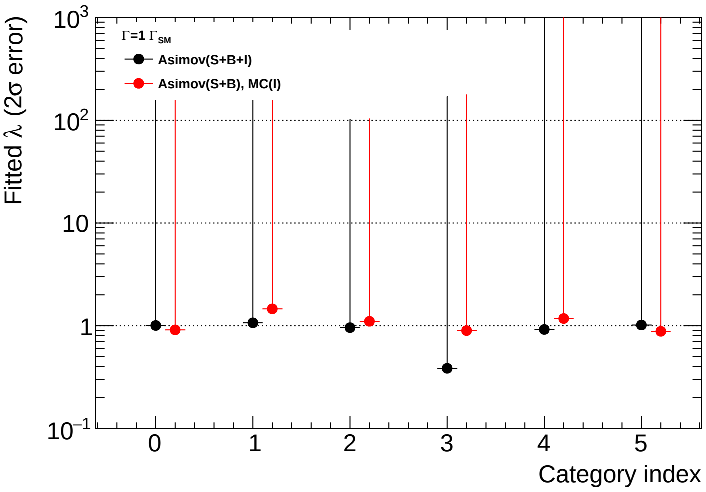

Figure 6.23: Results of the injection test and comparison with the nominal Asimov fit results per category.

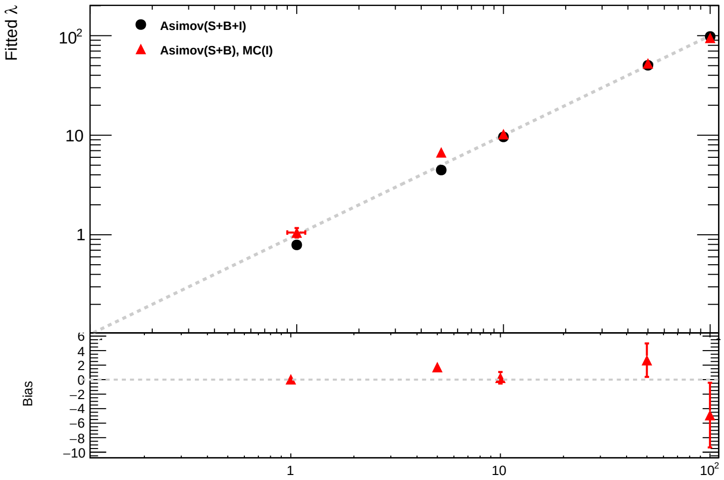

Figure 6.24: (x-axis title: Generated λ) Results of the injection test and comparison with the nominal Asimov fit results for each of the 5 width points. The bottom panel shows the difference with respect to the gray dashed line. Uncertainty on the red points is evaluated with a bootstrap.

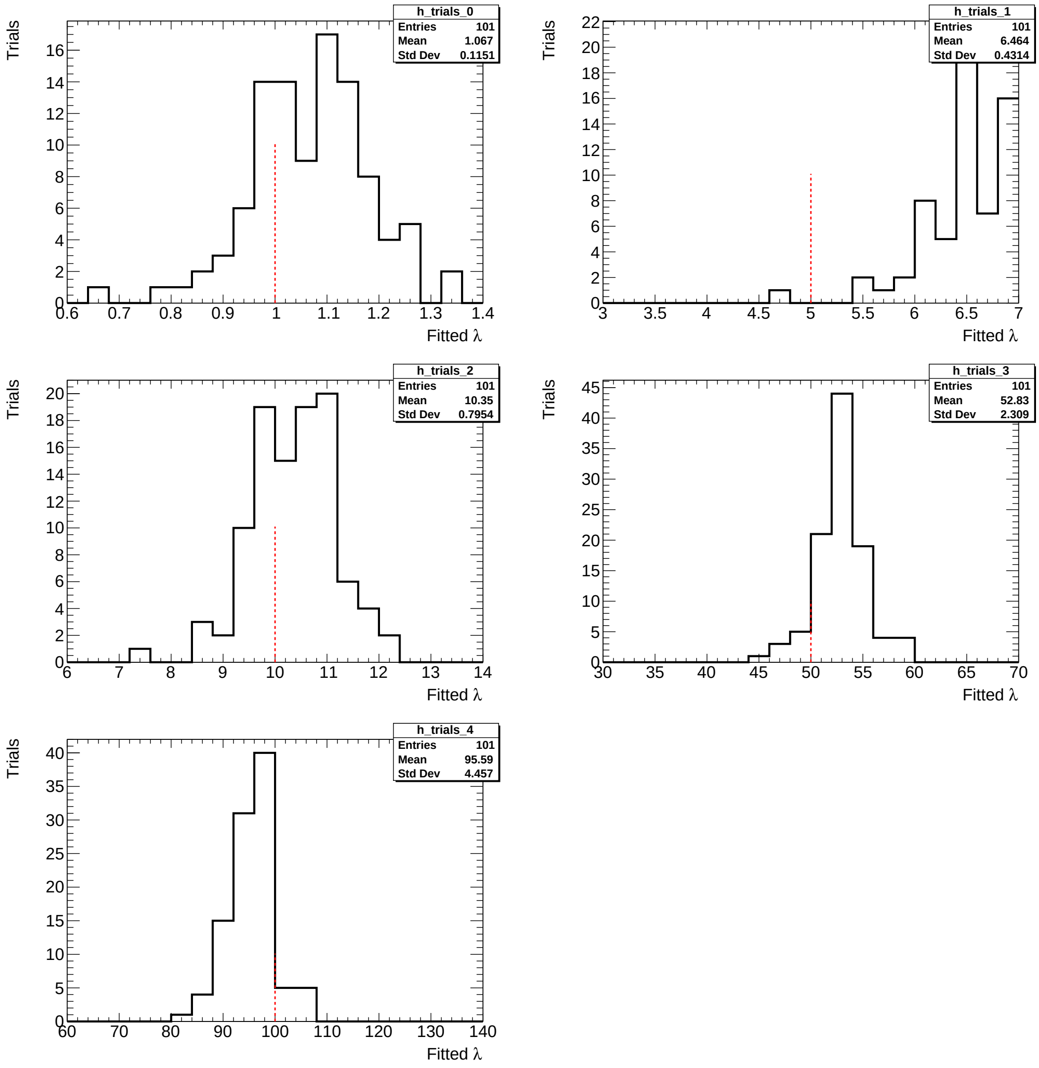

Figure 6.25: Distribution of the λ values fitted for each of the 5 width points using a bootstrap with 101 trials. The dotted red line represents the reference value.

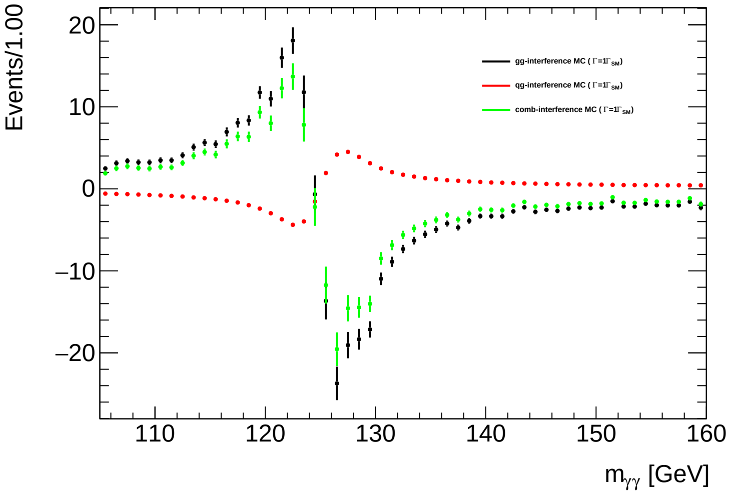

Figure 6.26: Distribution of $m_{\gamma\gamma}$ for the gg-interference (black), qg-interference (red) and their combination (green). Diphoton selection is applied.

6.7 Background model

The modeling of the background component mostly follows the procedure already described in Section 5.7. Background $m_{\gamma\gamma}$ templates for all categories are constructed from a combination of the $\gamma\gamma$, γj and jj processes. Purities of each of the three processes per category are shown in Figure 6.27. Figure 6.28 shows the plots of the background templates and these are compared with the data in the control regions $105 < m_{\gamma\gamma} < 120$ GeV or $130 < m_{\gamma\gamma} < 160$ GeV (sidebands). The total background template is normalized to the entries of the data in the mass sidebands, excluding the blinded region. As a measure of compatibility between the template and the data, the χ^2 probability between the two distributions is reported. The ratio of the data to the template is also shown in the bottom panel and is fitted with a first order polynomial to demonstrate that the slope is compatible with zero. The background-only templates are fitted using a candidate function for the background $\mathcal{B}(m_{\gamma\gamma})$ plus the signal PDF, which is the nominal DSCB[6]. The amount of spurious signal S_{sp} fitted from the template is a measure of the bias associated to the choice of $\mathcal{B}(m_{\gamma\gamma})$. The fit is repeated with different functions $\mathcal{B}(m_{\gamma\gamma})$ from a pool of candidates and every time the value of S_{sp} is reported. The analytic function describing the background shape in each category is chosen according to some requirements on the associated bias S_{sp} and on the χ^2 of the fit. Additional details on the spurious signal test can be found in Section 5.7. Results of the spurious signal test are reported from Table 6.7 to 6.12 for all categories. An overview of the tests is given in Table 6.6: `ExpPoly2`, which corresponds to the expression $\exp(\mathrm{a}_1\mathrm{m}_{\gamma\gamma}+\mathrm{a}_2\mathrm{m}_{\gamma\gamma}^2)$, was selected in all categories because it always fulfilled at least one of the relaxed criteria (2σ) of the test and is the function with less free parameters. Values of the spurious signal systematic associated to this choice are given in the same table. Fits of the background templates using the selected function are shown in Figure 6.29.

---

[6] The interference component is neglected in this study.

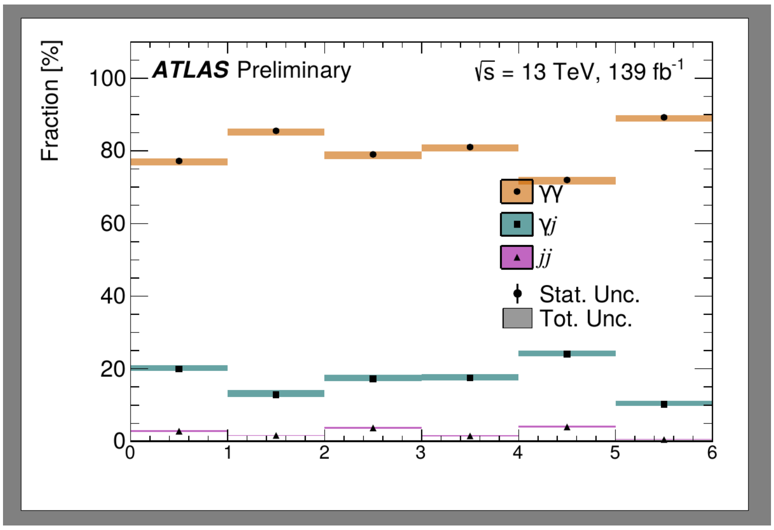

Figure 6.27: Fraction of events for the $\gamma\gamma$, γj and jj processes in all categories of the analysis.

Category	Function	Spurious signal
VetoLepMet_PTH_LT10_CEN	`ExpPoly2`	-47.1
VetoLepMet_PTH_LT10_FWD	`ExpPoly2`	-77.9
VetoLepMet_PTH_10_60_CEN	`ExpPoly2`	-52.2
VetoLepMet_PTH_10_60_FWD	`ExpPoly2`	-189
VetoLepMet_PTH_GT60_CEN	`ExpPoly2`	12.7
VetoLepMet_PTH_GT60_FWD	`ExpPoly2`	27.1

Table 6.6: Overview of the results of the spurious signal test for all categories.

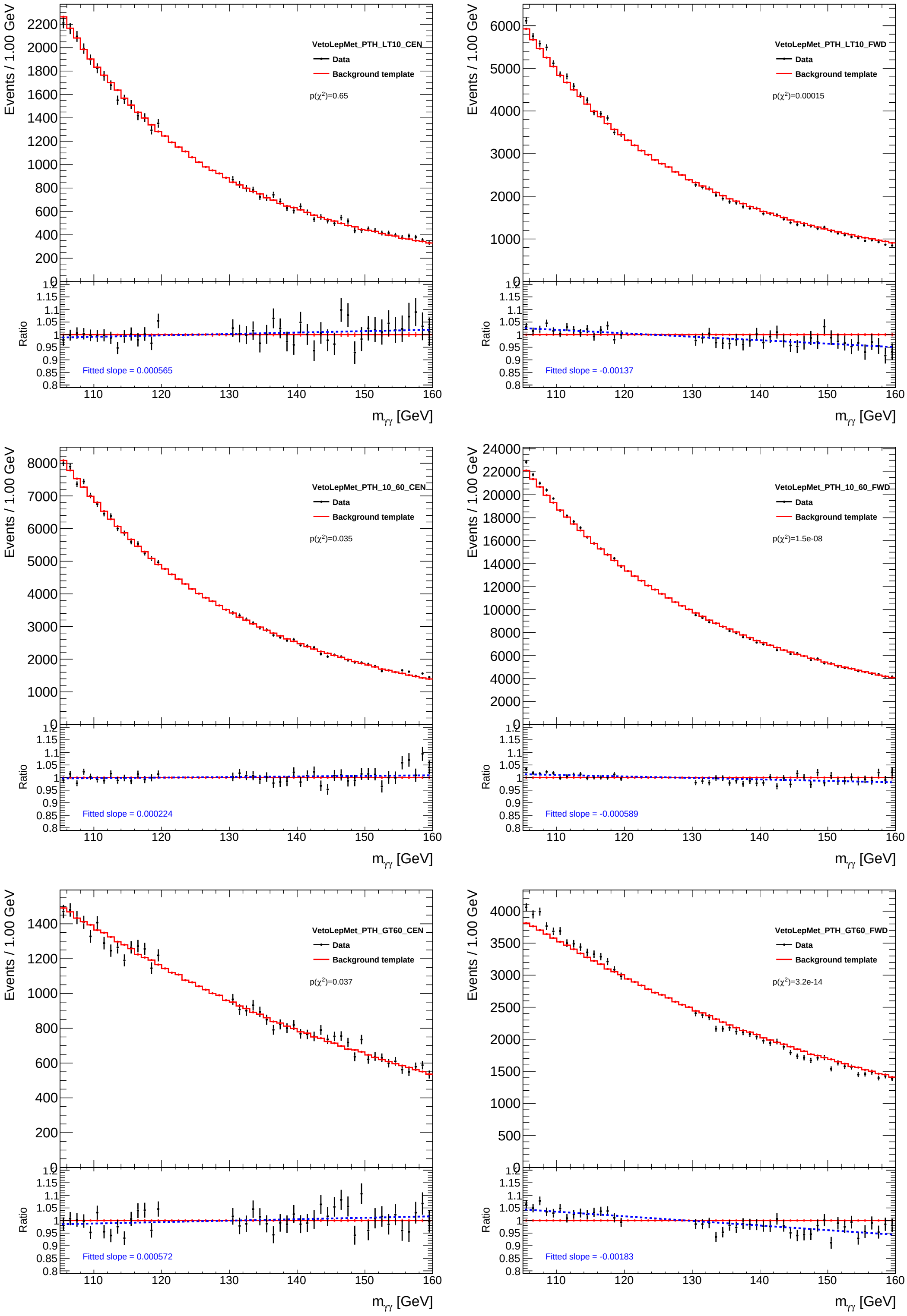

Figure 6.28: Plots of the background templates and comparison with the data sidebands for all the reconstructed categories of the analysis.

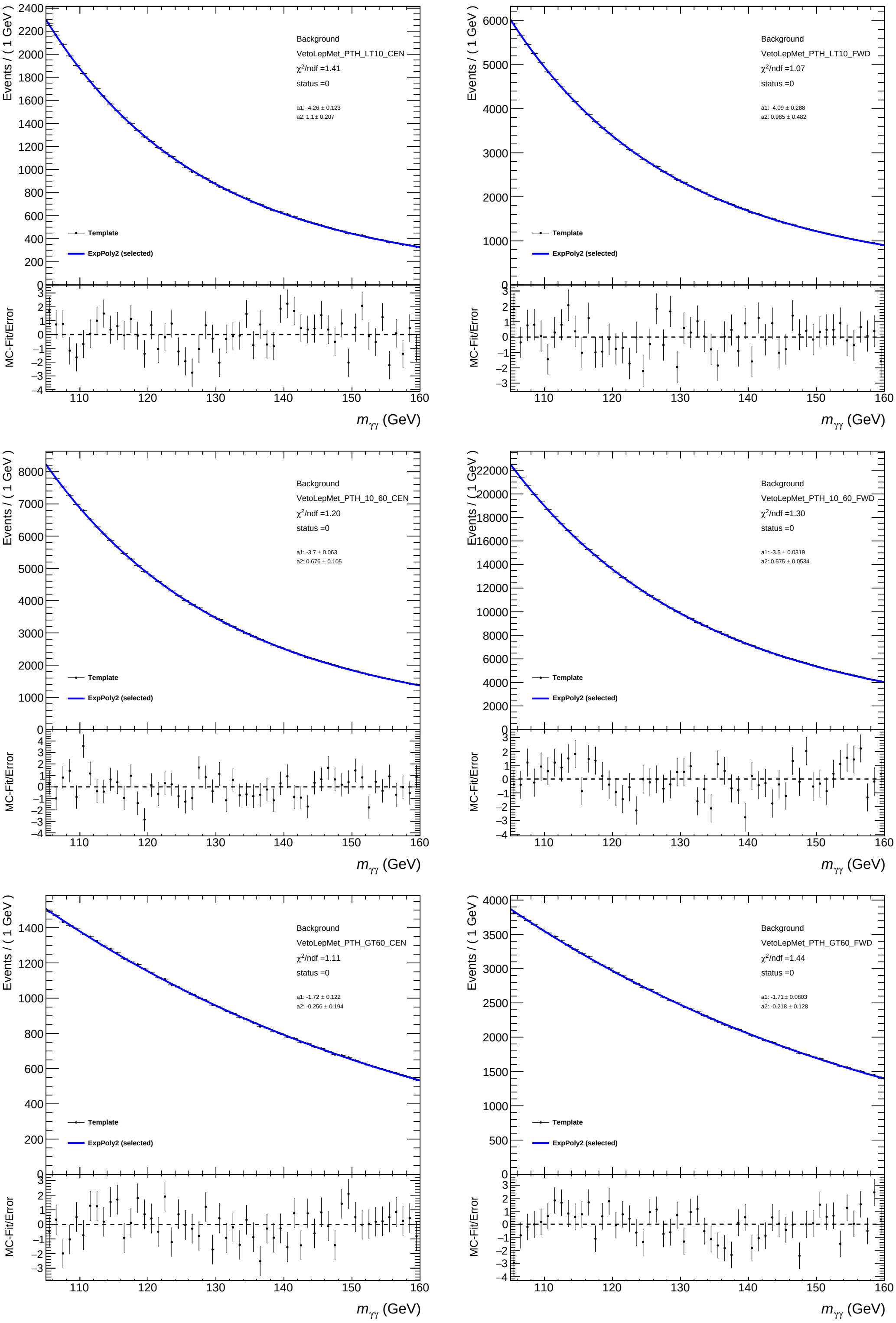

Figure 6.29: Fits of the background templates using the selected function from the spurious signal test for all the reconstructed categories of the analysis.

Name	max(S/δS) [%]	max(2σ/δS) [%]	max(S/S$_{ref}$) [%]	max(2σ/S$_{ref}$) [%]	max(S)	nPars	Prob(χ^2) [%]	Result
Bern4	-32.7	-8.25	-9.56	-2.48	-30.2	4	2.77	PASS
Bern5	-27.9	-6.02	-8.98	-1.94	-28.6	5	1.73	PASS
ExpPoly2*	-52.7	-27.5	-14.8	-7.71	-47.1	2	2.03	PASS
Bern3	-37.5	-13.1	-12	-4.21	-38.2	3	0	FAIL
Pow	53.4	26	15.3	7.49	48.7	1	0	FAIL
Exponential	-254	-226	-66.3	-59.1	-209	1	0	FAIL

Table 6.7: Results of the spurious signal test for all the candidate functions for category 1. The selected function is marked with a *.

Name	max(S/δS) [%]	max(2σ/δS) [%]	max(S/S$_{ref}$) [%]	max(2σ/S$_{ref}$) [%]	max(S)	nPars	Prob(χ^2) [%]	Result
ExpPoly2*	-42.2	-16.8	-14.2	-5.66	-77.9	2	30.4	PASS
Bern4	-51	-27.9	-20.1	-11	-110	4	1.33	FAIL
Bern5	-53.4	-30.6	-21.3	-12.2	-117	5	1.82	FAIL
Pow	139	107	39.5	30.4	217	1	0	FAIL
Exponential	-361	-331	-109	-100	-594	1	0	FAIL
Bern3	-95.8	-70.5	-34.5	-25.4	-189	3	0	FAIL

Table 6.8: Results of the spurious signal test for all the candidate functions for category 2. The selected function is marked with a *.

Name	max(S/δS) [%]	max(2σ/δS) [%]	max(S/S$_{ref}$) [%]	max(2σ/S$_{ref}$) [%]	max(S)	nPars	Prob(χ^2) [%]	Result
ExpPoly2*	-27.4	-0.236	-3.81	-0.0348	-52.2	2	13.2	PASS
Bern4	49.4	23.2	-7.02	-3.24	-96.3	4	0.114	FAIL
Bern5	63.3	40	9.04	5.72	124	5	0.029	FAIL
Bern3	-67.7	-41.2	-10	-6.13	-137	3	0	FAIL
Pow	234	207	28	24.1	385	1	0	FAIL
Exponential	-264	-235	-32.4	-28.9	-442	1	0	FAIL

Table 6.9: Results of the spurious signal test for all the candidate functions for category 3. The selected function is marked with a *.

Name	max(S/δS) [%]	max(2σ/δS) [%]	max(S/S$_{ref}$) [%]	max(2σ/S$_{ref}$) [%]	max(S)	nPars	Prob(χ^2) [%]	Result
ExpPoly2*	-53.3	-21.1	-8	-3.17	-189	2	5.82	PASS
Exponential	-430	-398	-59.4	-54.8	-1.39e+03	1	0	FAIL
Pow	454	421	60.8	56.3	1.44e+03	1	0	FAIL
Bern3	-123	-92.4	-19.9	-15	-464	3	0	FAIL
Bern4	-104	-77.5	-18.9	-14	-446	4	0	FAIL
Bern5	-99.7	-73.3	-18.3	-13.5	-432	5	0	FAIL

Table 6.10: Results of the spurious signal test for all the candidate functions for category 4. The selected function is marked with a *.

Name	max(S/δS) [%]	max(2σ/δS) [%]	max(S/S$_{ref}$) [%]	max(2σ/S$_{ref}$) [%]	max(S)	nPars	Prob(χ^2) [%]	Result
ExpPoly2*	14.2	0	2.18	0	12.7	2	24	PASS
Bern3	-10.5	0	1.64	0	9.71	3	29.3	PASS
Bern4	13.4	0	2	0	11.7	4	24	PASS
Bern5	16.1	0	2.55	0	14.9	5	25	PASS
Exponential	49	25.2	6.98	3.58	40.8	1	0	FAIL
Pow	177	154	24.1	20.9	141	1	0	FAIL

Table 6.11: Results of the spurious signal test for all the candidate functions for category 5. The selected function is marked with a *.

Name	max(S/δS) [%]	max(2σ/δS) [%]	max(S/S$_{ref}$) [%]	max(2σ/S$_{ref}$) [%]	max(S)	nPars	Prob(χ^2) [%]	Result
ExpPoly2*	17	0	2.98	0	27.1	2	1.59	PASS
Bern3	-22.6	0	-4.28	0	-39	3	15.6	PASS
Bern4	-34	-12.1	-6.56	-2.3	-59.9	4	1.6	PASS
Bern5	34.1	14.2	6.7	2.8	61	5	1.29	PASS
Exponential	73.2	47.3	11.5	7.45	105	1	0	FAIL
Pow	313	285	49	44.7	448	1	0	FAIL

Table 6.12: Results of the spurious signal test for all the candidate functions for category 6. The selected function is marked with a *.

6.8 Experimental systematics

Experimental uncertainties on the $m_{\gamma\gamma}$ shape are due to the photon energy scale (PES) and photon energy resolution (PER) variations. Their effect is included in the fit to data as response functions F_{PES} and F_{PER} on μ_{CB} and σ_{CB} of the signal DSCB:

$$\mu'_{\text{CB}} = (\mu_{\text{CB}} + m_H - 125.)F_{\text{PES}}(\delta^{\pm}, \theta) \tag{6.7}$$

$$\sigma'_{\text{CB}} = \sigma_{CB} F_{\text{PER}}(\delta^{\pm}, \theta) \tag{6.8}$$

Similarly, on $m0^{L(R)}$ and $\sigma^{L(R)}$ for the interference lineshape:

$$m0^{L(R)'} = (m0^{L(R)} + m_H - 125.)F_{\text{PES}}(\delta^{\pm}, \theta) \tag{6.9}$$

$$\sigma^{L(R)'} = \sigma^{L(R)} F_{\text{PER}}(\delta^{\pm}, \theta) \tag{6.10}$$

The other parameters of the analytic functions used to model the signal and the interference are not affected. These $\delta^{\pm}$ systematic variations are extracted for each analysis category and the corresponding NPs θ are treated as fully correlated among categories. A correlation scheme with 69 NPs for the scale θ_{PES} and 10 NPs for the resolution θ_{PER} is used. The uncertainties are computed from the MC signal sample with $\lambda = 1$, using the following techniques:

- for the **scale**, the ratio-of-mean technique is used: the means of $m_{\gamma\gamma}$ are computed for nominal and $\pm 1\sigma$ varied distributions. Then, the systematic uncertainty is evaluated as
  $$\delta^{\pm}_{\text{PES}} = \frac{\langle m^{\pm 1\sigma}_{\gamma\gamma} \rangle}{\langle m^{\text{nom}}_{\gamma\gamma} \rangle} - 1. \tag{6.11}$$
  As shown in Figure 6.30, the impact is different depending on the source, but in general less than 0.1% or between 0.1% and 0.2% for a few sources. Scale uncertainties are implemented in the fit to data with a Gaussian constraint using the $+1\sigma$ variation, because of the high symmetry observed. The constraint is applied to μ_{CB} and $m0^{L(R)}$ as a response function of the type $F_{\text{PES}}(\delta^{\pm}, \theta) = (1 + \delta^{+}_{\text{PES}}\theta_{\text{PES}})$.
- for the **resolution**, the ratio of inter-quartile distribution is used: the inter-quartile is computed as $S = CDF^{-1}(75\%) - CDF^{-1}(25\%)$, where CDF is the cumulative distribution function of the $m_{\gamma\gamma}$ nominal and varied distributions. Then, the uncertainty is evaluated as
  $$\delta^{\pm}_{\text{PER}} = \frac{S^{\pm 1\sigma}}{S^{\text{nom}}} - 1. \tag{6.12}$$
  As shown in Figure 6.31, the impact is different depending on the source, but it is almost always less than 5%. Resolution uncertainties are implemented in the fit with an asymmetric constraint, to take into account differences in the $+1\sigma$ and -1σ variations. The constraint is applied to σ_{CB} and $\sigma^{L(R)}$ as a response function $F_{\text{PER}}(\delta^{\pm}, \theta)$, which is a linear interpolation of θ_{PER} between $(1 + \delta^{-}_{\text{PER}})$ and $(1 + \delta^{+}_{\text{PER}})$.

6.9 Theoretical systematics

Theoretical uncertainties on the signal and interference yield are due to QCD scale and PDF+α_s variations. Their effect is evaluated directly on the MC samples using

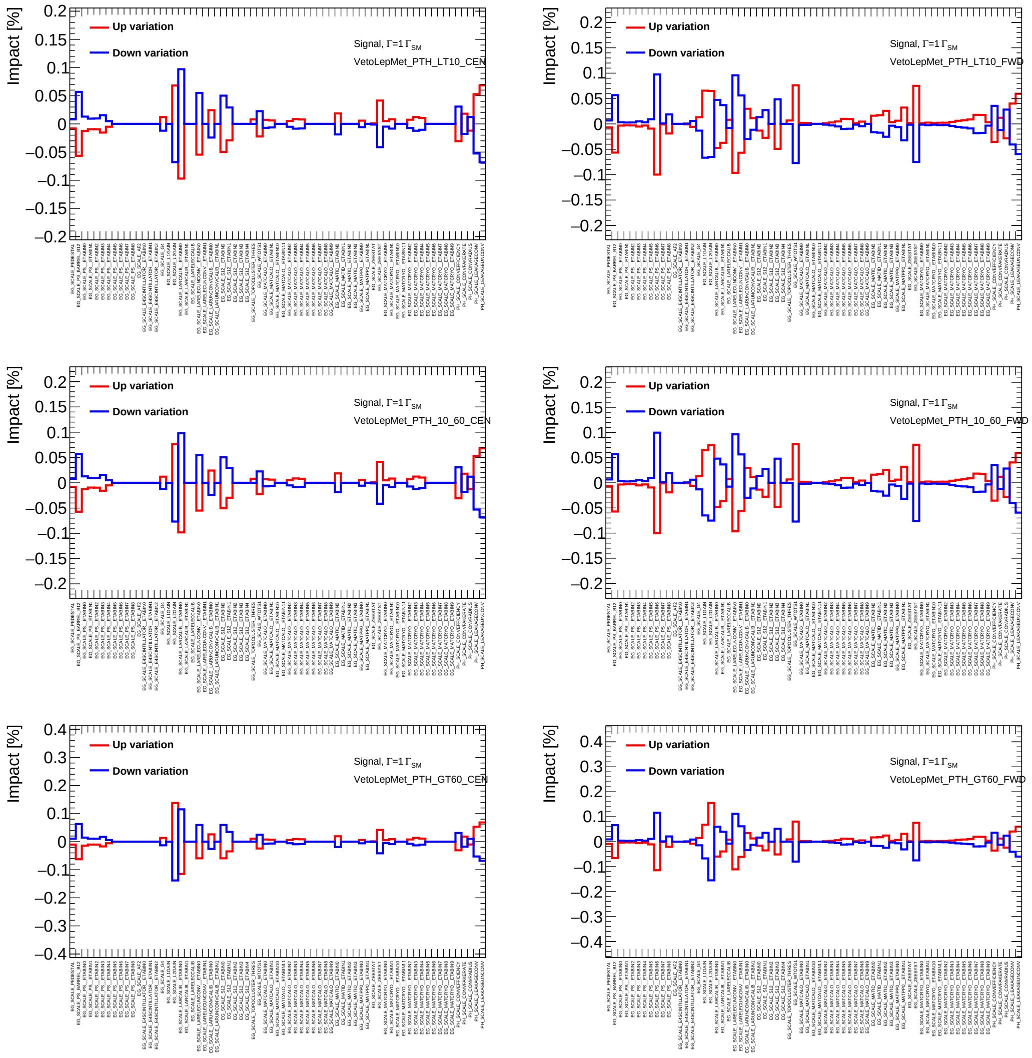

Figure 6.30: Overview of the computed variations due to the PES for all the reconstructed categories of the analysis.

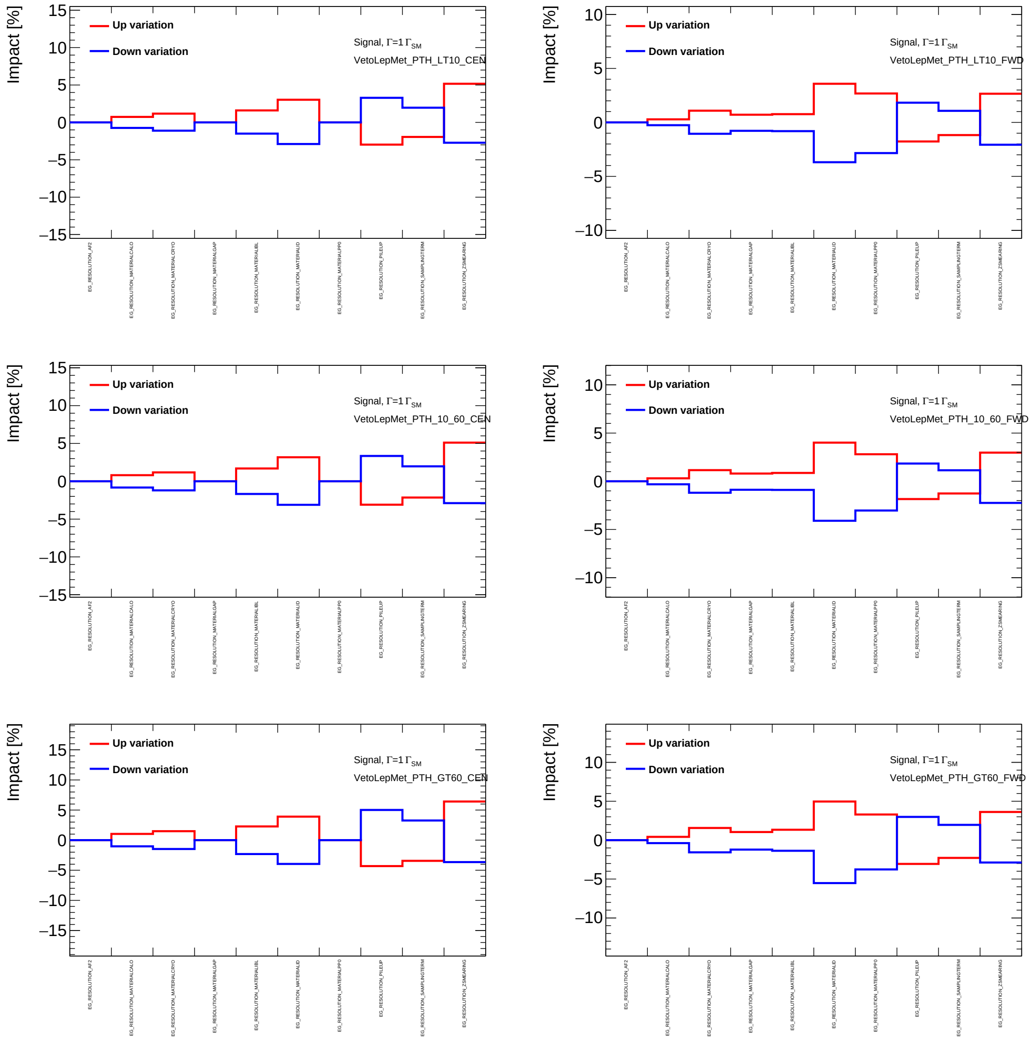

Figure 6.31: Overview of the computed variations due to the PER for all the reconstructed categories of the analysis.

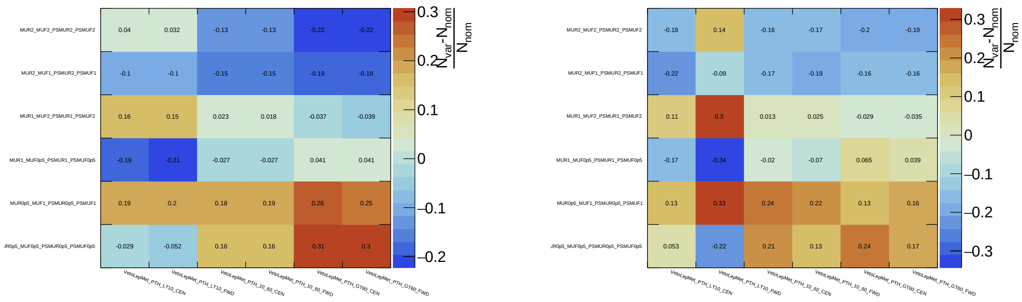

(a) Signal process.

(b) $gg-$interference process.

Figure 6.32: The relative difference of the integral of each variation with respect to the integral of the nominal, as defined by Eq.6.13.

generator-level variations coming from on-the-fly weights provided by SHERPA .

The effect of varying the renormalization scale μ_R and factorization scale μ_F is checked for the signal and for the interference in Figure 6.32, where for each category it is shown the relative difference of the integral of each variation with respect to the integral of the nominal, defined as

$$\frac{N_{\text{var}} - N_{\text{nom}}}{N_{\text{nom}}} \tag{6.13}$$

In all the plots, the label `MURXX` corresponds to the prefactor in front of the renormalization scale, while the label `MUFXX` corresponds to the prefactor in front of the factorization scale. The impact per category of the QCD scale systematic is defined as the maximum in absolute value among all variations[7] and the size is up to 30%, depending on the category.

The nominal set of PDF used is PDF4LHC15 at NLO which, apart from the central PDF, comes along with 30 error sets. Each of them corresponds to an eigenvector of the covariance matrix in the parameter space of the PDF fit. This is usually called the Hessian representation of the total PDF uncertainty and is computed using the master formula [115]:

$$\delta^{\text{pdf}}\sigma = \sqrt{\sum_{k=1}^{N_{\text{mem}}} (\sigma^{(k)} - \sigma^{(0)})^2} \tag{6.14}$$

Two additional PDF sets are provided with a different value of α_s assumed in the PDF fit. The nominal value of 0.118 is varied by ±0.0015 to compute the α_s uncertainty at the 68% of confidence level. These two variations are also included in the computation of the total PDF uncertainty, resulting in 32 effective contributions to 6.14. The master formula is then evaluated per category in order to estimate the effect on the yield (Table 6.13): the impact for the signal is around 5%, while for the interference the largest impact, up to 17%, is for low $pT_{\gamma\gamma}$ categories.

The QCD scale and PDF+α_s systematics are implemented in the model using a 2 NPs scheme for each, where the impact on the signal and the interference is decorrelated.

---

[7] It is then symmetrized for up/down variations.

	Signal	$gg-$interference
VetoLepMet PTH LT10 CEN	0.057	-0.11
VetoLepMet PTH LT10 FWD	0.047	-0.17
VetoLepMet PTH 10 60 CEN	0.038	-0.036
VetoLepMet PTH 10 60 FWD	0.036	-0.04
VetoLepMet PTH GT60 CEN	0.046	-0.056
VetoLepMet PTH GT60 FWD	0.046	-0.053

Table 6.13: Relative PDF+α_s uncertainty.

6.10 Statistical model

In each of the n_{cat} analysis categories, the $m_{\gamma\gamma}$ total PDF can be written as

$$\begin{aligned} f \equiv\ & \mu N_S f_S(m_{\gamma\gamma}; m_H, \boldsymbol{\theta}_{\text{shape}}) + \left((N_P + N_I)\sqrt{\mu\lambda K_S}\right) f_I(m_{\gamma\gamma}; \lambda, m_H, \boldsymbol{\theta}_{\text{shape}}) \\ & + N_B f_B(m_{\gamma\gamma}; \boldsymbol{\theta}_{\text{BS}}) - (N_P\sqrt{\mu\lambda K_S}) f_P(m_{\gamma\gamma}) \end{aligned} \tag{6.15}$$

With respect to 6.3, the pedestal P artificial component had to be included in order to preserve the right number of events: this subtracts the additional “fake” events which were added to the I component to make it a proper positive-definite PDF, as explained in Section 6.6. f_P is an uniform PDF which is there just to subtract the number of pedestal events N_P (one constant value per category) corresponding to the inclusion of the *ped* term in f_I.

The number of signal events in category c is given by:

$$N_S^c = \sigma_H^{\gamma\gamma}\epsilon^c \mathcal{L} K^c(\boldsymbol{\theta}_{\text{yield}}) + N_{\text{spur}}^c \theta_{\text{spur}}^c \tag{6.16}$$

where

- $\sigma_H^{\gamma\gamma}$ is the value of the diphoton branching ratio times Higgs production cross section;
- ϵ^c is the signal efficiency vector. It measures the probabilities for a truth-level Higgs event to end up in a given reconstructed category c;
- $\mathcal{L}$ is the integrated luminosity of the fitted sample;
- $K^c(\boldsymbol{\theta}_{\text{yield}})$ is a vector of multiplicative correction factors to the signal yields from systematic effects described in Section 6.9, as a function of NPs collectively denoted by $\boldsymbol{\theta}_{\text{yield}}$;
- N_{spur}^c is a vector of values of the background modeling uncertainty described in Section 6.7, implemented as an additive correction to the signal yield proportional to the NP θ_{spur}^c.

Similarly, the number of “true” interference events in category c is given by:

$$N_I^c = \sigma_I^{\gamma\gamma}\epsilon_I^c \mathcal{L} K^c(\boldsymbol{\theta}_{\text{yield}}) \tag{6.17}$$

where

- $\sigma_I^{\gamma\gamma}$ is the value of the interference cross section times diphoton branching ratio;
- ϵ_I^c is the interference efficiency vector. It measures the probabilities for a truth-level interference event to end up in a given reconstructed category c;

The likelihood function of the model is

$$L\left(\lambda, \mu, m_H, \boldsymbol{\theta}; m_{\gamma\gamma}\right) = \prod_{c=1}^{n_{\rm cat}} \mathrm{Pois}\left(o^c | \nu^c\left(\lambda, \mu, \boldsymbol{\theta}\right)\right) \prod_{i=1}^{o^c} \frac{1}{\nu^c} f^c\left(m^i_{\gamma\gamma}; \lambda, m_H, \boldsymbol{\theta}\right) \prod_j G\left(\theta_j\right). \tag{6.18}$$

The first product is the likelihood extended term and it spans the analysis categories: the number of observed events for each category o^c is modelled with a Poisson distribution with mean

$$\nu^c\left(\lambda, \mu, \boldsymbol{\theta}\right) = \mu N^c_S(\boldsymbol{\theta}) + \left((N^c_P + N^c_I)\sqrt{\mu\lambda K_S}\right) + N^c_B - (N^c_P\sqrt{\mu\lambda K_S}) \tag{6.19}$$

The second term in the likelihood function (6.18) is related to the total PDF presented in Eq. 6.3, while the last term is the product of constraint terms: each NP θ_j is constrained by an unitary Gaussian PDF $G\left(\theta\right)$ of mean 0 and width 1. The POI λ is estimated through a simultaneous maximum likelihood fit to the observable $m_{\gamma\gamma}$ over all categories. The $m_{\gamma\gamma}$ dataset is binned with $N_{bin} = 440$.

6.11 Results

Results from the simultaneous maximum likelihood fit to the $m_{\gamma\gamma}$ distribution in all analysis categories are provided in three configurations of the statistical model:

1. λ is the only free-to-float POI, while the signal is assumed to have SM yield ($\mu = 1$, constrained by SM theory uncertainties) and the Higgs boson mass is set to $m_H = 125.09$ GeV (constrained by the uncertainty of the mass measurement performed by ATLAS and CMS during Run 1);
2. λ is the free-to-float POI and μ is profiled (unconstrained), while the Higgs boson mass is set to $m_H = 125.09$ GeV;
3. λ is the free-to-float POI, μ and m_H are profiled (unconstrained).

Clearly, 1 is more dependent on assumptions than 2, which is more than 3.

6.11.1 Expected results

Expected results are obtained through a fit to an Asimov dataset, generated from the constructed total PDF (introduced in Section 6.10) where all the parameters are set to: $\lambda = 1$ (SM expectation), $\mu = 1$ (SM expectation) and $m_H = 125.09$ GeV (best measured value). To construct the Asimov dataset, the normalization and shape parameters of the background have to be initialized through a background-only fit to the data sidebands, excluding the signal region from 120 to 130 GeV. The plots of the fits to the data sidebands are given in Figure 6.33. The plots of the total-model fit to the Asimov data are given in Figure 6.34.

A small non-closure is present in the fit as the obtained central value of λ is 0.7 instead of 1.0. This effect is investigated in the Appendix A. The result of the fit is expressed in terms of the $+2\sigma$ uncertainty on λ, as obtained from a scan of the likelihood, which is shown in Figures 6.35, 6.36 and 6.37. This is considered as a proxy of the limit at 95% CL on λ. The results from the scans are in agreement with the output of the `MINOS` algorithm.

The limit on λ is presented in Table 6.14, where the fit is repeated for different scenarios: each row corresponds to one of the three configurations discussed above and each column corresponds to the specific set (or sets) of systematic uncertainties implemented in the model. In the configurations where μ and m_H are profiled, the value of their 1σ (symmetric) error is also given, to show the level of precision that this statistical model can achieve when measuring also the Higgs mass and/or the global signal strength. When comparing the numbers from different rows, it's clear that in the passage from configuration 2 to configuration 3 the upper limit on λ is deteriorated: in fact profiled m_H plays the role of unconstrained NP on the shape.

The theoretical uncertainty on the QCD scale is a dominant systematic of the result, as it pushes the limit on λ significantly higher. This is a direct consequence of the choice of the implementation of the theoretical systematics in the model: to be very conservative, these were inserted with decorrelated NPs between signal and interference.

The experimental systematic which has the largest impact on the result is the photon energy scale (PES), except in configuration 3 where part of its contribution to the uncertainty is already absorbed by the m_H NP.

The full result, which contains all sources of systematics, is in the rightmost column: in the worst case scenario (μ and m_H profiled) the expected limit is $\lambda < 90$, while in the best case scenario (μ and m_H fixed) it's $\lambda < 80$.

Figures 6.38 and 6.39 show the correlations between fitted parameters for the configurations where λ is not the only one free-to-float. The correlation between λ and m_H is quite large, but it gets reduced from 63% to 42% when the systematic uncertainties are included in the model: the inclusion of PES systematics have the effect to remove part of this correlation. For similar reasons, the correlation between λ and μ gets slightly reduced as well, from 15% to 11%. The correlation between μ and m_H is instead very low, 6-7%, because these two parameters act in a different way on the $m_{\gamma\gamma}$ spectrum: μ controls the normalization of the PDF while m_H shifts the position of the signal peak and the interference lineshape.

A detailed breakdown of the impact of the different systematic uncertainties is shown through the ranking plots in Figures 6.41, 6.42 and 6.43. To compute the postfit impact of a NP, the fit is repeated with this parameter fixed to its best-fit value (given by its pull) $\pm 1\sigma$. The relative difference of the fitted POI is then computed to get its impact. In the prefit case, the same procedure is done but with the NP fixed at a value of ± 1.

As a test of compatibility among categories, the fit has been repeated with an alternative configuration where, in addition to λ floating, multiple μ_i parameters decorrelated among categories are fitted and m_H is fixed constant. A similar test is repeated fitting multiple m_{H_i} parameters and floating λ and a single global μ. Results of the two tests are reported in Figure 6.40.

	Stat-only	PDF+α_s	QCD scale	Spur. Sig.	PES	PER	Tot
λ (2σ)	64	65	86.9	64	64.1	64	90
μ (1σ)	0.068	0.082	0.21	0.071	0.068	0.078	0.22
m_H (1σ)	0.19	0.19	0.191	0.191	0.382	0.19	0.382
λ (2σ)	40	40.3	56	39.6	54.9	39.7	81
μ (1σ)	0.068	0.081	0.21	0.071	0.068	0.078	0.22
λ (2σ)	40	40.2	55.6	39.6	54.8	39.6	80

Table 6.14: Upper limit ($+2\sigma$ uncertainty) on λ and 1σ uncertainties on μ and m_H obtained from the Asimov fit. The values are reported for different configurations of the fit, as well as for different sets of systematic uncertainties considered. The first column reports the results using only the statistical component of the uncertainty.

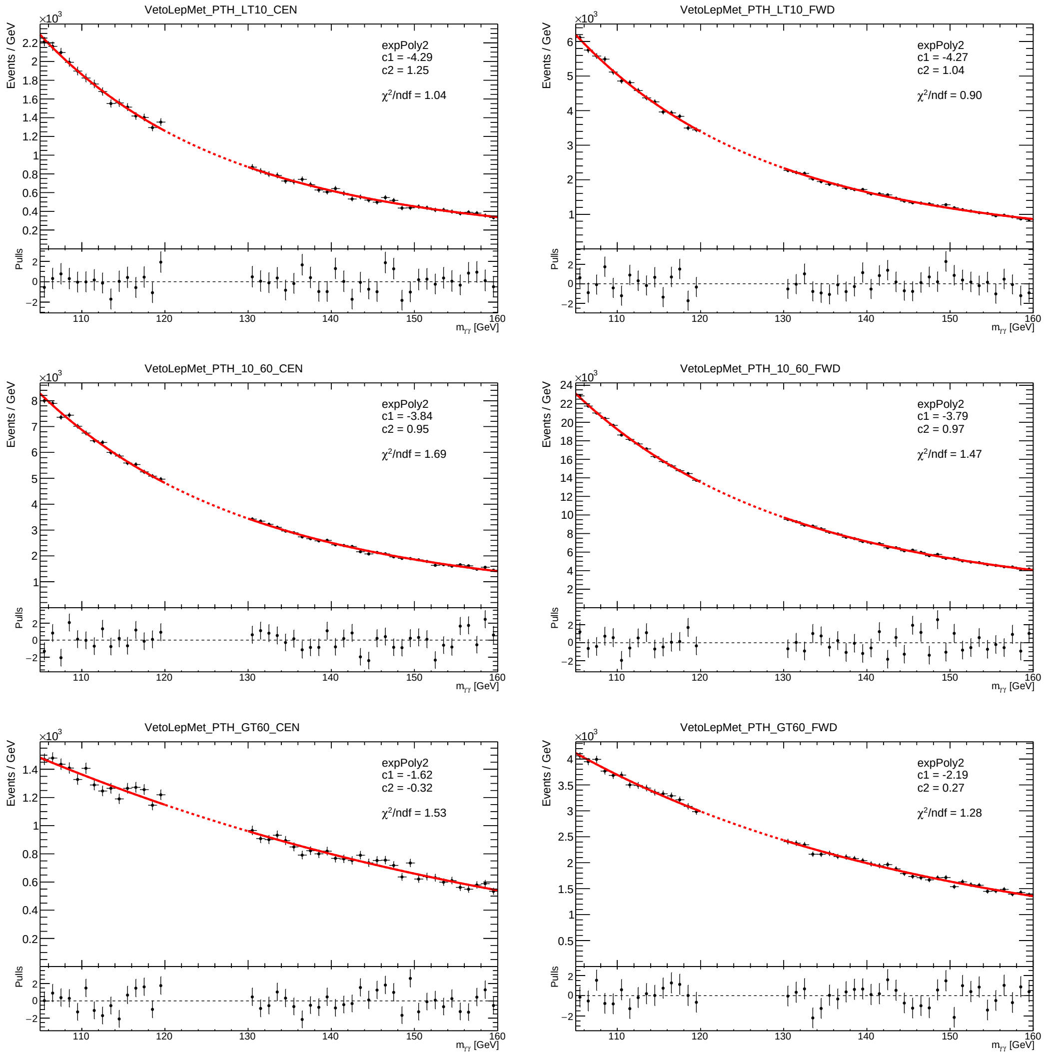

Figure 6.33: Background-only fits to the data sidebands for all reconstructed categories of the analysis.

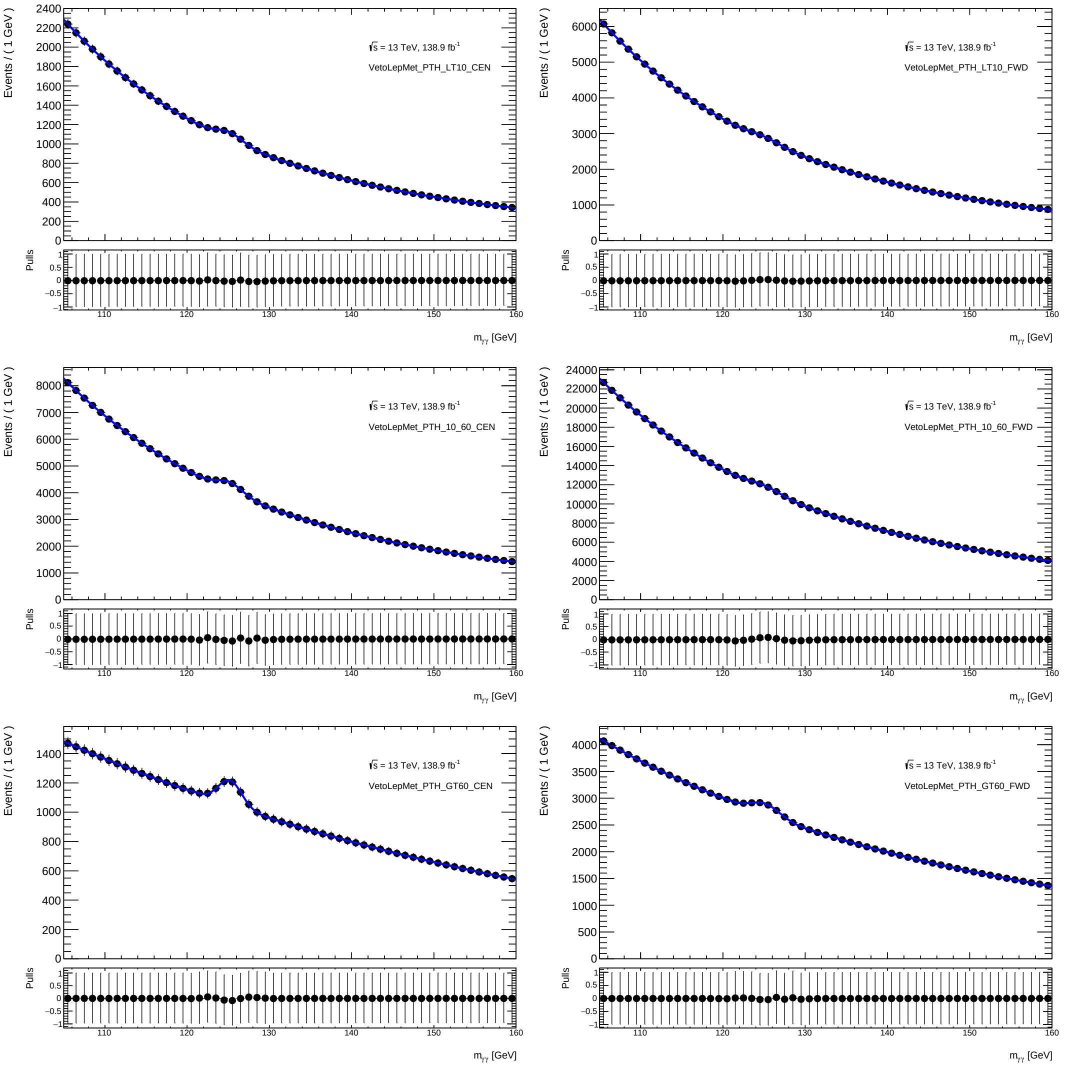

Figure 6.34: Total-model fit to the Asimov dataset for all reconstructed categories of the analysis.

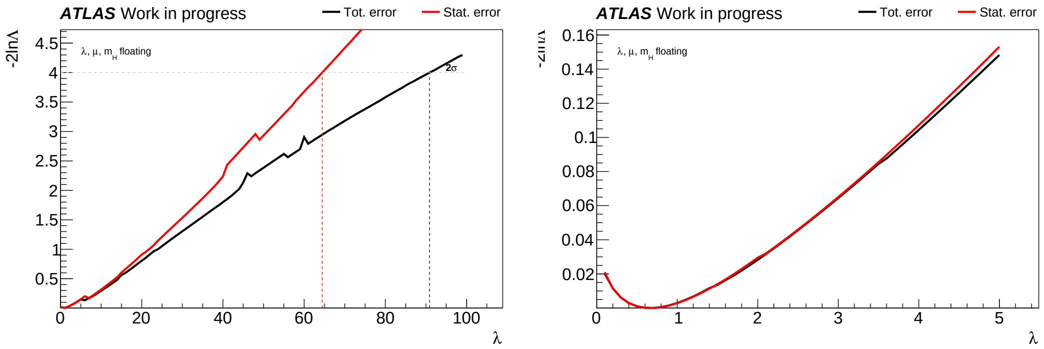

Figure 6.35: Expected profile likelihood scan of the λ POI, for configuration 3. Focus on the region around the minimum (right plot).

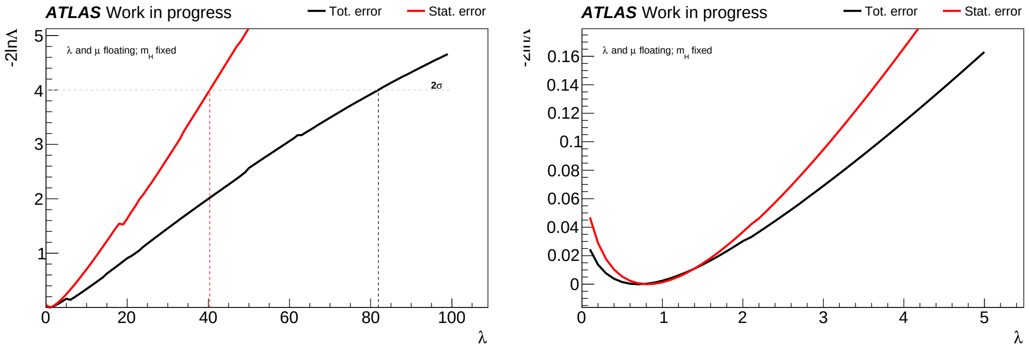

Figure 6.36: Expected profile likelihood scan of the λ POI, for configuration 2. Focus on the region around the minimum (right plot).

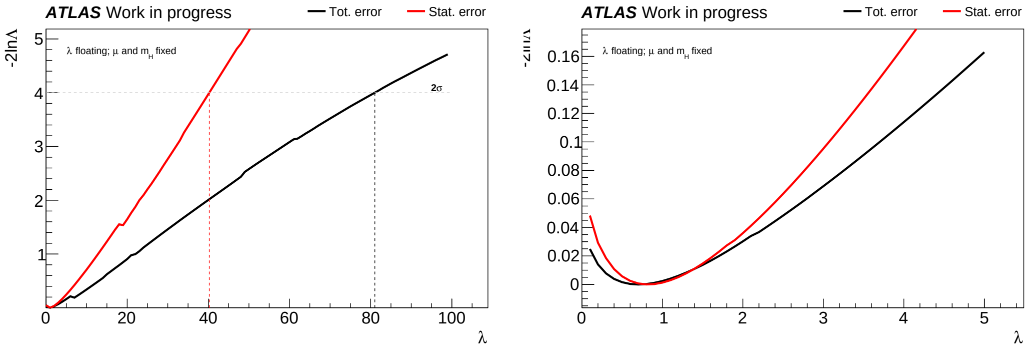

Figure 6.37: Expected profile likelihood scan of the λ POI, for configuration 1. Focus on the region around the minimum (right plot).

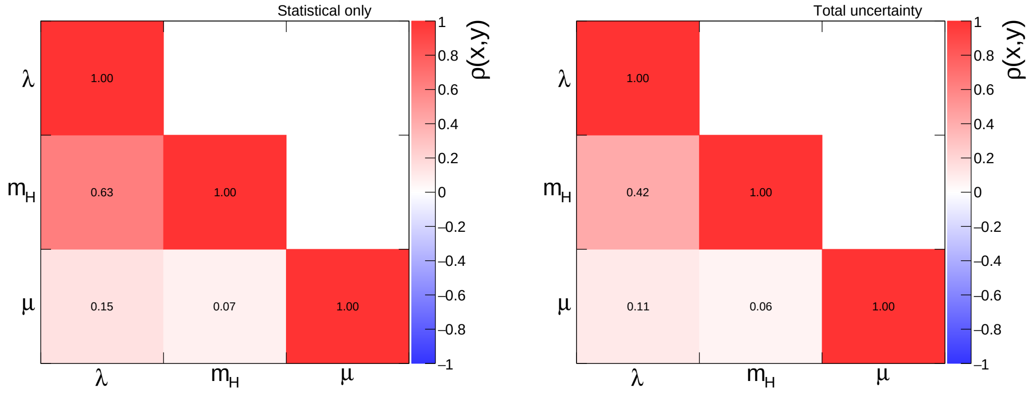

Figure 6.38: Expected correlation matrix considering statistical-only (left plot) and total (right plot) uncertainty, for configuration 3.

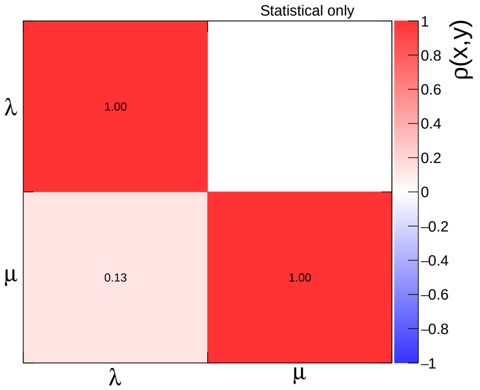

Figure 6.39: Expected correlation matrix considering statistical-only (left plot) and total (right plot) uncertainty, for configuration 2.

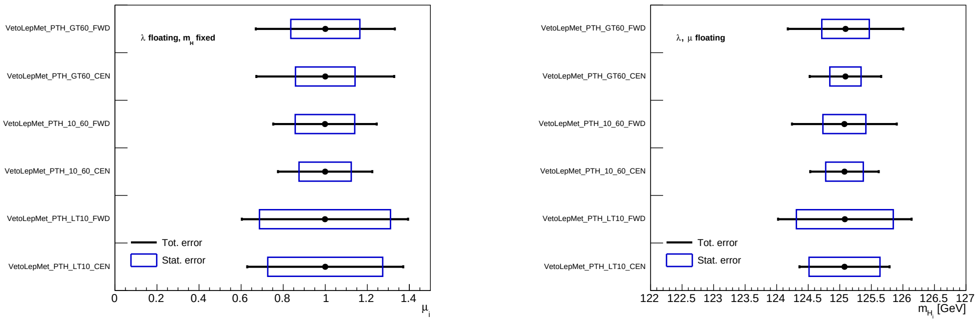

Figure 6.40: Expected compatibility among categories when fitting one μ_i per category (left plot) and when fitting one m_{H_i} per category (right plot).

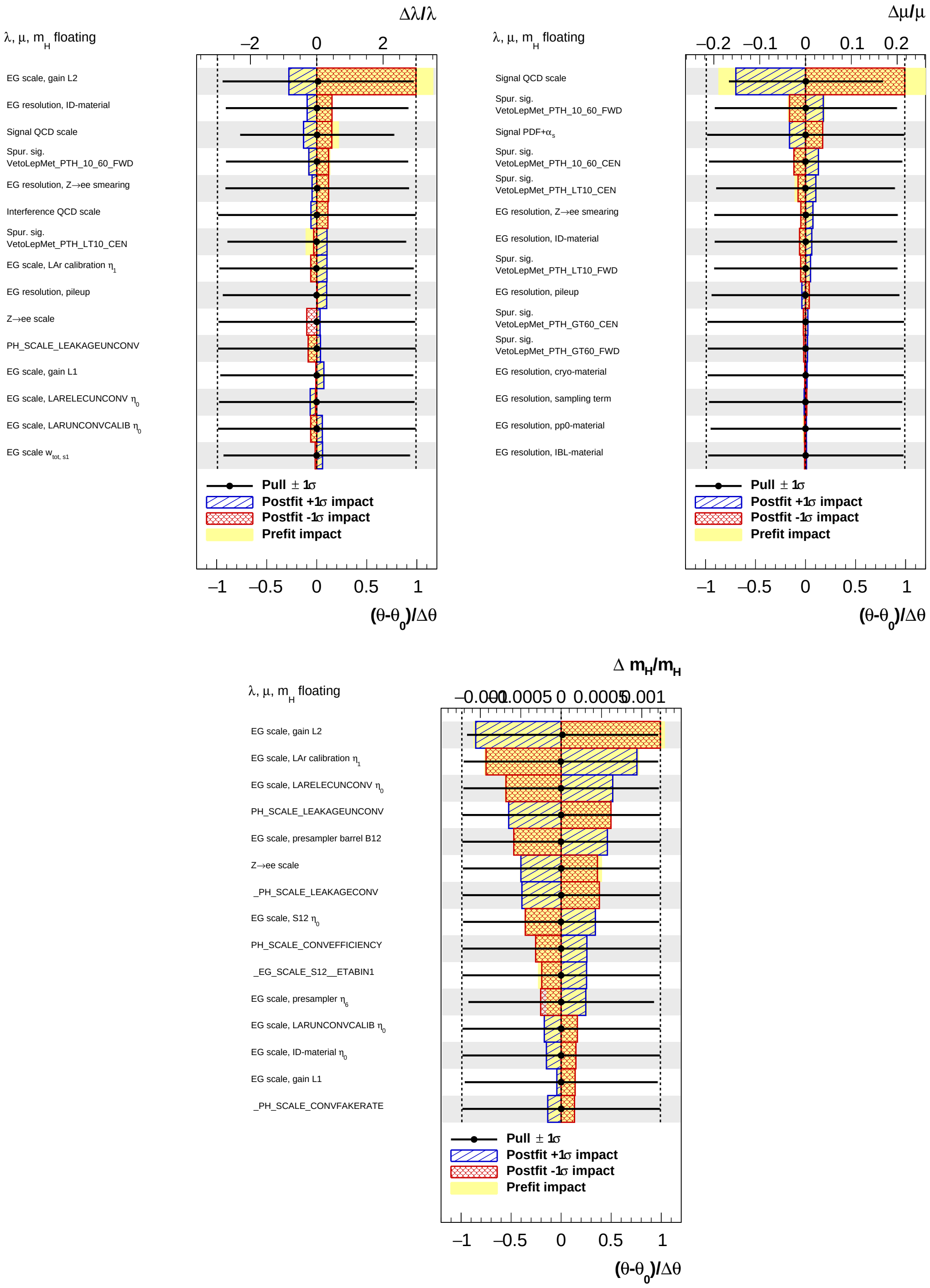

Figure 6.41: Expected ranking of the systematic uncertainties according to their postfit impact, for configuration 3. The top axis shows the relative difference of the measured POI, while the bottom axis quantifies the pulls.

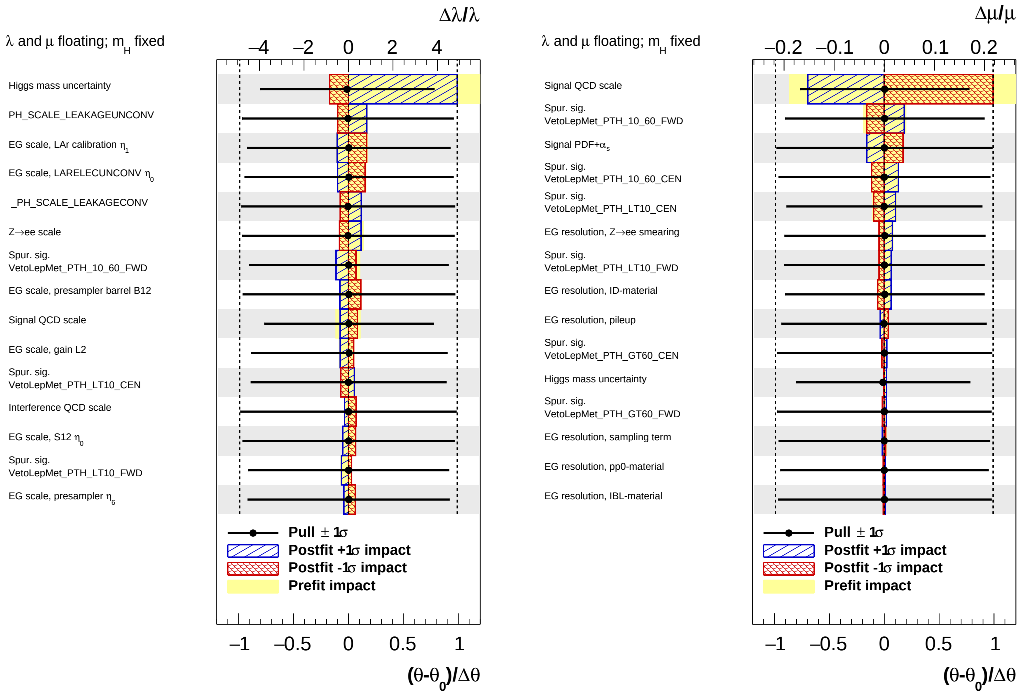

Figure 6.42: Expected ranking of the systematic uncertainties according to their postfit impact, for configuration 2. The top axis shows the relative difference of the measured POI, while the bottom axis quantifies the pulls.

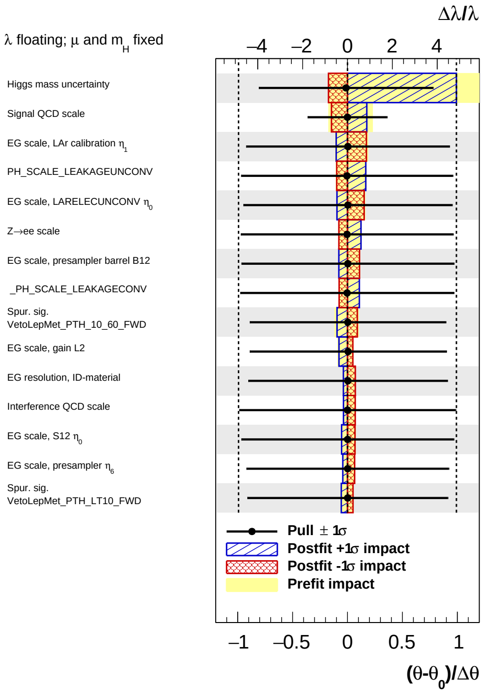

Figure 6.43: Expected ranking of the systematic uncertainties according to their postfit impact, for configuration 1. The top axis shows the relative difference of the measured POI, while the bottom axis quantifies the pulls.

	Stat-only	Exp	Theo	Tot
λ (2σ)	84	86	108	112
μ_G (1σ)	0.067	0.078	0.22	0.22
m_H (1σ)	0.179	0.368	0.179	0.368
λ (2σ)	53	77	75	101
μ_G (1σ)	0.067	0.078	0.22	0.22
λ (2σ)	53	76	74	98

Table 6.15: Upper limit ($+2\sigma$ uncertainty) on λ and 1σ uncertainties on μ and m_H obtained from the fit to the data. The values are reported for different configurations of the fit, as well as for different sets of systematic uncertainties considered. The first column reports the results using only the statistical component of the uncertainty.

6.11.2 Observed results

Observed results are obtained through a fit to the ATLAS full Run 2 dataset of proton-proton collisions at $\sqrt{s} = 13$ TeV, amounting to about 139 fb^{-1} of integrated luminosity. The plots of the total-model fit are given in Figure 6.44.
The central values obtained from the fit are $\lambda = 5.51$, $\mu = 0.99$ and $m_H = 125.224$ GeV for configuration 3; $\lambda = 4.08$ and $\mu = 0.99$ for configuration 2; $\lambda = 4.11$ for configuration 1. Results of the fit for the three different configurations are summarized in Table 6.15. The full result, which contains all sources of systematics, is in the rightmost column: in the worst case scenario (μ and m_H profiled) the observed limit is $\lambda < 112$, while in the best case scenario (μ and m_H fixed) it's $\lambda < 98$. The value of the observed limit is higher than the expected one and this is partially due to an higher central value of λ obtained from the fit. The scans of the likelihood are shown in Figures 6.45, 6.46 and 6.47. Figures 6.48 and 6.49 show the correlations between fitted parameters for the configurations where λ is not the only one free-to-float. A detailed breakdown of the impact of the different systematic uncertainties is shown through the ranking plots in Figures 6.51, 6.52 and 6.53. Results of the category compatibility tests are reported in Figure 6.50.

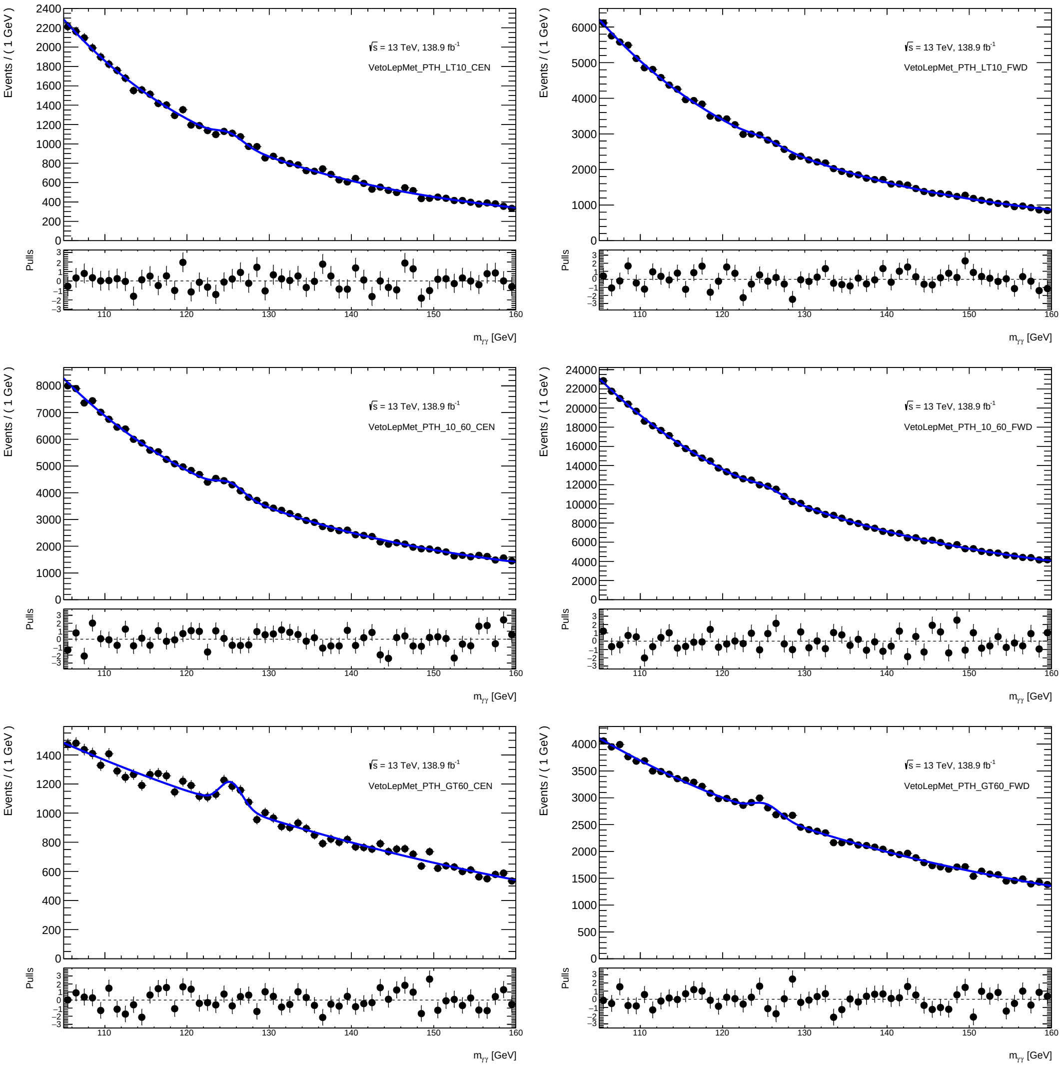

Figure 6.44: Total-model fit to the ATLAS full Run 2 dataset for all reconstructed categories of the analysis.

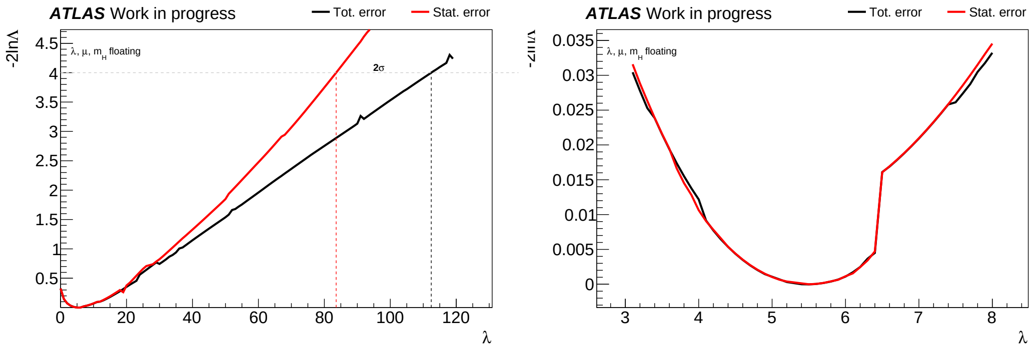

Figure 6.45: Observed profile likelihood scan of the λ POI, for configuration 3. Focus on the region around the minimum (right plot).

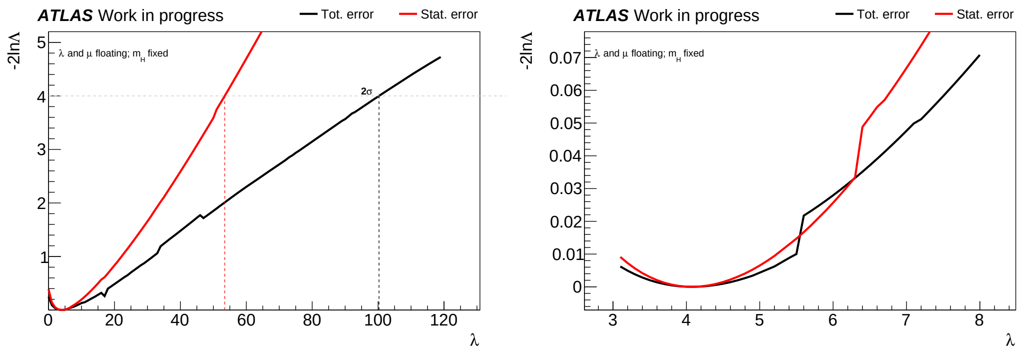

Figure 6.46: Observed profile likelihood scan of the λ POI, for configuration 2. Focus on the region around the minimum (right plot).

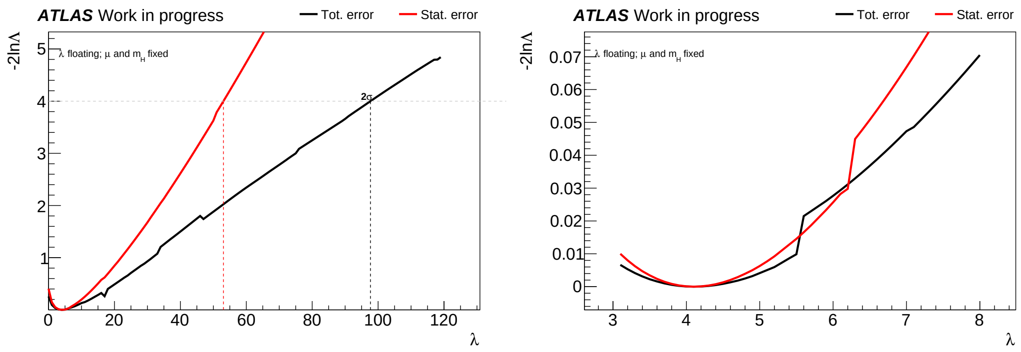

Figure 6.47: Observed profile likelihood scan of the λ POI, for configuration 1. Focus on the region around the minimum (right plot).

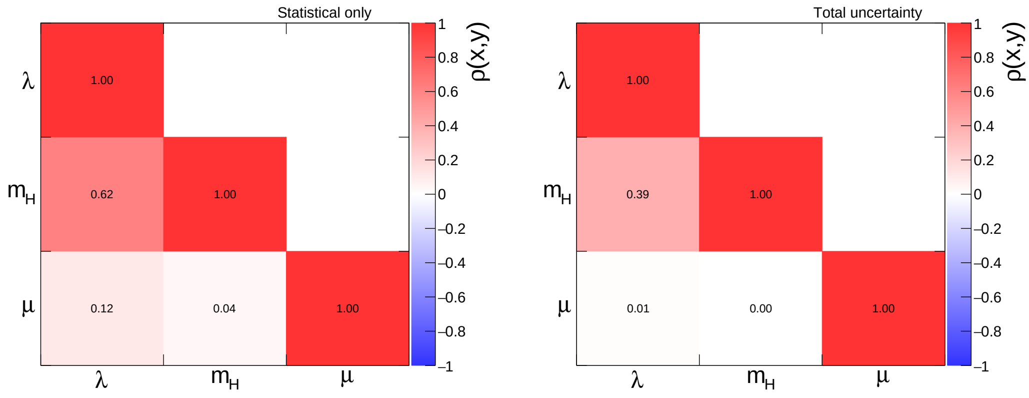

Figure 6.48: Observed correlation matrix considering statistical-only (left plot) and total (right plot) uncertainty, for configuration 3.

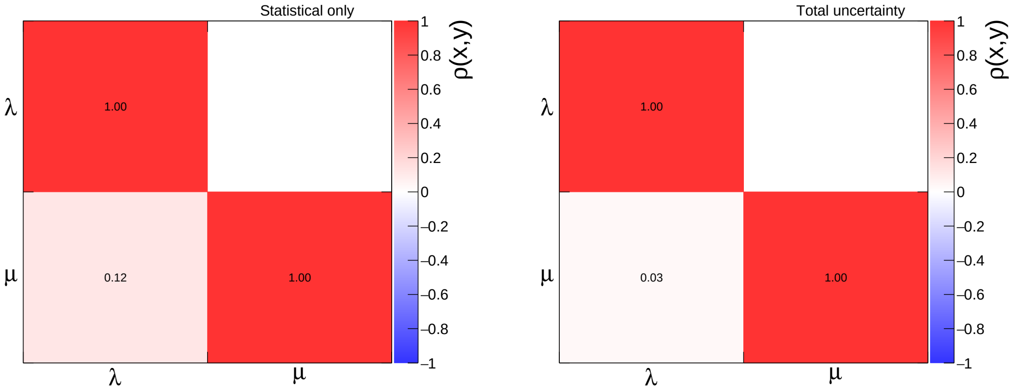

Figure 6.49: Observed correlation matrix considering statistical-only (left plot) and total (right plot) uncertainty, for configuration 2.

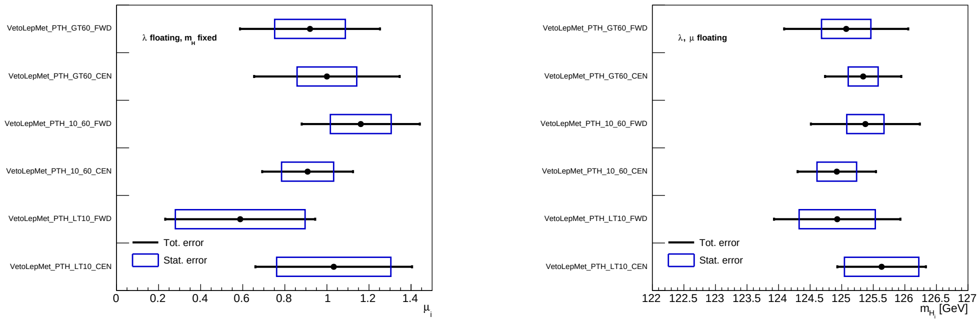

Figure 6.50: Observed compatibility among categories when fitting one μ_i per category (left plot) and when fitting one m_{H_i} per category (right plot).

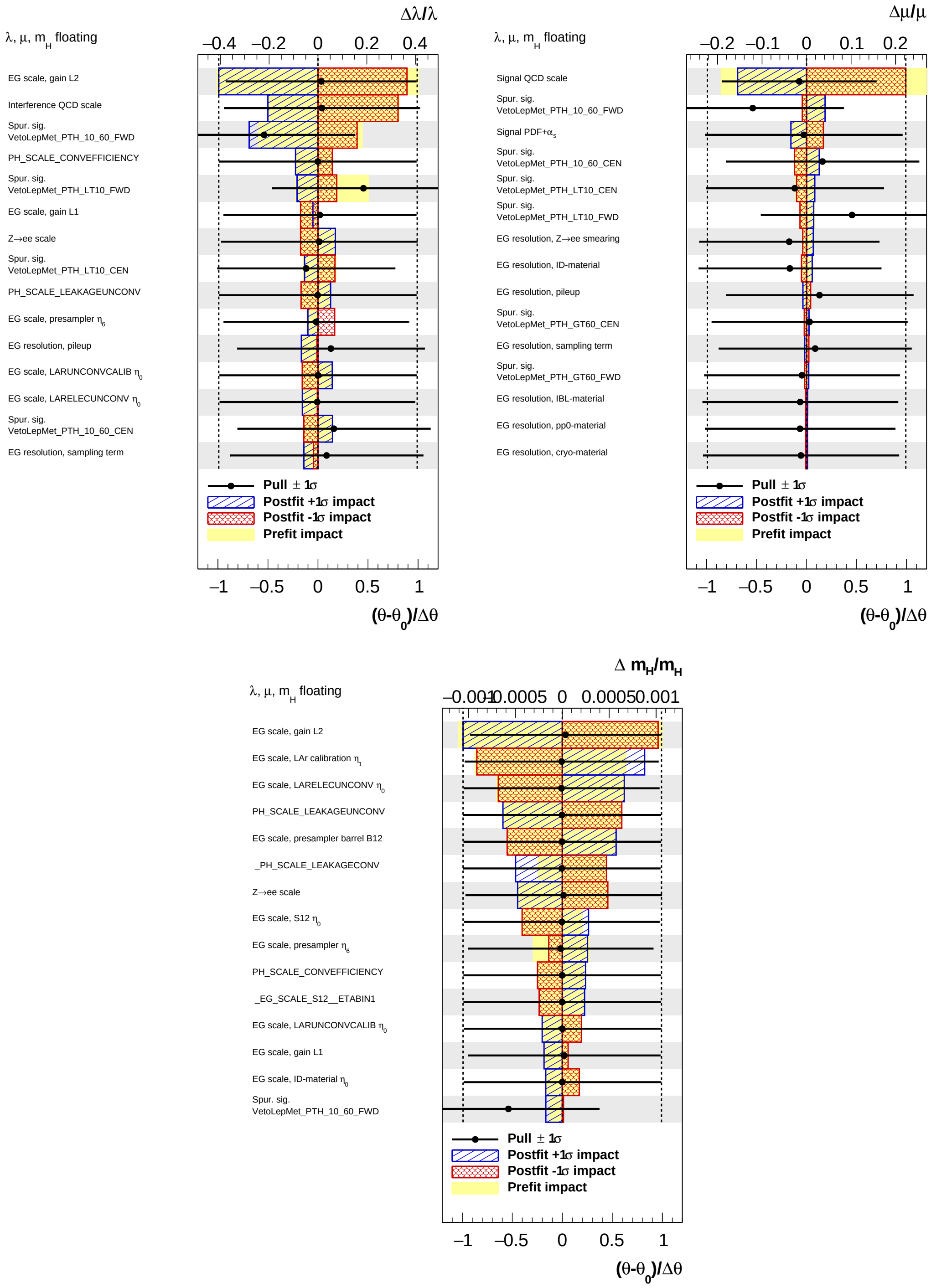

Figure 6.51: Observed ranking of the systematic uncertainties according to their postfit impact, for configuration 3. The top axis shows the relative difference of the measured POI, while the bottom axis quantifies the pulls.

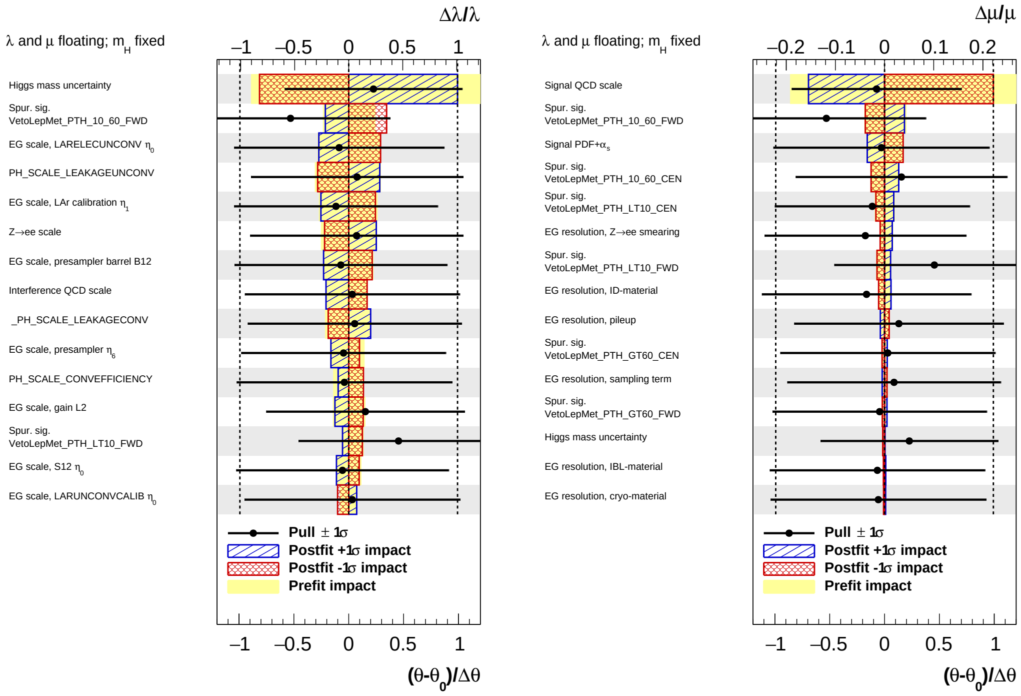

Figure 6.52: Observed ranking of the systematic uncertainties according to their postfit impact, for configuration 2. The top axis shows the relative difference of the measured POI, while the bottom axis quantifies the pulls.

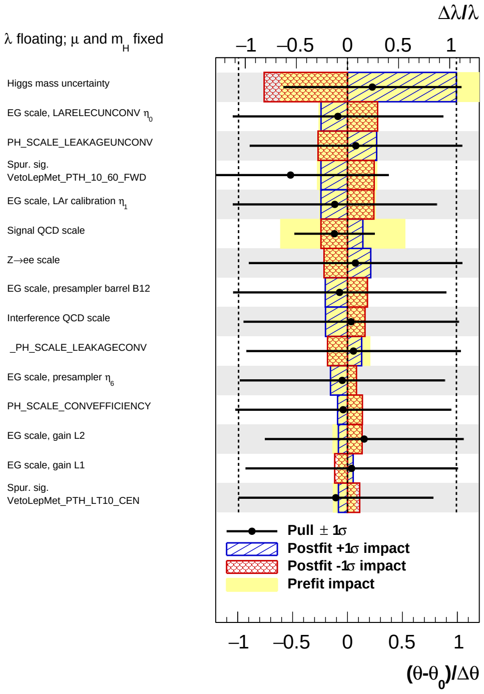

Figure 6.53: Observed ranking of the systematic uncertainties according to their postfit impact, for configuration 1. The top axis shows the relative difference of the measured POI, while the bottom axis quantifies the pulls.

Conclusions

The research work presented in this thesis addresses two classes of challenges in experimental high energy physics: detector performance studies and analyses of physics data from the experiment. From one side, the study of the energy calibration of the ATLAS electromagnetic calorimeter and, from the other one, the measurement of two fundamental properties of the Higgs boson: its production cross-sections and its decay width, using events where it decays to two photons.
The measurements of the Higgs boson properties in the diphoton decay channel that have been presented in this thesis were performed exploiting the full Run 2 dataset of proton-proton collisions at a center-of-mass energy of 13 TeV recorded by ATLAS at the LHC, amounting to about 139 fb^{-1}.

The Higgs boson total production cross-section in the fiducial region of Higgs rapidity $|y_H| < 2.5$ is measured to be $(\sigma \times B_{\gamma\gamma})_{\text{obs}} = 127 \pm 10\,\text{fb}$, in good agreement with the SM expectation of $115 \pm 5\,\text{fb}$. Cross-sections for the ggF+ bbH, VBF, WH, ZH and ttH+ tH production are also reported. Cross-sections are also measured in 27 regions of the STXS framework, including several measurements of ttH in p_T^H bins. The global level of compatibility between the measured STXS and their SM predictions is 60%.

Using a novel analysis method, consisting in exploiting the interference between the resonant Higgs production and the continuum diphoton background, an upper limit of 112 times the SM prediction has been set on the Higgs decay width. This constraint, while still far away from the SM predictions, is already significantly better than the one set by direct methods. The analysis is also considerably more model-independent than other indirect approaches (e.g. based on the measurement of the Higgs boson off-shell production) as it doesn't rely on assumptions on the strength of the Higgs couplings.

Additionally, a study has been performed to investigate the mis-calibration of the photon energy due to non-linearities in the read-out electronics of the ATLAS LAr electromagnetic calorimeter. The effect of the non-linearity response is the main source of systematic uncertainty on the Higgs boson mass measurement, as published in 2018 by the ATLAS collaboration. The results obtained in this thesis substantially improve the understanding of the non-linearity, allowing to derive a correction for it, which will contribute to reduce by 10% the total systematic uncertainty on the next mass measurement in the diphoton channel.

Appendix A

Investigation of the $H \to \gamma\gamma$ width Asimov fit

The non-closure seen in the expected results of the $H \to \gamma\gamma$ width analysis (Section 6.11.1) is addressed in this appendix.
It was found that the choice of modelization of the interference is at the origin of this issue. The interference PDF can be built in an alternative way, keeping the parameters $N^{L(R)}$ constant and reparametrizing $\sigma^{L(R)}$ in function of λ. In practice, Eq. 6.6 is replaced by the following:

$$\sigma^{L(R)} = \sigma^{L(R)}_{\lambda=1} + p_0^{L(R)} + p_1^{L(R)}(\lambda - 1) \tag{A.1}$$

All the rest of the procedure described in Section 6.6 is mantained and used to derive an alternative interference PDF. Fits of the lineshape per category are shown in Figure A.1. Figure A.2 shows how the interference lineshape changes with λ.
This alternative parametrization is used to derive the main result of the analysis and the related scan of the likelihood is shown in Figures A.3, A.4 and A.5. The minimum of the likelihood is now at $\lambda = 1$, as one would normally expect. The expected limit at 2σ is $\lambda < 59$ in the worst case scenario (μ and m_H profiled) and it's $\lambda < 55$ in the best case scenario (μ and m_H fixed).

However, in order to test the accuracy of this parametrization, an injection test similar to the one presented in Section 6.6.3 has been performed: the results of a total-PDF fit to the Asimov dataset per category are shown in Figure A.6 for the case $\lambda = 1$. The injection test is repeated for the other four points ($\lambda = 5, 10, 50, 100$), each time performing a simultaneous fit across all the categories of the analysis and the results are given in Figure A.7. After the point at $\lambda = 1$, the red points start to diverge from the reference line indicating the presence of a mismodeling bias, which increases with λ and its size is around 35% for $\lambda = 100$. Further studies are needed to understand and correct this mismodeling before deploying the alternative parametrization to derive the main results of the analysis.

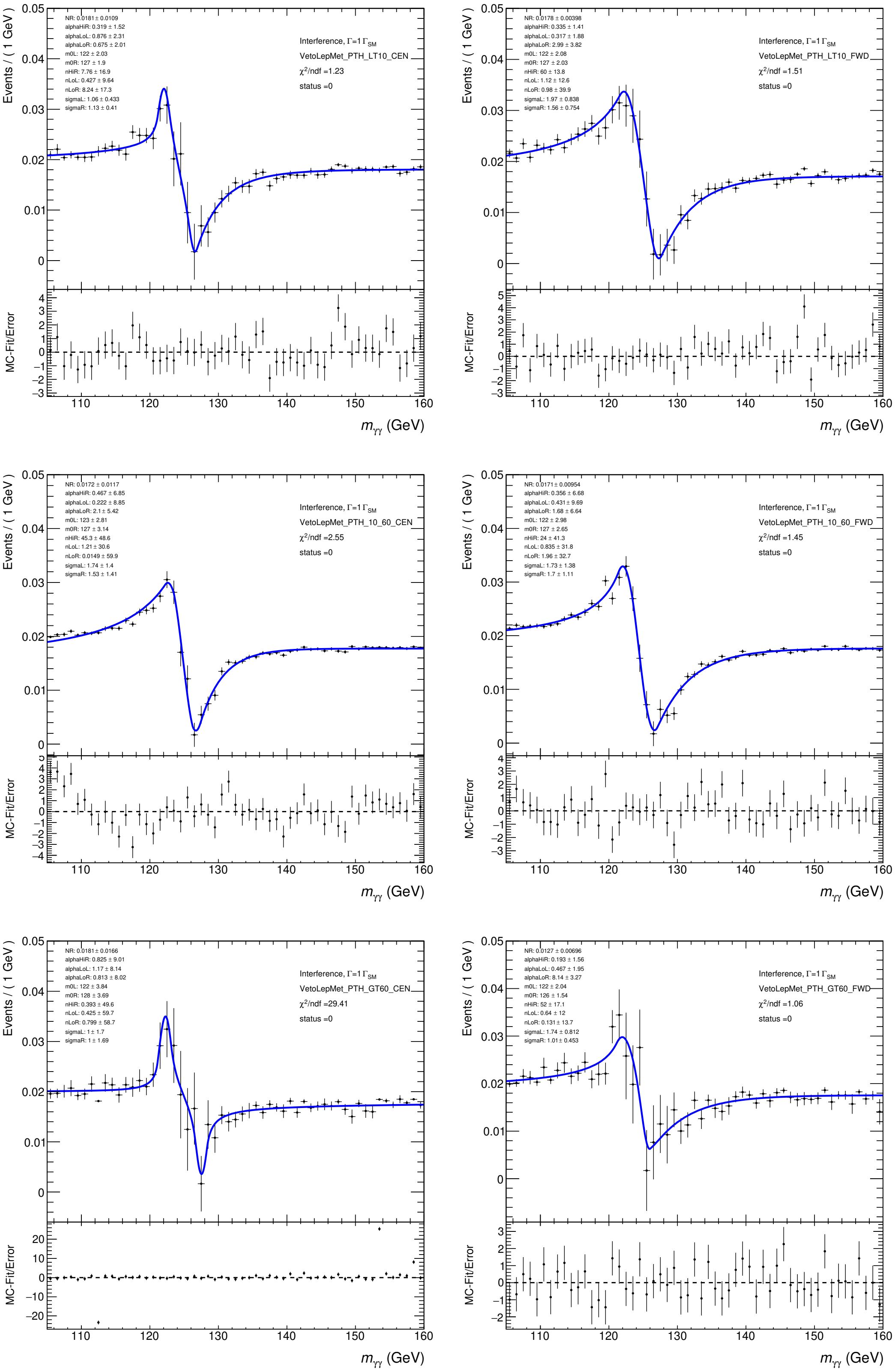

Figure A.1: Fitted interference shapes for all the reconstructed categories of the analysis, using the alternative parametrization.

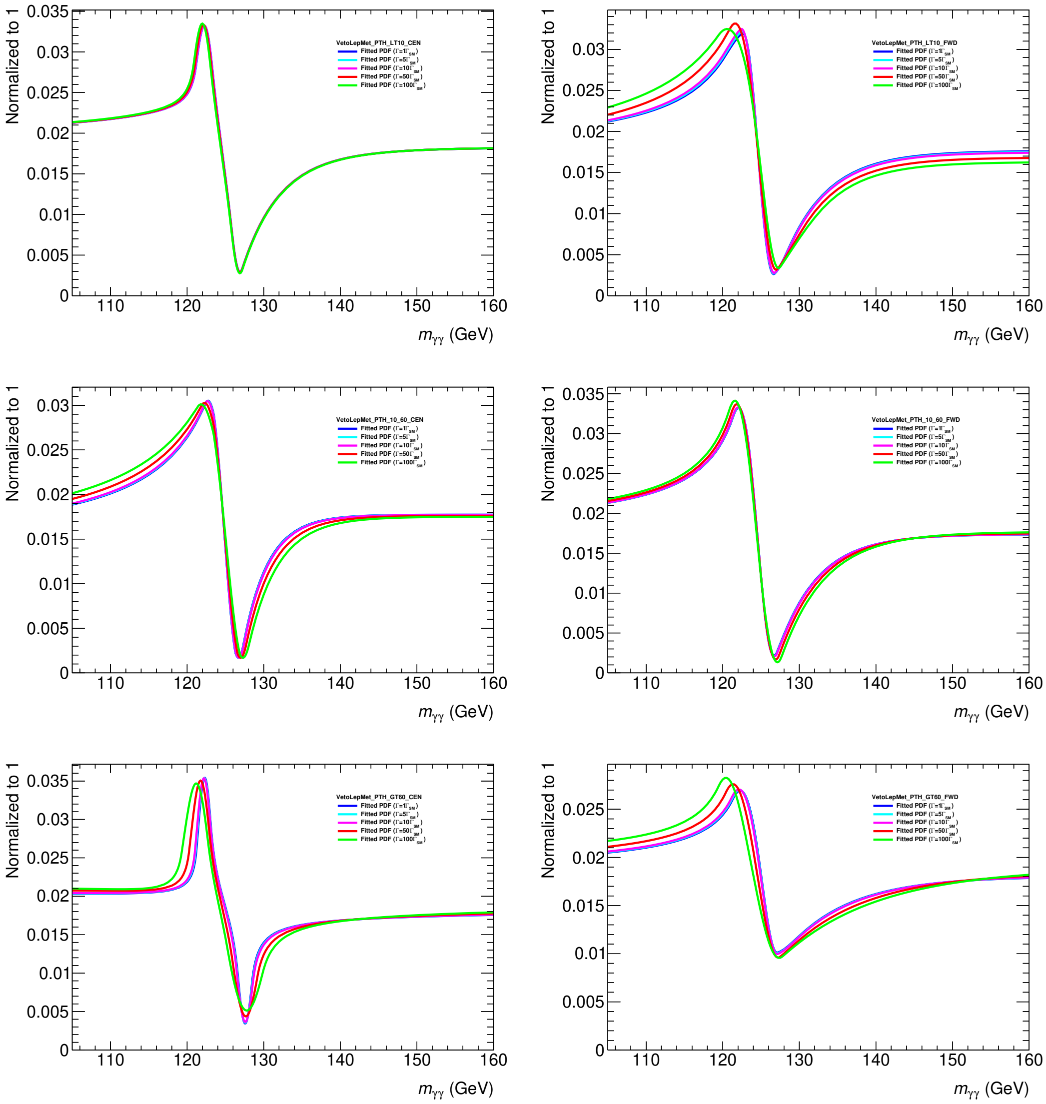

Figure A.2: Interference lineshape evaluated at different λ points for all the reconstructed categories of the analysis, using the alternative parametrization.

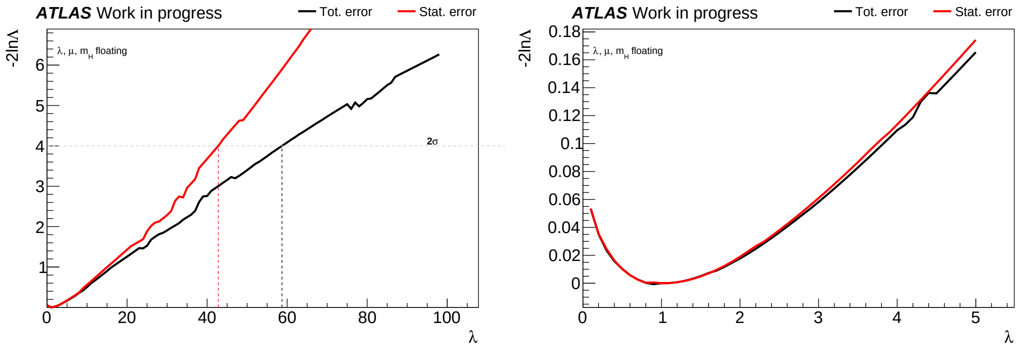

Figure A.3: Expected profile likelihood scan of the λ POI, for configuration 3, using the alternative parametrization. Focus on the region around the minimum (right plot).

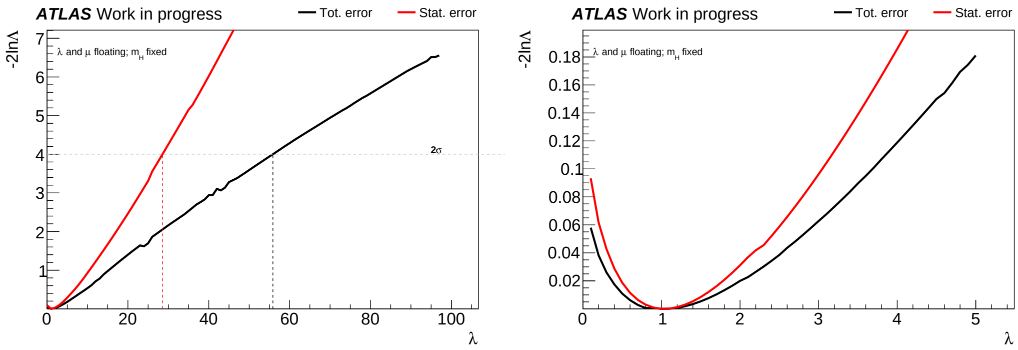

Figure A.4: Expected profile likelihood scan of the λ POI, for configuration 2, using the alternative parametrization. Focus on the region around the minimum (right plot).

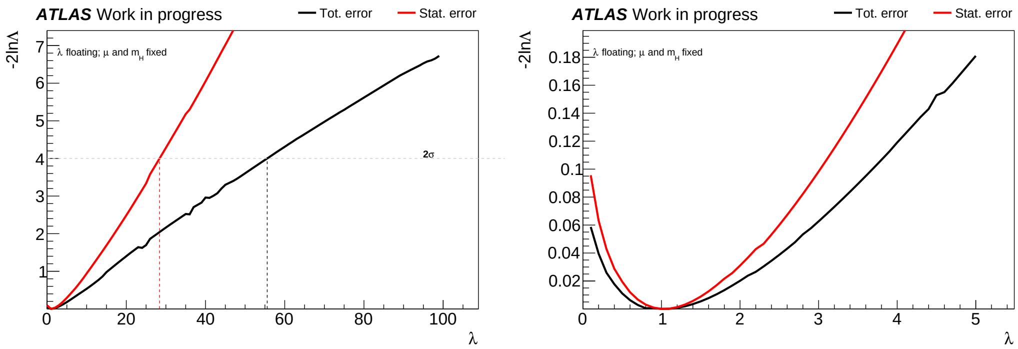

Figure A.5: Expected profile likelihood scan of the λ POI, for configuration 1, using the alternative parametrization. Focus on the region around the minimum (right plot).

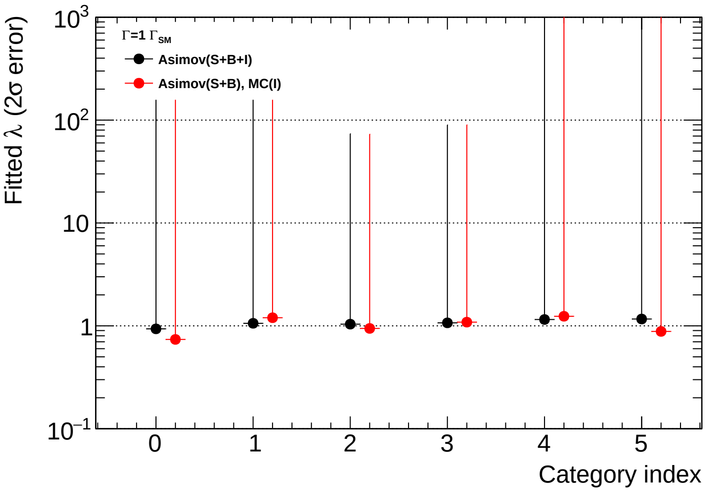

Figure A.6: Results of the injection test and comparison with the nominal Asimov fit results per category, using the alternative parametrization.

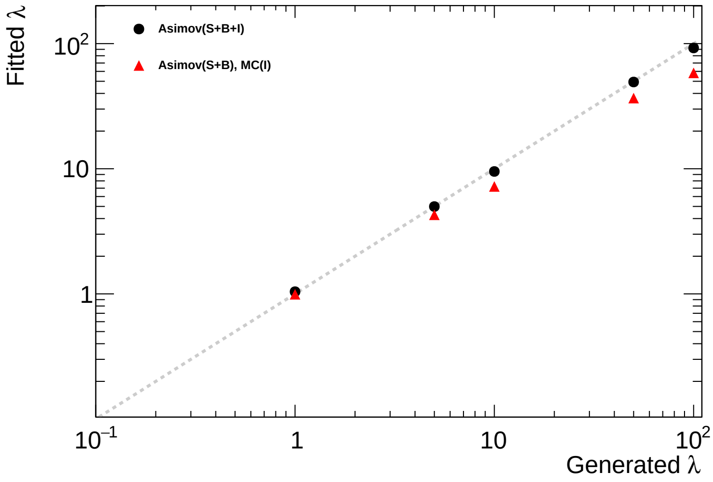

Figure A.7: (x-axis title: Generated λ) Results of the injection test and comparison with the nominal Asimov fit results for each of the 5 width points, using the alternative parametrization. The bottom panel shows the difference with respect to the gray dashed line. Uncertainty on the red points is evaluated with a bootstrap.

List of Tables

List of Figures

Bibliography

[1] The ATLAS Collaboration. « Observation of a new particle in the search for the Standard Model Higgs boson with the ATLAS detector at the LHC ». In: (2012). DOI: `10.1016/j.physletb.2012.08.020`. eprint: `arXiv:1207.7214`.

[2] Sheldon L. Glashow. « Partial-symmetries of weak interactions ». In: *Nuclear Physics* 22.4 (1961), pp. 579 –588. ISSN: 0029-5582. DOI: `https://doi.org/10.1016/0029-5582(61)90469-2`. URL: `http://www.sciencedirect.com/science/article/pii/0029558261904692`.

[3] Steven Weinberg. « A Model of Leptons ». In: *Phys. Rev. Lett.* 19 (21 1967), pp. 1264–1266. DOI: `10.1103/PhysRevLett.19.1264`. URL: `https://link.aps.org/doi/10.1103/PhysRevLett.19.1264`.

[4] Abdus Salam. « Weak and Electromagnetic Interactions ». In: *Conf. Proc.* C680519 (1968), pp. 367–377.

[5] *CERN website.* URL: `https://home.cern/about`.

[6] G. 't Hooft and M. Veltman. « Regularization and renormalization of gauge fields ». In: *Nuclear Physics B* 44.1 (1972), pp. 189–213. ISSN: 0550-3213. DOI: `https://doi.org/10.1016/0550-3213(72)90279-9`. URL: `https://www.sciencedirect.com/science/article/pii/0550321372902799`.

[7] G. 't Hooft. « Dimensional regularization and the renormalization group ». In: *Nuclear Physics B* 61 (1973), pp. 455–468. ISSN: 0550-3213. DOI: `https://doi.org/10.1016/0550-3213(73)90376-3`. URL: `https://www.sciencedirect.com/science/article/pii/0550321373903763`.

[8] D. J. Gross and F. Wilczek. « Ultraviolet Behavior of Non-Abelian Gauge Theories ». In: *Physical Review Letters* 30 (June 1973), pp. 1343–1346. DOI: `10.1103/PhysRevLett.30.1343`.

[9] H. David Politzer. « Reliable Perturbative Results for Strong Interactions? » In: *Phys. Rev. Lett.* 30 (26 1973), pp. 1346–1349. DOI: `10.1103/PhysRevLett.30.1346`. URL: `https://link.aps.org/doi/10.1103/PhysRevLett.30.1346`.

[10] ATLAS Collaboration. « Determination of the strong coupling constant α_s from transverse energy-energy correlations in multijet events at $\sqrt{s} = 8$ TeV using the ATLAS detector ». In: (2017). DOI: `10.1140/epjc/s10052-017-5442-0`. eprint: `arXiv:1707.02562`.

[11] John C. Collins, Davison E. Soper, and George Sterman. « Factorization of Hard Processes in QCD ». In: (2004). eprint: `arXiv:hep-ph/0409313`.

[12] Guido Altarelli and G. Parisi. « Asymptotic Freedom in Parton Language ». In: *Nucl. Phys.* B126 (1977), pp. 298–318. DOI: `10.1016/0550-3213(77)90384-4`.

[13] Yuri L. Dokshitzer. « Calculation of the Structure Functions for Deep Inelastic Scattering and e+ e- Annihilation by Perturbation Theory in Quantum Chromodynamics. » In: *Sov. Phys. JETP* 46 (1977). [Zh. Eksp. Teor. Fiz.73,1216(1977)], pp. 641–653.

[14] V. N. Gribov and L. N. Lipatov. « Deep inelastic e p scattering in perturbation theory ». In: *Sov. J. Nucl. Phys.* 15 (1972). [Yad. Fiz.15,781(1972)], pp. 438–450.

[15] Sayipjamal Dulat et al. « New parton distribution functions from a global analysis of quantum chromodynamics ». In: *Phys. Rev. D* 93 (3 2016), p. 033006. DOI: `10.1103/PhysRevD.93.033006`. URL: `https://link.aps.org/doi/10.1103/PhysRevD.93.033006`.

[16] Torbjorn Sjostrand, Stephen Mrenna, and Peter Skands. « PYTHIA 6.4 Physics and Manual ». In: (2006). DOI: `10.1088/1126-6708/2006/05/026`. eprint: `arXiv:hep-ph/0603175`.

[17] T. Gleisberg et al. « Event generation with SHERPA 1.1 ». In: (2008). DOI: `10.1088/1126-6708/2009/02/007`. eprint: `arXiv:0811.4622`.

[18] George Sterman and Steven Weinberg. « Jets from Quantum Chromodynamics ». In: *Phys. Rev. Lett.* 39 (23 1977), pp. 1436–1439. DOI: `10.1103/PhysRevLett.39.1436`. URL: `https://link.aps.org/doi/10.1103/PhysRevLett.39.1436`.

[19] Matteo Cacciari. *Phenomenological and theoretical developments in jet physics at the LHC*. 2015. eprint: `arXiv:1509.02272`.

[20] Peter W. Higgs. « Broken Symmetries and the Masses of Gauge Bosons ». In: *Phys. Rev. Lett.* 13 (16 1964), pp. 508–509. DOI: `10.1103/PhysRevLett.13.508`. URL: `https://link.aps.org/doi/10.1103/PhysRevLett.13.508`.

[21] F. Englert and R. Brout. « Broken Symmetry and the Mass of Gauge Vector Mesons ». In: *Phys. Rev. Lett.* 13 (9 1964), pp. 321–323. DOI: `10.1103/PhysRevLett.13.321`. URL: `https://link.aps.org/doi/10.1103/PhysRevLett.13.321`.

[22] G. S. Guralnik, C. R. Hagen, and T. W. B. Kibble. « Global Conservation Laws and Massless Particles ». In: *Phys. Rev. Lett.* 13 (20 1964), pp. 585–587. DOI: `10.1103/PhysRevLett.13.585`. URL: `https://link.aps.org/doi/10.1103/PhysRevLett.13.585`.

[23] Jeffrey Goldstone, Abdus Salam, and Steven Weinberg. « Broken Symmetries ». In: *Phys. Rev.* 127 (3 1962), pp. 965–970. DOI: `10.1103/PhysRev.127.965`. URL: `https://link.aps.org/doi/10.1103/PhysRev.127.965`.

[24] Chris Quigg. *LHC Physics Potential vs. Energy*. 2009. eprint: `arXiv:0908.3660`.

[25] Charalampos Anastasiou et al. « High precision determination of the gluon fusion Higgs boson cross-section at the LHC ». In: *Journal of High Energy Physics* 2016.5 (May 2016). DOI: `10.1007/jhep05(2016)058`. URL: `https://doi.org/10.1007/jhep05(2016)058`.

[26] Stefano Actis et al. « NLO electroweak corrections to Higgs boson production at hadron colliders ». In: *Physics Letters B* 670.1 (Dec. 2008), pp. 12–17. DOI: `10.1016/j.physletb.2008.10.018`. URL: `https://doi.org/10.1016/j.physletb.2008.10.018`.

[27] Charalampos Anastasiou, Radja Boughezal, and Frank Petriello. ≪ Mixed QCD-electroweak corrections to Higgs boson production in gluon fusion ≫. In: *Journal of High Energy Physics* 2009.04 (2009), pp. 003–003. DOI: `10.1088/1126-6708/2009/04/003`. URL: `https://doi.org/10.1088/1126-6708/2009/04/003`.

[28] Matteo Cacciari et al. ≪ Fully Differential Vector-Boson-Fusion Higgs Production at Next-to-Next-to-Leading Order ≫. In: *Phys. Rev. Lett.* 115 (8 2015), p. 082002. DOI: `10.1103/PhysRevLett.115.082002`. URL: `https://link.aps.org/doi/10.1103/PhysRevLett.115.082002`.

[29] Ansgar Denner et al. ≪ HAWK 2.0: A Monte Carlo program for Higgs production in vector-boson fusion and Higgs strahlung at hadron colliders ≫. In: *Computer Physics Communications* 195 (Oct. 2015), pp. 161–171. DOI: `10.1016/j.cpc.2015.04.021`. URL: `https://doi.org/10.1016/j.cpc.2015.04.021`.

[30] Oliver Brein, Abdelhak Djouadi, and Robert Harlander. ≪ NNLO QCD corrections to the Higgs-strahlung processes at hadron colliders ≫. In: *Physics Letters B* 579.1-2 (Jan. 2004), pp. 149–156. DOI: `10.1016/j.physletb.2003.10.112`. URL: `https://doi.org/10.1016/j.physletb.2003.10.112`.

[31] Oliver Brein, Robert V. Harlander, and Tom J.E. Zirke. ≪ vh@nnlo—Higgs Strahlung at hadron colliders ≫. In: *Computer Physics Communications* 184.3 (Mar. 2013), pp. 998–1003. DOI: `10.1016/j.cpc.2012.11.002`. URL: `https://doi.org/10.1016/j.cpc.2012.11.002`.

[32] Robert V. Harlander, Stefan Liebler, and Tom Zirke. ≪ Higgs Strahlung at the Large Hadron Collider in the 2-Higgs-doublet model ≫. In: *Journal of High Energy Physics* 2014.2 (Feb. 2014). DOI: `10.1007/jhep02(2014)023`. URL: `https://doi.org/10.1007/jhep02(2014)023`.

[33] Lukas Altenkamp et al. ≪ Gluon-induced Higgs-strahlung at next-to-leading order QCD ≫. In: *Journal of High Energy Physics* 2013.2 (Feb. 2013). DOI: `10.1007/jhep02(2013)078`. URL: `https://doi.org/10.1007/jhep02(2013)078`.

[34] L. Reina and S. Dawson. ≪ Next-to-Leading Order Results for $t\bar{t}h$ Production at the Tevatron ≫. In: *Phys. Rev. Lett.* 87 (20 2001), p. 201804. DOI: `10.1103/PhysRevLett.87.201804`. URL: `https://link.aps.org/doi/10.1103/PhysRevLett.87.201804`.

[35] S. Dawson et al. ≪ Next-to-leading order QCD corrections to $p\ \vec{p}\ t\bar{t}h$ at the CERN Large Hadron Collider ≫. In: *Phys. Rev. D* 67 (7 2003), p. 071503. DOI: `10.1103/PhysRevD.67.071503`. URL: `https://link.aps.org/doi/10.1103/PhysRevD.67.071503`.

[36] S. Dawson et al. ≪ Associated Higgs boson production with top quarks at the CERN Large Hadron Collider: NLO QCD corrections ≫. In: *Phys. Rev. D* 68 (3 2003), p. 034022. DOI: `10.1103/PhysRevD.68.034022`. URL: `https://link.aps.org/doi/10.1103/PhysRevD.68.034022`.

[37] W. Beenakker et al. ≪ Higgs Radiation Off Top Quarks at the Tevatron and the LHC ≫. In: *Phys. Rev. Lett.* 87 (20 2001), p. 201805. DOI: `10.1103/PhysRevLett.87.201805`. URL: `https://link.aps.org/doi/10.1103/PhysRevLett.87.201805`.

[38] W. Beenakker et al. ≪ NLO QCD corrections to ttH production in hadron collisions ≫. In: *Nuclear Physics B* 653.1-2 (Mar. 2003), pp. 151–203. DOI: `10.1016/s0550-3213(03)00044-0`. URL: `https://doi.org/10.1016/s0550-3213(03)00044-0`.

[39] Yu Zhang et al. ≪ QCD NLO and EW NLO corrections to ttH production with top quark decays at hadron collider ≫. In: *Physics Letters B* 738 (Nov. 2014), pp. 1–5. DOI: `10.1016/j.physletb.2014.09.022`. URL: `https://doi.org/10.1016/j.physletb.2014.09.022`.

[40] S. Frixione et al. ≪ Weak corrections to Higgs hadroproduction in association with a top-quark pair ≫. In: *Journal of High Energy Physics* 2014.9 (Sept. 2014). DOI: `10.1007/jhep09(2014)065`. URL: `https://doi.org/10.1007/jhep09(2014)065`.

[41] S. Frixione et al. ≪ Electroweak and QCD corrections to top-pair hadroproduction in association with heavy bosons ≫. In: *Journal of High Energy Physics* 2015.6 (June 2015). DOI: `10.1007/jhep06(2015)184`. URL: `https://doi.org/10.1007/jhep06(2015)184`.

[42] LHC Higgs Cross Section Working Group. ≪ Handbook of LHC Higgs Cross Sections: 4. Deciphering the Nature of the Higgs Sector ≫. In: (2016). DOI: `10.23731/CYRM-2017-002`. eprint: `arXiv:1610.07922`.

[43] G. Abbiendi. ≪ Search for the Standard Model Higgs Boson at LEP ≫. In: (2003). DOI: `10.1016/S0370-2693(03)00614-2`. eprint: `arXiv:hep-ex/0306033`.

[44] The CDF Collaboration et al. *Updated Combination of CDF and D0 Searches for Standard Model Higgs Boson Production with up to 10.0 fb-1 of Data.* 2012. eprint: `arXiv:1207.0449`.

[45] The ALEPH Collaboration et al. ≪ Precision Electroweak Measurements on the Z Resonance ≫. In: (2005). DOI: `10.1016/j.physrep.2005.12.006`. eprint: `arXiv:hep-ex/0509008`.

[46] The CMS Collaboration. ≪ Observation of a new boson at a mass of 125 GeV with the CMS experiment at the LHC ≫. In: (2012). DOI: `10.1016/j.physletb.2012.08.021`. eprint: `arXiv:1207.7235`.

[47] ATLAS and CMS Collaborations. ≪ Combined Measurement of the Higgs Boson Mass in pp Collisions at $\sqrt{s} = 7$ and 8 TeV with the ATLAS and CMS Experiments ≫. In: (2015). DOI: `10.1103/PhysRevLett.114.191803`. eprint: `arXiv:1503.07589`.

[48] ATLAS Collaboration. ≪ Study of the spin and parity of the Higgs boson in diboson decays with the ATLAS detector ≫. In: (2015). DOI: `10.1140/epjc/s10052-015-3685-1`. eprint: `arXiv:1506.05669`.

[49] ATLAS and CMS Collaborations. ≪ Measurements of the Higgs boson production and decay rates and constraints on its couplings from a combined ATLAS and CMS analysis of the LHC pp collision data at $\sqrt{s} = 7$ and 8 TeV ≫. In: (2016). DOI: `10.1007/JHEP08(2016)045`. eprint: `arXiv:1606.02266`.

[50] ATLAS Collaboration. *Observation of* $H \to b\bar{b}$ *decays and* VH *production with the ATLAS detector.* 2018. eprint: `arXiv:1808.08238`.

[51] A. M. Sirunyan et al. ≪ Evidence for Higgs boson decay to a pair of muons ≫. In: *Journal of High Energy Physics* 2021.1 (Jan. 2021). DOI: `10.1007/jhep01(2021)148`. URL: `https://doi.org/10.1007/jhep01(2021)148`.

[52] M. Aaboud et al. ≪ Measurement of the Higgs boson mass in the $H \to ZZ^* \to 4l$ and $H \to \gamma\gamma$ channels with $\sqrt{s} = 13$ TeV *pp* collisions using the ATLAS detector ≫. In: *Physics Letters B* 784 (2018), pp. 345–366. ISSN: 0370-2693. DOI: `https://doi.org/10.1016/j.physletb.2018.07.050`. URL: `https://www.sciencedirect.com/science/article/pii/S0370269318305884`.

[53] ATLAS Collaboration. ≪ Measurement of the Higgs boson mass from the $H \to \gamma\gamma$ and $H \to ZZ^* \to 4\ell$ channels with the ATLAS detector using 25 fb^{-1} of *pp* collision data ≫. In: (2014). DOI: `10.1103/PhysRevD.90.052004`. eprint: `arXiv:1406.3827`.

[54] *Constraints on the Higgs boson width from off-shell production and decay to ZZ to llll and llvv.* Tech. rep. Geneva: CERN, 2014. URL: `https://cds.cern.ch/record/1670066`.

[55] *Evidence for off-shell Higgs boson production and first measurement of its width.* Tech. rep. Geneva: CERN, 2021. URL: `https://cds.cern.ch/record/2784590`.

[56] ATLAS Collaboration. ≪ Constraints on off-shell Higgs boson production and the Higgs boson total width in $ZZ \to 4\ell$ and $ZZ \to 2\ell 2\nu$ final states with the ATLAS detector ≫. In: (2018). DOI: `10.1016/j.physletb.2018.09.048`. eprint: `arXiv:1808.01191`.

[57] John Campbell et al. ≪ Interference in the $gg \to h \to \gamma\gamma$ On-Shell Rate and the Higgs Boson Total Width ≫. In: (2017). DOI: `10.1103/PhysRevLett.119.181801`. eprint: `arXiv:1704.08259`.

[58] Lance J. Dixon and Ye Li. ≪ Bounding the Higgs Boson Width Through Interferometry ≫. In: (2013). DOI: `10.1103/PhysRevLett.111.111802`. eprint: `arXiv:1305.3854`.

[59] Stephen P. Martin. ≪ Interference of Higgs diphoton signal and background in production with a jet at the LHC ≫. In: (2013). DOI: `10.1103/PhysRevD.88.013004`. eprint: `arXiv:1303.3342`.

[60] F. Coradeschi et al. ≪ Interference effects in the $H(\to \gamma\gamma) + 2$ jets channel at the LHC ≫. In: (2015). DOI: `10.1103/PhysRevD.92.013004`. eprint: `arXiv:1504.05215`.

[61] *Estimate of the m_H shift due to interference between signal and background processes in the $H \to \gamma\gamma$ channel, for the $\sqrt{s} = 8$ TeV dataset recorded by ATLAS.* Tech. rep. ATL-PHYS-PUB-2016-009. Geneva: CERN, 2016. URL: `http://cds.cern.ch/record/2146386`.

[62] J. R. Andersen et al. *Les Houches 2015: Physics at TeV Colliders Standard Model Working Group Report.* 2016. eprint: `arXiv:1605.04692`.

[63] Nicolas Berger et al. *Simplified Template Cross Sections - Stage 1.1.* 2019. eprint: `arXiv:1906.02754`.

[64] S. Amoroso et al. *Les Houches 2019: Physics at TeV Colliders: Standard Model Working Group Report.* 2020. eprint: `arXiv:2003.01700`.

[65] ATLAS Collaboration. *Measurements of Higgs boson properties in the diphoton decay channel with 36 fb^{-1} of pp collision data at $\sqrt{s} = 13$ TeV with the ATLAS detector.* 2018. eprint: `arXiv:1802.04146`.

[66] The ATLAS Collaboration. ≪ The ATLAS Experiment at the CERN Large Hadron Collider ≫. In: *Journal of Instrumentation* 3.08 (2008), S08003. URL: `http://stacks.iop.org/1748-0221/3/i=08/a=S08003`.

[67] S. Chatrchyan et al. « The CMS Experiment at the CERN LHC ». In: *JINST* 3 (2008), S08004. DOI: `10.1088/1748-0221/3/08/S08004`.

[68] K. Aamodt et al. « The ALICE experiment at the CERN LHC ». In: *JINST* 3 (2008), S08002. DOI: `10.1088/1748-0221/3/08/S08002`.

[69] A. Augusto Alves Jr. et al. « The LHCb Detector at the LHC ». In: *JINST* 3 (2008), S08005. DOI: `10.1088/1748-0221/3/08/S08005`.

[70] Lyndon Evans and Philip Bryant. « LHC Machine ». In: *JINST* 3 (2008), S08001. DOI: `10.1088/1748-0221/3/08/S08001`.

[71] *ATLAS experiment - public results*. URL: `https://twiki.cern.ch/twiki/bin/view/AtlasPublic/LuminosityPublicResultsRun2`.

[72] The ATLAS Collaboration. *Luminosity public results*. URL: `https://twiki.cern.ch/twiki/bin/view/AtlasPublic/LuminosityPublicResultsRun2#Multiple_Year_Collision_Plots`.

[73] *Pile-up corrections for jets from proton-proton collisions at $\sqrt{s} = 7$ TeV in ATLAS in 2011*. Tech. rep. ATLAS-CONF-2012-064. Geneva: CERN, 2012. URL: `https://cds.cern.ch/record/1459529`.

[74] B. Abbott et al. « Production and Integration of the ATLAS Insertable B-Layer ». In: *JINST* 13.05 (2018), T05008. DOI: `10.1088/1748-0221/13/05/T05008`. arXiv: `1803.00844 [physics.ins-det]`.

[75] The ATLAS Collaboration. *ATLAS detector and physics performance: Technical Design Report, 1*. Technical design report. ATLAS. Geneva: CERN, 1999. URL: `https://cds.cern.ch/record/391176`.

[76] A. Hrynevich. « Performance of the ATLAS Tile Calorimeter ». In: *Journal of Instrumentation* 12.06 (2017), pp. C06021–C06021. DOI: `10.1088/1748-0221/12/06/c06021`. URL: `https://doi.org/10.1088/1748-0221/12/06/c06021`.

[77] ATLAS Collaboration. « Performance of the ATLAS Trigger System in 2015 ». In: (2016). DOI: `10.1140/epjc/s10052-017-4852-3`. eprint: `arXiv:1611.09661`.

[78] ATLAS Collaboration. « Electron and photon performance measurements with the ATLAS detector using the 2015-2017 LHC proton-proton collision data ». In: (2019). DOI: `10.1088/1748-0221/14/12/P12006`. eprint: `arXiv:1908.00005`.

[79] *Photon identification in 2015 ATLAS data*. Tech. rep. ATL-PHYS-PUB-2016-014. Geneva: CERN, 2016. URL: `https://cds.cern.ch/record/2203125`.

[80] ATLAS Collaboration. « Topological cell clustering in the ATLAS calorimeters and its performance in LHC Run 1 ». In: (2016). DOI: `10.1140/epjc/s10052-017-5004-5`. eprint: `arXiv:1603.02934`.

[81] Matteo Cacciari, Gavin P. Salam, and Gregory Soyez. « The anti-k_t jet clustering algorithm ». In: (2008). DOI: `10.1088/1126-6708/2008/04/063`. eprint: `arXiv:0802.1189`.

[82] ATLAS Collaboration. « Measurements of Higgs boson properties in the diphoton decay channel with 36 fb^{-1} of pp collision data at $\sqrt{s} = 13$ TeV with the ATLAS detector ». In: (2018). DOI: `10.1103/PhysRevD.98.052005`. eprint: `arXiv:1802.04146`.

[83] G. Aad et al. ≪ Performance of pile-up mitigation techniques for jets in *pp* collisions a $\sqrt{s} = 8$ TeV using the ATLAS detector ≫. In: *The European Physical Journal C* 76.11 (Oct. 2016). DOI: `10.1140/epjc/s10052-016-4395-z`. URL: `https://doi.org/10.1140/epjc/s10052-016-4395-z`.

[84] ATLAS Collaboration. ≪ ATLAS b-jet identification performance and efficiency measurement with $t\bar{t}$ events in *pp* collisions at $\sqrt{s} = 13$ TeV ≫. In: (2019). DOI: `10.1140/epjc/s10052-019-7450-8`. eprint: `arXiv:1907.05120`.

[85] ATLAS Collaboration. *Jet energy scale and resolution measured in proton-proton collisions at* $\sqrt{s} = 13$ *TeV with the ATLAS detector*. 2020. eprint: `arXiv:2007.02645`.

[86] ATLAS Collaboration. ≪ Muon reconstruction performance of the ATLAS detector in proton–proton collision data at $\sqrt{s}$=13 TeV ≫. In: (2016). DOI: `10.1140/epjc/s10052-016-4120-y`. eprint: `arXiv:1603.05598`.

[87] D et al. Adams. *Recommendations of the Physics Objects and Analysis Harmonisation Study Groups 2014*. Tech. rep. ATL-COM-PHYS-2014-451. Geneva: CERN, 2014. URL: `https://cds.cern.ch/record/1700874`.

[88] ATLAS Collaboration. ≪ Performance of missing transverse momentum reconstruction with the ATLAS detector using proton-proton collisions at $\sqrt{s} = 13$ TeV ≫. In: (2018). DOI: `10.1140/epjc/s10052-018-6288-9`. eprint: `arXiv:1802.08168`.

[89] G. Aad et al. ≪ Electron and photon energy calibration with the ATLAS detector using LHC Run 1 data ≫. In: *The European Physical Journal C* 74.10 (Oct. 2014). DOI: `10.1140/epjc/s10052-014-3071-4`. URL: `https://doi.org/10.1140/epjc/s10052-014-3071-4`.

[90] M. Aaboud et al. ≪ Electron and photon energy calibration with the ATLAS detector using 2015–2016 LHC proton-proton collision data ≫. In: *Journal of Instrumentation* 14.03 (2019), P03017–P03017. DOI: `10.1088/1748-0221/14/03/p03017`. URL: `https://doi.org/10.1088/1748-0221/14/03/p03017`.

[91] Marco Delmastro, Luca Franco, and Guillaume Unal. *Intercalibration of the Liquid Argon electronic High and Medium gain using special* $Z \to e^+e^-$ *data*. Tech. rep. (restricted access). Geneva: CERN, 2020. URL: `https://cds.cern.ch/record/2725589`.

[92] C Becot et al. ≪ Difference of energy response between the high and medium gain of the ATLAS electromagnetic calorimeter ≫. In: (2013). (restricted access). URL: `https://cds.cern.ch/record/1637736`.

[93] Georges Aad et al. ≪ Electron performance measurements with the ATLAS detector using the 2010 LHC proton-proton collision data ≫. In: *Eur. Phys. J.* C72 (2012), p. 1909. DOI: `10.1140/epjc/s10052-012-1909-1`. arXiv: `1110.3174 [hep-ex]`.

[94] Martin Aleksa et al. ≪ Calibration stability, uniformity and linearity measurements of electrons and photons ≫. In: (2017). (restricted access). URL: `https://cds.cern.ch/record/2268802`.

[95] ATLAS Collaboration. ≪ Electron and photon energy calibration with the ATLAS detector using 2015–2016 LHC proton-proton collision data ≫. In: *JINST* 14.03 (2019), P03017. DOI: `10.1088/1748-0221/14/03/P03017`. arXiv: `1812.03848 [hep-ex]`.

[96] L Courneyea et al. ≪ Computation and validation of the electronic calibration constants for the ATLAS Liquid Argon Calorimeters ≫. In: (2010). (restricted access). URL: `https://cds.cern.ch/record/1278462`.

[97] Fanti Marcello. Private communication.

[98] Laurent Serin. Private communication.

[99] Guillaume Unal. Private communication.

[100] Davide Mungo. Private communication.

[101] *Measurement of the properties of Higgs boson production at* $\sqrt{s}$*=13 TeV in the* $H \rightarrow \gamma\gamma$ *channel using 139* fb^{-1} *of pp collision data with the ATLAS experiment.* Tech. rep. All figures including auxiliary figures are available at https://atlas.web.cern.ch/Atlas/GROUPS/PHYSICS/CONFNOTES/ATLAS-CONF-2020-026. Geneva: CERN, 2020. URL: `https://cds.cern.ch/record/2725727`.

[102] ATLAS Collaboration. *Luminosity determination in pp collisions at* $\sqrt{s} = 13$ *TeV using the ATLAS detector at the LHC.* ATLAS-CONF-2019-021. 2019. URL: `https://cds.cern.ch/record/2677054`.

[103] G. Avoni et al. ≪ The new LUCID-2 detector for luminosity measurement and monitoring in ATLAS ≫. In: *JINST* 13.07 (2018), P07017. DOI: `10.1088/1748-0221/13/07/P07017`.

[104] ATLAS Collaboration. ≪ ATLAS data quality operations and performance for 2015–2018 data-taking ≫. In: *JINST* 15 (2020), P04003. DOI: `10.1088/1748-0221/15/04/P04003`. arXiv: `1911.04632 [physics.ins-det]`.

[105] ATLAS Collaboration. ≪ Performance of electron and photon triggers in ATLAS during LHC Run 2 ≫. In: *Eur. Phys. J. C* 80 (2020), p. 47. DOI: `10.1140/epjc/s10052-019-7500-2`. arXiv: `1909.00761 [hep-ex]`.

[106] Keith Hamilton et al. ≪ NNLOPS simulation of Higgs boson production ≫. In: (2013). DOI: `10.1007/JHEP10(2013)222`. eprint: `arXiv:1309.0017`.

[107] Paolo Nason. ≪ A New Method for Combining NLO QCD with Shower Monte Carlo Algorithms ≫. In: (2004). DOI: `10.1088/1126-6708/2004/11/040`. eprint: `arXiv:hep-ph/0409146`.

[108] Stefano Frixione, Paolo Nason, and Carlo Oleari. ≪ Matching NLO QCD computations with Parton Shower simulations: the POWHEG method ≫. In: (2007). DOI: `10.1088/1126-6708/2007/11/070`. eprint: `arXiv:0709.2092`.

[109] Simone Alioli et al. ≪ A general framework for implementing NLO calculations in shower Monte Carlo programs: the POWHEG BOX ≫. In: (2010). DOI: `10.1007/JHEP06(2010)043`. eprint: `arXiv:1002.2581`.

[110] Paolo Nason and Carlo Oleari. ≪ NLO Higgs boson production via vector-boson fusion matched with shower in POWHEG ≫. In: (2009). DOI: `10.1007/JHEP02(2010)037`. eprint: `arXiv:0911.5299`.

[111] Ken Mimasu, Veronica Sanz, and Ciaran Williams. ≪ Higher order QCD predictions for associated Higgs production with anomalous couplings to gauge bosons ≫. In: *JHEP* 08 (2016), p. 039. DOI: `10.1007/JHEP08(2016)039`. arXiv: `1512.02572 [hep-ph]`.

[112] John M. Campbell et al. ≪ NLO Higgs boson production plus one and two jets using the POWHEG BOX, MadGraph4 and MCFM ≫. In: *JHEP* 07 (2012), p. 092. DOI: `10.1007/JHEP07(2012)092`. arXiv: `1202.5475 [hep-ph]`.

[113] Gionata Luisoni et al. « $HW^{\pm}$/HZ + 0 and 1 jet at NLO with the POWHEG BOX interfaced to GoSam and their merging within MiNLO ». In: *JHEP* 10 (2013), p. 083. DOI: `10.1007/JHEP10(2013)083`. arXiv: `1306.2542 [hep-ph]`.

[114] Heribertus B. Hartanto et al. « Higgs boson production in association with top quarks in the POWHEG BOX ». In: *Phys. Rev. D* 91.9 (2015), p. 094003. DOI: `10.1103/PhysRevD.91.094003`. arXiv: `1501.04498 [hep-ph]`.

[115] Jon Butterworth et al. « PDF4LHC recommendations for LHC Run II ». In: (2015). DOI: `10.1088/0954-3899/43/2/023001`. eprint: `arXiv:1510.03865`.

[116] Torbjörn Sjöstrand, Stephen Mrenna, and Peter Skands. « A Brief Introduction to PYTHIA 8.1 ». In: (2007). DOI: `10.1016/j.cpc.2008.01.036`. eprint: `arXiv:0710.3820`.

[117] Torbjörn Sjöstrand et al. « An introduction to PYTHIA 8.2 ». In: *Comput. Phys. Commun.* 191 (2015), pp. 159–177. DOI: `10.1016/j.cpc.2015.01.024`. arXiv: `1410.3012 [hep-ph]`.

[118] ATLAS Collaboration. « Measurement of the Z/γ^* boson transverse momentum distribution in pp collisions at $\sqrt{s} = 7$ TeV with the ATLAS detector ». In: (2014). DOI: `10.1007/JHEP09(2014)145`. eprint: `arXiv:1406.3660`.

[119] Keith Hamilton, Paolo Nason, and Giulia Zanderighi. « MINLO: Multi-Scale Improved NLO ». In: *JHEP* 10 (2012), p. 155. DOI: `10.1007/JHEP10(2012)155`. arXiv: `1206.3572 [hep-ph]`.

[120] Keith Hamilton et al. « Merging H/W/Z + 0 and 1 jet at NLO with no merging scale: a path to parton shower + NNLO matching ». In: *JHEP* 05 (2013), p. 082. DOI: `10.1007/JHEP05(2013)082`. arXiv: `1212.4504 [hep-ph]`.

[121] Stefano Catani and Massimiliano Grazzini. « An NNLO subtraction formalism in hadron collisions and its application to Higgs boson production at the LHC ». In: *Phys. Rev. Lett.* 98 (2007), p. 222002. DOI: `10.1103/PhysRevLett.98.222002`. arXiv: `hep-ph/0703012 [hep-ph]`.

[122] Giuseppe Bozzi et al. « Transverse-momentum resummation and the spectrum of the Higgs boson at the LHC ». In: *Nucl. Phys. B* 737 (2006), pp. 73–120. DOI: `10.1016/j.nuclphysb.2005.12.022`. arXiv: `hep-ph/0508068 [hep-ph]`.

[123] Daniel de Florian et al. « Transverse-momentum resummation: Higgs boson production at the Tevatron and the LHC ». In: *JHEP* 11 (2011), p. 064. DOI: `10.1007/JHEP11(2011)064`. arXiv: `1109.2109 [hep-ph]`.

[124] Stefano Frixione, Paolo Nason, and Giovanni Ridolfi. « A positive-weight next-to-leading-order Monte Carlo for heavy flavour hadroproduction ». In: *JHEP* 09 (2007), p. 126. DOI: `10.1088/1126-6708/2007/09/126`. arXiv: `0707.3088 [hep-ph]`.

[125] NNPDF Collaboration, R.D. Ball et al. « Parton distributions for the LHC Run II ». In: *JHEP* 04 (2015), p. 040. DOI: `10.1007/JHEP04(2015)040`. arXiv: `1410.8849 [hep-ph]`.

[126] *ATLAS Pythia 8 tunes to 7 TeV data.* Tech. rep. All figures including auxiliary figures are available at https://atlas.web.cern.ch/Atlas/GROUPS/PHYSICS/PUBNOTES/ATL-PHYS-PUB-2014-021. Geneva: CERN, 2014. URL: `https://cds.cern.ch/record/1966419`.

[127] D. J. Lange. ≪ The EvtGen particle decay simulation package ≫. In: *Nucl. Instrum. Meth. A* 462 (2001), p. 152. DOI: `10.1016/S0168-9002(01)00089-4`.

[128] Pierre Artoisenet et al. ≪ Automatic spin-entangled decays of heavy resonances in Monte Carlo simulations ≫. In: *JHEP* 03 (2013), p. 015. DOI: `10.1007/JHEP03(2013)015`. arXiv: `1212.3460 [hep-ph]`.

[129] Stefano Frixione et al. ≪ Single-top hadroproduction in association with a W boson ≫. In: *JHEP* 07 (2008), p. 029. DOI: `10.1088/1126-6708/2008/07/029`. arXiv: `0805.3067 [hep-ph]`.

[130] Federico Demartin et al. ≪ tWH associated production at the LHC ≫. In: *Eur. Phys. J. C* 77.1 (2017), p. 34. DOI: `10.1140/epjc/s10052-017-4601-7`. arXiv: `1607.05862 [hep-ph]`.

[131] Johannes Bellm et al. ≪ Herwig 7.1 Release Note ≫. In: (2017). arXiv: `1705.06919 [hep-ph]`.

[132] Johannes Bellm et al. ≪ Herwig 7.0/Herwig++ 3.0 release note ≫. In: *Eur. Phys. J. C* 76.4 (2016), p. 196. DOI: `10.1140/epjc/s10052-016-4018-8`. arXiv: `1512.01178 [hep-ph]`.

[133] J. Alwall et al. ≪ The automated computation of tree-level and next-to-leading order differential cross sections, and their matching to parton shower simulations ≫. In: *JHEP* 07 (2014), p. 079. DOI: `10.1007/JHEP07(2014)079`. arXiv: `1405.0301 [hep-ph]`.

[134] Rikkert Frederix and Stefano Frixione. ≪ Merging meets matching in MC@NLO ≫. In: *JHEP* 12 (2012), p. 061. DOI: `10.1007/JHEP12(2012)061`. arXiv: `1209.6215 [hep-ph]`.

[135] The ATLAS Collaboration. ≪ The ATLAS Simulation Infrastructure ≫. In: (2010). DOI: `10.1140/epjc/s10052-010-1429-9`. eprint: `arXiv:1005.4568`.

[136] Geant4 Collaboration. ≪ Geant4—a simulation toolkit ≫. In: *Nuclear Instruments and Methods in Physics Research Section A: Accelerators, Spectrometers, Detectors and Associated Equipment* 506.3 (2003), pp. 250 –303. ISSN: 0168-9002. DOI: `https://doi.org/10.1016/S0168-9002(03)01368-8`. URL: `http://www.sciencedirect.com/science/article/pii/S0168900203013688`.

[137] Charalampos Anastasiou et al. ≪ Higgs Boson Gluon-Fusion Production in QCD at Three Loops ≫. In: *Phys. Rev. Lett.* 114 (2015), p. 212001. DOI: `10.1103/PhysRevLett.114.212001`. arXiv: `1503.06056 [hep-ph]`.

[138] Falko Dulat, Achilleas Lazopoulos, and Bernhard Mistlberger. ≪ iHixs 2 – Inclusive Higgs cross sections ≫. In: *Comput. Phys. Commun.* 233 (2018), pp. 243–260. DOI: `10.1016/j.cpc.2018.06.025`. arXiv: `1802.00827 [hep-ph]`.

[139] Robert V. Harlander and Kemal J. Ozeren. ≪ Finite top mass effects for hadronic Higgs production at next-to-next-to-leading order ≫. In: *JHEP* 11 (2009), p. 088. DOI: `10.1088/1126-6708/2009/11/088`. arXiv: `0909.3420 [hep-ph]`.

[140] Robert V. Harlander and Kemal J. Ozeren. ≪ Top mass effects in Higgs production at next-to-next-to-leading order QCD: Virtual corrections ≫. In: *Phys. Lett. B* 679 (2009), pp. 467–472. DOI: `10.1016/j.physletb.2009.08.012`. arXiv: `0907.2997 [hep-ph]`.

[141] Robert V. Harlander et al. « Higgs production in gluon fusion at next-to-next-to-leading order QCD for finite top mass ». In: *Eur. Phys. J. C* 66 (2010), pp. 359–372. DOI: `10.1140/epjc/s10052-010-1258-x`. arXiv: `0912.2104 [hep-ph]`.

[142] Alexey Pak, Mikhail Rogal, and Matthias Steinhauser. « Finite top quark mass effects in NNLO Higgs boson production at LHC ». In: *JHEP* 02 (2010), p. 025. DOI: `10.1007/JHEP02(2010)025`. arXiv: `0911.4662 [hep-ph]`.

[143] S. Actis et al. « NLO Electroweak Corrections to Higgs Boson Production at Hadron Colliders ». In: (2008). DOI: `10.1016/j.physletb.2008.10.018`. eprint: `arXiv:0809.1301`.

[144] Stefano Actis et al. « NNLO computational techniques: The cases $H \to \gamma\gamma$ and $H \to gg$ ». In: *Nucl. Phys. B* 811 (2009), pp. 182–273. DOI: `10.1016/j.nuclphysb.2008.11.024`. arXiv: `0809.3667 [hep-ph]`.

[145] Marco Bonetti, Kirill Melnikov, and Lorenzo Tancredi. « Higher order corrections to mixed QCD-EW contributions to Higgs boson production in gluon fusion ». In: *Phys. Rev. D* 97.5 (2018). [Erratum: Phys. Rev. D 97 (2018) 099906], p. 056017. DOI: `10.1103/PhysRevD.97.056017`. arXiv: `1801.10403 [hep-ph]`.

[146] U. Aglietti et al. « Two-loop light fermion contribution to Higgs production and decays ». In: *Phys. Lett. B* 595 (2004), pp. 432–441. DOI: `10.1016/j.physletb.2004.06.063`. arXiv: `hep-ph/0404071`.

[147] ATLAS Collaboration. « Measurement of the Higgs boson coupling properties in the $H \to ZZ^* \to 4\ell$ decay channel at $\sqrt{s} = 13$ TeV with the ATLAS detector ». In: *JHEP* 03 (2018), p. 095. DOI: `10.1007/JHEP03(2018)095`. arXiv: `1712.02304 [hep-ex]`.

[148] E. Bagnaschi et al. « Higgs production via gluon fusion in the POWHEG approach in the SM and in the MSSM ». In: *JHEP* 02 (2012), p. 088. DOI: `10.1007/JHEP02(2012)088`. arXiv: `1111.2854 [hep-ph]`.

[149] Keith Hamilton, Paolo Nason, and Giulia Zanderighi. « Finite quark-mass effects in the NNLOPS POWHEG+MiNLO Higgs generator ». In: *JHEP* 05 (2015), p. 140. DOI: `10.1007/JHEP05(2015)140`. arXiv: `1501.04637 [hep-ph]`.

[150] M. Ciccolini, A. Denner, and S. Dittmaier. « Strong and electroweak corrections to the production of Higgs+2jets via weak interactions at the LHC ». In: (2007). DOI: `10.1103/PhysRevLett.99.161803`. eprint: `arXiv:0707.0381`.

[151] Mariano Ciccolini, Ansgar Denner, and Stefan Dittmaier. « Electroweak and QCD corrections to Higgs production via vector-boson fusion at the LHC ». In: (2007). DOI: `10.1103/PhysRevD.77.013002`. eprint: `arXiv:0710.4749`.

[152] Paolo Bolzoni et al. « Higgs production via vector-boson fusion at NNLO in QCD ». In: (2010). DOI: `10.1103/PhysRevLett.105.011801`. eprint: `arXiv:1003.4451`.

[153] Robert V. Harlander et al. « vh@nnlo-v2: new physics in Higgs Strahlung ». In: *JHEP* 05 (2018), p. 089. DOI: `10.1007/JHEP05(2018)089`. arXiv: `1802.04817 [hep-ph]`.

[154] Oliver Brein, Abdelhak Djouadi, and Robert Harlander. « NNLO QCD corrections to the Higgs-strahlung processes at hadron colliders ». In: *Phys. Lett. B* 579 (2004), pp. 149–156. DOI: `10.1016/j.physletb.2003.10.112`. arXiv: `hep-ph/0307206`.

[155] Oliver Brein et al. ≪ Top-Quark Mediated Effects in Hadronic Higgs-Strahlung ≫. In: *Eur. Phys. J. C* 72 (2012), p. 1868. DOI: `10.1140/epjc/s10052-012-1868-6`. arXiv: `1111.0761 [hep-ph]`.

[156] Robert V. Harlander et al. ≪ Soft gluon resummation for gluon-induced Higgs Strahlung ≫. In: *JHEP* 11 (2014), p. 082. DOI: `10.1007/JHEP11(2014)082`. arXiv: `1410.0217 [hep-ph]`.

[157] M. L. Ciccolini, S. Dittmaier, and M. Krämer. ≪ Electroweak radiative corrections to associated WH and ZH production at hadron colliders ≫. In: *Phys. Rev. D* 68 (2003), p. 073003. DOI: `10.1103/PhysRevD.68.073003`. arXiv: `hep-ph/0306234 [hep-ph]`.

[158] W. Beenakker et al. ≪ NLO QCD corrections to $t\bar{t}H$ production in hadron collisions ≫. In: *Nucl. Phys. B* 653 (2003), pp. 151–203. DOI: `10.1016/S0550-3213(03)00044-0`. arXiv: `hep-ph/0211352`.

[159] S. Dawson et al. ≪ Associated Higgs production with top quarks at the large hadron collider: NLO QCD corrections ≫. In: *Phys. Rev. D* 68 (2003), p. 034022. DOI: `10.1103/PhysRevD.68.034022`. arXiv: `hep-ph/0305087`.

[160] Yu Zhang et al. ≪ QCD NLO and EW NLO corrections to $t\bar{t}H$ production with top quark decays at hadron collider ≫. In: *Phys. Lett. B* 738 (2014), pp. 1–5. DOI: `10.1016/j.physletb.2014.09.022`. arXiv: `1407.1110 [hep-ph]`.

[161] S. Frixione et al. ≪ Electroweak and QCD corrections to top-pair hadroproduction in association with heavy bosons ≫. In: *JHEP* 06 (2015), p. 184. DOI: `10.1007/JHEP06(2015)184`. arXiv: `1504.03446 [hep-ph]`.

[162] S. Dawson et al. ≪ Exclusive Higgs boson production with bottom quarks at hadron colliders ≫. In: *Phys. Rev. D* 69 (2004), p. 074027. DOI: `10.1103/PhysRevD.69.074027`. arXiv: `hep-ph/0311067`.

[163] Stefan Dittmaier, Michael Krämer, and Michael Spira. ≪ Higgs radiation off bottom quarks at the Tevatron and the CERN LHC ≫. In: *Phys. Rev. D* 70 (2004), p. 074010. DOI: `10.1103/PhysRevD.70.074010`. arXiv: `hep-ph/0309204`.

[164] Robert Harlander, Michael Kramer, and Markus Schumacher. *Bottom-quark associated Higgs-boson production: reconciling the four- and five-flavour scheme approach.* 2011. arXiv: `1112.3478 [hep-ph]`.

[165] Federico Demartin et al. ≪ Higgs production in association with a single top quark at the LHC ≫. In: *Eur. Phys. J. C* 75 (2015), p. 267. DOI: `10.1140/epjc/s10052-015-3475-9`. arXiv: `1504.00611 [hep-ph]`.

[166] A. Djouadi, J. Kalinowski, and M. Spira. ≪ HDECAY: a Program for Higgs Boson Decays in the Standard Model and its Supersymmetric Extension ≫. In: (1997). DOI: `10.1016/S0010-4655(97)00123-9`. eprint: `arXiv:hep-ph/9704448`.

[167] Michael Spira. ≪ QCD Effects in Higgs physics ≫. In: *Fortsch. Phys.* 46 (1998), pp. 203–284. DOI: `10.1002/(SICI)1521-3978(199804)46:3<203::AID-PROP203>3.0.CO;2-4`. arXiv: `hep-ph/9705337`.

[168] A. Djouadi, M. M. Muhlleitner, and M. Spira. ≪ Decays of Supersymmetric Particles: the program SUSY-HIT (SUspect-SdecaY-Hdecay-InTerface) ≫. In: (2006). eprint: `arXiv:hep-ph/0609292`.

[169] A. Bredenstein et al. « Radiative corrections to the semileptonic and hadronic Higgs-boson decays $H \to WW/ZZ \to 4$ fermions ». In: (2006). DOI: 10.1088/1126-6708/2007/02/080. eprint: arXiv:hep-ph/0611234.

[170] A. Bredenstein et al. « Precise predictions for the Higgs-boson decay H —¿ WW/ZZ —¿ 4 leptons ». In: *Phys. Rev. D* 74 (2006), p. 013004. DOI: 10.1103/PhysRevD.74.013004. arXiv: hep-ph/0604011 [hep-ph].

[171] A. Bredenstein et al. « Precision calculations for the Higgs decays H —¿ ZZ/WW —¿ 4 leptons ». In: *Nucl. Phys. Proc. Suppl.* 160 (2006). [,131(2006)], pp. 131–135. DOI: 10.1016/j.nuclphysbps.2006.09.104. arXiv: hep-ph/0607060 [hep-ph].

[172] Enrico Bothmann et al. « Event Generation with Sherpa 2.2 ». In: *SciPost Phys.* 7.3 (2019), p. 034. DOI: 10.21468/SciPostPhys.7.3.034. arXiv: 1905.09127 [hep-ph].

[173] Tanju Gleisberg and Stefan Höche. « Comix, a new matrix element generator ». In: *JHEP* 12 (2008), p. 039. DOI: 10.1088/1126-6708/2008/12/039. arXiv: 0808.3674 [hep-ph].

[174] Federico Buccioni et al. « OpenLoops 2 ». In: *Eur. Phys. J. C* 79.10 (2019), p. 866. DOI: 10.1140/epjc/s10052-019-7306-2. arXiv: 1907.13071 [hep-ph].

[175] Fabio Cascioli, Philipp Maierhöfer, and Stefano Pozzorini. « Scattering Amplitudes with Open Loops ». In: *Phys. Rev. Lett.* 108 (2012), p. 111601. DOI: 10.1103/PhysRevLett.108.111601. arXiv: 1111.5206 [hep-ph].

[176] Ansgar Denner, Stefan Dittmaier, and Lars Hofer. « Collier: A fortran-based complex one-loop library in extended regularizations ». In: *Comput. Phys. Commun.* 212 (2017), pp. 220–238. DOI: 10.1016/j.cpc.2016.10.013. arXiv: 1604.06792 [hep-ph].

[177] Steffen Schumann and Frank Krauss. « A parton shower algorithm based on Catani-Seymour dipole factorisation ». In: (2007). DOI: 10.1088/1126-6708/2008/03/038. eprint: arXiv:0709.1027.

[178] Stefan Höche et al. « A critical appraisal of NLO+PS matching methods ». In: *JHEP* 09 (2012), p. 049. DOI: 10.1007/JHEP09(2012)049. arXiv: 1111.1220 [hep-ph].

[179] Stefan Höche et al. « QCD matrix elements + parton showers. The NLO case ». In: *JHEP* 04 (2013), p. 027. DOI: 10.1007/JHEP04(2013)027. arXiv: 1207.5030 [hep-ph].

[180] S. Catani et al. « QCD Matrix Elements + Parton Showers ». In: *JHEP* 11 (2001), p. 063. DOI: 10.1088/1126-6708/2001/11/063. arXiv: hep-ph/0109231.

[181] Stefan Hoeche et al. « QCD matrix elements and truncated showers ». In: (2009). DOI: 10.1088/1126-6708/2009/05/053. eprint: arXiv:0903.1219.

[182] Frank Siegert. « A practical guide to event generation for prompt photon production with Sherpa ». In: *J. Phys. G* 44.4 (2017), p. 044007. DOI: 10.1088/1361-6471/aa5f29. arXiv: 1611.07226 [hep-ph].

[183] Stefano Frixione. « Isolated photons in perturbative QCD ». In: *Phys. Lett. B* 429 (1998), pp. 369–374. DOI: 10.1016/S0370-2693(98)00454-7. arXiv: hep-ph/9801442.

[184] Richard D. Ball et al. « Parton distributions with LHC data ». In: *Nucl. Phys. B* 867 (2013), pp. 244–289. DOI: `10.1016/j.nuclphysb.2012.10.003`. arXiv: `1207.1303 [hep-ph]`.

[185] *The Pythia 8 A3 tune description of ATLAS minimum bias and inelastic measurements incorporating the Donnachie-Landshoff diffractive model.* Tech. rep. All figures including auxiliary figures are available at https://atlas.web.cern.ch/Atlas/GROUPS/PI PHYS-PUB-2016-017. Geneva: CERN, 2016. URL: `https://cds.cern.ch/record/2206965`.

[186] Charalampos Anastasiou, Radja Boughezal, and Frank Petriello. « Mixed QCD-electroweak corrections to Higgs boson production in gluon fusion ». In: (2008). DOI: `10.1088/1126-6708/2009/04/003`. eprint: `arXiv:0811.3458`.

[187] Ansgar Denner et al. « Electroweak corrections to Higgs-strahlung off W/Z bosons at the Tevatron and the LHC with HAWK ». In: *JHEP* 03 (2012), p. 075. DOI: `10.1007/JHEP03(2012)075`. arXiv: `1112.5142 [hep-ph]`.

[188] ATLAS Collaboration. « Measurement of Higgs boson production in the diphoton decay channel in *pp* collisions at center-of-mass energies of 7 and 8 TeV with the ATLAS detector ». In: (2014). DOI: `10.1103/PhysRevD.90.112015`. eprint: `arXiv:1408.7084`.

[189] ATLAS Collaboration. *Measurements and interpretations of Higgs-boson fiducial cross sections in the diphoton decay channel using* $139\,fb^{-1}$ *of pp collision data at* $\sqrt{s} = 13$ *TeV with the ATLAS detector*. ATLAS-CONF-2019-029. 2019. URL: `https://cds.cern.ch/record/2682800`.

[190] ATLAS Collaboration. « Study of the CP properties of the interaction of the Higgs boson with top quarks using top quark associated production of the Higgs boson and its decay into two photons with the ATLAS detector at the LHC ». In: (Apr. 2020). arXiv: `2004.04545 [hep-ex]`.

[191] Guolin Ke et al. « LightGBM: A Highly Efficient Gradient Boosting Decision Tree ». In: *Advances in Neural Information Processing Systems 30.* Ed. by I. Guyon et al. Curran Associates, Inc., 2017, pp. 3146–3154. URL: `http://papers.nips.cc/paper/6907-lightgbm-a-highly-efficient-gradient-boosting-decision-tree.pdf`.

[192] D. V. Lindley. « On a Measure of the Information Provided by an Experiment ». In: *Ann. Math. Statist.* 27.4 (Dec. 1956), pp. 986–1005. DOI: `10.1214/aoms/1177728069`. URL: `https://doi.org/10.1214/aoms/1177728069`.

[193] ATLAS Collaboration. « Measurements of Higgs boson properties in the diphoton decay channel with 80 fb^{-1} of *pp* collision data at $\sqrt{s} = 13$ TeV with the ATLAS detector ». In: (2018). ATLAS-CONF-2018-028. URL: `http://cdsweb.cern.ch/record/2628771`.

[194] Glen Cowan et al. « Asymptotic formulae for likelihood-based tests of new physics ». In: *Eur. Phys. J. C* 71 (2011), p. 1554. DOI: `10.1140/epjc/s10052-011-1554-0`. arXiv: `1007.1727 [physics.data-an]`. Erratum: Eur. Phys. J. C73 (2013) 2501.

[195] Sepp Hochreiter and Jürgen Schmidhuber. « Long Short-Term Memory ». In: *Neural Computation* 9 (1997), pp. 1735–1780.

[196] M. Oreglia. « A Study of the Reactions $\psi' \to \gamma\gamma\psi$ ». thesis. Dec. 1980.

[197] ATLAS Collaboration. « Search for Scalar Diphoton Resonances in the Mass Range 65–600 GeV with the ATLAS Detector in pp Collision Data at $\sqrt{s} = 8\,\text{TeV}$ ». In: *Phys. Rev. Lett.* 113 (2014), p. 171801. DOI: `10.1103/PhysRevLett.113.171801`. arXiv: `1407.6583 [hep-ex]`.

[198] Bernstein, S. « Démonstration du Théorème de Weierstrass fondée sur le calcul des Probabilités ». In: *Comm. Soc. Math. Kharkov* 13 (1912), p. 1.

[199] Xiaohui Liu and Frank Petriello. « Reducing theoretical uncertainties for exclusive Higgs-boson plus one-jet production at the LHC ». In: *Phys. Rev. D* 87.9 (2013), p. 094027. DOI: `10.1103/PhysRevD.87.094027`. arXiv: `1303.4405 [hep-ph]`.

[200] Iain W. Stewart et al. « Jet p_T Resummation in Higgs Production at $NNLL' + NNLO$ ». In: *Phys. Rev. D* 89.5 (2014), p. 054001. DOI: `10.1103/PhysRevD.89.054001`. arXiv: `1307.1808 [hep-ph]`.

[201] Radja Boughezal et al. « Combining resummed Higgs predictions across jet bins ». In: *Phys. Rev. D* 89 (2014), p. 074044. DOI: `10.1103/PhysRevD.89.074044`. arXiv: `1312.4535 [hep-ph]`.

[202] Iain W. Stewart and Frank J. Tackmann. « Theory uncertainties for Higgs and other searches using jet bins ». In: *Phys. Rev. D* 85 (2012), p. 034011. DOI: `10.1103/PhysRevD.85.034011`. arXiv: `1107.2117 [hep-ph]`.

[203] Shireen Gangal and Frank J. Tackmann. « Next-to-leading-order uncertainties in Higgs+2 jets from gluon fusion ». In: *Phys. Rev. D* 87.9 (2013), p. 093008. DOI: `10.1103/PhysRevD.87.093008`. arXiv: `1302.5437 [hep-ph]`.

[204] ATLAS Collaboration. « Measurements of the Higgs boson inclusive and differential fiducial cross sections in the 4ℓ decay channel at $\sqrt{s} = 13\,\text{TeV}$ ». In: *Eur. Phys. J.* (2020). arXiv: `2004.03969 [hep-ex]`.

[205] ATLAS Collaboration. « Measurements of fiducial cross-sections for $t\bar{t}$ production with one or two additional b-jets in pp collisions at $\sqrt{s} = 8\,\text{TeV}$ using the ATLAS detector ». In: *Eur. Phys. J. C* 76 (2016), p. 11. DOI: `10.1140/epjc/s10052-015-3852-4`. arXiv: `1508.06868 [hep-ex]`.

[206] ATLAS Collaboration. « Measurement of differential production cross-sections for a Z boson in association with b-jets in 7 TeV proton–proton collisions with the ATLAS detector ». In: *JHEP* 10 (2014), p. 141. DOI: `10.1007/JHEP10(2014)141`. arXiv: `1407.3643 [hep-ex]`.

[207] ATLAS Collaboration. « Measurement of the cross-section for W boson production in association with b-jets in pp collisions at $\sqrt{s} = 7\,\text{TeV}$ with the ATLAS detector ». In: *JHEP* 06 (2013), p. 084. DOI: `10.1007/JHEP06(2013)084`. arXiv: `1302.2929 [hep-ex]`.

[208] Alexander L. Read. « Presentation of search results: the CL_S technique ». In: *J. Phys. G* 28 (2002), p. 2693. DOI: `10.1088/0954-3899/28/10/313`.

Acknowledgements

At this point, I think that it is important to spend a few words to mention some people who, in one way or another, have been part of the journey that was my PhD.

First of all, I want to express my most sincere and deep gratitude to my supervisor Marco. It is needless to say that without him this thesis wouldn't be what it is, so I will focus on what is not so obvious. When Marco welcomed me in Annecy almost four years ago, I was super excited to start my research career with the person who probably inspired me to study physics at the university in the first place, next to the place where I had always dreamt to work since I was in high school. He fueled my enthusiasm for particle physics everyday since then, always guiding me towards the right decisions, giving the wisest advice and literally teaching me plenty of lessons, about physics but not only. Thank you very much for giving me the opportunity to do my thesis at LAPP, it has been an honor and a pleasure.

I want to thank all the members of my jury, first for having the patience to read so carefully my manuscript, then for giving so many useful suggestions, and finally for attending my defense in Annecy. I had the chance to discuss individually with each of you in different occasions and from each conversation I took away so much knowledge.

To my analysis teammates of the ATLAS HGam subgroup, Ana, Ashley, Davide, Stefano, I say thank you for being just one Skype message away from me and for helping me whenever I needed. It was a pleasure to work with you and I really hope to continue to collaborate again in the future.

To all the people whom I met during my stay at LAPP, especially the colleagues of the ATLAS group and the community of postdocs and PhD students of the lab, thanks for being so nice and kind with me. Here I have learnt the importance of being in a welcoming and positive working environment. I enjoyed a lot the lunches, coffee breaks and moments of conviviality that we have spent together, both at LAPP and *Around the lake*. I will miss them.

A very special mention goes to my officemate, PhDmate and true friend Mohamed: we shared so much together and I am very happy that we did. I like the fact that we could always count on one another, that we always celebrated each other's achievements and that we have never been in competition one with another, even when we were in competition for real! Good luck to both of us with our next adventures!
And I can't forget to mention Francesco! Who has been like an older brother to the two of us during the entire course of our PhDs, always available to hear our problems and complaints and always ready to provide us with support, protection, wisdom, a lot of

help, sometimes some pranks, a little bit of laughs and our daily dose of procrastination.

To Cicco, Davide and my brother Marcolino, who travelled across all Italy just to see my "performance": thank you very much, it felt really good to have a small group of supporters in the most crucial moment, it meant a lot to me. In particular thanks, Davide, for showing me the ways of the *DM method*. I still have much to learn but I hope that you, as its inventor, are proud of my progresses.

I also want to thank my parents. Since when I was at the university, they gave me the opportunity to do what I liked the most, they always trusted my choices and they never put any pressure on me. In moments like this, it's beautiful to see the pride in their eyes.

Last but absolutely not least, Giovanna: you are the only person who knows exactly what I have been through during these years. You were there every single moment and you know how many sacrifices I did and how much effort I put in this. Thank you for believing in me, even when I myself didn't, and for the unconditional support that you give me everyday.